University of Oxford

D.Phil. Thesis

# Fluid injection and migration in layered aquifers

Luke T. Jenkins

*Supervisors:* Prof. C. W. MacMinn and Prof. J. A. Cartwright


*A thesis submitted for the degree of Doctor of Philosophy*

Department of Earth Sciences

Exeter College

Trinity Term 2019

# Declaration of Authorship

I, Luke T. Jenkins, declare that this project, titled 'Fluid injection and migration in layered aquifers' and the work presented in it are my own. I hereby certify that the work presented in this project is all my own unaided work and that all material obtained from published or unpublished sources of any type, including the internet, have been fully acknowledged at the proper point in the text and included in the list of references.

Signed: 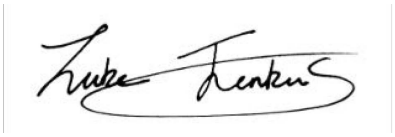

Date: 15-Feb-2020

# Abstract

Large-scale fluid injection into the subsurface is important for a number of industrial applications, including the injection and storage of $CO_2$ for the mitigation of anthropogenic climate change. A vast amount of seismic data suggests that vertical heterogeneity dominates the distribution of fluids in layered aquifers. However, most studies of fluid injection typically neglect layering. This thesis aims to characterise the fundamental dynamics of subsurface fluid injection and migration in a layered aquifer system. This goal is achieved via the derivation of a novel theoretical model that is both accurate and computationally efficient. This vertically integrated sharp-interface model utilises a weakly compressible gravity-current formulation that accounts for vertical flow of water and gas across a stratified system—consisting of relatively thick higher permeability aquifers, alternating with thinner and much lower permeability seals. The coupling with vertical water leakage, and the corresponding vertical dissipation of pressure out of the injection aquifer, is found to have a leading-order role on lateral gas migration. Results demonstrate that vertical pressure dissipation acts to significantly reduce the lateral extent of the plume. Furthermore, vertical pressure dissipation has a significant impact on gas leakage—which occurs when a capillary entry threshold is exceeded—by controlling the magnitude, and style, of capillary pressure buildup. Results further indicate that distributed $CO_2$ leakage during $CO_2$ injection into layered aquifers—such as at Sleipner—is more likely than previously considered. As the model developed here retains the plume shape and pressure field at the end of injection, the model can be used to provide unique insights into post-injection migration. Results suggest that due to the strongly tongued shape present at the end of $CO_2$ injection, a period of stagnant lateral migration occurs after an initial phase of depressurisation, and before the transition towards late-time self-similar spreading.

# Extended Abstract

The injection of fluids into the subsurface is important for several industrial applications and natural processes, including large-scale $CO_2$ injection for carbon capture and storage (CCS)—a strategy for mitigating the effects of anthropogenic climate change. Despite seismic evidence that demonstrates the leading order importance of geological stratification on the injection and migration of fluids in the subsurface, most previous studies of fluid injection neglect layering. In this thesis, a novel reduced-order theoretical model is derived to explore the injection of a buoyant non-wetting phase—namely 'gas' (e.g., $CO_2$ )—into a layered aquifer system that is otherwise saturated with ambient water. Through reference cases motivated by CCS, this thesis subsequently explores the interplay between the physical mechanisms that govern two-phase fluid dynamics in a stratified aquifer.

The domain used throughout this thesis consists of a regular layering of relatively thick and highly permeable 'aquifers' that are separated by relatively thin, low permeability, 'seals'. For simplicity, the system is bounded at its base and top by impermeable seals (i.e. boundary conditions of no vertical flow). The aquifer system is laterally extensive over 10-100s of kilometres, and has a cumulative thickness on the order of 100s of meters. These systems naturally involve high-aspect-ratio flows that prompt many of the fundamental assumptions of the theoretical model developed in this thesis. For simplicity, the aquifers and seals are uniform in their distribution of parameters.

The model invokes a classical gravity current approach, by assuming that two immiscible fluids are strongly segregated by gravity, such that a region primarily saturated with gas resides above a region fully saturated with water. A crucial aspect of this work is the accurate modelling of pressure buildup during fluid injection into a stratified aquifer. As such, both of the fluids and the rock matrix are assumed to be weakly compressible. By neglecting capillary effects, the model assumes that the gas and water are separated by a sharp interface. Models for

a gravity current in a single aquifer assume that vertical fluid motion can be neglected, meaning that the pressure distribution is approximately hydrostatic. The model developed in this thesis relaxes this assumption and includes terms that account for non-hydrostatic contributions associated with weak vertical flow. Invoking vertically integrated mass conversation for each phase within this context leads to a lengthy, but procedurally straightforward, derivation that yields coupled partial differential equations (PDEs) for each fluid that describe lateral transport and pressure propagation in each aquifer. Subsequently applying mass conservation to vertical flow across the seals yields: (a) a coupled system of algebraic equations for vertical water flow and (b) iterative algebraic expressions for vertical gas flow. Vertical integration of conservation of mass means that a 2D planar $(x-z)$ flow is described by a set of coupled 1D PDEs and algebraic equations that solve for the location of the gas-water interface, and the pressure distribution along the interface. In Chapter 2, the accuracy of the model is validated by comparing the pressure distribution arising from water injection into the central aquifer of a seven-aquifer system with the prediction of a full 2D groundwater-flow model. The reduced-order model developed in this thesis is found to accurately reproduce the full 2D pressure field at a fraction ($\sim 1/1200$) of the computational cost—0.4 seconds versus 8 minutes.

Wettability provides two major constraints on vertical fluid leakage in a system of layered aquifers. The wetting phase—water—remains vertically connected, and will therefore always have the potential to leak vertically. The non-wetting phase—nominally gas (e.g., $CO_2$ )—can only leak if the capillary pressure along the base of the seal exceeds an entry threshold associated with the pore structure of the seal rock. In Chapter 2, the entry pressure is assumed to be infinite (or never exceeded). This assumption allows for a systematic study of the controls on, and impacts, of vertical and horizontal pressure dissipation on fluid transport and pressure buildup. In Chapter 3, a finite and exceedable entry pressure is permitted, allowing for the dynamic controls on distributed gas leakage to be studied.

Chapter 2 begins by outlining previous works that study subsurface pressure buildup and fluid migration, mostly within the context of $CO_2$ injection for CCS. There are two main mechanisms that limit $CO_2$ storage capacity: Pressure buildup and fluid migration. A derivation in Chapter 2 combines approaches typically used to separately study each mechanism. Later, it is demonstrated that pressure buildup and fluid migration are intrinsically coupled and should not be considered independently. After a theoretical model is derived for fluid injection in a layered aquifer system, that accounts for vertical water leakage, a non-dimensionalisation exercise is performed to tease out the key dimensionless parameters. A key output of non-dimensionalisation is the leakage number—which measures the resistance of vertical water flow, relative to lateral water flow through the aquifers $[\Lambda_w^s \equiv \lambda_w^s H/(\lambda_w b)]$.

Subsequently, a series of benchmarking exercises are performed to validate the model, and to explore core aspects of the parameter space. For water injection, two endmember limits for pressure buildup are identified. When $\Lambda_w^s = 0$, or is very small, pressure buildup is exclusively confined to the injection layer. For large leakage numbers ($\Lambda_w^s \sim 1/R_A^2$), the seals offers negligible resistance to vertical flow. As such, pressure buildup is vertically uniform across the entire layered system. In both limits, the system of $2N_z$ coupled PDEs reduces to a single PDE that permits analytical solutions that provide excellent agreement with the full model. For intermediate leakage numbers, pressure buildup is more complicated. Comparison with a full 2D groundwater flow model demonstrates the accuracy and computational efficiency of the model for all values $\Lambda_w^s$.

To demonstrate the ability of the model to recover the well-established, leading order controls on the shape of an injected gas plume, the effects of fluid mobility, buoyancy and compressibility are explored in the single-aquifer limit of the model. The characteristic 'tongued' plume shape that arises during $CO_2$ injection is a direct consequence of the strong contrast in mobility between the gas and water.

As $CO_2$ is buoyant and highly mobile ($\mathcal{M} \gg 1$), it will rise and spread. Compressibility acts to compact the plume shape, but has a relatively small impact on the plume shape relative to other parameters.

Finally, the coupling between vertical pressure dissipation and gas migration is explored. It is demonstrated that vertical pressure dissipation acts to compact the plume—markedly reducing the width of the plume at the end of injection. This previously unknown effect is attributed to vertical pressure dissipation reducing the lateral pressure gradient that—alongside buoyancy—drives horizontal flow. Dissipation induced compaction is strengthened by increasing the leakage number or the number of layers in the system. The model additionally accounts for weak vertical water flow in connected residual films through the gas plume. As such, the strength of vertical pressure dissipation upward through the gas plume is controlled by the relative permeability to water in this region ($k^\star_{rw}$). Decreasing $k^\star_{rw}$ suppresses vertical pressure dissipation locally, as well as lateral compaction. However, as pressure dissipation still occurs downwards under the plume and also over length scales much greater than the plume width, $k^\star_{rw}$ has a limited effect on suppressing vertical pressure dissipation. By developing a model that, for the first time, couples pressure dissipation to lateral gas transport, it was demonstrated that both aspects are inherently coupled to one another, and should therefore not be considered independently.

Lastly, it is argued in Chapter 2 that vertical pressure dissipation is likely to have a significant impact on $CO_2$ injection during CCS. For reference parameters, the maximum pressure and plume width—both crucial metrics in identifying storage capacity for $CO_2$ injection—are reduced by about two thirds and by about one third, respectively. The associated compaction of the plume will likely alter trapping associated with capillarity and convective dissolution.

In Chapter 3, the model derived in the previous chapter is extended to include distributed gas leakage, which occurs when a capillary entry threshold is exceeded. As

for water in Chapter 2, the model accounts for non-gas-static contributions to the vertical pressure distribution associated with vertical gas leakage. Otherwise, the derivation, once again, follows an extended version of the classical gravity current formulation. Mass conservation must be applied to vertical gas flow—yielding algebraic expressions for the unknown vertical gas fluxes that provide closure to the system of equations. The capillary entry threshold is imposed through a smoothed step-like function that is evaluated using the globally reconstructed pressure field. Under the insufficient capillary pressure limit (i.e $p_c^{n,T} < p_c^E$) the model derived in Chapter 3 exactly reduces to the model derived in Chapter 2.

The model is non-dimensionalised, introducing an additional grouping that accounts for the relative mobility of both fluids in the seals. To understand the dynamics that govern gas leakage, the model is first applied to the study of capillary pressure buildup in a simple two-aquifer system with an infinite entry pressure. As the capillary pressure is governed by the plume shape and the global pressure distribution, the capillary pressure is inherently coupled to the complex mechanisms governing pressure dissipation outlined in Chapter 2. Mathematical exploration of the governing expression for capillary pressure reveals that two endmember limits exist that produce two contrasting styles of capillary pressure buildup. In the $k_{rw}^{\star} \gg \Lambda_w^s h^n$ limit, vertical water flow is unobstructed by the gas plume and the capillary pressure is given by a phase-static difference taken upwards from the gas-water interface. The resulting capillary pressure distribution mirrors the plume shape and is relatively small in magnitude. In the $k_{rw}^{\star} \ll \Lambda_w^s h^n$ limit, the gas completely obstructs vertical water flow. The contribution from the water to the capillary pressure is hydrostatic through the overlying seal, meaning that the capillary pressure is strongly coupled to vertical pressure dissipation. The resulting capillary pressure distribution is much broader in shape and several orders of magnitude larger than in the $k_{rw}^{\star} \gg \Lambda_w^s h^n$ limit. These limits highlight that the capillary pressure is more strongly coupled to pressure dissipation through the gas plume than previously thought. It is argued that $k_{rw}^{\star}$ is likely to be very small,

and that the capillary pressure may be exceeded in layered aquifers, such as at Sleipner—something previously assumed to be unlikely by several studies.

After the controls of capillary pressure buildup are understood, the capillary entry pressure is taken to be finite and exceedable—allowing for the study on the controls on gas leakage, and interactions with the dynamics of migrating and leaking gas plume. The ability for gas to leak, and the subsequent length scale over which gas leakage occurs, are determined by the magnitude and distribution of the capillary pressure at the top of each gas-bearing aquifer, relative to the entry pressure. The amount of gas leakage is found to result from the interaction between pressure dissipation, capillary pressure buildup, and fluid migration. It is also demonstrated that reducing the relative permeability of water in the gas region can initiate or significantly increase gas leakage.

In Chapter 4, the model derived in Chapters 2 and 3 is used to investigate the dynamics of post-injection gas migration in layered aquifers. Typically, previous studies of post-injection spreading are concerned with the long-term fate of injected $CO_2$. As late-time behaviour is governed by self-similar spreading, these studies typically neglect the imprint from injection by assuming incompressibility (i.e. a hydrostatic pressure distribution) and using a greatly simplified initial plume shape. In Chapter 4, it is argued that retaining the end-of-injection state (i.e. the pressure field and fluid distributions at $t = 1$) is crucial for modelling post-injection migration. The end-of-injection state is governed by dynamics described in detail in earlier chapters. Three distinct regimes of post-injection migration are observed: Depressurisation, stalling and classical gravity current spreading.

Depressurisation is characterised by plume slumping that occurs synchronous to the dissipation of the overpressure from injection. After times have elapsed that are on the scale of tens of injection timescales, the pressure tends toward a phase-static distribution. The rate of depressurisation is governed by the interplay between horizontal and vertical pressure dissipation. As in Chapter 2, bounding

limits for pressure evolution are found for large and very small leakage numbers. Due to the delay in vertically dissipating pressure for intermediate leakage numbers, the pressure in overlying or underlying aquifers can increase for a substantial length of time during post-injection depressurisation. Later, it is argued that depressurisation is a largely overlooked regime that must be fully understood within the context of pressure-limited capacity estimates for $CO_2$ storage.

The subsequent post-injection regime—stalling—is marked by a relatively sudden stagnation in the evolution of the width of the plume. This is a direct consequence of the tongued shape of the plume. After depressurisation has dissipated the overpressure from injection, the nose of the plume advances at a rate that is proportional to the lateral gradient in the thickness of the plume. For a tongued plume, this gradient drives negligible lateral flow. Stalling is not observed during depressurisation, as the overpressure associated with injection drives a decaying lateral flow. Stalling is also not observed for initial plume shapes that are not tongue-like. Plume stalling is likely to be important for post-injection monitoring, particularly because it could easily be confused with secondary trapping mechanisms.

During stalling, the slumping plume drives a thickening front towards the nose, eventually increasing the thickness gradient enough to drive spreading as a classical gravity current. Accordingly, after stalling, the plume asymptotically approaches the late-time spreading regime, for which the width scales as $w \sim t^{1/3}$.

Finally in Chapter 4, a brief study is performed to elucidate the physical mechanisms that lead to the termination of gas leakage. It is shown that gas slumping, gas expansion and pressure dissipation are inherently coupled to one another, producing a complex interplay of competing mechanisms that ultimately set the final fluid distribution in a system of layered aquifers.

The model developed in this thesis constitutes a unique tool for the investigation of pressurisation and migration, both during and after fluid injection in layered

aquifers. The flexibility of the model, combined with its high accuracy and computational efficiency, naturally lends itself to a diverse array of potential applications and extensions that are discussed in detail in Chapter 5.

# *Acknowledgements*

I am indebted to Chris MacMinn for his support, knowledge, and guidance throughout my time in Oxford. I am also grateful to Chris for providing feedback on manuscripts, derivations, various bits of code, and this thesis. I would also like to thank Joe Cartwright for numerous interesting discussions about countless aspects of subsurface flow, and for always trying to ground the theoretical aspects of this work with observations and geophysical data. A special thanks must also be given to Martino Foschi for his support and assistance, and for his work on Vertical Anomaly Clusters which inspired this project.

I'd like to thank my examiners, Marc Hesse and Rich Katz, for their time in reading my thesis, and for facilitating a fascinating and insightful discussion during my viva voce.

My thanks must go to the Department of Earth Sciences, the Department of Engineering Science, and Exeter College for assisting me throughout my DPhil. A special thanks must go to the Middle Common Room of Exeter College for providing a comfortable environment in which I wrote my thesis and consumed innumerable gallons of their coffee.

I feel truly privileged to have so many wonderful friends in Oxford and beyond. It is impossible to list them all, but I would like to thank a special few for keeping me sane. So, thanks to Alistair, Simon, Hilary, Ricky, Ally, Sietske, Lauren, Parker, Roger, Cornelius, Lawrence, Katherine, Becca, Rob, Tom, and Neil.

I'd like to give special thanks to my family for their unwavering support, and for providing me the freedom to pursue my studies. Lastly, I must thank my partner, Naomi, for her constant love and for always having time for me whenever I needed it. To everyone who has supported me over the last four years, I am truly grateful.

# Contents

# Chapter 1

# Introduction

## 1.1 Introduction to carbon capture and storage

### 1.1.1 Climate change

Recent changes in the Earth's climate have been widely attributed to anthropogenic emissions of greenhouse gases (GHGs), notably Carbon Dioxide ($CO_2$) [e.g., Broecker, 1975, Houghton et al., 1996, Feely et al., 2004, Oreskes, 2004, Raupach et al., 2007, Solomon et al., 2007]. An increase in average global temperature is producing a rise in sea level, due to both thermal expansion of the oceans and the melting of grounded ice caps, threatening many coastal population centres with an increased risk of flooding. Additional atmospheric energy is also expected to result in an increase in the frequency and severity of storms and other extreme weather events. A consensus of scientists, the public and an ever-increasing number of policy-makers agree that there is a global obligation to reduce $CO_2$ emissions to minimise the impacts of climate change.

Two broad methods exist for reducing GHG emissions to the atmosphere. The first is producing less GHGs by improving efficiency and reducing societal demand for processes and products that generate GHGs. Significant work has been done on improving the efficiency of combustion processes, which result in the bulk of global

GHG emissions. Furthermore, many governments have introduced legislation to commit to reducing their GHG emissions through gradually 'decarbonising' their energy infrastructure and incentivising citizens and businesses to emit less GHGs. The second emissions reduction approach is to proactively capture and store GHGs before emission to the atmosphere. A promising technology for the reduction of $CO_2$ emissions is geological carbon capture and storage (CCS).

### 1.1.2 Geological carbon capture and storage

Geological carbon capture and storage involves capturing $CO_2$ and injecting in into the subsurface for long-term storage. Two main methods exist for capturing $CO_2$ for subsequent sequestration: separation from concentrated streams at the point of production (e.g., at industrial plants and power stations) and separation directly from atmospheric air [e.g., Benson and Orr, 2008]. In both cases, the very large quantities of captured $CO_2$ must then be injected into the subsurface for secure, long-term storage. This work focuses on the fluid dynamics of $CO_2$ storage in 'deep' porous formations. Below a critical depth $CO_2$ is supercritical, meaning that the $CO_2$ is considerably more dense than at surface—which is beneficial for storage efficiency. The critical point for $CO_2$ is approximately 30.9782 °C and 7.3773 MPa [Lemmon, 1998]. For typical reservoirs this critical point is located at a depth of ∼800 m, above which CCS is impractical. As the supercritical $CO_2$ is less dense, and much less viscous (i.e., more mobile) than the ambient water, the $CO_2$ migrates as a coherent buoyancy-driven plume [e.g., Huppert and Neufeld, 2014]. The interactions between buoyancy and viscosity dominate the leading-order dynamics of $CO_2$ spreading (see Chapter 2).

Two principal physical mechanisms limit the storage capacity of an aquifer: Pressure buildup and $CO_2$ migration [Szulczewski et al., 2012]. $CO_2$ injection must be controlled at a rate that limits pressure buildup to below a threshold associated with geomechanical failure. Furthermore, it must be ensured that the $CO_2$ does

not migrate outside a predesignated target region. Several theoretical studies have outlined the physics that, in principle, enable large quantities (many MT/year) to be securely stored at sites like Sleipner (see 1.1.3, below). However, many of these studies focus on fluid storage in geologically simple systems (e.g., single layer, uniform parameterisation, lateral heterogeneity etc). In reality, the subsurface is extremely heterogeneous across a wide spectrum of scales, and is therefore difficult to characterise. This creates huge uncertainty in the geological model domains in which flow is simulated. Therefore the use of computationally efficient models to simulate multiphase flow, in geologically complex domains, is crucial in understanding the processes that govern the risks associated with storing $CO_2$ in the subsurface. A key aspect of ensuring that $CO_2$ can be stored securely is understanding the role of several mechanisms that act to trap the $CO_2$ in the target formation. These mechanisms, which act on differing timescales, are summarised below.

#### 1.1.2.1 Hydrodynamic trapping

Hydrodynamic trapping—also commonly referred to as structural trapping—is defined, within the context of CCS, as the retention of $CO_2$ in the injection aquifer due to presence of a relatively thick, fine-grained seal or cap rock (e.g., mudstone) that overlies the injection aquifer. The fine grained nature of this overlying seal provides two principal mechanisms to impede leakage of $CO_2$ out of the injection aquifer. First, is that a large capillary entry pressure is required for $CO_2$ to invade the tight, water-wet pores and throats of the overlying seal (see §1.2.3.2). Previous studies have suggested that capillary pressures built-up during $CO_2$ injection are insufficient for $CO_2$ to leak through the overlying seal [e.g., Chadwick et al., 2004, Woods and Farcas, 2009]. Second, the low permeability of the overlying cap rock ensures that if any $CO_2$ invades the overlying seal, the travel time for $CO_2$ flowing in the seal is sufficiently long ($\gg 10^4$ years) that the $CO_2$ remains effectively trapped over 'human timescales' [Bachu et al., 1994]. Global reserves of natural gas

demonstrate that cap rocks can retain buoyant, highly mobile fluids for timescales $\gg 10^6$ years [e.g., Ballentine et al., 2001]. As both hydrocarbon reserves and $CO_2$ in storage sites share similar hydrodynamic sealing properties, site characterisation for CCS can draw on standard techniques from the hydrocarbon industry for assessing trap integrity [Bachu, 2000].

#### 1.1.2.2 Residual trapping

Residual trapping is a direct consequence of wettability—the manifestation of pore-scale interactions between the various interfacial tensions of both fluid phases with the solid rock (see §1.2.3.1). The non-wetting $CO_2$ acts to minimise its surface energy by minimising its contact with the solid surface. Whereas, water—the wetting phase—acts to maximise its contact with the solid surface. During post-injection migration, water displaces the $CO_2$ at the trailing edge of the migrating $CO_2$ plume. During the displacement of $CO_2$ by water, the capillary pressure decreases—destabilising the $CO_2$-water interface, which results in a rapid filling of the pore throats, potentially isolating and immobilising ganglia of $CO_2$ [Roof, 1970, Andrew et al., 2014]. At the macroscopic scale, the migrating $CO_2$ plume leaves behind a zone containing residually trapped ganglia of $CO_2$. The immobilisation of $CO_2$, via capillary trapping, has been shown to greatly increase the storage efficiency of CCS [Hesse et al., 2008, Juanes et al., 2010] with up to 35% of $CO_2$ being immobilised by residual trapping [Pentland et al., 2011].

#### 1.1.2.3 Solubility trapping

$CO_2$ is weakly soluble in water and the long interface between the two phases provides a large surface for mass transfer. The resulting $CO_2$–water mixture is denser than both the $CO_2$ and the water, resulting in a gravitationally unstable interface [Xu et al., 2006, Hidalgo et al., 2012, Hewitt et al., 2012]. Several experimental studies, using both real and analogue fluids [e.g., Kneafsey and Pruess, 2010,

Neufeld et al., 2010, MacMinn et al., 2012, MacMinn and Juanes, 2013, Liang et al., 2018], and computational studies [e.g., Riaz et al., 2006] have shown that this unstable interface results in gravitational fingering, whereby dense fingers of water with dissolved $CO_2$ sink downward. These sinking fingers drive convection within the layer, which increases the length of the $CO_2$-water interface, promoting further dissolution. This process of 'convective dissolution' removes buoyant $CO_2$ from the migrating plume and therefore reduces the fraction of $CO_2$ that can potentially leak out of the system through buoyancy driven vertical migration. The mass of $CO_2$ removed from the plume has been shown to become significant for timescales much longer than the duration of injection (i.e. $\gg 10^2$ years) [Neufeld et al., 2010].

#### 1.1.2.4 Mineral trapping

The migrating $CO_2$ can react with silicate minerals to precipitate carbonate minerals and therefore remove mobile $CO_2$ from the migrating plume [e.g., Oelkers et al., 2008]. Sedimentary rocks suitable for CCS display a vast and diverse mineralogy. Two of many possible reaction pathways are:

$$\underset{\text{Forsterite}}{Mg_2SiO_4} + 2CO_2 \longrightarrow \underset{\text{Magnesite}}{2MgCO_3} + \underset{\text{Quartz}}{SiO_2}$$

$$\underset{\text{Anorthite}}{CaAl_2Si_2O_8} + CO_2 + 2H_2O \longrightarrow \underset{\text{Calcite}}{CaCO_3} + \underset{\text{Kaolinite}}{Al_2Si_2O_5(OH)_4}$$

As the kinetics of carbonate precipitation reactions are very slow [Xu et al., 2004] relative to the timescale of $CO_2$ injection, a long period of post-injection

($\gg 10^3$ years) is required for mineral trapping to immobilise a non-negligible fraction of the migrating $CO_2$ plume. Therefore mineral trapping is widely considered the least important secondary trapping mechanism [e.g., Benson and Cole, 2008] and is often neglected from fluid dynamical studies.

#### 1.1.2.5 Implementing carbon capture and storage

Despite grave climatic forecasts, CCS has not yet been deployed at meaningful scales and global GHG emissions continue to rise [e.g., Nejat et al., 2015]. This is largely due to the cost of this technology, the lack of supporting policy framework, and the difficulty in guaranteeing that $CO_2$ can be safely and effectively stored on 'human timescales'. Although this thesis focuses on further developing theoretical models for fluid injection into a layered subsurface, for completeness a brief discussion is provided of two additional principle hindrances to the widespread implementation of CCS as a climate change mitigation technique: 'Economics' and 'scalability'.

The economics of injecting $CO_2$ into the subsurface are complex. Vast costs are experienced during distinct phases of: (1) exploration and site evaluation; (2) infrastructural installation; (3) injection and monitoring; (4) post-injection monitoring and decommissioning. These costs are somewhat similar to those experienced during the lifetime of a producing hydrocarbon field. However, unlike extracting oil or gas, storing $CO_2$ does not produce a commodity that is sold to generate a profit. For CCS to be successfully implemented it must therefore be incentivised within an appropriate policy framework. Injection and storage of $CO_2$ at Sleipner (see §1.1.3) was only made possible by tax incentives, provided by the Norwegian government. Following the implementation of a carbon tax in 1991, which taxed $CO_2$ released to the atmosphere during hydrocarbon production, it became economic to sequester the $CO_2$ that is produced during hydrocarbon extraction from the Sleipner West field [Celius and Ingeberg, 1996, Jaccard et al., 2007].

Enhanced Oil Recovery (EOR) is another way in which the injection of $CO_2$ can be stored. During the tertiary phase of oil recovery, when the natural overpressure that drives production begins to diminish, the injection of fluid (e.g., water, $CO_2$ etc) can further displace oil by increasing overpressure (gradients); subsequently increasing recovery. Using $CO_2$ as the displacing fluid during EOR allows for, in principle, immobilisation and storage of up to 60% of the injected $CO_2$ [Gozalpour et al., 2005], thus preventing substantial volumes of $CO_2$ from being released into the atmosphere.

Deploying CCS on a scale that is able to achieve a meaningful reduction in atmospheric emissions is clearly challenging. To meet the Paris Climate agreement's target of minimising global warming to $\sim$1.5 °C would require—according to current projections—reducing $CO_2$ emissions by 7-13 $\mathrm{GT\,yr^{-1}}$, relative to current emissions [Rogelj et al., 2016]. Achieving this reduction exclusively via CCS would require introducing $\sim 10^4$ additional Sleipner-sized projects ($\sim$1 $\mathrm{MT\,yr^{-1}}$). Clearly, such a vast scale of CCS deployment is a challenging prospect. In reality, climate change mitigation that utilises CCS can only be effective as part of an array of emissions-reduction techniques (e.g., reduced societal demand, decarbonising energy production, increasing combustion efficiency). For now, economic, societal and political trends suggest that CCS is likely to continue in a limited number of small projects and for $CO_2$–EOR.

### 1.1.3 $CO_2$ storage at Sleipner

In §1.1.2.5, the reasons for limited current deployment of CCS were outlined. As a result of these reasons, there is a considerable deficit of available data to study 'real-world' CCS projects. This section provides a brief overview of $CO_2$ injection and storage at Sleipner, where since 1996 $\sim$ 1 $\mathrm{MT\,yr^{-1}}$ of $CO_2$ has been injected. Geophysical monitoring of $CO_2$ injection at Sleipner has provided a vast amount of data, yielding theoretical and modelling constrains. This data is a primary

motivation for the work presented in this thesis. Outlined below are the geological setting, geophysical monitoring and interpretations of $CO_2$ flow at Sleipner.

At Sleipner, $CO_2$ is injected into the Utsira Sandstone—a laterally extensive unit of Miocene-Pliocene age [Eidvin et al., 1999] that is located beneath the northern North Sea, off the western coast of Norway. The thickness of the Utsira Sandstone varies laterally and reaches a maximum thickness of $\sim 300$ m towards its southern extent, which is where $CO_2$ injection occurs. The formation has a pronounced 'dogleg' shape, and is approximately 400 km long and 50-100 km wide. Overlying the Utsira Sandstone is a thick ($> 100$ m) package of shales [Zweigel et al., 2004] that acts as a hydrodynamic seal/trap—limiting $CO_2$ migration, in principle, to within the Ustira Sandstone.

The Utsira formation was initially thought to be internally homogeneous and was assumed to contain negligible internal layering that could impede vertical $CO_2$ migration [Baklid et al., 1996]. More recent analysis of 3D seismic data, calibrated with core data and wireline logs, has yielded an updated reservoir model that predicts pervasive internal stratification [Zweigel et al., 2004], suggesting that the Utsira Sandstone is comprised of several high porosity (35–40%), high permeability ($> 1$D), $\sim 30$ m thick sandstone units that are separated by thinner ($\sim 1$ m) low permeability mudstone/shale units [e.g., Chadwick et al., 2004, Zweigel et al., 2004].

4D seismic and seabed gravimetric surveys have been used to monitor the spreading of injected $CO_2$ in the Utsira formation—providing constraints on subsurface parameters and physical processes operating at Sleipner. Measuring time-lapse anomalies in the gravitational field strength, using seabed gravimeters, has yielded an estimate of the mean $CO_2$ density of $\rho_{CO_2} \sim 700$ kg m$^{-3}$ [Alnes et al., 2008, 2011]. Incorporating temperature variation into modelling gravity data has also allowed for a simple estimate of dissolution rate of up to $\sim$1.8% yr$^{-1}$ [Alnes et al., 2011]. 3D seismic surveys carried out before $CO_2$ injection (1994), and after [1999,

2001, 2002, 2004, 2006, and 2008, 2010, 2013 and 2016: Furre et al., 2017] have allowed for time-lapse imaging of the plume, yielding insights into the processes controlling the lateral and vertical migration of the $CO_2$ in the Utsira formation. These seismic surveys have been interpreted as showing lateral $CO_2$ migration in nine distinct high permeability sandstone layers [e.g Arts et al., 2004, Chadwick et al., 2010]. The $CO_2$ ponds beneath the thin low permeability shales/mudstones that separate the sandstones, leading to a stack of $CO_2$–water gravity currents [e.g., Bickle et al., 2007]. The fine-grained nature of the intermediate mudstones are considered to obstruct vertical $CO_2$ flow—due to their high capillary entry pressure (see §1.2.3.2). Entry pressure estimates of a few MPa [e.g., Chadwick et al., 2004, Woods and Farcas, 2009], combined with the assumption that the capillary pressure in a single layer containing a $CO_2$ plume of thickness $h$ is given by $p_c \approx \Delta\rho g h$ implies that $h > 100$ m is required for $CO_2$ leakage across the intermediate mudstones. Vertical leakage across these mudstones is instead assumed to be focused through a higher permeability 'chimney', the existence of which is largely inferred from seismic observations of a "prominent vertical feature" that appears coincident with the leakage source [Arts et al., 2004].

Sleipner is a well-studied example of $CO_2$ injection into the subsurface. Geophysical monitoring, in particular 4D seismic imaging, demonstrates that stratification significantly impacts the migration of $CO_2$ in the Utsira formation. Despite this, the physics that governs injection and migration of a buoyant phase into a stratified subsurface remain poorly understood. Before developing a model to address this problem, the physical concepts required to formulate a generic model for multiphase fluid injection and migration in layered aquifers are introduced in the following section.

## 1.2 Introduction to flow in geological porous media

This thesis further develops models for gas injection and migration in layered aquifers. As such, theoretical models developed in later chapters build on a substantial amount of previous work—notably from the 'gravity-currents' community. This introductory section provides the reader with a brief overview of flow in porous media, and the physics that are important for large-scale subsurface flows (e.g., CCS).

### 1.2.1 Flow at the pore scale

Single-phase fluid flow in porous media at the pore scale is, like all fundamental fluid mechanics problems, governed by the Navier-Stokes equations. Typically, natural subsurface flows are of low Reynolds number (Re), meaning that inertial forces are negligible and flow is dominated by viscous forces. However, for some industrial flows (e.g., flow near an extraction well) inertial forces are non-negligible—introducing turbulent terms into the governing equations [e.g., Forchheimer, 1901, Şen, 1990]. The complex pore geometry of rocks, combined with the mathematical complexity of Navier-Stokes, do not allow for meaningful analytical solutions. Therefore, to fully solve for flow in sedimentary rocks, or even simplified micromodels, numerical solutions must be found. Modelling flow at a large scale ($> 100$ pore lengths) rapidly becomes computationally intractable—especially in three dimensions—due to the fine mesh required to capture pore geometries. Instead simulations, often in combination with micromodel experiments, over imagined pore geometries in a relatively small domain (10s of pore lengths) can be used to investigate the stochasticity of flow and transport in heterogeneous porous media [e.g., de Anna et al., 2017]. Additionally, the pore-geometry of the subsurface can

never be known—meaning that an approach to modelling subsurface flow must be used that does not require a Navier-Stokes formulation.

### 1.2.2 Single-phase flow

In 1856, Henry Darcy—a French civil engineer—was employed to provide a report on the water supply of Dijon [Freeze, 1994]. The appendix of this report contained the eponymous empirical law for averaged single-phase flow through a porous medium [Darcy, 1856]. Darcy discovered, through a series of simple experiments, that the flux of fluid through a cross-section of porous material ($q$) is proportional to the pressure gradient that drives the flow ($\nabla p$). In three dimensions, Darcy's law is commonly written as:

$$\boldsymbol{q} = -\frac{k}{\mu}\left(\boldsymbol{\nabla} p + \rho g \hat{\boldsymbol{e}}_z\right), \tag{1.1}$$

where $\mu$ is the dynamic fluid viscosity, $g$ is the body force per unit mass due to gravity, and $\hat{\boldsymbol{e}}_z$ is the unit vector pointing vertically upwards. The permeability $k$ measures the conductivity of the porous material to fluid flow. The Eulerian fluid velocity $u$ is related to the Darcy velocity by $u = q/\phi$, where $\phi$ is the porosity of the fluid medium, which measures the fraction of void space relative to total volume. Although Darcy's law was discovered empirically, it can be derived theoretically by volume-averaging Navier-Stokes over a Representative Elementary Volume (REV) [e.g., Neuman, 1977]. The REV constitutes the minimum volume for which Darcy's law is valid and the rock, or portion of rock, can be characterised by averaged properties—the permeability and porosity. For volumes smaller than the REV, flow is dominated by microscopic heterogeneity; Darcy's law is no longer valid, and pore-scale modeling of flow must be used.

Conservation of mass for a single fluid phase in a porous medium is given by

$$\frac{\partial}{\partial t}(\rho\phi) + \boldsymbol{\nabla} \cdot (\rho \boldsymbol{q}) = \mathcal{I}, \tag{1.2}$$

where $\mathcal{I}$ is a source/sink term that prescribes the local mass injection/extraction rate per unit volume. This conservation equation states that the divergence of mass flux is balanced by either gaining or losing fluid to a source of sink respectively, and by changes in the fluid density and/or pore space. Assuming that density is a function of pressure only (i.e., neglecting thermal effects), changes in fluid density or porosity are therefore solely attributed to the effects of compressibility. The compressibility of rock ($c_r$) and a fluid phase ($c_f$) are defined by Bear [1972] as:

$$c_r \equiv (1/\phi)(\partial\phi/\partial p) \tag{1.3a}$$

$$c_f \equiv (1/\rho)(\partial\rho/\partial p). \tag{1.3b}$$

The rock compressibility expression arises from the simplification of (full) poroelasticity theory under the common geological assumptions of constant vertical stress and negligible lateral strain [*e.g.*, van der Kamp and Gale, 1983, Green and Wang, 1990]. Substituting 1.1 and 1.3a-b into 1.2 yields a governing partial differential equation (PDE) for saturated single-phase compressible flow in a heterogeneous porous medium:

$$\rho\phi(c_r + c_f)\frac{\partial p}{\partial t} - \boldsymbol{\nabla} \cdot \left(\rho \frac{k}{\mu}(\boldsymbol{\nabla} p + \rho g \hat{\boldsymbol{e}}_z)\right) = \mathcal{I}. \tag{1.4}$$

Equation (1.4) is a nonlinear PDE with parabolic (diffusive) character. The nonlinearity arises from the divergence of $\rho(p)\boldsymbol{\nabla} p$, given the pressure dependence of density. In the incompressible limit ($c_r = c_f = 0$), Equation (1.4) reduces to

Poisson's equation for pressure. In the absence of compressibility, heterogeneity ($k \neq k(\mathbf{x})$), and sources/sinks ($\mathcal{I} = 0$), Equation (1.4) further reduces to Laplace's equation—an elliptic equation for the pressure field, from which the fluid flux can be calculated. In a single-phase system, the rate at which pressure is transported is determined by the pressure diffusivity $\mathcal{D} = k/(\mu\phi c_f)$ [e.g., Talwani and Acree, 1985]. The pressure diffusivity, therefore, implies that pressure is propagated infinitely quickly for incompressible flows ($c_r = c_f = 0$). For aquifer-scale flows (i.e., $> 10$ km horizontal lengthscale), even very weak compressibility becomes important and must be accounted for to ensure an accurate prediction of the pressure field. The loss of incompressibility, however, adds significant complexity to this equation and makes deriving analytical solutions difficult. For compressible multi-phase flow, analytical solutions are typically unobtainable. This thesis studies the effect of gas injection into the subsurface, and it is worth highlighting here that gas is far more compressible than water—a property that will be repeatedly utilised in derivations throughout this thesis.

### 1.2.3 Multi-phase flow

Now consider the introduction of a second fluid. As this thesis focuses on gas injection, and the displacement of water, this additional phase is referred herein as 'gas'; however, it could instead be another liquid phase (e.g., oil or supercritical $CO_2$). The introduction of an additional phase leads to an additional set of forces—interfacial forces at the pore scale. Interfacial tension ($\sigma$) measures the energy per unit area of an interface between two different substances. In a three-phase system (gas, water, and rock), three interfacial tensions exist: gas–water ($\sigma_{gw}$), gas–rock ($\sigma_{gr}$) and water–rock ($\sigma_{wr}$). The tendency of the system to try to minimise total interfacial energy, combined with viscous and other forces, adds significant complexity to multi-phase subsurface flow. Before governing equations for multi-phase flow are formulated, the concept of 'wettability' must be introduced.

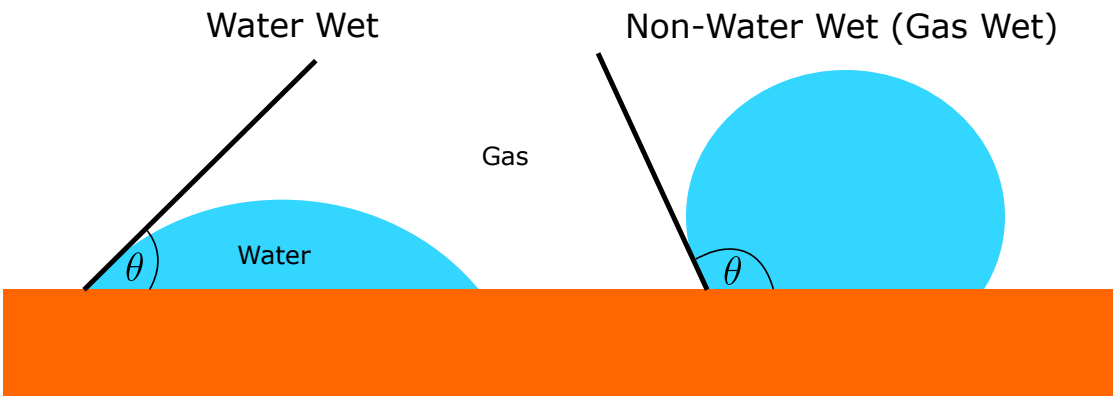


**Figure 1.1:** Schematic diagram illustrating the shape of a 'water-wet' and 'gas-wet' water droplet on a solid substrate.

#### 1.2.3.1 Wettability

Wettability is defined as the ability of a fluid to maintain contact with a solid surface, and is as such the expression of the interaction between surface energies. Consider a static water droplet on a solid substrate in a gaseous atmosphere (Figure 1.1). If the water-rock interfacial tension dominates, then the water spreads along the solid surface. This spreading can be considered as the water droplet acting to maximise its surface contact area, which has the effect of minimising the surface energy of the droplet; giving the appearance that the surface has an affinity for water, relative to gas. When the interfacial tension between gas and rock dominates, the gas has a higher affinity (relative to water) to the solid substrate. The water droplet will subsequently act to minimise its contact with the surface—i.e., minimising surface energy by maximising the gas-solid contact area—resulting in the 'beading up' of the droplet (Figure 1.1).

The competition between the three principal interfacial tensions was first considered by Young [Young, 1805, De Gennes et al., 2013], who derived the relation:

$$\sigma_{gr} = \sigma_{wr} + \sigma_{gw}\cos(\theta), \tag{1.5}$$

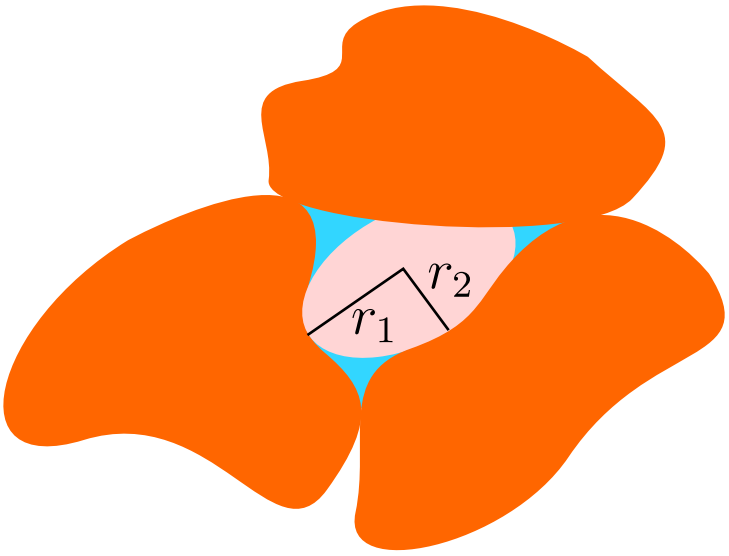


**Figure 1.2:** A static ganglion of non-wetting gas (pink) surrounded by water (blue) in a water-wet pore formed of three solid grains (orange).

where $\theta$ is the 'contact angle' (see Figure 1.1) of the droplet, measured through the denser phase (water), on the solid surface. Young's equation is crucial as it allows to quantitatively describe 'wettability'—a term used to describe the degree to which a liquid can maintain contact with a solid surface. The contact angle is the macroscopic expression of wettability. The solid surface is said to be 'water-wet', if water preferentially spreads on the solid substrate (i.e., $0 < \theta < 90$). If the water does not spread and beads up (i.e., $90 < \theta < 180$), gas is the 'wetting phase' and the surface is 'non-wetting' to water. A contact angle of $\theta = 90$ is observed for a neutrally-wetting surface [e.g., Dake, 1983].

The same complex interplay between capillary forces that act on droplets on solid substrates act on a fluids in sedimentary rocks, where the solid surface is now a tortuous three-dimensional network of grains. A static wetting droplet will—as on a solid substrate—act to maximise its contact with solid and therefore preferentially occupy the rough grain surface and the corners where grains meet. Similarly, a static non-wetting phase does not have an affinity for the grains, and minimises its surface-contact by occupying the pore centre (Figure 1.2). This capillary segregation of immiscible phases assists in the development of separate networks, in which a fluid phase can flow independently (see §1.2.3.3).

In reality, solid grains in sedimentary rocks—which are comprised of a diverse array of minerals—are chemically heterogeneous, meaning that the contact angle can vary substantially. Therefore, it is often difficult to characterise the interactions of a given pair of fluids in a given rock with a single contact angle. In aquifers that are suitable for CCS, water tends to be the wetting phase—with contact angles of $\theta < 90$ typically observed [e.g., Chalbaud et al., 2009, Farokhpoor et al., 2013]. However, there has been some suggestion that past migration of oil can leave a residue on the grain surface that effectively alters the wettability of the grains during subsequent exposure to water and gas, resulting in neutrally-wetting or even $CO_2$-wetting conditions [e.g., Iglauer et al., 2015]. For this study, wettability alteration is neglected and it is assumed that water is always the wetting phase.

#### 1.2.3.2 Capillary pressure

Capillary pressure ($p_c$) is defined as the difference in pressure between the non-wetting and wetting phases, and is given by

$$p_c \equiv p_g - p_w, \tag{1.6}$$

where $p_g$ and $p_w$ are the gas (e.g., $CO_2$) and water pressures, respectively. Numerous core-flooding experiments have demonstrated that capillary pressure at the Darcy scale, during drainage and imbibition, is a hysteretic function of saturation (Figure 1.3). Saturation ($s_\alpha$) is defined, at the Darcy scale, as the fraction a fluid phase occupies relative to the total pore volume in a REV. Drainage is a multiphase displacement process in which the non-wetting phase displaces the wetting phase. During primary drainage, the non-wetting phase invades a porous medium that is fully-saturated with the wetting phase. Drainage processes result

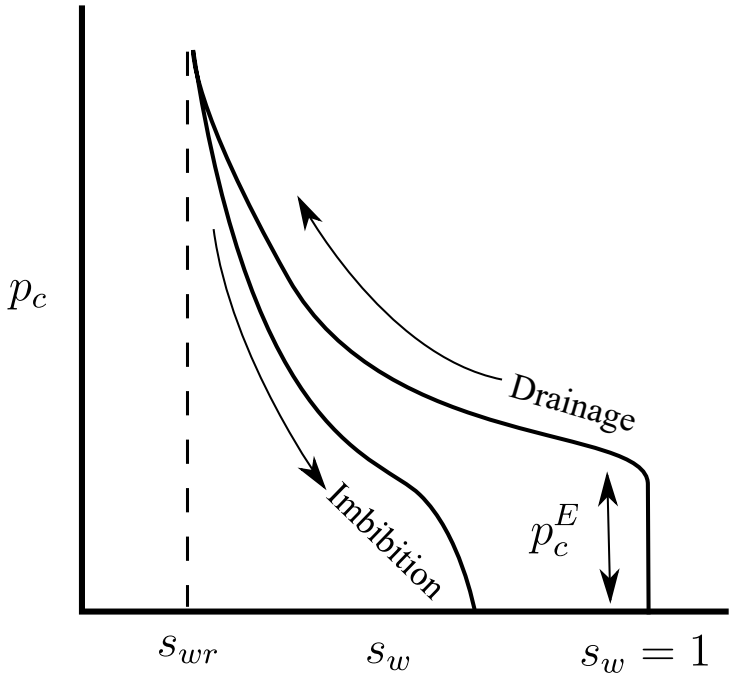


**Figure 1.3:** Typical evolution of capillary pressure as a function of saturation during (primary) drainage and (secondary) imbibition in a water-wet rock.

in a monotonic increase in capillary pressure with decreasing wetting-phase saturation (Figure 1.3). The capillary pressure increases up to a maximum at the residual wetting-phase saturation ($s_{wr}$), at which the wetting phase can no longer be displaced. For this study, it has already specified been that gas and water are taken to be the non-wetting and wetting phases, respectively. Therefore the injection and migration of gas, which displaces water, is an example of (primary) drainage. Figure 1.3 shows that, for the non-wetting phase to initially invade the saturated porous medium, a threshold capillary pressure must be exceeded. This 'capillary entry pressure' ($p_c^E$) provides a barrier to the flow of $CO_2$ across mudstones at $CO_2$ storage sites and forms a crucial component of the theoretical model developed in later chapters. The entry pressure of a rock can be estimated using the Young-Laplace equation,

$$p_c = \sigma_{gw} \left( \frac{1}{r_1} + \frac{1}{r_2} \right), \tag{1.7}$$

where $\sigma_{gw}$ is the gas–water interfacial tension, and $r_1$ and $r_2$ are the principal

radii of curvature of the gas–water interface (see Figure 1.2). Assuming that the radii of curvature are both of the order of the pore size, the entry pressure can be estimated as $p_c^E \sim \sigma/r$, where $r$ is now the characteristic pore radius. This simple approximation demonstrates that finer grained rocks will have a higher entry pressure and will therefore provide a greater resistance to the invasion of gas. In Sleipner, the entry pressure of thin mudstone units has been estimated to be a few MPa [e.g., Chadwick et al., 2004]. If it is assumed that the capillary pressure in a column of gas that contains a residual network of water can be approximated by phase-static buoyancy ($p_c \approx \Delta\rho g h$) [e.g., Woods and Farcas, 2009], then for typical reservoir conditions ($\Delta\rho \sim 300$ kgm$^{-3}$), several hundred metres of $CO_2$ are required to build up a sufficient capillary pressure that will allow for $CO_2$ drainage in mudstones. This simple analysis suggests that fine-grained mudstones provide a capillary barrier to upwards migration of $CO_2$, allowing for safe storage of huge volumes of $CO_2$. In Chapter 3 it is demonstrated that due to viscous pressure losses associated with vertical water flow, it is easier to build up capillary pressure than this approximation suggests.

Imbibition is an invasion process in a porous medium whereby the wetting phase displaces the non-wetting phase. Secondary imbibition is imbibition in a porous medium that already contains a residual network of wetting films. An example of secondary imbibition is buoyancy-driven post-injection migration of $CO_2$, where the rising and spreading plume of $CO_2$ draws water back into the pore space at its trailing edge. Imbibition in geological porous media is a non-reversible hysteretic process. During imbibition, the capillary pressure decreases, but does not follow the drainage capillary pressure-saturation curve (Figure 1.3). In the zero-capillary-pressure limit, the wetting phase is no longer fully saturated ($s_{wr} < s_w < 1$) due to the presence of residually-trapped non-wetting phase in the pore space. This is related to the immobilisation of ganglia of the non-wetting phase by capillary forces. During post-injection migration, this 'residual trapping' of $CO_2$ eats away at the migrating plume and increases storage efficiency (see §1.1.2.2).

The concepts of wettability and capillary pressure prompt the understanding that multiple phases in porous media flow in separate networks with semi-decoupled pressure fields. This now allows for the introduction of 'relative permeability', before beginning to formulate governing equations for multi-phase subsurface flows.

#### 1.2.3.3 Relative permeability

The widely used, phenomenological extension of Darcy's law to include multiple fluid phases was suggested by Muskat and Meres [1936]. For an arbitrary phase, denoted with subscript $\alpha$, the multi-phase extension of Darcy's law is written as:

$$\boldsymbol{q}_\alpha = -\frac{k k_{r\alpha}(s_\alpha)}{\mu_\alpha} \left(\boldsymbol{\nabla} p_\alpha + \rho_\alpha g \hat{\boldsymbol{e}}_z\right), \tag{1.8}$$

where $k_{r\alpha}(s_\alpha)$ is the 'relative permeability' of phase $\alpha$. The relative permeability is a dimensionless function of saturation, over the interval $0 \leq k_{r\alpha} \leq 1$. A single fluid phase, in a porous medium occupied by multiple phases, flows in its own network and therefore does not sample all of the intrinsic permeability of the porous medium. The relative permeability, which accounts for this impediment to flow, is a constitutive function. Through data-fitting, Brooks and Corey [1966] found that the relative permeabilities of the wetting ($k_{rw}$) and non-wetting phase ($k_{rnw}$) are best fit by:

$$k_{rw} = (s_w)^{\frac{2+3n}{n}} \tag{1.9a}$$

$$k_{rnw} = (1 - s_w)^2 \left[1 - (s_w)^{\frac{2+n}{n}}\right] \tag{1.9b}$$

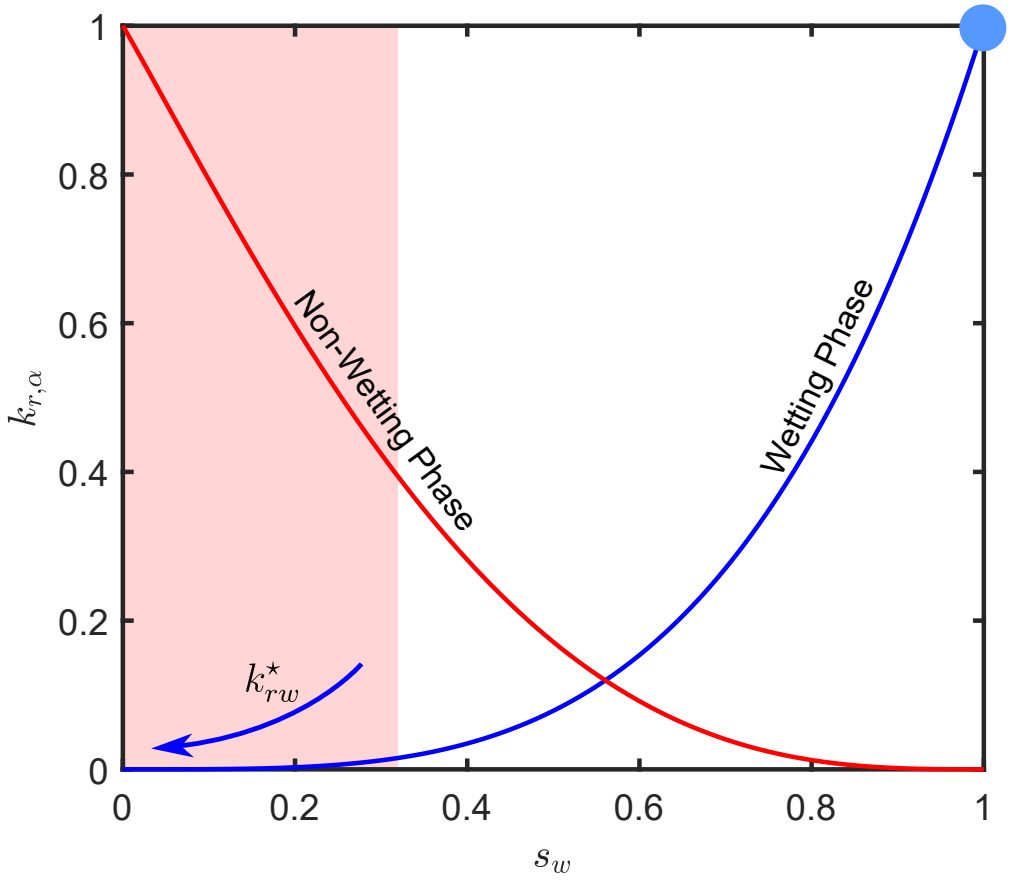


**Figure 1.4:** Brooks-Corey curves for a wetting and non-wetting phase, with $n = 3$. The blue dot and pink shading indicate likely values for relative permeability associated with CCS in the water-saturated and $CO_2$-saturated regions, respectively.

where $s_w$ remains the wetting phase saturation and $n$ is an exponent related to the distribution of pore sizes. Although many empirical relative permeability-saturation functions exist, the Brooks-Corey relation is still widely used by the reservoir-engineering community. These two monotonic polynomial equations (Figure 1.4) highlight the complex interplay between saturation and the degree of retardation of a fluid phase in a porous medium.

During $CO_2$ injection, buoyancy segregates the fluids into two regions: A plume mostly saturated with gas overlies a region fully saturated with water. As $s_w = 1$ in the water region, single-phase flow applies and therefore $k_{rw} = 1$ (Figure 1.4). In the gas region, the small residual water saturation reduces the pore space available for gas to flow, reducing $k_{rg}$ below the single-phase limit (Figure 1.4). If patches

of residual water remain connected across the gas region via thin films, they may transmit weak flows. This is represented by a low relative permeability for water in this region ($k^{\star}_{rw}$) (Figure 1.4). The value of $k^{\star}_{rw}$ is poorly constrained but thought to be as low as $\sim 10^{-9}$ [Blunt, 2017]. In later chapters, $k^{\star}_{rw}$ is shown to have a significant impact on lateral flow and vertical leakage of both gas and water during gas injection into layered aquifers.

#### 1.2.3.4 Multi-phase flow equations

The formulation of governing PDEs for multiphase flow in porous media begins by noting that the porous medium is fully saturated by multiple phases and therefore, the sum of saturations must equal unity:

$$\sum_{\alpha=1}^{N} s_\alpha \equiv 1, \tag{1.10}$$

where $N$ denotes the total number of phases ($\alpha$). Conservation of mass for each phase is typically written as

$$\frac{\partial}{\partial t}\left(\rho_\alpha \phi s_\alpha\right) + \boldsymbol{\nabla} \cdot \left(\rho_\alpha \boldsymbol{q}_\alpha\right) = \mathcal{I}_\alpha, \tag{1.11}$$

where $\mathcal{I}_\alpha$ is a source/sink term prescribing the mass rate of injection/extraction of phase $\alpha$. Substituting Equations (1.8) into (1.11) and expanding out the first term, making use of the compressibility relations 1.3a-b yields:

$$\rho_\alpha \phi s_\alpha \left[\frac{1}{s_\alpha}\frac{\partial s_\alpha}{\partial t} + (c_r + c_\alpha)\frac{\partial p_\alpha}{\partial t}\right] - \boldsymbol{\nabla} \cdot \left[\rho_\alpha \frac{k k_{r\alpha}(s_\alpha)}{\mu_\alpha}\left(\boldsymbol{\nabla} p_\alpha + \rho_\alpha g \hat{\boldsymbol{e}}_z\right)\right] = \mathcal{I}_\alpha, \tag{1.12}$$

[e.g., Bear, 1972]. The extension to multiple phases sufficiently increases the complexity, nonlinearity and number of governing equations such that numerical methods must be used to find solutions. Derivatives of saturation can be very large, and often require extremely fine grids to resolve. Furthermore, density and viscosity can vary with temperature, thus requiring additional constitutive equations. Reservoir simulation often requires, at great computational cost, the input of thermodynamical constraints to deal with multicomponent phases, phase changes, precipitation, dissolution, chemical reactions and miscibility.

During $CO_2$ injection into the subsurface (e.g., during CCS), the balance between viscosity and buoyancy leads to the development of a migrating $CO_2$ plume that has a characteristic tongued shape. Furthermore, the $CO_2$ migrates much slower than the corresponding pressure front, meaning that the lateral extent of the domain must be very large ($> 50$ km) in order to ensure that boundary effects do not play a role in numerical studies. Therefore the $CO_2$ only occupies a small fraction of the computational domain, and to resolve the $CO_2$ plume—and saturation variations within it—requires a remarkably fine horizontal grid spacing. The main goal of this study is to understand the role of layering on gas migration. The addition of vertical heterogeneity—particularly thin layers—drastically increases the domain size and the vertical resolution necessary to accurately simulate two-phase flow in a layered system. Solving full two-phase flow in a vertically heterogeneous layered domain and in two or three dimensions is extremely computationally expensive—prohibiting a detailed analysis of the fluid dynamics of this problem. Therefore, to explore a substantial parameter space, these equations must be simplified without compromising the key underlying physics. To achieve this, a compressible gravity current formulation for two-phase flow in porous media is adopted throughout this thesis.

A gravity current is a predominantly horizontal flow that is driven by the density contrast between the two fluids in the presence of gravitational field [e.g., Simpson, 1982]. The horizontal nature of these flows permits simplification of the vertical

pressure field and subsequent vertical integration, reducing the dimensionality of the problem by 1 order (i.e. a 2D $x-z$ planar gravity current can be approximated by 1D equations). The horizontal nature of these flows means that order-reduction of the governing equations does not result in a significant loss of accuracy. Comparisons between gravity-current models and 'full' solvers—such as the popular multi-phase flow simulator for CCS applications `TOUGH2-ECO2N' [Pruess et al., 1999, Pruess, 2005]— typically show excellent agreement as long as key assumptions underpinning the gravity-current framework are satisfied [e.g., Mathias et al., 2011b]. The key underlying assumptions used in a gravity current formulation are described in detail in Chapter 2. The classical gravity-current formulation is extended in Chapter 2 to account for weak vertical flow of water in a layered-aquifer system, and further extended in Chapter 3 to account for vertical gas leakage. In the limit of no vertical leakage of water and gas, the governing PDEs reduce to those for a compressible gravity current in a single aquifer (Appendix A).

# Chapter 2

# Coupling pressure dissipation and fluid migration

*The theoretical model, results and analysis presented in this chapter have been published in Jenkins et al. [2019a]. This chapter constitutes a minor reformatting of that work to fit within the context of this thesis.*

## 2.1 Introduction

Carbon capture and geological storage involves capturing carbon dioxide and injecting it into saline aquifers for long-term storage. The goal of CCS is to reduce $CO_2$ emissions to the atmosphere in order to mitigate climate change [*e.g.*, IPCC, 2005]. To achieve a meaningful reduction in $CO_2$ emissions, very large quantities of $CO_2$ would need to be captured and stored. Two key physical mechanisms limit the potential storage capacity of a particular aquifer: Pressure buildup and $CO_2$ migration [Szulczewski et al., 2012]. Pressure buildup limits capacity because the pressure in the target aquifer will increase during injection. The local geology and geomechanics impose a maximum allowable pressure that, if exceeded, could lead to fracturing or fault activation, enabling leakage of $CO_2$ into overlying aquifers. Migration limits capacity because, after injection, the buoyant $CO_2$ will slowly

rise, spread, and migrate relative to the denser water. The injection scenario must be designed such that this $CO_2$ will not migrate outside of its designated storage area. Pressure buildup and migration have been studied extensively, but almost exclusively as separate problems due to computational limitations and the widespread view that these processes are essentially independent. In this chapter, a new model is developed that captures both processes simultaneously. This model is subsequently used to show that fluid migration and pressure buildup are inherently coupled.

A saline aquifer is a layer of rock with a relatively high permeability, such as sandstone, that is bounded above and below by sealing layers ("seals"), which are layers of rock with much lower permeability, such as shale or mudstone. Aquifers range in thickness from a few metres to a few hundreds of metres; seals are typically about an order of magnitude thinner, from a few centimetres to a few tens of metres. Both aquifers and seals are laterally extensive over tens to hundreds of kilometres, are nearly horizontal (slopes of at most a few degrees), and are saturated with saline groundwater ("water"). A typical sedimentary basin comprises many repetitions of this fundamental sequence (seal–aquifer–seal) over a total thickness of a few kilometres.

Most previous studies of $CO_2$ migration are at the aquifer scale, focusing on the target aquifer only and taking the associated seals to be perfectly impermeable (as in Appendix A). In this setting, it is common to assume that the $CO_2$ will remain separated from the water by a sharp interface (the capillary pressure being much smaller than the hydrostatic pressure) and that the vertical pressure variation within both fluids will remain essentially hydrostatic (the vertical dimension of the flow being much smaller than the horizontal one). These assumptions together imply that the buoyant $CO_2$ will take the form of a coherent plume known as a gravity current [Huppert and Woods, 1995]. The resulting models are convenient for analytical and computational analysis because they eliminate the vertical

dimension, leading to a 1D (or 2D) flow problem in the lateral plane. Gravity-current models (also known as "vertically integrated" models) have been studied extensively, yielding a variety of important qualitative insights as well as quantitative analytical and semi-analytical predictions [e.g., Nordbotten et al., 2005, Nordbotten and Celia, 2006b, Hesse et al., 2007, Gasda et al., 2009, Juanes et al., 2010, Mathias et al., 2009, MacMinn et al., 2010, Pegler et al., 2014a, Zheng et al., 2015, Golding et al., 2017]. However, the majority of these studies provide no insight on pressure buildup or dissipation because they assume that the fluids and the rock are incompressible. Two noteworthy exceptions are the work of Mathias et al. [2009, 2011b] and that of Hewitt et al. [2015]. The former considered the impact of compressibility on $CO_2$ injection, pressure buildup, and lateral pressure dissipation within an isolated aquifer; the latter considered the impact of poroelastic deformation on the same problem, but for a system with incompressible constituents.

The pressure perturbation due to $CO_2$ injection travels orders of magnitude faster and farther than the $CO_2$ itself [*e.g.*, Nicot, 2008, Birkholzer et al., 2009, Chang et al., 2013]. As a result, most previous studies of pressure buildup consider much larger, basin-scale systems that allow for pressure dissipation via water migration both laterally within aquifers and vertically across seals. Fluid and rock compressibility are central to the rate of pressure buildup and dissipation in these basin-scale systems. Because of the importance of both vertical and lateral flow, models for pressure dissipation are typically fully 2D (or 3D) and are therefore less analytically tractable and more computationally expensive than gravity-current models. The primary computational challenge for these models is resolving the fine-scale features of the long, thin $CO_2$ plume in what is necessarily a large computational domain. As a result, these models typically produce a fairly coarse view of the evolution of the $CO_2$ plume [*e.g.*, Birkholzer et al., 2009]. Many studies of pressure buildup simplify the problem by replacing $CO_2$ injection with water injection, reducing the two-phase flow problem to a single-phase flow problem. This

simplification, which greatly reduces the computational cost, is motivated by the argument that the features of pressure buildup and dissipation away from the target aquifer depend mainly on the rate, duration, and location of injection, but are relatively insensitive to the properties of the injected fluid [Nicot, 2008, Nicot et al., 2011, Chang et al., 2013]. However, the resulting models cannot be used to predict anything about the $CO_2$ plume or its coupling with pressure buildup and dissipation.

Studies of pressure buildup and dissipation have consistently shown that vertical pressure dissipation, in particular, has a very strong impact on both overall pressure buildup and lateral pressure propagation [Birkholzer et al., 2009, Chang et al., 2013]. This implies that vertical pressure dissipation should also have a strong impact on the shape of the $CO_2$ plume. In this chapter, it is shown that the shape of the $CO_2$ plume is indeed strongly coupled to vertical pressure dissipation and, further, that this coupling is two-way: Vertical pressure dissipation near the injection well is itself influenced by the shape of the $CO_2$ plume. This is achieved by developing a novel model that extends the traditional gravity-current approach to allow for compressibility, weak vertical flow, and vertical water migration in a domain comprising an arbitrarily extensive sequence of aquifers and seals. In §2.2, the derivation of the model is outlined. The model is computationally inexpensive, but sufficiently complex that analytical solutions are not readily available; in §2.3, the numerical scheme is outlined before the model is benchmarked against 1D analytical solutions and a full 2D numerical solution for a single-phase model problem (water injection). The model is then applied to $CO_2$ injection and a detailed exploration of the associated parameter space is conducted. In §2.4, the chapter concludes by considering the implications of these results for CCS.

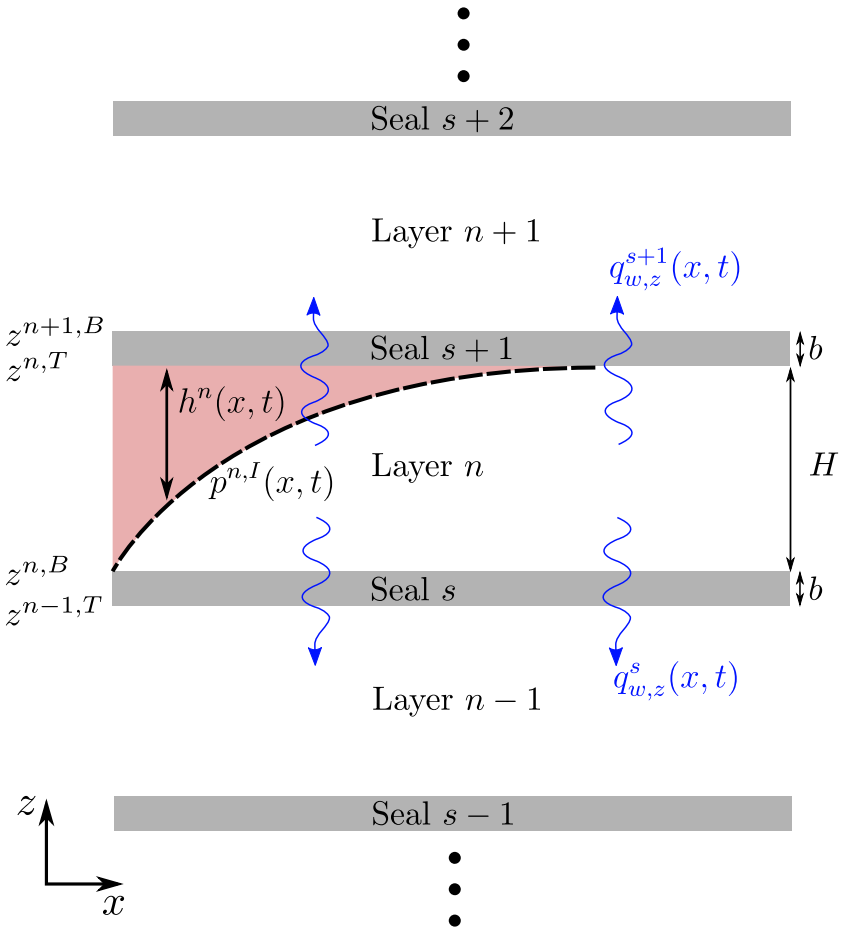


**Figure 2.1:** A section of the model system, which comprises a sequence of aquifers of thickness $H$ and seals of thickness $b$. The gas-saturated region is show in red.

## 2.2 Theoretical model

The geological setting for the model is a sequence of $N_z$ horizontal aquifers alternating with $N_z + 1$ horizontal seals (Figure 2.1). For simplicity, it is assumed that all aquifers have the same uniform thickness $H$, porosity $\phi$, and isotropic permeability $k$, and that all of the thinner and less-permeable intervening seals have the same uniform thickness $b$ ($b \ll H$), porosity $\phi_s$, and isotropic permeability $k_s$ ($k_s \ll k$). The system is bounded above and below by impermeable seals, and aquifers and seals are counted from the bottom up. As a result, the deepest and shallowest seals are seals 1 and $N_z + 1$, respectively, the deepest and shallowest aquifers are aquifers 1 and $N_z$, respectively, and, in general, aquifer $n$ is bounded by seals $s$ and $s + 1$.

In the context of this geological setting, the model is used to study the flow of two immiscible phases of different density: A dense, wetting phase and a buoyant, nonwetting phase. The wetting phase is groundwater ("water"); the buoyant, nonwetting phase is referred to as "gas" for simplicity, but it could be natural gas, oil, or supercritical $CO_2$.

The identity of a fluid-phase is denoted with a subscript $\alpha$, with $\alpha = w$ for water and $\alpha = g$ for gas (or any other buoyant, nonwetting phase). The weak compressibility of both fluids is accounted for by allowing their densities $\rho_\alpha$ to vary linearly with pressure about a reference state,

$$\rho_\alpha(p) = \rho_\alpha^0 \left[1 + c_\alpha(p_\alpha - p^0)\right], \tag{2.1}$$

where $p_\alpha$ is the pressure of phase $\alpha$, $\rho_\alpha^0$ is the density of phase $\alpha$ at reference pressure $p^0$, and $c_\alpha$ is the compressibility of phase $\alpha$ about $p^0$ ($c_\alpha \equiv (1/\rho_\alpha^0)(\mathrm{d}\rho_\alpha/\mathrm{d}p)|_{p^0}$).

For the range of pressures typically experienced during both natural fluid migration and subsurface-engineering operations, it is expected that $c_w(p_w - p^0) \ll 1$ and therefore that $\rho_w \approx \rho_w^0$. This simplification is repeatedly taken advantage of in the analysis below. This assumption is not made for gas since $c_g \gg c_w$.

Below, a model is developed for flow of gas and water in aquifer $n$. To enable vertical and lateral pressure dissipation, the model allows for water exchange with the aquifers above and below via flow through the intervening seals. Importantly, in this chapter gas exchange across the seals ("gas leakage") is not allowed. For a competent seal, gas leakage is blocked by a large capillary entry pressure due to the fine-grained microstructure of the seal rock. However, gas leakage can be enabled by injection pressures that exceed this entry pressure, by the presence of heterogeneities in the seal with much lower entry pressure (*e.g.*, sandy patches), or by focused leakage pathways such as faults or fractures. Gas leakage is addressed in detail in Chapter 3.

A planar (2D) model problem in the $x$-$z$ plane is considered, with $z$ the vertically upward coordinate and $x$ the horizontal (lateral) coordinate (Figure 2.1). Note that the vertical position of the top and bottom of aquifer $n$ is denoted by $z^{n,T}$ and $z^{n,B}$, respectively, such that $z^{n,T} - z^{n,B} \equiv H$. To allow for the future incorporation of lateral heterogeneity (see §5.3.5), a Cartesian frame is adopted by neglecting variations along the y direction. This scenario is also relevant to simultaneous injection from a linear ('line-drive') array of wells ([e.g., Nicot, 2008, Juanes et al., 2010]), provided that the inter-well spacing ($\delta_{\text{well}}$) is sufficiently small such that gas plumes merge over a timescale less than that of injection. During injection, the radial width of the gas plume can be approximated by

$$r(t) \approx R_c \sqrt{\mathcal{M} t/\tau}, \tag{2.2}$$

where $\mathcal{M}$ is the (mobility) ratio of fluid viscosity, $\tau$ is the duration of injection, and the characteristic radius ($R_c$) is given by

$$R_c \equiv \sqrt{\dot{M}\tau/(\pi H \phi s_g)}, \tag{2.3}$$

where $\dot{M}$ is the mass injection rate at a given well [Nordbotten and Celia, 2006b, MacMinn and Juanes, 2009]. Therefore the assumption of planar symmetry becomes valid when $t \gg \delta^2 \pi H \phi s_g/(\dot{M}\mathcal{M})$, which approximately occurs over timescales much greater than 20 days for reference parameters (see Table 2.1) and an assumed well spacing of 5 km. For a thicker aquifer more typical of large scale storage ($H \sim 100$) this interference will occur over a timescale of $\sim$200 days. In both scenarios, this timescale is much less than the usual duration of injection, which is typically decades.

### 2.2.1 Flow in aquifer $n$

The derivation begins by assuming that the two fluids are strongly segregated by gravity, such that there exists a region saturated primarily with gas above a region saturated exclusively with water (Figure 2.1). The saturation of both fluids would vary in space and time within these regions; however, when capillarity is weak relative to buoyancy, these variations are localised to a relatively thin "capillary fringe" that separates a region containing mostly mobile gas from a region containing mostly mobile water, both at nearly constant and uniform saturation within these regions. The evolution of the capillary fringe does not have a leading-order impact on the motion of the gas plume [Golding et al., 2017]. It is therefore assumed that the gas region and the water region are separated by a sharp interface, and that the gas region contains mobile gas with a uniform and constant saturation of residual water. These assumptions are standard for large-scale gas injection and migration [Nordbotten et al., 2005, Nordbotten and Celia, 2006b, Hesse et al., 2007, Gasda et al., 2009, Juanes et al., 2010, Mathias et al., 2009, MacMinn et al., 2010].

As discussed in more detail below, the residual water is assumed to exist in a network of connected wetting films and bridges that, although immobile, can conduct a net vertical flow of water. It is further assumed that the water region in each aquifer contains only water. Residual gas in the water region can be included in a relatively straightforward way [*e.g.*, Kochina et al., 1983, Barenblatt, 1996, Hesse et al., 2008, Gasda et al., 2009, Juanes et al., 2010, MacMinn et al., 2010], but it is neglected it here for simplicity. Lastly, it is assumed that the seals contain only water.

#### 2.2.1.1 Gas in aquifer $n$

Conservation of mass for gas in aquifer $n$ is given by

$$\frac{\partial}{\partial t}\left(\rho_g \phi s_g\right) + \boldsymbol{\nabla} \cdot \left(\rho_g \boldsymbol{q}_g\right) = \mathcal{I}_g, \tag{2.4}$$

where $s_g$ is the saturation of gas, $\boldsymbol{q}_g$ is the Darcy flux of gas, and $\mathcal{I}_g$ is a source term that prescribes the local mass rate of gas injection per unit volume. The Darcy flux of gas is given by Darcy's law,

$$\boldsymbol{q}_g = -\frac{k k_{rg}}{\mu_g}\left(\boldsymbol{\nabla} p_g + \rho_g g \hat{\boldsymbol{e}}_z\right), \tag{2.5}$$

where $k_{rg}$ is the relative permeability to gas flow, $\mu_g$ is the dynamic viscosity of gas, which is taken to be constant and uniform, $p_g$ is the gas pressure, $g$ is the body force per unit mass due to gravity, and $\hat{\boldsymbol{e}}_z$ is the unit vector in the positive $z$ direction.

The gas is assumed to be in vertical equilibrium; meaning that the vertical component of gas flow is negligible relative to the horizontal components ($q_{g,z} \ll q_{g,x}$). This standard assumption is motivated by the long-and-thin aspect ratio typical of these flows, and can be justified rigorously as the leading-order problem under a lubrication-type approximation [Yortsos, 1995, de Loubens and Ramakrishnan, 2011]. The vertical pressure distribution in the gas is therefore nearly hydrostatic,

$$\frac{\partial p_g}{\partial z} \approx -\rho_g g \qquad z^{n,I} \leq z \leq z^{n,T}, \tag{2.6}$$

where $z^{n,I}(x,t)$ is the vertical position of the gas–water interface. Equation (2.6) is integrated to arrive at an expression for the vertical pressure distribution in the gas. In doing so, variations in density arising from variations in phase-static pressure over the span of a single aquifer are neglected—more specifically, it is assumed that $\rho_g^0 g H c_g \ll 1$. This assumption is used repeatedly below. The

resulting pressure profile is

$$p_g(x,z,t) \approx p^n(x,t) - \rho_g^n g[z - z^{n,I}(x,t)] \qquad z^{n,I} \le z \le z^{n,T}, \tag{2.7}$$

where $p^n(x,t)$ is the pressure at the interface, $\rho_g^n(x,t)$ is the vertically averaged gas density, and $h^n(x,t) = z^{n,T} - z^{n,I}(x,t)$ is the thickness of the gas layer. Note that capillary pressure is neglected at the gas–water interface relative to typical phase-static pressures, $p_c \ll \rho_g^0 g H$, taking the water pressure and the gas pressure to be approximately equal along the interface within each aquifer. This is a standard assumption [*e.g.,* Nordbotten and Celia, 2006a, Hesse et al., 2007, Juanes et al., 2010]. A constant and uniform capillary pressure can easily be included, but would not change the results below.

Equation (2.7) implies that the lateral pressure gradient in the gas is given by

$$\frac{\partial p_g}{\partial x} \approx \frac{\partial p^n}{\partial x} - \rho_g^n g \frac{\partial h^n}{\partial x} \qquad z^{n,I} \le z \le z^{n,T}, \tag{2.8}$$

where terms of order $\rho_g^0 g H c_g \ll 1$ have once again been neglected. Equation (2.8) implies that the lateral gas flux is given by

$$q_{g,x}(x,z,t) \approx -\frac{k k_{rg}}{\mu_g}\left(\frac{\partial p^n}{\partial x} - \rho_g^n g \frac{\partial h^n}{\partial x}\right) \qquad z^{n,I} \le z \le z^{n,T}, \tag{2.9}$$

where $k_{rg}$ is the relative permeability to gas in the gas region. Relative permeability is traditionally taken to be a nonlinear and hysteretic constitutive function of saturation, $k_{rg}(s_g)$; however, having assumed that $s_g$ is constant and uniform within the gas region (see beginning of §2.1), $k_{rg}$ is taken to be constant and uniform. There is no gas below the interface, so $q_{g,x} = 0$ for $z^{n,B} \le z < z^{n,I}$.

Equation (2.4) is now integrated vertically over the full thickness of aquifer $n$,

$$\int_{z^{n,B}}^{z^{n,T}} \frac{\partial}{\partial t}\left(\rho_g s_g \phi\right) \mathrm{d}z + \int_{z^{n,B}}^{z^{n,T}} \boldsymbol{\nabla} \cdot \left(\rho_g \boldsymbol{q}_g\right) \mathrm{d}z = \int_{z^{n,B}}^{z^{n,T}} \mathcal{I}_g \, \mathrm{d}z. \tag{2.10}$$

This integration procedure is well established [*e.g.,* Bear, 1972, Gasda et al., 2009]; the key results are summarised below, while highlighting the non-standard aspects of the model.

The first term on the left-hand side of Eq. (2.10) becomes

$$\begin{aligned}\int_{z^{n,B}}^{z^{n,T}} \frac{\partial}{\partial t}(\rho_g \phi s_g)\,\mathrm{d}z &\approx \frac{\partial}{\partial t}(\rho_g^n \phi s_g h^n) \\ &\approx \rho_g^n \phi s_g \left[\left(c_r + \frac{\rho_g^0}{\rho_g^n} c_g\right) h^n \frac{\partial p^n}{\partial t} + \frac{\partial h^n}{\partial t}\right],\end{aligned} \tag{2.11}$$

where $s_g$ is now the constant and uniform saturation of gas in the gas region, $c_r \equiv (1/\phi)(\mathrm{d}\phi/\mathrm{d}p)$ is the rock (matrix) compressibility, and once again it is assumed that $\rho_g^0 g H c_g \ll 1$ [Mathias et al., 2011b]. Note that the density ratio multiplying $c_g$ is usually approximated as unity, but this approximation introduces errors in mass conservation of order $c_g(p_g - p^0)$, which is not negligible when the gas is moderately compressible (*e.g.*, in the context of methane migration). Note also that the introduction of rock compressibility to capture the impact of matrix deformation on pressure propagation is a standard and very widely used result from groundwater hydraulics. This approach is strictly valid under the assumptions of negligible lateral strain (*i.e.*, expansion or contraction that is primarily vertical) and constant vertical effective stress (*i.e.*, dominated by gravity), and conveniently decouples pressure propagation from the full machinery of poroelasticity and geomechanics [*e.g.*, van der Kamp and Gale, 1983, Green and Wang, 1990].

The second term on the left-hand side of Eq. (2.10) becomes

$$\begin{aligned}\int_{z^{n,B}}^{z^{n,T}} \boldsymbol{\nabla}\cdot\left(\rho_g \boldsymbol{q}_g\right)\,\mathrm{d}z &= \frac{\partial}{\partial x}\left(\int_{z^{n,B}}^{z^{n,T}} \rho_g q_{g,x}\,\mathrm{d}z\right) + \left(\rho_g q_{g,z}\right)\Big|_{z^{n,B}}^{z^{n,T}} \\ &\approx \frac{\partial}{\partial x}\left[-\rho_g^n h^n \frac{k k_{rg}}{\mu_g}\left(\frac{\partial p^n}{\partial x} - \rho_g^n g \frac{\partial h^n}{\partial x}\right)\right],\end{aligned} \tag{2.12}$$

after using Equations (2.5) and (2.8), and again assuming that $\rho_g^0 g H c_g \ll 1$. The

vertical gas fluxes at $z = z^{n,B}$ and $z = z^{n,T}$ vanish because gas leakage is not allowed. In Chapter 3 this constraint is relaxed and these fluxes remain for a derivation that includes gas leakage.

Recombining Equations (2.11) and (2.12) with Equation (2.10), yields

$$\rho_g^n \phi s_g \left[ (c_r + \frac{\rho_g^0}{\rho_g^n} c_g) h^n \frac{\partial p^n}{\partial t} + \frac{\partial h^n}{\partial t} \right] - \frac{\partial}{\partial x} \left[ \rho_g^n h^n \lambda_g \left( \frac{\partial p^n}{\partial x} - \rho_g^n g \frac{\partial h^n}{\partial x} \right) \right] = \mathcal{I}_g^n H, \quad (2.13)$$

where $\lambda_g \equiv k k_{rg}/\mu_g$ is the mobility of gas in the gas region and $\mathcal{I}_g^n$ is the vertically averaged mass injection rate of gas per unit volume into aquifer $n$.

#### 2.2.1.2 Water in aquifer $n$

Conservation of mass for the water in aquifer $n$ is given by

$$\frac{\partial}{\partial t} (\rho_w \phi s_w) + \boldsymbol{\nabla} \cdot (\rho_w \boldsymbol{q}_w) = \mathcal{I}_w, \quad (2.14)$$

where $s_w$ is the water saturation, $\boldsymbol{q}_w$ is the Darcy flux of water, and $\mathcal{I}_w$ is a source term that prescribes the local mass rate of water injection per unit volume. The Darcy flux of water is given by Darcy's law,

$$\boldsymbol{q}_w = -\frac{k k_{rw}}{\mu_w} \left( \boldsymbol{\nabla} p_w + \rho_w g \hat{\boldsymbol{e}}_z \right), \quad (2.15)$$

where $k_{rw}$ is the relative permeability to water flow, $\mu_w$ is the dynamic viscosity of water, and $p_w$ is the water pressure. The relative permeability to water flow is again typically taken to be a function of water saturation, $k_{rw}(s_w)$; here, the assumptions of no gas in the water region ($s_w = 1$ for $z^{n,B} < z < z^{n,I}$) and a constant and uniform saturation of residual water in the gas region ($s_w = 1 - s_g$ for $z^{n,I} < z < z^{n,T}$) imply that $k_{rw} = 1$ in the water region and $k_{rw} = k_{rw}^\star < 1$ in the gas region, where $k_{rw}^\star$ is constant and uniform. Note that $\mu_w$ is taken to be constant and uniform.

Above it is assumed that the gas is in vertical equilibrium, meaning that the vertical component of the gas flux is negligible relative to the horizontal component, such that the vertical pressure distribution is approximately hydrostatic (Equation 2.6). Conversely, for the water it is expected a weak but non-negligible vertical flow through the aquifers and the seals. For aquifers containing gas, this upward flow of water must also pass through the connected network of residual water films in the gas region before entering the seal, although the associated relative permeability may be very low (see §2.3.4).

To allow for weak vertical flow of water, this derivation adopts the ansatz that $q_{w,z}$ has the simplest continuous vertical flow structure that allows for different vertical fluxes at the bottom and top of the aquifer: Piecewise linear in $z$. Nordbotten and Celia [2006a] suggested this approach in the context of flow near a well in an aquifer with impermeable seals. Below, this approach is extended to account for the gas region and the permeable seals by assuming that $q_{w,z}$ has the following form:

$$q_{w,z}(x,z,t) \approx \begin{cases} q_{w,z}^{n,B} + \left(\dfrac{z - z^{n,B}}{z^{n,I} - z^{n,B}}\right)(q_{w,z}^{n,T} - q_{w,z}^{n,B}) & z^{n,B} \leq z < z^{n,I}, \\ q_{w,z}^{n,T} & z^{n,I} \leq z \leq z^{n,T}, \end{cases} \tag{2.16}$$

such that $q_{w,z}$ in aquifer $n$ varies linearly from to $q_{w,z}^{n,B}(x,t)$ at the bottom seal to $q_{w,z}^{n,T}(x,t)$ at the gas–water interface, and is then uniform and equal to $q_{w,z}^{n,T}(x,t)$ from the gas–water interface to the top seal. This structure implies that water flow in the gas region is primarily vertical, neglecting lateral transport through the gas region relative to lateral transport within the water region. Note that nothing is assumed about the magnitude of the vertical flux or its variation in $x$ or $t$, or about the horizontal flux in the water region—these aspects emerge naturally from Darcy's law and conservation of mass. The limitations of this assumed structure are discussed at the end of §2.2.

Equation (2.16) implies that the vertical pressure variation within the water is given by

$$\frac{\partial p_w}{\partial z} \approx \begin{cases} -\rho_w g - \dfrac{\mu_w}{k}\left[q_{w,z}^{n,B} + \left(\dfrac{z - z^{n,B}}{z^{n,I} - z^{n,B}}\right)(q_{w,z}^{n,T} - q_{w,z}^{n,B})\right] & z^{n,B} \le z < z^{n,I}, \\ -\rho_w g - \dfrac{\mu_w}{k k_{rw}^{\star}}\, q_{w,z}^{n,T} & z^{n,I} \le z \le z^{n,T}. \end{cases} \tag{2.17}$$

This expression is then integrated vertically to arrive at

$$p_w(x,z,t) \approx \begin{cases} p^n + (z^{n,I} - z)\Bigg\{\rho_w^n g \\ \quad + \dfrac{\mu_w}{2k}\left[(q_{w,z}^{n,T} + q_{w,z}^{n,B}) + \left(\dfrac{z - z^{n,B}}{z^{n,I} - z^{n,B}}\right)(q_{w,z}^{n,T} - q_{w,z}^{n,B})\right]\Bigg\} & z^{n,B} \le z < z^{n,I}, \\ p^n - (z - z^{n,I})\left\{\rho_w^n g + \dfrac{\mu_w}{k k_{rw}^{\star}}\, q_{w,z}^{n,T}\right\} & z^{n,I} \le z \le z^{n,T}, \end{cases} \tag{2.18}$$

where $p^n$ is the pressure along the gas–water interface, which is assumed to be the same for both water and gas, as discussed above. As with the derivation for gas, variations in density resulting from variations in hydrostatic pressure over the span of a single aquifer are neglected—more specifically, it is assumed that $\rho_w^0 g H c_w \ll 1$. Note that $p_w$ is parabolic in $z$ in the water region, linear in $z$ in the gas region, and continuous in $z$ throughout the domain, including across the gas–water interface. Equation (2.18) is now differentiated with respect to $x$ to give the lateral pressure gradient, and thereby the lateral water flux, as presented above for gas. This procedure is straightforward, although more laborious than for gas because $p^n$, $z^{n,I}$, $q_{w,z}^{n,T}$, and $q_{w,z}^{n,B}$ all vary in $x$. The result is

$$\begin{aligned} q_{w,x}(x,z,t) \approx\ & -\frac{k}{\mu_w}\left(\frac{\partial p^n}{\partial x} - \rho_w^n g \frac{\partial h^n}{\partial x}\right) \\ & -\frac{1}{2}\Bigg\{(z^{n,I} - z)\left[\frac{\partial}{\partial x}(q_{w,z}^{n,T} + q_{w,z}^{n,B}) + \left(\frac{z - z^{n,B}}{z^{n,I} - z^{n,B}}\right)\frac{\partial}{\partial x}(q_{w,z}^{n,T} - q_{w,z}^{n,B})\right] \\ & \quad -\frac{\partial h^n}{\partial x}\left[(q_{w,z}^{n,T} + q_{w,z}^{n,B}) + \left(\frac{z - z^{n,B}}{z^{n,I} - z^{n,B}}\right)^2 (q_{w,z}^{n,T} - q_{w,z}^{n,B})\right]\Bigg\}. \end{aligned} \tag{2.19}$$

for $z^{n,B} \leq z < z^{n,I}$, and recall that lateral flow of water in the gas region is neglected (*i.e.*, $q_{w,x} = 0$ for $z^{n,I} \leq z \leq z^{n,T}$).

Proceeding as above, Equation (2.14) is now integrated vertically over the full thickness of aquifer $n$,

$$\int_{z^{n,B}}^{z^{n,T}} \frac{\partial}{\partial t}\left(\rho_w \phi s_w\right)\,\mathrm{d}z + \int_{z^{n,B}}^{z^{n,T}} \boldsymbol{\nabla}\cdot\left(\rho_w \boldsymbol{q}_w\right)\,\mathrm{d}z = \int_{z^{n,B}}^{z^{n,T}} \mathcal{I}_w\,\mathrm{d}z. \tag{2.20}$$

Much like for gas, the first term on the left-hand side of Equation (2.20) becomes

$$\begin{aligned}\int_{z^{n,B}}^{z^{n,T}} \frac{\partial}{\partial t}(\rho_w \phi s_w)\,\mathrm{d}z &\approx \frac{\partial}{\partial t}[\rho_w^n \phi (H - h^n) + \rho_w^n \phi (1 - s_g) h^n] \\ &\approx \rho_w^n \phi \left[(c_r + c_w)(H - s_g h^n)\frac{\partial p^n}{\partial t} - s_g \frac{\partial h^n}{\partial t}\right].\end{aligned} \tag{2.21}$$

Recall that, unlike for gas, it is assumed that $c_w(p_w - p^0) \ll 1$ and therefore that $\rho_w \approx \rho_w^0$, as discussed above.

The second term on the left-hand side of Equation (2.20) becomes

$$\begin{aligned}\int_{z^{n,B}}^{z^{n,T}} \boldsymbol{\nabla}\cdot\left(\rho_w \boldsymbol{q}_w\right)\mathrm{d}z &= \frac{\partial}{\partial x}\left(\int_{z^{n,B}}^{z^{n,T}} \rho_w q_{w,x}\,\mathrm{d}z\right) + \left(\rho_w q_{w,z}\right)\Big|_{z^{n,B}}^{z^{n,T}} \\ &\approx \frac{\partial}{\partial x}\left\{-\rho_w^0 \frac{k}{\mu_w}(H - h^n)\left[\frac{\partial p^n}{\partial x} - \rho_w^0 g \frac{\partial h^n}{\partial x}\right]\right. \\ &\qquad \left. - \rho_w^0 \frac{\partial}{\partial x}\left[\frac{1}{6}(H - h^n)^2 (q_{w,z}^{n,B} + 2q_{w,z}^{n,T})\right]\right\} + \rho_w^0 (q_{w,z}^{n,T} - q_{w,z}^{n,B}),\end{aligned} \tag{2.22}$$

where horizontal flow of water in the gas region has been neglected ($q_{w,x} \approx 0$ for $z^{n,I} < z < z^{n,T}$), and once again it has been assumed that $\rho_w^0 g H c_w \ll 1$ and that $\rho_w \approx \rho_w^0$. Recombining Equations (2.21) and (2.22) with Equation (2.20), yields

$$\begin{aligned}\phi\left[(H - s_g h^n)(c_r + c_w)\frac{\partial p^n}{\partial t} - s_g \frac{\partial h^n}{\partial t}\right] - \frac{\partial}{\partial x}\left\{\lambda_w (H - h^n)\left[\frac{\partial p^n}{\partial x} - \rho_w g \frac{\partial h^n}{\partial x}\right]\right. \\ \left. + \frac{1}{6}\frac{\partial}{\partial x}\left[(H - h^n)^2 (q_{w,z}^{n,B} + 2q_{w,z}^{n,T})\right]\right\} = -(q_{w,z}^{n,T} - q_{w,z}^{n,B}) + \frac{\mathcal{I}_w^n H}{\rho_w},\end{aligned} \tag{2.23}$$

where $\lambda_w \equiv k/\mu_w$ is the mobility of water in the water region.

Equations (2.13) and (2.23) are $2N_z$ coupled nonlinear partial differential equations (PDEs) in $p^n$ and $h^n$. For a system with permeable seals, the $N_z$ aquifers are coupled by vertical pressure dissipation and the system is closed via expressions for the vertical water fluxes $q_{w,z}^{n,B}$ and $q_{w,z}^{n,T}$ in terms of $p^n$ and $h^n$.

For a system with impermeable seals, the aquifers are uncoupled and flow and pressurisation are constrained to the injection aquifer. With impermeable seals and no gas, Equation (2.23) then reduces to the classical groundwater-flow equation from groundwater hydraulics [Bear, 1979] (see §2.3.1), which is equivalent to the vertically integrated form of the governing equation presented in §1.2.2. With impermeable seals and gas, Equations (2.13) and (2.23) instead reduce to the widely used model for a gravity current in a horizontal aquifer for an incompressible system [*e.g.*, Bear, 1972, Huppert and Woods, 1995], and to the model of Mathias et al. [2009] for a compressible system (see §2.3.3 and Appendix A).

### 2.2.2 Coupling the aquifers with vertical fluxes

The approach of coupling multiple aquifers with vertical fluxes across the intervening seals was previously suggested by Hunt [1985]. For incompressible and strictly vertical flow of water through seals, conservation of mass requires that the mass flux of water into seal $s$ from aquifer $n-1$ must equal the mass flux of water out of seal $s$ and into aquifer $n$ at the same position $x$ and time $t$. Taking the water density to be approximately uniform and constant throughout the system ($c_w(p_w - p^0) \ll 1 \implies \rho_w \approx \rho_w^0$), there must then be a single water flux $q_{w,z}^s$ associated with each seal $s$:

$$q_{w,z}^s = q_{w,z}^{n-1,T} = q_{w,z}^{n,B}. \tag{2.24}$$

This flux is calculated via Darcy's law,

$$q^s_{w,z} = -\frac{k_s}{\mu_w}\left(\frac{p^{n,B}_w - p^{n-1,T}_w}{b} + \rho_w g\right), \tag{2.25}$$

where the assumption of no gas in the seals implies that $k_{rw} = 1$, and where $p^{n,B}_w = p_w(z^{n,B})$ and $p^{n-1,T}_w = p_w(z^{n-1,T})$. These unknown pressures are written in terms of the fluxes through the seals by combining Equation (2.18) with Equation (2.24),

$$p^{n-1,T}_w = p^{n-1} - h^{n-1}\left[\rho_w g + \frac{\mu_w}{k k^\star_{rw}} q^s_{w,z}\right], \tag{2.26a}$$

$$p^{n,B}_w = p^n + (H - h^n)\left[\rho_w g + \frac{\mu_w}{2k}(q^{s+1}_{w,z} + q^s_{w,z})\right]. \tag{2.26b}$$

Combining Equations (2.25) and (2.26) and rearranging, yields

$$\left(\frac{H-h^n}{2\lambda_w}\right) q^{s+1}_{w,z} + \left(\frac{h^{n-1}}{\lambda^\star_w} + \frac{b}{\lambda^s_w} + \frac{H-h^n}{2\lambda_w}\right) q^s_{w,z} = -\left[p^n - p^{n-1} + \rho^0_w g(h^{n-1} + b + H - h^n)\right], \tag{2.27}$$

where $\lambda^\star_w = k k^\star_{rw}/\mu_w$ is the mobility of water in the gas regions of the aquifers and $\lambda_s = k_s/\mu_w$ is the mobility of water in the seals. Equation (2.27) is a linear system of $N_z - 1$ coupled algebraic equations in the $N_z - 1$ unknown fluxes $q^s_{w,z}$ for $s = 2 \ldots N_z$, from which $q^s_{w,z}$ can be solved for in terms of $p^n$ and $h^n$. Recall that the bottom-most and top-most seals are impermeable, so that $q^1_{w,z} = q^{N_z+1}_{w,z} = 0$.

### 2.2.3 Boundary and initial conditions

The model domain comprises a system of $N_z$ aquifers and $N_z + 1$ seals, all of which extend horizontally from $x = -L_x/2$ to $x = L_x/2$. This layered aquifer system is assumed to be initially fully saturated with water (no gas), and the initial pressure distribution is assumed to be hydrostatic. For simplicity, the pressure at the

lateral boundaries is assumed to remain hydrostatic throughout; this implies that simulated results are independent of lateral domain size for scenarios where the system is sufficiently laterally extensive that changes in pressure due to injection never reach the boundaries, which is true for the reference case (see Figure 2.2).

For injection of phase $\alpha$ into the horizontal centre of aquifer $n$ at a mass flow rate $\dot{M}^n_\alpha(t)$ per unit length into the page, the relevant vertically integrated source term $\mathcal{I}^n_\alpha$ can be written

$$\mathcal{I}^n_\alpha = \frac{\dot{M}^n_\alpha(t)}{H}\,\delta(x), \tag{2.28}$$

where $\delta(x)$ is the Dirac delta function.

### 2.2.4 Non-dimensionalization

Consider the injection of gas at a mass flow rate $\dot{M}$ per unit length into the page for a time $\mathcal{T}$. This scenario motivates the following characteristic scales for length, pressure, and vertical flux:

$$\mathcal{L} \equiv \frac{\dot{M}\mathcal{T}}{2\phi s_g \rho^0_g H}\ , \quad \mathcal{P} \equiv \frac{\phi\mathcal{L}^2}{\lambda_w \mathcal{T}} = \frac{\dot{M}\mathcal{L}}{2\lambda_w s_g \rho^0_g H}\ , \quad \text{and} \quad \mathcal{Q}_z \equiv \frac{\lambda^s_w \mathcal{P}}{b}. \tag{2.29}$$

The characteristic length $\mathcal{L}$ is the half-width of an incompressible plug (box) of gas of mass $\dot{M}\mathcal{T}$ per unit length into the page. The characteristic pressure $\mathcal{P}$ is the pressure drop associated with a Darcy flux $\phi\mathcal{L}/\mathcal{T}$ of water over a distance $\mathcal{L}$. The characteristic vertical flux $\mathcal{Q}_z$ is the vertical flux of water associated with a characteristic pressure drop $\mathcal{P}$ across a seal of thickness $b$.

The above scales are used in conjunction with existing parameters to define the following dimensionless quantities:

$$\begin{gathered} \tilde{x} \equiv \frac{x}{\mathcal{L}}, \quad \tilde{t} \equiv \frac{t}{\mathcal{T}}, \quad \tilde{h} \equiv \frac{h}{H}, \quad \tilde{p} \equiv \frac{p}{\mathcal{P}}, \quad \tilde{q} \equiv \frac{q}{\mathcal{Q}_z}, \\ \tilde{b} \equiv \frac{b}{H}, \quad \tilde{\rho}_\alpha \equiv \frac{\rho_\alpha}{\rho^0_g}, \quad \tilde{\mathcal{I}}^n_\alpha \equiv \frac{2\mathcal{L}H\,\mathcal{I}^n_\alpha}{\dot{M}}. \end{gathered} \tag{2.30}$$

The following dimensionless groups are also introduced:

$$N_{cw} \equiv c_w \mathcal{P} \tag{2.31a}$$

$$R_{cw} \equiv c_r / c_w \tag{2.31b}$$

$$R_{cf} \equiv c_g / c_w \tag{2.31c}$$

$$R_A \equiv \mathcal{L} / H \tag{2.31d}$$

$$R_d \equiv \rho_g^0 / \rho_w^0 \tag{2.31e}$$

$$N_g \equiv \rho_w^0 g H / \mathcal{P} \tag{2.31f}$$

$$\mathcal{M} \equiv \lambda_g / (s_g \lambda_w) \tag{2.31g}$$

$$\Lambda_w^s \equiv \lambda_w^s H / (\lambda_w b) \tag{2.31h}$$

The first three of these groups capture the effects of the compressibility: The 'compressibility number' $N_{cw}$ measures the overall importance of compressibility within the system, whereas the two compressibility ratios $R_{cw}$ and $R_{cf}$ compare the compressibilities of the various phases. The aspect ratio $R_A$ compares the characteristic length of the plume to the aquifer thickness, capturing the importance of horizontal-to-vertical flow within and around the gas plume. The density ratio $R_d$ compares the fluid densities and the 'gravity number' compares hydrostatic pressure to the characteristic injection pressure, such that the grouping $(1 - R_d)N_g$ measures the importance of buoyancy relative to injection. The mobility ratio $\mathcal{M}$ compares the mobility of gas within the aquifer to that of water, incorporating the gas saturation for convenience. Lastly, the 'leakage number' $\Lambda_w^s$ measures the resistance to vertical flow through the aquifers relative to the seals, such that the grouping $R_A^2 \Lambda_w^s$ measures the importance of vertical pressure dissipation relative to lateral pressure dissipation.

### 2.2.5 Model summary

Dropping the tildes, the coupled system of partial differential equations can now be written in dimensionless form as:

$$N_{cw}(R_{cw}\rho_g^n + R_{cf})h^n\frac{\partial p^n}{\partial t} + \rho_g^n\frac{\partial h^n}{\partial t} - \mathcal{M}\frac{\partial}{\partial x}\left[\rho_g^n h^n\left(\frac{\partial p^n}{\partial x} - \rho_g^n R_d N_g\frac{\partial h^n}{\partial x}\right)\right] = \mathcal{I}_g^n, \tag{2.32}$$

and

$$N_{cw}(R_{cw}+1)(1-s_g h^n)\frac{\partial p^n}{\partial t} - s_g\frac{\partial h^n}{\partial t} - \frac{\partial}{\partial x}\left\{(1-h^n)\left[\frac{\partial p^n}{\partial x} - N_g\frac{\partial h^n}{\partial x}\right] + \frac{\Lambda_w^s}{6}\frac{\partial}{\partial x}\left[(1-h^n)^2(q_{w,z}^s + 2q_{w,z}^{s+1})\right]\right\} = -{R_A}^2\Lambda_w^s(q_{w,z}^{s+1} - q_{w,z}^s) + s_g R_d\mathcal{I}_w^n \tag{2.33}$$

with

$$\rho_g^n(p^n) = 1 + N_{cw}R_{cf}(p^n - p^0) \tag{2.34}$$

and

$$\frac{\Lambda_w^s}{2}(1-h^n)q_{w,z}^{s+1} + \left[\frac{\Lambda_w^s}{k_{rw}^\star}h^{n-1} + 1 + \frac{\Lambda_w^s}{2}(1-h^n)\right]q_{w,z}^s = -\left[p^n - p^{n-1} + N_g(h^{n-1} + b + 1 - h^n)\right]. \tag{2.35}$$

For a system with $N_z$ aquifers, Equations (2.32) and (2.33) provide $2N_z$ coupled PDEs enforcing conservation of mass for gas and for water, respectively, in each aquifer $n = 1 \dots N_z$. Equation (2.34) is the dimensionless form of the linear constitutive relationship for gas density. Lastly, Equation (2.35) is a linear system of $N_z - 1$ algebraic equations in the dimensionless vertical fluxes of water across each interior seal, $q_{w,z}^s$ for $s = 2 \dots N_z$, where $q_{w,z}^1 = q_{w,z}^{N_z+1} = 0$.

Initially, it is assumed that there is no gas in the system, $h^n(x, t = 0) = 0$, and it is ensured that the gas never reaches the lateral boundaries. It is additionally

assumed that the pressure is initially hydrostatic, and that the pressure at the boundaries remains hydrostatic:

$$p^n(x, t = 0) = p^n(-L_x/2, t) = p^n(L_x/2, t) = p^0 - N_g[n + (n - 1)b], \qquad (2.36)$$

recalling that the pressures $p^n$ are the pressures at the gas–water interface in each aquifer, which is the top of the aquifer in the absence of gas, and that $p^0$ is the initial pressure at the bottom of aquifer 1.

Vertical pressure dissipation does not appear explicitly in Equation (2.32) because the gas is limited to vertical equilibrium, which is valid for $R_A \gg 1$. Vertical pressure dissipation is responsible for two of the terms in Equation (2.33), both of which are multiplied by $\Lambda_w^s$. The term on the right-hand side measures the net mass of water that enters layer $n$ through seals $s$ and $s + 1$, and its dimensionless coefficient measures the importance vertical pressure dissipation relative to lateral pressure dissipation: A pressure difference of size $\mathcal{P}$ over a lateral distance $\mathcal{L}$ would drive a flow rate $Q_l \sim \lambda_w \mathcal{P} H/\mathcal{L}$ laterally through the aquifer, and a flow rate $Q_s \sim \lambda_w^s \mathcal{P}\mathcal{L}/b$ vertically across the associated seals. The ratio of these flow rates is $Q_s/Q_l = \lambda_w^s \mathcal{L}^2/(\lambda_w H b) = R_A^2 \Lambda_w^s$, highlighting that the extensive contact area between the aquifers and the seals enables vertical pressure dissipation to have a strong impact on the pressure field even when $\lambda_w^s \ll \lambda_w$ ($\Lambda_w^s \ll 1$). The term proportional to $\Lambda_w^s$ on the left-hand side is a consequence of conservation of mass, introducing weak lateral variations in $q_{w,x}$ to compensate for vertical variations in $q_{w,z}$. The assumed piecewise-linear structure for the vertical flux determines the specific structure of this term, but it will always be proportional to $\Lambda_w^s$ and involve the horizontal divergence of some function of $h^n$ times the fluxes through the seals. The model is valid as long as this term is indeed a weak perturbation to horizontal flow, meaning that $\Lambda_w^s \ll 1$. In general, this term is clearly less important than the one proportional to $R_A^2 \Lambda_w^s$ since $R_A \gg 1$, and could safely be neglected, but is retained to preserve the consistency of the model formulation.

## 2.3 Results

For illustrative purposes, a reference scenario involving fluid injection into the central aquifer ($n = 4$) of a seven-aquifer system ($N_z = 7$) is considered. Rock properties are chosen to be consistent with sandstone aquifers and mudstone seals and fluid properties are chosen to be consistent with water and $CO_2$ at a depth of $\sim$1 km, where the reference pressure is the pressure at the bottom of aquifer 1 [e.g., Lemmon, 1998, Szulczewski et al., 2012, Arts et al., 2004]. Note that the residual water saturation in the gas region ($s_{wr} = 1 - s_g = 0.2$) represents an upscaled (Darcy-scale) value for the minimum water saturation (also commonly referred to as the 'connate' or 'irreducible' water saturation). Also note that the precise value of $s_{wr}$ does not have an important qualitative effect on the predictions of the model. As $s_{wr}$ is an upscaled quantity, it is likely that significant local variations in the residual water saturation are present in most aquifers. The concept of residual water saturation is often introduced within the Darcy-scale description of capillary pressure: As the pore-space becomes increasingly saturated with gas, the capillary pressure increases up to a maximum value that corresponds to the maximum gas-fraction in the pore space. Although the water is minimally-saturated at this limit, it can remain connected through thin films and transmit weak flows [e.g., Teige et al., 2006, Blunt, 2017]. In this study, horizontal water flow in the gas region is neglected. However, a weak vertical flow of water through the gas is permitted. For simplicity, changes to saturation in the gas region are neglected, and this weak vertical flow is exclusively parameterized through the relative permeability of water flowing through thin, but connected, films ($k^\star_{rw}$). The value of $k^\star_{rw}$ is poorly constrained but has been shown to be as low as $5 \times 10^{-9}$ [Blunt, 2017]. Note that the reference value of $k^\star_{rw}$ is unimportant, as $k^\star_{rw}$ is always considered across its full potential range. This becomes especially important in Chapter 3, when limits for capillary pressure buildup naturally emerge for extreme values of $k^\star_{rw}$.

The reference case considers an injection rate of ∼1 Mt per year distributed along a 30 km long array of injection wells for a period of 10 years [Szulczewski et al., 2012]. Based on this scenario, a set of reference values are chosen for dimensional parameters, which are subsequently used to calculate corresponding reference values for dimensionless parameters. Both sets of values are reported in Table 2.1. These values are used in the rest of this chapter except where noted otherwise.

In the context of this reference scenario, the predictions of the model are considered for several test problems: (i) water injection with impermeable seals, which allows for the verification of the model against a classical analytical solution; (ii) water injection with permeable seals, which allows for the model to be benchmarked against a fully 2D groundwater-flow model; (iii) gas injection with impermeable seals, which allows for the verification of the model against previous results for gas injection; and (iv) gas injection with permeable seals, which allows for the study the impact of pressure dissipation on gas injection.

In all cases, the model is solved numerically by discretising in space using a standard finite-volume method on a uniform grid and then integrating in time using `MATLAB`'s built-in adaptive implicit solver for stiff ODEs, `ODE15s` [see Appendices B and C, and Shampine and Reichelt, 1997]. For the quasi-2D model, the advective terms are discretized using standard first order upwinding. The coefficients multiplying diffusive terms in the quasi-2D model are calculated using an arithmetic mean. Note that an arithmetic mean is used instead of a harmonic mean to avoid degenerate coefficients around the nose of the plume ($h \to 0$). In cases with permeable seals, the linear system of equations for the leakage fluxes (Equation 2.35) becomes $N_x$ uncoupled linear algebraic systems of size $N_z - 1$, where $N_x$ is the number of horizontal gridblocks; these systems are inverted at each timestep using a standard linear solver, which is computationally inexpensive.

| **Parameter** | **Symbol** | **Value** |
|---|---|---|
| Number of aquifers | $N_z$ | 7 |
| Horizontal extent | $L_x$ | 100 km |
| Aquifer thickness | $H$ | 10 m |
| Aquifer porosity | $\phi$ | 0.3 |
| Aquifer permeability | $k$ | $10^{-13}$ m$^2$ |
| Seal thickness | $b$ | 1 m |
| Seal permeability | $k_s$ | $10^{-18}$ m$^2$ |
| Rock compressibility | $c_r$ | $3.0 \times 10^{-11}$ Pa$^{-1}$ |
| Reference pressure | $p^0$ | 10 MPa |
| Water viscosity | $\mu_w$ | $8 \times 10^{-4}$ Pa·s |
| Water density | $\rho_w$ | 1000 kg·m$^{-3}$ |
| Water compressibility | $c_w$ | $4.5 \times 10^{-10}$ Pa$^{-1}$ |
| Saturation of water in gas region | $s_{wr}$ | 0.2 |
| Relative permeability to water in gas region | $k^\star_{rw}$ | 0.01 |
| Gas viscosity | $\mu_g$ | $4 \times 10^{-5}$ Pa·s |
| Gas density | $\rho^0_g$ | 700 kg·m$^{-3}$ |
| Gas compressibility | $c_g$ | $1.5 \times 10^{-8}$ Pa$^{-1}$ |
| Saturation of gas in gas region | $s_g$ | 0.8 |
| Relative permeability to gas in gas region | $k_{rg}$ | 1 |
| Mass injection rate | $\dot{M}$ | $10^{-3}$ kg·s$^{-1}$·m$^{-1}$ |
| Injection time | $\mathcal{T}$ | 10 years |
| Compressibility number | $N_{cw}$ | $3.02 \times 10^{-5}$ |
| Rock-to-water compressibility ratio | $R_{cw}$ | $6.67 \times 10^{-2}$ |
| Gas-to-water compressibility ratio | $R_{cf}$ | 33.3 |
| Aspect ratio | $R_A$ | 9.39 |
| Density ratio | $R_d$ | 0.7 |
| Gravity number | $N_g$ | 1.46 |
| Mobility ratio | $\mathcal{M}$ | 25 |
| Water-leakage strength | $\Lambda^s_w$ | $10^{-4}$ |
| Seal-to-aquifer thickness ratio | $\tilde{b}$ | 0.1 |
| Horizontal extent | $\tilde{L}_x$ | 1062 |

**Table 2.1:** Reference parameter values. The dimensionless values (below the double-line) are calculated directly from the dimensional values (above the double-line).

### 2.3.1 Water injection with impermeable seals

The first model problem considered is that of water injection into a one-aquifer system ($n = N_z = 1$) with impermeable seals ($\Lambda_w^s = 0$) and containing no gas ($h^1 = 0$), in which case the model reduces to the classical linear groundwater-flow equation from hydrology and hydrogeology,

$$N_{cw}(R_{cw} + 1)\frac{\partial p^1}{\partial t} - \frac{\partial^2 p^1}{\partial x^2} = s_g R_d \mathcal{I}_w^1(x) = 2 s_g R_d \, \delta(x) \, u(t), \tag{2.37}$$

where $\dot{M}_g^1 = 0$ and $\dot{M}_w^1 = \dot{M} u(t)$, where $u(t)$ is the unit (Heaviside) step function and $\delta(x)$ is now the dimensionless Dirac delta function. The factor of $s_g R_d$ on the right-hand side is a consequence of using of a characteristic length based on gas injection (Equation 2.29). It is awkward for gas properties to appear in a problem with no gas, and they could be eliminated by suitable rescaling of the characteristic length, but their values have no impact on the dimensional solution.

The pressure $p^1$ is the pressure along the gas–water interface in the aquifer (see §2.2.1.1). In the absence of gas, this degenerates to the pressure at the top of the aquifer. Recall that the reference pressure is the initial pressure at the bottom of aquifer 1; in the absence of vertical flow, the dimensionless pressure at the top will be lower than the dimensionless pressure at the bottom by the dimensionless hydrostatic contribution over the thickness of one aquifer, $N_g$. Therefore the following initial and boundary conditions are imposed: $p^1(x, 0) = p^1(-L_x/2, t) = p^1(L_x/2, t) = p^0 - N_g$.

Equation (2.37) is a linear diffusion problem that can be solved analytically. To do so, symmetry across $x = 0$ is assumed, before focusing on the positive sub-domain $0 \leq x \leq L_x/2$. Subsequently, the injection term can be rewritten as a boundary

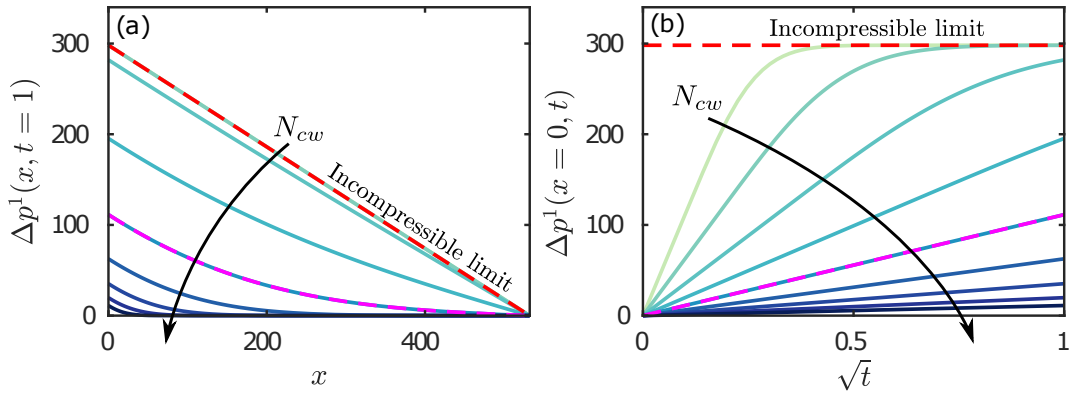


**Figure 2.2:** Pressure perturbation during water injection into a one-aquifer system with impermeable seals for a wide range of compressibilities, $\log_{10}(N_{cw}) \approx -6.5$, $-6$, $-5.5$, $-5$, $-4.5$, $-4$, $-3.5$, $-3$, and $-2.5$. The plots show: (a) the pressure perturbation at the end of injection, $\Delta p^1(x, t = 1)$, against $x$, and (b) the injection pressure, $\Delta p^1(x = 0, t)$, against $\sqrt{t}$. The dashed red line is the incompressible limit ($N_{cw} \to 0$) and the dashed magenta line is the analytical solution for the reference scenario ($\log_{10}(N_{cw}) \approx -4.5$). Note that the curve for $\log_{10}(N_{cw}) \approx -6.5$ is not visible in panel (a).

condition: $\partial p^1/\partial x(0, t) = -s_g R_d u(t)$. Standard separation of variables then yields

$$p^1(x, t) = \begin{cases} p^0 - N_g + s_g R_d (x + L_x/2) + \Omega(x, t) & \text{for } x \leq 0, \\ \\ p^0 - N_g - s_g R_d (x - L_x/2) + \Omega(x, t) & \text{for } x \geq 0, \end{cases} \tag{2.38}$$

where $\Omega(x, t)$ is given by

$$\Omega(x, t) = -\sum_{n=0}^{\infty} \frac{4 s_g R_d}{L_x \lambda_n^2} \exp\left[-\frac{\lambda_n^2 t}{N_{cw}(R_{cw} + 1)}\right] \cos(\lambda_n x) \tag{2.39}$$

with

$$\lambda_n = \frac{(2n + 1)\pi}{L_x}. \tag{2.40}$$

This solution is well known, and it is not surprising that the numerical scheme can reproduce it. It is used here as an instructive reminder of the impact of compressibility on lateral pressure dissipation.

In Figure 2.2, the pressure perturbation due to injection is plotted, $\Delta p^1 \equiv p^1 - (p^0 - N_g)$, for different values of the compressibility number $N_{cw}$. Recall that $N_{cw}$

compares the characteristic compressibility to the characteristic pressure, so that larger values (due either to larger compressibility or to larger pressure) imply an increasingly compressible system, whereas $N_{cw} \to 0$ implies an incompressible system. As $N_{cw}$ increases, $\Delta p^1$ is smaller and more concentrated near the injection point ($x = 0$)—that is, compressibility mitigates pressure buildup in both magnitude and extent for a fixed injection time (Figure 2.2a). For all values of $N_{cw}$, the injection pressure is proportional to $\sqrt{t}$ until the perturbation reaches the boundaries (Figure 2.2b). Thereafter, interaction with the fixed pressure at $x = \pm L_x$ drives a transition toward a steady-state profile that is linear in $x$. The system reaches this steady state more quickly as $N_{cw}$ decreases, and instantaneously in the incompressible limit ($N_{cw} \to 0$).

### 2.3.2 Water injection with permeable seals

The model developed in this chapter captures vertical pressure dissipation at the basin scale by allowing for a weak vertical flow of water through the aquifers and across the seals, assuming that this vertical water flux has a continuous, piecewise-linear structure. The model also neglects compressibility and lateral transport within the seals by assuming that the vertical fluxes of water in and out must be equal.

To test these assumptions, a scenario is considered in which water is injected into the central aquifer ($n = 4$) of a seven-aquifer system ($N_z = 7$) with permeable seals, but no gas ($h^n = 0$ for all $n$). In this context, the model is most similar to the linear groundwater-flow model proposed by Hunt [1985] for coupling layered aquifers via vertical flow across the intervening seals; Hunt [1985] neglected vertical flow except across the seals, whereas the model developed above allows for weak

vertical flow throughout the system. The model becomes

$$N_{cw}(R_{cw}+1)\frac{\partial p^n}{\partial t} - \frac{\partial}{\partial x}\left[\frac{\partial p^n}{\partial x} + \frac{\Lambda_w^s}{6}\frac{\partial}{\partial x}\left(q_{w,z}^s + 2q_{w,z}^{s+1}\right)\right] = -R_A^2\Lambda_w^s(q_{w,z}^{s+1} - q_{w,z}^s) + s_g R_d \mathcal{I}_w^n(x), \tag{2.41}$$

for $n = s = 1 \ldots 7$, with

$$\frac{\Lambda_w^s}{2}q_{w,z}^{s+1} + \left[1 + \frac{\Lambda_w^s}{2}\right]q_{w,z}^s = -\left[p^n - p^{n-1} + N_g(b+1)\right], \tag{2.42}$$

for $n = s = 2 \ldots 6$, where $\mathcal{I}_w^4 = 2s_g R_d \delta(x)u(t)$, $\mathcal{I}_w^n = 0$ for $n \neq 4$, and $q_{w,z}^1 = q_{w,z}^8 = 0$. The initial and boundary conditions are as in Equation (2.36).

To assess the accuracy of the model, it is compared with a classical 2D groundwater-flow model, which can be written in the above notation as

$$N_{cw}(R_{cw}+1)\frac{\partial p}{\partial t} - \Lambda_w^{2\mathrm{D}}\frac{\partial^2 p}{\partial x^2} - \frac{\partial}{\partial z}\left(\Lambda_w^{2\mathrm{D}}\frac{\partial p}{\partial z}\right) = s_g R_d \mathcal{I}_w^{2\mathrm{D}}, \tag{2.43}$$

where $p(x,z,t)$ is the full 2D pressure field, $\Lambda_w^{2\mathrm{D}}$ is equal to 1 within the aquifers and to $b\Lambda_w^s$ within the seals, and $\mathcal{I}_w^{2\mathrm{D}}$ is equal to $2s_g R_d \delta(x)u(t)$ within aquifer 4 and to 0 elsewhere. This model allows for full 2D flow, as well as compressibility in both the aquifers and the seals [*e.g.*, Bear, 1979]. The following initial and boundary conditions are imposed: $p(x,z,0) = p(-L_x/2,z,t) = p(L_x/2,z,t) = p^0 - N_g(z - z^{1,B})$ and $\partial p/\partial z(x,z^{1,B},t) = \partial p/\partial z(x,z^{7,T},t) = 0$. As with the reduced-order model, Equation (2.43) is solved numerically by discretising in space using a standard finite-volume method on a uniform 2D grid and integrating in time using `MATLAB`'s built-in implicit solver for stiff ODEs, `ODE15s` [Shampine and Reichelt, 1997]. Upward biased coefficients for the diffusive fluxes were used in the 2D groundwater model for the original results, but a subsequent comparison with harmonic-averaged coefficients revealed that the choice of averaging method does not noticeably change the results, with associated errors comparable to the

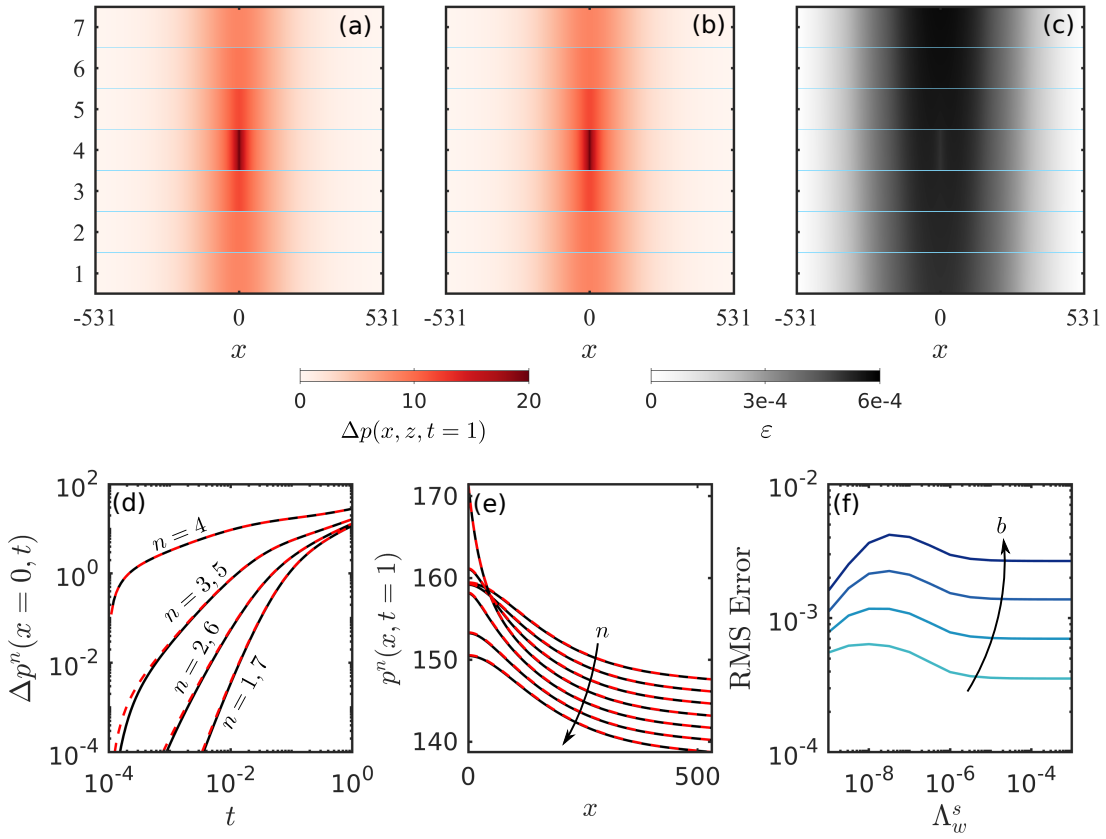


**Figure 2.3:** Pressure perturbation during water injection into aquifer 4 of a seven-aquifer system with permeable seals, comparing the quasi-2D model against a full 2D model. Plotted here is: (a) the reconstructed 2D pressure perturbation from the quasi-2D model at $t = 1$ for $b = 0.0125$ and $\Lambda_w^s = 10^{-5}$, (b) the same thing for the full 2D model, and (c) the magnitude of the relative error $\varepsilon$ between the two, disregarding the seals (shown in light blue). Also plotted: (d) the pressure perturbation at the top of each aquifer at $x = 0$ against $t$ for the quasi-2D model (dashed red) and the full 2D model (solid black), (e) the pressure at the top of each aquifer at $t = 1$ against $x$ for the quasi-2D model (dashed red) and the full 2D model (solid black), and (f) the root-mean-square (RMS) relative error between the two models at $t = 1$ against $\Lambda_w^s$ for $b = 0.0125$, $0.025$, $0.05$, and $0.1$.

relative tolerance of the solver ($\sim 10^{-6}$). To ensure a fair comparison between the two models, the same resolution in $x$ and the same absolute and relative tolerances in time are used for both solutions.

Figure 2.3(a), shows the pressure perturbation predicted by the quasi-2D model at the end of injection ($t = 1$) for $b = 0.0125$ and $\Lambda_w^s = 10^{-5}$. The same quantity for the full 2D model is shown in Figure 2.3(b), and the relative error between the two is shown in Figure 2.3(c). For reference, solving the full 2D model took about 8 minutes on a single core of a standard desktop PC, whereas solving the

quasi-2D model for the same scenario took about 0.4 seconds. Both the full 2D model, and quasi-2D model, used a horizontal resolution of 401 uniformly spaced grid blocks, which was found to be sufficiently converged. The choice of vertical resolution for the full 2D model is more complex due the limits imposed by the thickness of the seals. For simplicity, a uniformly spaced vertical grid was used. The requirements of a uniform grid and at least two grid blocks in the thinnest seal ($b = 0.0125$) leads to 160 grid blocks per aquifer, and 16 grid blocks for the thickest seal ($b = 0.1$). This resolution was found to be sufficiently converged, with an increase in vertical resolution producing errors on the order of the relative tolerance of the solver ($\sim 10^{-6}$). The low resolution required to capture pressure dissipation across the seals is likely due to the fact that compressibility in the seals becomes unimportant at very early times (see below). Accordingly, a fine resolution is not needed to capture the approximately linear pressure gradient across the seals, once seal compressibility can be neglected.

The predictions of both models are compared in more detail in Figures 2.3(d), 2.3(e), and 2.3(f). Because the quasi-2D model neglects compressibility within the seals, it begins pressurising the overlying and underlying aquifers slightly faster than the full 2D model, leading to a small disagreement in $p^n$ outside of the injection layer at early times (Figure 2.3d). This error decays as the seals pressurise, which happens over a dimensionless timescale $bN_{cw}(1+R_{cw})/(R_A^2\Lambda_w^s) \ll 1$ (dimensional timescale $b^2\phi(c_w+c_r)/\lambda_w^s \ll \mathcal{T}$). For the scenario shown in Figure 2.3(a–e), this timescale is $bN_{cw}(1+R_{cw})/(R_A^2\Lambda_w^s) \approx 4\times 10^{-4}$ and the error does indeed become negligible for dimensionless times sufficiently greater than this value. Figure 2.3(f) shows that this source of error increases monotonically with $b$, but varies non-monotically with $\Lambda_w^s$: For small values of $\Lambda_w^s$, the seals pressurise more slowly but vertical pressure dissipation is less important, whereas for larger values of $\Lambda_w^s$, vertical pressure dissipation is more important and the seals pressurise more quickly. The maximum root-mean-square (RMS) relative error between the two

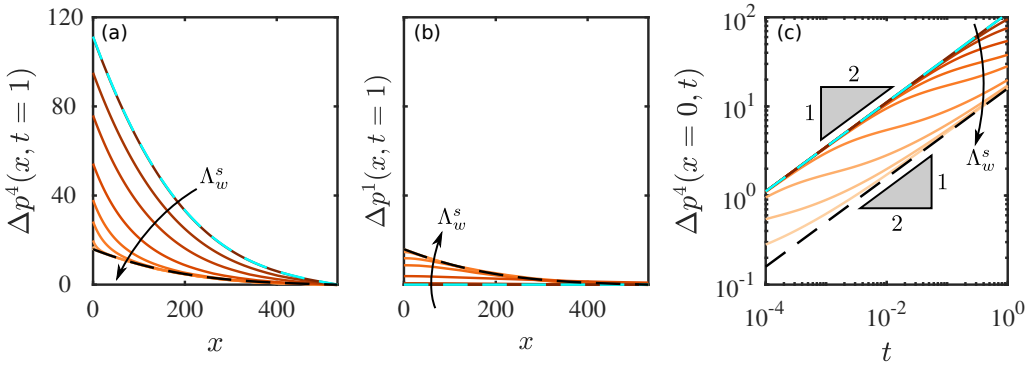


**Figure 2.4:** Pressure perturbation during water injection into aquifer 4 of a seven-aquifer system with permeable seals for a wide range of leakage strengths, $\log_{10}(\Lambda_w^s) = -9,\ -7,\ -6.5,\ -6,\ -5.5,\ -5,\ -4,\ -3,\ -2$, and $-1$. The pressure perturbation at $t = 1$ is plotted against $x$ in (a) the injection aquifer ($n = 4$) and in (b) the bottom-most aquifer ($n = 1$). Also plotted is (c) the pressure perturbation at $x = 0$ against $t$ on a log scale. All three panels include the analytical solutions for the 'no-leakage' limit (dashed cyan) and the 'strong-leakage' limit (dashed black).

solutions is about 0.004 for $b = 0.1$, the largest value tested. These results suggest that the 1D model reproduces the full 2D pressure field both accurately and efficiently.

The model is now used to investigate the impact of vertical pressure dissipation in more detail. To do so, the water-injection problem described above is solved for a wide range of leakage strengths $\Lambda_w^s$. It is found that the pressure in the injection aquifer decreases monotonically with $\Lambda_w^s$, whereas the pressure in all other aquifers increases monotonically with $\Lambda_w^s$ (Figure 2.4a–b). Note that compressibility moderates the importance of leakage since increasing compressibility reduces the strength and extent of the pressure perturbation in both $x$ and $z$.

For small values of $\Lambda_w^s$ ($\Lambda_w^s \lesssim 10^{-7}$), vertical pressure dissipation is unimportant and there is effectively no pressure communication between aquifers. The injection pressure is completely confined to the injection aquifer and evolves according to the solution derived in §2.3.1, such that the pressure perturbation in the injection aquifer evolves as $\Delta p^4 \sim \sqrt{t}$ (Figure 2.4c). The other aquifers are unperturbed by injection, such that $p^n$ remains hydrostatic and $\Delta p^n = 0$ for $n \neq 4$. This is the 'no-leakage' limit shown in Figure 2.4.

For large values of $\Lambda_w^s$ ($\Lambda_w^s \gtrsim 10^{-3}$), the seals provide essentially no barrier to vertical pressure dissipation. As a result, pressure equilibrates rapidly in the vertical direction and the system behaves like a single aquifer with an effective thickness of $N_z H$, with each aquifer experiencing $1/N_z$ of the total injection rate. The pressures can therefore be described by an effective model,

$$N_{cw}(R_{cw}+1)\frac{\partial p^n}{\partial t} - \frac{\partial^2 p^n}{\partial x^2} = \frac{2 s_g R_d}{N_z}\,\delta(x)\,u(t) \tag{2.44}$$

for $n = 1 \ldots N_z$, with the same boundary and initial conditions as Equation (2.41). This has the analytical solution

$$p^n(x,t) = \begin{cases} p^0 - N_g[n+(n-1)b] + \dfrac{s_g R_d}{N_z}(x + L_x/2) + \dfrac{\Omega(x,t)}{N_z} & \text{for } x \le 0, \\ p^0 - N_g[n+(n-1)b] - \dfrac{s_g R_d}{N_z}(x - L_x/2) + \dfrac{\Omega(x,t)}{N_z} & \text{for } x \ge 0, \end{cases} \tag{2.45}$$

where $\Omega(x,t)$ is given in Equation (2.39) above. This is the 'strong-leakage' limit shown in Figure 2.4. In this limit, the pressure perturbation is the same in all aquifers and evolves according to $\Delta p^n \sim \sqrt{t}$ (Figure 2.4c).

For all nonzero values of $\Lambda_w^s$, the pressure perturbation in the injection aquifer follows the 'no-leakage' limit at early times before transitioning to the 'strong-leakage' limit at late times. The latter transition occurs once the pressure perturbation reaches the top and bottom boundaries. Both transitions happen earlier as $\Lambda_w^s$ increases (Figure 2.4c). At intermediate times, the pressure is in a transitional state between the two limiting cases. Chang et al. [2013] noted the same departure from the early-time $\sqrt{t}$ scaling due to vertical pressure dissipation, but did not capture the late-time return to a $\sqrt{t}$ scaling because their system was vertically infinite.

### 2.3.3 Gas injection with impermeable seals

Next a scenario is considered in which gas is injected into a single-aquifer system ($n = N_z = 1$) with impermeable seals ($\Lambda_w^s = 0$). For this case, the above model is equivalent to that of Mathias et al. [2009] but for a planar (rather than axisymmetric) geometry and accounting for moderate gas compressibility. To describe gas injection into a single-aquifer system, the model requires that $\dot{M}_g^1 = \dot{M}\, u(t)$ and $\dot{M}_w^1 = 0$. The equation for gas is then Equation (2.32) for $n = 1$ and $\mathcal{I}_g^1 = 2\,\delta(x)\, u(t)$, and the equation for water is Equation (2.33) for $n = 1$ and $q_{w,z}^1 = q_{w,z}^2 = \mathcal{I}_w^1 = 0$.

As the gas is injected, the gas will spread along the top of the aquifer as a buoyant gravity current. The characteristic tongued shape of the gas plume is governed by the interplay between injection pressure, mobility contrast, buoyancy, and compressibility, and is therefore dictated by several different dimensionless parameters: $\mathcal{M}$, $N_g$, $N_{cw}$, $R_{cw}$, $R_{cf}$, $R_d$, and $s_g$. The impacts of these parameters on the shape of the gas plume are, for the most part, well understood from previous work in one-aquifer systems [*e.g.*, Mathias et al., 2009] and are not the focus of the present study. The impacts of $\mathcal{M}$, $N_g$, $N_{cw}$ are illustrated in Figure 2.5. The mobility ratio $\mathcal{M}$ measures the (much higher) mobility of the gas relative to the water and is ultimately responsible for the strongly tongued shape of the gas plume [Nordbotten and Celia, 2006b]. Increasing $\mathcal{M}$ increases the severity of this tonguing; decreasing $\mathcal{M}$ suppresses tonguing and focuses the gas near the injection well (Figure 2.5a). As a pair, density ratio $R_d$ and gravity number $N_g$ measure the importance of buoyancy relative to injection pressure. Typically it is expected that $R_d < 1$ (gas buoyant relative to water), in which case $N_g > 1$ implies that the gas will tend to rise and spread significantly due to buoyancy during the injection process, whereas $N_g < 1$ implies that buoyancy will play little role during injection [Nordbotten and Celia, 2006b, and Figure 2.5b]. The compressibility number $N_{cw}$ has the weakest

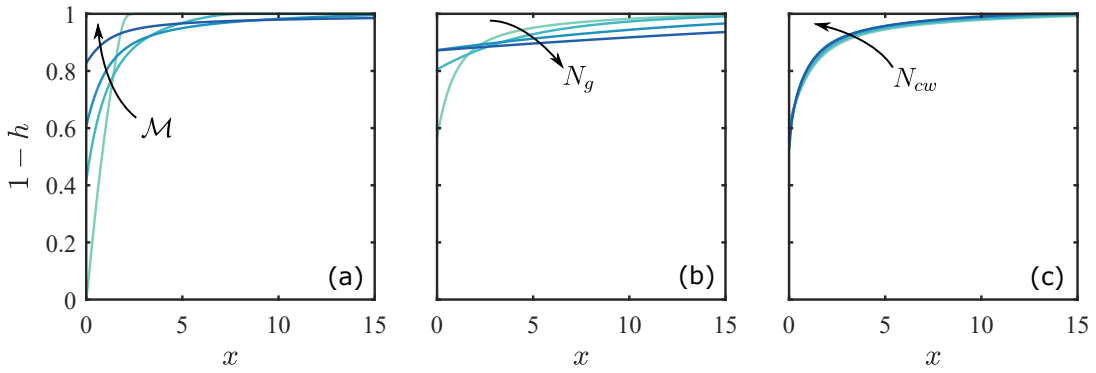


**Figure 2.5:** The shape of the gas plume at the end of gas injection into a one-aquifer system with impermeable seals, shown here for (a) $\mathcal{M} = 2,\ 10,\ 25$ & $150$, (b) $N_g = 1,\ 20,\ 100$ & $200$, and (c) $N_{cw} = 3.02 \times 10^{-6},\ 3.02 \times 10^{-5},\ 3.02 \times 10^{-4}$, & $3.02 \times 10^{-3}$. Decreasing $\mathcal{M}$ suppresses tonguing, increasing $N_g$ leads to faster spreading, and increasing $N_{cw}$ makes the gas plume somewhat more compact. The former two parameters have much stronger impacts than the latter.

impact among these three parameters, despite varying over the largest range. Increasing $N_{cw}$ leads to a slightly more compact and less tongued plume by reducing the strength of the injection pressure and increasing the density of the gas (Figure 2.5c). Although the impact of compressibility on plume shape is relatively small in the scenarios shown here, it can have a stronger effect in other regions of the parameter space [Mathias et al., 2009, Vilarrasa et al., 2010].

### 2.3.4 Gas injection with permeable seals

Finally, a scenario is considered involving gas injection into the central aquifer ($n = 4$) of a seven-aquifer system ($N_z = 7$) with permeable seals in order to study the impact of vertical pressure dissipation on the shape of the gas plume. The presence of gas complicates vertical pressure dissipation in the sense that the gas itself presents additional resistance to vertical water flow between the injection aquifer (aquifer 4) and the overlying aquifer (aquifer 5) by obstructing a portion of the seal, and by doing so in the region that is likely to have the highest pressure. Water is likely to be the wetting phase, and may therefore still be able to flow through the gas region via a connected network of residual films.

The resistance to this flow is likely to be significantly higher than if the gas were not present. This resistance is quantified by the reduced relative permeability to water in the gas region, $k^{\star}_{rw}$. Unfortunately, the magnitude of $k^{\star}_{rw}$ for a network of residual wetting films is very poorly constrained. Although the existence of a connected and conductive network of residual wetting films has been confirmed experimentally [Teige et al., 2006], it is not included in standard models for residual saturation and relative permeability. Considered first is the interaction of gas injection with pressure dissipation in the case where the gas does not offer any additional resistance to vertical water flow ($k^{\star}_{rw} = 1$). Subsequently the more general case of $0 \leq k^{\star}_{rw} \leq 1$ is considered, with an emphasis on the most likely scenario of $k^{\star}_{rw} \ll 1$.

#### 2.3.4.1 Gas does not obstruct vertical water flow ($k^{\star}_{rw} = 1$)

If the gas provides no additional resistance to vertical flow of water, then gas injection into the central layer of a homogeneous system is expected to lead to a sequence of vertical water fluxes and a pressure distribution that are vertically symmetric across the injection layer—that is, all vertical fluxes should be oriented away from the injection layer and their magnitudes, as well as the pressure in each layer, should depend only on distance from the injection layer. Much like for water injection (§2.3.2), it is expected that the pressure in the injection aquifer to decrease and the pressure in all other aquifers to increase as $\Lambda^s_w$ increases. Accordingly, all vertical water fluxes will increase monotonically in magnitude as $\Lambda^s_w$ increases.

The shape and width of the gas plume for different values of $\Lambda^s_w$ are plotted in Figure 2.6. For $\Lambda^s_w \ll 1$, the no-leakage limit from §2.3.3 is reproduced. As $\Lambda^s_w$ increases, it is observed that increasingly strong pressure dissipation leads to an increasingly compact plume by suppressing tonguing and thickening the gas column around $x = 0$. This is similar to the effect of increasing $N_{cw}$ (Figure 2.5),

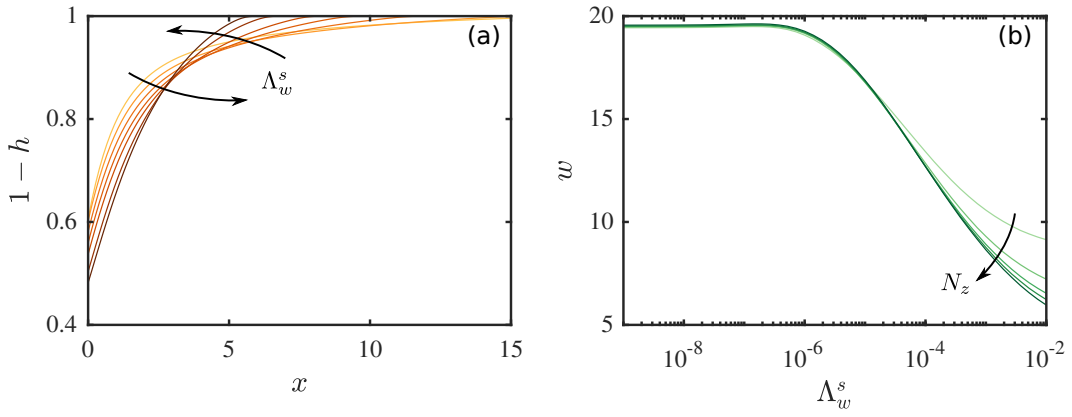


**Figure 2.6:** The shape of the gas plume during gas injection into the central aquifer of a seven-aquifer system with permeable seals: (a) Plume shapes at the end of injection for $\log_{10}(\Lambda_w^s) = -10$, $-5$, $-4$, $-3.4$, $-3$, $-2.4$, and $-2$, and (b) plume width $w$ as a function of $\Lambda_w^s$ for injection into systems of $N_z = 3$, 5, 7, 9, and 13 aquifers.

but substantially stronger. To rationalise this behaviour, consider the impact of vertical pressure dissipation on the pressure gradient driving gas flow.

During injection, the tonguing of the gas plume is driven by the strong pressure gradient and the high mobility of the gas relative to the water. The pressure in the injection layer decreases monotonically with distance from the injection well, and it is shown above that it also decreases monotonically with increasing $\Lambda_w^s$; Figure 2.4(a) illustrates these trends for water injection at $t = 1$, and gas injection is qualitatively similar. These trends result from the fact that the injected gas must displace water. For $\Lambda_w^s = 0$, all of this water is forced laterally through the single injection aquifer, which requires a relatively large pressure gradient. As $\Lambda_w^s$ increases, an increasing fraction of the water is also displaced vertically through the extensive seals and then laterally through other aquifers, thus reducing the pressure gradient in the injection aquifer itself. For strong injection, the lateral gas flow rate is given to a first approximation by $q_{g,x}^n \sim -\lambda_g h^n \partial p^n / \partial x$ (Equation 2.9). As the pressure gradient $\partial p^n / \partial x$ decreases due to vertical pressure dissipation, the plume thickness $h^n$ must increase in order to achieve the injection rate imposed at $x = 0$, thus producing a thicker and more compact gas plume.

To quantify this effect, the width $w$ of the gas plume is measured as a function

of $\Lambda_w^s$ and $N_z$, where $w$ is defined as the distance between the injection point and the place where the plume thickness falls below an arbitrary threshold value (here, $10^{-6}$). Note that, in the above scaling, a perfectly un-tongued plume (a rectangular block of gas) would have a width of $\sim$1. It is observed that pressure dissipation can decrease the width of the plume by a factor of 2 or more, even for seemingly small values of the leakage strength ($\Lambda_w^s \sim 10^{-3}$). This effect is amplified by increasing $N_z$, and particularly so for larger values of $\Lambda_w^s$. This effect occurs because pressure dissipation reduces the lateral pressure gradients that drive gas flow (Figure 2.4).

#### 2.3.4.2 Gas obstructs vertical water flow ($0 \leq k_{rw}^\star \leq 1$)

If the gas does provide additional resistance to upward water flow in the injection aquifer, then it is expected that this resistance suppresses upward pressure dissipation and enhances downward pressure dissipation, leading to vertical asymmetry in the water fluxes and in the pressure distribution. The importance of this resistance is determined by both $\Lambda_w^s$ and $k_{rw}^\star$. In order for the additional resistance from gas in the aquifer to impact pressure dissipation, it must be comparable to (or larger than) the resistance already provided by the seals (roughly, $k_{rw}^\star < \Lambda_w^s$).

The impact of this resistance is illustrated in Figure 2.7. For injection into aquifer 4, the pressure in the aquifer below (aquifer 3) increases as $k_{rw}^\star$ decreases (Figure 2.7a) and the pressure in the aquifer above (aquifer 5) decreases as $k_{rw}^\star$ decreases (Figure 2.7b). For $k_{rw}^\star = 1$, the vertical water fluxes through the bottom and top seals of the injection aquifer (seals 4 and 5, respectively) are equal in magnitude and opposite in direction, so they sum to zero (Figure 2.7c, outer plot). As $k_{rw}^\star$ decreases, there is a net downward flow of water immediately under the gas plume and a net upward flow of water elsewhere. The former occurs because the gas obstructs upward flow, as expected; the latter occurs because this obstruction leads to a lower pressure in the aquifer above than in the aquifer below

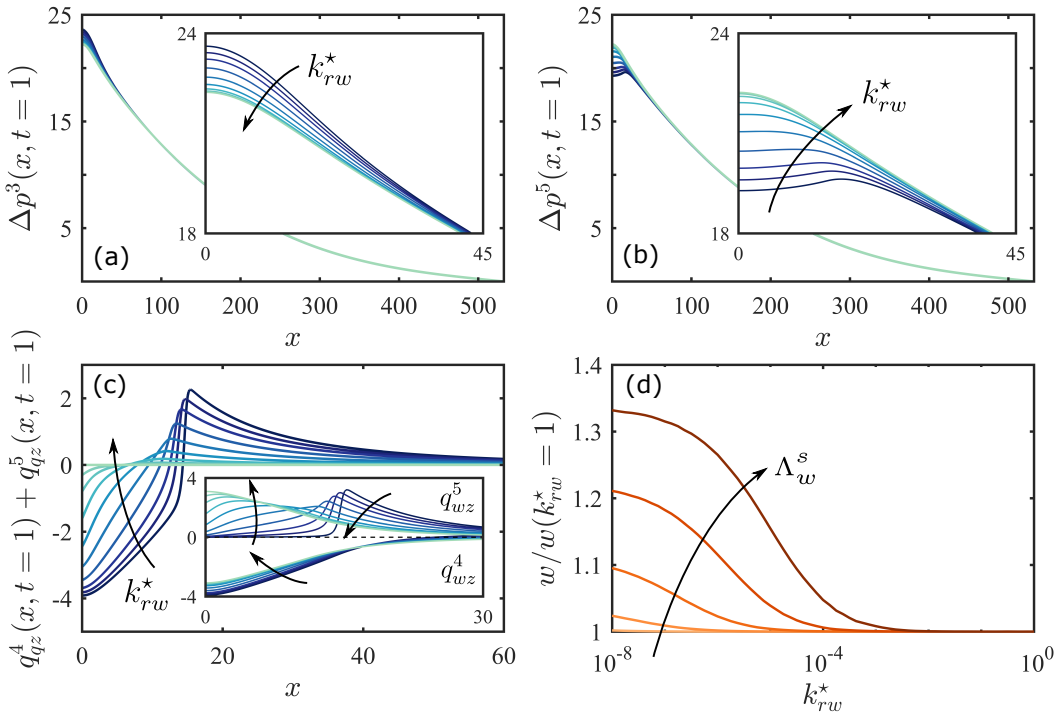


**Figure 2.7:** The reduced relative permeability to water within the gas region leads to vertical asymmetry in the pressure field and the vertical water fluxes. Plotted is: The pressure perturbation at $t = 1$ in (a) the aquifer immediately beneath the injection aquifer ($n = 3$) and in (b) the aquifer immediately above the injection aquifer ($n = 5$), as well as (c) the net vertical water flux through the injection aquifer ($q^4_{wz} + q^5_{wz}$) at $t = 1$ (inset: $q^4_{wz}$ and $q^5_{wz}$ individually). Curves are for $\log_{10}(k^\star_{rw}) = -8$, $-7$, $-6.5$, $-6$, $-5.5$, $-5$, $-4.5$, $-4$, $-3.5$, and $0$. Also plotted is: (d) the width of the gas plume at $t = 1$ against $k^\star_{rw}$, normalised by the plume width for $k^\star_{rw} = 1$, for $\log_{10}(\Lambda^s_w) = -7$, $-6$, $-5$, $-4$ and $-3$. Note that the horizontal axis of panel (c) is focused near the gas plume.

(Figure 2.7a,b), leading to a net upward flow of water in regions unobstructed by gas. Note that all of these effects are localised around the gas plume, and are relatively unimportant in the far field.

Recall that pressure dissipation decreases the width of the gas plume by suppressing tonguing (Figure 2.6). The resistance to flow of water through gas obstructs pressure dissipation and therefore has the opposite effect, increasing the width of the gas plume relative to its width when $k^\star_{rw} = 1$ (Figure 2.7d).

## 2.4 Discussion & Conclusions

In this chapter, a new model has been developed that couples gas injection and migration with lateral and vertical pressure dissipation in a layered aquifer system. The model combines a gravity-current representation of the gas with weak vertical flow of water both through the aquifers [Nordbotten and Celia, 2006a] and across the seals [Hunt, 1985]. The model constitutes a unique and computationally efficient tool for simultaneously studying the near-field and far-field aspects of gas injection.

The model was used to show that vertical pressure dissipation decreases the pressure in the injection aquifer as well as the width of the gas plume, while increasing the pressure in all other aquifers. For reference parameters (see table 2.1), the maximum injection pressure and the width of the gas plume are reduced by about two thirds and by about one third, respectively, relative to their values without vertical pressure dissipation ($\Lambda_w^s = 0$). Vertical pressure dissipation also slows lateral pressure dissipation, localising pressure buildup around the injection well. These effects have important implications for CCS. The reduction in pressure buildup near the injection well reduces the likelihood of fracturing the caprock. The reduction in lateral pressure dissipation reduces the radius of influence of the injection well, and also the impact of nearby wells and other geological features on injection [Chang et al., 2013]. All of these effects serve to relax the pressure constraint on storage capacity, allowing for longer injection times, larger injection rates, and/or storage in aquifers that are less laterally extensive [Szulczewski et al., 2012]. In addition, decreasing the width of the $CO_2$ plume by suppressing tonguing leads to a more compact shape at the end of injection, increasing the amount of residual trapping that would occur as the plume later rises, spreads, and migrates [MacMinn and Juanes, 2009]. However, a more compact $CO_2$ plume will also have a smaller interfacial area, likely reducing post-injection trapping associated with convective dissolution [*e.g.*, MacMinn et al., 2011].

Although the model has been developed and demonstrated in the context of $CO_2$ injection for CCS, the model can be readily adapted to other subsurface injection problems—for example, waste-water disposal or enhanced oil recovery (EOR). Changing the sign of the source term (*i.e.*, replacing injection with extraction) would allow for exploration of the role of pressure dissipation during hydrocarbon production. Vertical pressure dissipation is likely to have a similarly large impact on fluid extraction in a layered system due to its impact on the lateral pressure gradient that draws fluid toward the extraction well.

Vertical pressure dissipation reduces pressure buildup and dissipation in the injection layer [above and Chang et al., 2013]. In addition, the injection pressure does not scale with $\sqrt{t}$ at intermediate times and/or intermediate values of $\Lambda_w^s$. These results have import implications for gas leakage, which occurs when the capillary pressure at the top of the gas plume exceeds the entry pressure of the overlying seal. With negligible vertical water flow, the capillary pressure at the top of the layer is determined by buoyancy and is approximately $p_c \approx (\rho_w - \rho_g)gh$. This work has demonstrated that pressure dissipation results in compaction and thickening of the gas plume, which would increase the contribution of buoyancy to capillary pressure. The impacts of vertical water flow and the connectivity of the water through the gas region are less clear. The extension of the model to account for these effects and an exploration of gas leakage is the subject of the next chapter.

# Chapter 3

# Capillary pressure buildup and gas leakage

*The work presented in this chapter is, as of writing, under review. A preprint is available on the arXiv server [Jenkins et al., 2019b]. This chapter constitutes a reformatting of that work to fit within the context of this thesis.*

## 3.1 Introduction

As discussed in Chapter 2, a key factor in the design and implementation of CCS is that of *storage security*: The injected $CO_2$ should remain safely within the target aquifer. Upward leakage of $CO_2$ into overlying layers could have undesirable environmental consequences, such as the contamination of drinking water [*e.g.*, West et al., 2005, Little and Jackson, 2010].

During CCS, the buoyant and relatively low-viscosity $CO_2$ will tend to rise, spread, and migrate as a coherent plume known as a gravity current [*e.g.*, Huppert and Woods, 1995, Nordbotten and Celia, 2006b, Hesse et al., 2007, Gasda et al., 2009, Juanes et al., 2010]. As a result, the primary barrier to leakage of $CO_2$ out of the target aquifer is the integrity of the aquifer's caprock, which is the seal that forms

its uppermost boundary. For a competent seal, gas leakage is blocked by a large capillary entry pressure due to the fine-grained microstructure of the rock.

The injection and subsequent migration of the $CO_2$ at Sleipner has been monitored via periodic seismic surveys. The resulting images show a striking and unanticipated example of $CO_2$ leakage, revealing as many as nine separate $CO_2$ plumes stratified across a sequence of thin mudstone seals interbedded with the sandstone of the aquifer [Zweigel et al., 2004, Boait et al., 2012]. These mudstone layers are too thin to be resolved in seismic images, so their lateral extent and the precise mechanism by which the $CO_2$ is able to leak across them remains unclear. If the layers lack lateral continuity then the $CO_2$ could be spilling over their lateral edges [*e.g.*, Hesse and Woods, 2010]. Alternatively, the $CO_2$ could be flowing across these layers via a focused conduit such as a cross-cutting fault or fracture, or it could be flowing through the pore space of the layers themselves [*e.g.*, Foschi et al., 2018]. The latter is only possible if pressure in the gas exceeds the capillary entry pressure of the seal due to some combination of buoyancy and injection pressure.

Leakage across a seal via focused conduits ('focused leakage') has attracted particular attention, and has been studied from a variety of perspectives. For example, several studies have considered the impact of leakage through a fault or fracture on the migration of a buoyant plume along the top seal (or a dense plume along the bottom seal) of a semi-infinite porous layer [*e.g.*, Pritchard, 2007, Neufeld et al., 2009, 2011, Vella et al., 2011]. Leakage through a seal by overcoming its capillary entry pressure ('distributed leakage') has attracted less attention. Pritchard et al. [2001], Acton et al. [2001], and Farcas and Woods [2009] all studied the impact of distributed leakage on the migration of an unconfined plume (*i.e.*, neglecting the ambient fluid); all of these studies neglected capillary entry pressure, such that the plume always leaks and the local leakage rate is proportional to the local plume thickness. Woods and Farcas [2009] introduced capillary entry pressure to this

problem, such that there is a minimum local plume thickness for which leakage will occur.

In leakage from an unconfined porous layer, the ambient fluid is irrelevant to the problem and the migration and leakage of the plume are driven strictly by buoyancy (see references above). In the confined version of this problem, where the porous layer has a finite thickness, migration and leakage of the plume become strongly coupled to migration and leakage of the ambient fluid [Gunn and Woods, 2011, Kang et al., 2014, Pegler et al., 2014b, 2015]. Of the studies mentioned above on both focused and distributed leakage, only Pegler et al. [2014b] considered what happens to the fluids after leaking; they assumed that leaked fluids were injected into an overlying aquifer where they would continue to migrate due to pressure and buoyancy, such that the subsequent rate of leakage was then coupled with flow in the overlying aquifer.

In a confined layer, distributed leakage is complicated by the fact that both fluids can cross the seals at any point, leading to a rich flow problem that has not previously been explored. Chapter 2 studied the distributed leakage of the ambient fluid (water) during gas injection into a layered system of horizontal aquifers separated by thin seals, but assuming that the gas cannot leak (*i.e.*, that the entry pressure is never exceeded). Distributed water leakage is interesting and important in its own right, because it enables strong vertical pressure dissipation and therefore plays an important role in mitigating pressure buildup during gas injection [Birkholzer et al., 2009, Nicot, 2008, Chang et al., 2013, Jenkins et al., 2019a]. It was demonstrated in Chapter 2 that vertical pressure dissipation is also coupled to the motion of the gas plume, leading to a more compact plume shape by suppressing the formation of the advancing gas tongue. In this chapter the model introduced in Chapter 2 is extended to account for distributed gas leakage.

A key aspect of this study is that, as in Chapter 2, the model focuses on a layered system. This enables a strong coupling between injection, migration, leakage, and

pressure dissipation across layers. For example, gas injection drives water leakage by pressurising the target aquifer relative to the over- and underlying aquifers, but this water leakage acts to dissipate the injection pressure into the over- and underlying aquifers and thereby imposes a negative feedback on further leakage. This chapter demonstrates that this coupling becomes more complex when gas leakage is introduced. In §3.2, the model presented in Chapter 2 is reviewed and extended to include gas leakage. In §3.3, the numerical scheme is outlined, followed by an exploration of the different factors that control the buildup of capillary pressure along the underside of the seal. Subsequently the parameter space that governs gas leakage is investigated. In §3.4, the implications of the results for CCS are discussed, with a particular focus on $CO_2$ injection at Sleipner. Note that this chapter focuses on the likelihood of gas leakage and on the impact of gas leakage on the spatial distribution of gas at the end of injection. The time evolution of the gas plume and the pressure field, both during and after injection, is studied in Chapter 4.

## 3.2 Theoretical model

The geological setting is the same as outlined in Chapter 2. The model considers a layered system comprising an alternating stack of $N_z$ aquifers and $N_z + 1$ seals (Figure 3.1). Each aquifer is bounded above and below by a seal, and the aquifers and seals are counted from the bottom up, such that the deepest and shallowest aquifers are 1 and $N_z$ respectively, and the deepest and shallowest seals are 1 and $N_z + 1$ respectively.

It is again assumed that all aquifers have the same uniform thickness $H$, porosity $\phi$, and isotropic permeability $k$, and that all seals have the same uniform thickness $b$ ($b \ll H$) and isotropic permeability $k_s$ ($k_s \ll k$). It would be straightforward to extend the model to include anisotropy, variations in layer properties, or lateral heterogeneity, but these complications are omitted here for simplicity.

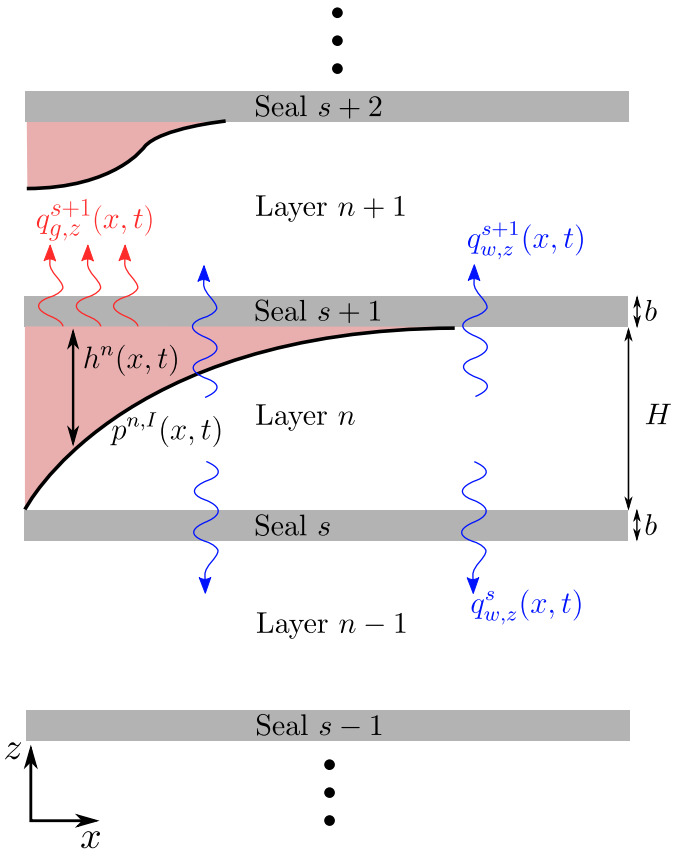


**Figure 3.1:** A section of the model system, which comprises a sequence of aquifers of thickness $H$ alternating with seals of thickness $b$. The gas-saturated regions are shown in red.

As in Chapter 2, the model accounts for vertical and lateral pressure dissipation via water flow through the aquifers and across the seals. Unlike in Chapter 2, the model also incorporates vertical gas flow across the seals, subject to an appropriate capillary entry threshold. The central goal of this chapter is to explore the coupling between pressure dissipation and gas leakage during injection.

The model considers flow in the Cartesian $x$–$z$ plane, where gravity points in the negative $z$ direction. Symmetry is assumed along the $y$ direction (into the page). The top and bottom of aquifer $n$ are denoted by $z^{n,T}$ and $z^{n,B}$, respectively, such that $z^{n,T} - z^{n,B} \equiv H$ and $z^{n+1,B} - z^{n,T} \equiv b$ for all $n$ (Figure 3.1).

### 3.2.1 Flow in aquifer $n$

The theoretical framework for this model and the majority of the underlying assumptions are the same as those presented in Chapter 2. As a result, the derivation in this chapter proceeds by outlining the key points and highlighting the differences from the work presented in Chapter 2. Once again, a two-phase gravity-current formulation is invoked, in which the fluids are strongly segregated by gravity; that is, this model studies the flow of a coherent plume of gas relative to ambient water.

#### 3.2.1.1 Water in aquifer $n$

The additional terms relating to vertical gas leakage appear exclusively in the extended governing PDE for gas (see below). Therefore, the underlying assumptions in deriving a PDE that describes the flow of water in this system remain unchanged. As such, the governing PDE for water, with additional terms related to vertical pressure dissipation, remains unchanged from Chapter 2. Below is a brief summary of the derivation for water performed in Chapter 2. Conservation of mass for the water in aquifer $n$ is given by

$$\frac{\partial}{\partial t}\left(\rho_w \phi s_w\right) + \boldsymbol{\nabla} \cdot \left(\rho_w \boldsymbol{q}_w\right) = \mathcal{I}_w, \tag{3.1}$$

where $s_w$ is the water saturation, $\boldsymbol{q}_w$ is the Darcy flux of water, and $\mathcal{I}_w$ is the local mass rate of water injection per unit volume. The Darcy flux of water is given by Darcy's law,

$$\boldsymbol{q}_w = -\frac{k k_{rw}}{\mu_w}\left(\boldsymbol{\nabla} p_w + \rho_w g \hat{\boldsymbol{e}}_z\right), \tag{3.2}$$

where $k_{rw}$ is the relative permeability of water, $\mu_w$ is the dynamic viscosity of water, which is taken to be constant and uniform, $p_w$ is the water pressure, $g$ is body force per unit mass due to gravity, and $\hat{\boldsymbol{e}}_z$ is the unit vector in the positive $z$ direction.

The vertical component of Darcy's law (Eq. 3.2) can be rearranged to give an expression for the vertical pressure gradient,

$$\frac{\partial p_w}{\partial z} = -\rho_w g - \frac{q_{w,z}}{\lambda_w}, \tag{3.3}$$

where $q_{w,z}$ is the vertical component of the water flux and $\lambda_w \equiv k k_{rw}/\mu_w$ is the water mobility. The classical model for a gravity current in an aquifer with impermeable seals involves assuming that the fluids are in 'vertical equilibrium', meaning that the flow is predominantly horizontal and the vertical pressure distribution is therefore nearly hydrostatic (*i.e.*, $q_{w,z} \ll \rho_w g \lambda_w \implies \partial p_w/\partial z \approx -\rho_w g$) [*e.g.*, Bear, 1972, Huppert and Woods, 1995]. This assumption allows for direct calculation of $p_w$ by integrating Equation (3.3), with the resulting expression for $p_w$ being linear in $z$. Chapter 2 extended this concept to allow for weak vertical flow of water by instead assuming that $q_{w,z}$ has a simple, continuous and piecewise-linear structure in $z$, as originally suggested by Nordbotten and Celia [2006a] for flow near a well. The expression is

$$q_{w,z}(x,z,t) \approx \begin{cases} q_{w,z}^{n,B} + \left(\dfrac{z - z^{n,B}}{z^{n,I} - z^{n,B}}\right)\left(q_{w,z}^{n,T} - q_{w,z}^{n,B}\right) & z^{n,B} \le z < z^{n,I}, \\ q_{w,z}^{n,T} & z^{n,I} \le z \le z^{n,T}, \end{cases} \tag{3.4}$$

where $q_{w,z}^{n,B}(x,t)$ and $q_{w,z}^{n,T}(x,t)$ are the vertical fluxes of water through the lower and upper seals of aquifer $n$, respectively. Thus, $q_{w,z}$ varies linearly from $q_{w,z}^{n,B}$ at the bottom seal to $q_{w,z}^{n,T}$ at the gas–water interface, and is then uniform and equal to $q_{w,z}^{n,T}$ from the gas–water interface to the top seal. This approach still allows for direct calculation of $p_w$ by integrating Equation (3.3), with the resulting expression for $p_w$ being continuous and piecewise-parabolic in $z$. Note that the fluxes $q_{w,z}^{n,B}$ and $q_{w,z}^{n,T}$ are unknown, and will be determined through global conservation of mass. Combining this result with the horizontal component of Equation (3.2), and then substituting into Equation (3.1) and integrating over the full thickness

of the aquifer yields the governing equation for water:

$$\phi\left[(H-s_g h^n)(c_r+c_w)\frac{\partial p^n}{\partial t}-s_g\frac{\partial h^n}{\partial t}\right]-\frac{\partial}{\partial x}\left\{\lambda_w(H-h^n)\left[\frac{\partial p^n}{\partial x}-\rho_w g\frac{\partial h^n}{\partial x}\right]\right.$$
$$\left.+\frac{1}{6}\frac{\partial}{\partial x}\left[(H-h^n)^2(q_{w,z}^{n,B}+2q_{w,z}^{n,T})\right]\right\}=-(q_{w,z}^{n,T}-q_{w,z}^{n,B})+\frac{\mathcal{I}_w^n H}{\rho_w}, \tag{3.5}$$

where $c_r$ is the rock compressibility, $h^n$ is the thickness of the gas layer in aquifer $n$, $p^n$ is the water pressure along the gas–water interface in aquifer $n$, and $\mathcal{I}_w^n$ is the vertically averaged mass injection rate of water per unit volume into aquifer $n$ (Figure 3.1). Recall that this has been assumed throughout that $\rho_w \approx \rho_w^0$. The reader is referred to Chapter 2 for more details and discussion related to this derivation.

#### 3.2.1.2 Gas in aquifer $n$

Conservation of mass for gas in aquifer $n$ is given by

$$\frac{\partial}{\partial t}\left(\rho_g\phi s_g\right)+\boldsymbol{\nabla}\cdot\left(\rho_g\boldsymbol{q}_g\right)=\mathcal{I}_g, \tag{3.6}$$

where $s_g$ is the saturation of gas, $\boldsymbol{q}_g$ is the Darcy flux of gas, and $\mathcal{I}_g$ is the local mass rate of gas injection per unit volume. The Darcy flux of gas is given by Darcy's law,

$$\boldsymbol{q}_g=-\frac{kk_{rg}}{\mu_g}\left(\boldsymbol{\nabla}p_g+\rho_g g\hat{\boldsymbol{e}}_z\right), \tag{3.7}$$

where $k_{rg}$ is the relative permeability of gas, $\mu_g$ is the dynamic viscosity of gas, which is taken to be constant and uniform, and $p_g$ is the gas pressure.

The vertical component of Darcy's law (Eq. 3.7) can again be rearranged to give an expression for the vertical pressure gradient,

$$\frac{\partial p_g}{\partial z}=-\rho_g g-\frac{q_{g,z}}{\lambda_g}, \tag{3.8}$$

where $q_{g,z}$ is the vertical component of the gas flux and $\lambda_g \equiv kk_{rg}/\mu_g$ is the mobility of the gas. As for water, the classical approach is to calculate $p_g$ by assuming vertical equilibrium in the gas (*i.e.*, $q_{g,z} \ll \rho_g g \lambda_g \implies \partial p_g/\partial z \approx -\rho_g g$) and then integrating in $z$ [*e.g.*, Bear, 1972, Huppert and Woods, 1995]. The same assumption was made in Chapter 2, motivated by the scenario where the capillary entry pressure of the seals, $p_c^E$, was large enough to prevent gas from entering. This assumption is now relaxed, allowing for gas leakage through the seals when this entry pressure is exceeded by assuming a weak vertical flow of gas in the gas region. This vertical gas flux $q_{g,z}$ is assumed to be uniform in $z$,

$$q_{g,z}(x,z,t) \approx q_{g,z}^{n,T} \quad z^{n,I} \leq z < z^{n,T}, \tag{3.9}$$

where $q_{g,z}^{n,T}(x,t)$ is the vertical flux of gas through the upper seal of aquifer $n$.

Substituting Eq. (3.9) into Eq. (3.8) and integrating, yields

$$p_g^n(x,z,t) = p^n - \left(\rho_g^n g + \frac{q_{g,z}^{n,T}}{\lambda_g}\right)(z - z^{n,I}), \tag{3.10}$$

where $\rho_g^n$ is the vertically averaged gas density in aquifer $n$. Note that the capillary pressure at the gas–water interface (*i.e.*, the entry pressure of the aquifer) has been neglected relative to hydrostatic variations. Note also that terms of size $\rho_g^0 g H c_g \ll 1$ have also been neglected in this calculation, taking the gas density to be approximately vertically uniform within the aquifer.

Substituting Eq. (3.10) into the horizontal component of Eq. (3.7) and continuing to neglect terms of order $\rho_{g,0} g H c_g \ll 1$, yields an expression for the horizontal flux of gas in aquifer $n$,

$$q_{g,x}^n = -\lambda_g \left[\frac{\partial p_g^n}{\partial x} - \left(\rho_g^n g + \frac{q_{g,z}^{n,T}}{\lambda_g}\right)\frac{\partial h^n}{\partial x} - \frac{1}{\lambda_g}\frac{\partial q_{g,z}^{n,T}}{\partial x}\left(z - z^{n,I}\right)\right], \tag{3.11}$$

where the fact that $z^{n,I} = z^{n,T} - h^n$ has been used.

Integrating Eq. (3.6) over the thickness of the aquifer,

$$\int_{z_n^B}^{z_n^T} \frac{\partial}{\partial t}\left(\rho_g s_g \phi\right) \mathrm{d}z + \int_{z_n^B}^{z_n^T} \boldsymbol{\nabla} \cdot \left(\rho_g \boldsymbol{q}_g\right) \mathrm{d}z = \int_{z_n^B}^{z_n^T} \mathcal{I}_g \, \mathrm{d}z. \tag{3.12}$$

As in Chapter 2, the first term of Eq. (3.12) becomes

$$\begin{aligned} \int_{z_n^B}^{z_n^T} \frac{\partial}{\partial t}(\rho_g \phi s_g) \, \mathrm{d}z &\approx \frac{\partial}{\partial t}(\rho_g^n \phi s_g h^n) \\ &\approx \rho_g^n \phi s_g \left[ (c_r + \frac{\rho_g^0}{\rho_g^n} c_g) h^n \frac{\partial p^n}{\partial t} + \frac{\partial h^n}{\partial t} \right], \end{aligned} \tag{3.13}$$

where $s_g$ is now the constant and uniform saturation of gas in the gas region and $c_r \equiv (1/\phi)(\partial\phi/\partial p)$ is the rock compressibility [*e.g.*, Bear, 1972]. The density ratio $\rho_g^0/\rho_g^n$ is often approximated as unity; this approximation is avoided to ensure conservation of mass when the gas phase is moderately compressible, as would be the case for methane. The second term of Eq. (3.12) becomes

$$\begin{aligned} \int_{z^{n,B}}^{z^{n,T}} \boldsymbol{\nabla} \cdot \left(\rho_g \boldsymbol{q}_g\right) \mathrm{d}z &= \frac{\partial}{\partial x}\left( \int_{z^{n,B}}^{z^{n,T}} \rho_g q_{g,x} \, \mathrm{d}z \right) + \left(\rho_g q_{g,z}\right)\Big|_{z^{n,B}}^{z^{n,T}} \\ &\approx \frac{\partial}{\partial x}\left\{ -\rho_g^n \lambda_g h^n \left[ \frac{\partial p^n}{\partial x} - \rho_g^n g \frac{\partial h^n}{\partial x} \right] + \rho_g^n \frac{\partial}{\partial x}\left[ \frac{1}{2}(h^n)^2 q_{g,z}^{n,T} \right] \right\} \\ &\quad + \left(\rho_g^n q_{g,z}^{n,T} - \rho_g^n q_{g,z}^{n,B}\right), \end{aligned} \tag{3.14}$$

Recombining Eqs. (3.13) and (3.14) with Eq. (3.12) yields the governing equation for a compressible buoyant gravity current of gas with additional terms related to injection, weak vertical gas flow, and gas leakage,

$$\begin{aligned} \rho_g^n \phi s_g \left[ \left( c_r + \frac{\rho_g^0}{\rho_g^n} c_g \right) h^n \frac{\partial p^n}{\partial t} + \frac{\partial h^n}{\partial t} \right] - \frac{\partial}{\partial x}\Bigg\{ \rho_g^n \lambda_g h^n \left[ \frac{\partial p^n}{\partial x} - \rho_g^n g \frac{\partial h^n}{\partial x} \right] \\ + \rho_g^n \frac{\partial}{\partial x}\left[ \frac{1}{2}(h^n)^2 \, q_{g,z}^{n,T} \right] \Bigg\} = -\left(\rho_g^n q_{g,z}^{n,T} - \rho_g^n q_{g,z}^{n,B}\right) + \mathcal{I}_g^n H, \end{aligned} \tag{3.15}$$

where $\mathcal{I}_g^n$ is the vertically averaged mass injection rate of gas per unit volume into aquifer $n$. Equations (3.5) and (3.15) are two coupled nonlinear partial differential

equations (PDEs) in $h^n$ and $p^n$. To close this system, expressions are needed for the vertical fluxes of water ($q_{w,z}^{n,B}$ and $q_{w,z}^{n,T}$) and gas ($q_{g,z}^{n,B}$ and $q_{g,z}^{n,T}$). Note that, because it has been assumed that there is no gas in the seals or the water regions of the aquifers, gas that leaks upward out of one aquifer appears immediately in the gas plume in the aquifer above; in other words, the model neglects the transit time between one gas plume and the next.

## 3.2.2 Coupling the aquifers with vertical fluxes

### 3.2.2.1 Vertical water fluxes

For the vertical fluxes of water across the seals, the approach and results are identical to those presented in Chapter 2. Once again, it is assume that there is horizontal flow and no storage within the seals, such that the mass flux of water entering seal $s$ from aquifer $n-1$ must equal the mass flux of water exiting seal $s$ into aquifer $n$:

$$\rho_w^{n-1} q_{w,z}^{n-1,T} = \rho_w^n q_{w,z}^{n,B} = \rho_w^s q_{w,z}^s, \tag{3.16}$$

where $\rho_w^s$ is the density of water in seal $s$ and $q_{w,z}^s$ is the flux of water through seal $s$. Recall that it is assumed that $\rho_w \approx \rho_w^0$ throughout the system, such that $\rho_w^{n-1} \approx \rho_w^n \approx \rho_w^s \approx \rho_w^0$. Next, the vertical flux $q_{w,z}^s$ is calculated via Darcy's law, introducing expressions for the pressures at the top and bottom of each aquifer from the analysis above. The result can be written

$$\left(\frac{H-h^n}{2\lambda_w}\right) q_{w,z}^{s+1} + \left(\frac{h^{n-1}}{\lambda_w^\star} + \frac{b}{\lambda_w^s} + \frac{H-h^n}{2\lambda_w}\right) q_{w,z}^s = -\Big[p^n - p^{n-1} + \rho_w^0 g(h^{n-1} + b + H - h^n)\Big], \tag{3.17}$$

where $\lambda_w^\star = k k_{rw}^\star / \mu_w$ is the mobility of water in the gas regions of the aquifers, with $k_{rw}^\star$ the relative permeability of water in those regions, and $\lambda_w^s = k_s/\mu_w$ is the

mobility of water in the seals. Equation (3.17) is a linear system of $N_z - 1$ coupled algebraic equations in the $N_z - 1$ unknown fluxes $q^s_{w,z}$ for $s = 2 \dots N_z - 1$, from which $q^s_{w,z}$ can be solved for in terms of $p^n$ and $h^n$. Recall that the bottom-most and top-most seals are taken to be impermeable, such that $q^1_{w,z} = q^{N_z+1}_{w,z} = 0$.

#### 3.2.2.2 Vertical gas fluxes

For the vertical fluxes of gas across the seals, a similar procedure to that for water is followed. With no horizontal flow and no storage within the seals, the mass flux of gas entering seal $s$ from aquifer $n-1$ must equal the mass flux of gas exiting seal $s$ into aquifer $n$:

$$\rho^{n-1}_g q^{n-1,T}_{g,z} = \rho^n_g q^{n,B}_{g,z} = \rho^s_g q^s_{g,z}, \tag{3.18}$$

where $\rho^s_g$ is the density of gas in seal $s$ and $q^s_{g,z}$ is the flux of gas through seal $s$. Unlike the water, the gas is allowed to be moderately compressible; as a result, the three gas densities $\rho^{n-1}_g$, $\rho^n_g$, and $\rho^s_g$ are not necessarily equal. The former two densities are calculated from the associated pressures $p^{n-1}$ and $p^n$ via Eq. (2.1), and the latter is taken to be the average of the former two,

$$\rho^s_g = \frac{1}{2}(\rho^{n-1}_g + \rho^n_g). \tag{3.19}$$

Next, Darcy's law is written for $q^s_{g,z}$, including a capillary threshold condition that prevents gas leakage unless the capillary pressure along the underside of seal $s$ exceeds the associated entry pressure $p^E_c$,

$$q^s_{g,z}(x,t) = \begin{cases} -\lambda^s_g \left( \dfrac{p^{n,B}_g - p^{n-1,T}_g}{b} + \rho^s_g \right) & p^{n-1,T}_c > p^E_c, \\ 0 & p^{n-1,T}_c < p^E_c, \end{cases} \tag{3.20}$$

where $p^{n-1,T}_c = p^{n-1,T}_g - p^{n-1,T}_w$ is the capillary pressure at the top of aquifer $n-1$ (bottom of seal $s$). The sharp transition across $p^E_c$ is smoothed by introducing a

step-like transition function $\mathcal{R}(p_c^{n-1,T})$ and rewriting Eq. (3.20) as

$$q_{g,z}^s(x,t) = -\mathcal{R}\lambda_g^s\left(\frac{p_g^{n,B} - p_g^{n-1,T}}{b} + \rho_g^s\right), \tag{3.21}$$

with

$$\mathcal{R}(p_c^{n-1,T}) = \frac{1}{2}\left\{1 + \tanh\left[\left(\frac{p_c^{n-1,T} - p_c^E}{p_c^E}\right)\vartheta\right]\right\}, \tag{3.22}$$

such that $\mathcal{R} \to 0$ for $p_c^{n-1,T} < p_c^E$ and $\mathcal{R} \to 1$ for $p_c^{n-1,T} > p_c^E$. The parameter $\vartheta$ controls the sharpness of this transition, with Eq. (3.22) converging to a unit step, and therefore Eq. (3.21) converging to Eq. (3.20), for $\vartheta \gg 1$. Note that $\mathcal{R}(p_c^{n,T} = p_c^E) = 1/2$ for all $\vartheta$. Results should be independent of the particular value of $\vartheta$ as long as it is sufficiently large; for all results below $\vartheta = 300$ is used.

Finally, the pressures $p_g^{n-1,T}$ and $p_g^{n,B}$ must be related to known quantities. Equation (3.10) suggests that the former pressure is given by

$$p_g^{n-1,T} = p^{n-1} - \left(\rho_g^{n-1}g + \frac{q_{g,z}^{n-1,T}}{\lambda_g}\right)h^{n-1}. \tag{3.23}$$

For the latter pressure, once again, it is expected that the gas column through seal $s$ and within the water region of aquifer $n$ is discontinuous. As a result, the gas pressure at the bottom of aquifer $n$ is expected to be controlled by the continuous water column, $p_g^{n,B} \approx p_w^{n,B}$, where once again the capillary pressure in the aquifers is neglected. This water pressure is itself determined via the separate system of equations for water leakage, Eq. (3.17). Rearranging Eq. (2.16), the relevant expression is

$$p_w^{n,B} = p^n + (H - h^n)\left(\rho_w g + \frac{q_{w,z}^{s+1} + q_{w,z}^s}{2\lambda_w}\right). \tag{3.24}$$

Combining all of these ingredients, $q_{g,z}^{n-1,T}$ is eliminated from Eq. (3.23), which now becomes

$$p_g^{n-1,T} = \frac{1}{\xi_g^s}\Big[p^{n-1} - \rho_g^{n-1}gh^{n-1} + (\xi_g^s - 1)(p_w^{n,B} + \rho_g^s g b)\Big], \tag{3.25}$$

where the dimensionless quantity $\xi_g^s$ is given by

$$\xi_g^s = 1 + \left( \frac{\rho_g^s \lambda_g^s h^{n-1}}{\rho_g^{n-1} \lambda_g b} \right) \mathcal{R}. \tag{3.26}$$

With Eq. (3.25), the gas-leakage flux can now be evaluated directly from

$$q_{g,z}^s(x,t) = -\mathcal{R}\lambda_g^s \left( \frac{p_w^{n,B} - p_g^{n-1,T}}{b} + \rho_g^s \right), \tag{3.27}$$

where $\mathcal{R}(p_c^{n-1,T})$ is as defined in Eq. (3.22). Note that Eqs. (3.25)–(3.27) reduce to the standard result from vertical equilibrium, $p_g^{n-1,T} = p^{n-1} - \rho_g^{n-1} g h^{n-1}$ and $q_{g,z}^s = 0$, when the entry pressure is not exceeded ($p_c^{n-1,T} < p_c^E \implies \mathcal{R} = 0$).

To assess the entry-pressure condition and determine the value of $\mathcal{R}$, the capillary pressure at the top of each aquifer must be calculated. Equation (3.25) is an expression for the gas pressure at the top of aquifer $n-1$. Equations (2.23) and (2.24a) can be rearranged to provide an expression for the water pressure at the top of aquifer $n-1$,

$$p_w^{n-1,T} = \frac{1}{\xi_w^s} \left[ p^{n-1} - \rho_w g h^{n-1} + (\xi_w^s - 1)(p_w^{n,B} + \rho_w g b) \right], \tag{3.28}$$

with

$$\xi_w^s = 1 + \frac{\lambda_w^s h^{n-1}}{\lambda_w^\star b}. \tag{3.29}$$

The capillary pressure $p_c^{n-1,T} = p_g^{n-1,T} - p_w^{n-1,T}$ is then given by

$$\begin{aligned} p_c^{n-1,T} = &\left( \frac{1}{\xi_g^s} - \frac{1}{\xi_w^s} \right) p^{n-1} - \left( \frac{\rho_g^{n-1}}{\xi_g^s} - \frac{\rho_w}{\xi_w^s} \right) g h^{n-1} \\ &- \left( \frac{1}{\xi_g^s} - \frac{1}{\xi_w^s} \right) p_w^{n,B} - \left( \frac{\rho_g^s}{\xi_g^s} - \frac{\rho_w}{\xi_w^s} \right) g b - (\rho_w - \rho_g^s) g b. \end{aligned} \tag{3.30}$$

Note that this expression for $p_c^{n-1,T}$ depends on $\mathcal{R}$ via $\xi_g^s$ because the gas pressure at the top of aquifer $n$ depends on whether or not the gas is actively leaking. In

principle, Eqs. (3.25)–(3.30) should be evaluated iteratively to assess the entry-pressure condition and calculate the gas-leakage flux. In practice, $\xi_g^s$ is insensitive to the value of $\mathcal{R}$ because $\lambda_g^s \ll \lambda_g$, so it is safe and efficient to assume $\xi_g^s \approx 1$ and calculate the other quantities accordingly. Note also that, whereas the connected water column and the resulting continuous water pressure field lead to a system of coupled equations for the $N_z - 1$ unknown water leakage fluxes (Eq. 3.17), the disconnected gas column leads to an explicit expression for each of the $N_z - 1$ unknown gas-leakage fluxes (Eq. 3.27), where again $q_{g,z}^1 = q_{g,z}^{N_z+1} = 0$. Importantly, however, the capillary pressure and the gas-leakage fluxes are strongly coupled to the water pressure field; this coupling is explored in detail below.

### 3.2.3 Boundary and initial conditions

The boundary and initial conditions are identical to those used in Chapter 2. For completeness, they are reiterated here. As in Chapter 2, this chapter considers a system comprised of $N_z$ aquifers alternating with $N_z + 1$ seals, all of which extend horizontally from $x = -L_x/2$ to $x = L_x/2$. It is assumed that the system is initially fully saturated with water (no gas), and that the pressure distribution is initially hydrostatic. Furthermore, it is assumed the pressure at the lateral boundaries remains hydrostatic for all time and the bottom-most and top-most seals are taken to be impermeable ($s = 1$ and $s = N_z + 1$, respectively). For injection of phase $\alpha$ into the horizontal centre of aquifer $n$ at a mass flow rate $\dot{M}_\alpha^n(t)$ per unit length into the page, the appropriate vertically integrated source term is

$$\mathcal{I}_\alpha^n = \frac{\dot{M}_\alpha^n(t)}{H}\,\delta(x), \tag{3.31}$$

where $\delta(x)$ is the Dirac delta function.

### 3.2.4 Non-dimensionalization

As in Chapter 2, characteristic scales are chosen based on the injection of gas at a mass flow rate $\dot{M}$ per unit length into the page for a time $\mathcal{T}$. The associated characteristic scales for length, pressure, and vertical flux are

$$\mathcal{L} \equiv \frac{\dot{M}\mathcal{T}}{2\phi s_g \rho_g^0 H}\ , \quad \mathcal{P} \equiv \frac{\phi \mathcal{L}^2}{\lambda_w \mathcal{T}} = \frac{\dot{M}\mathcal{L}}{2\lambda_w s_g \rho_g^0 H}\ , \quad \text{and} \quad \mathcal{Q}_z \equiv \frac{\Lambda_w^s \mathcal{P}}{b}. \tag{3.32}$$

The characteristic length $\mathcal{L}$ is the half-width of an incompressible box of gas of mass $\dot{M}\mathcal{T}$ per unit length into the page. The characteristic pressure $\mathcal{P}$ is the pressure drop associated with a Darcy flux $\phi\mathcal{L}/\mathcal{T}$ of water over a distance $\mathcal{L}$. The characteristic vertical flux $\mathcal{Q}_z$ is the vertical flux of water driven by a pressure drop $\mathcal{P}$ across a seal of thickness $b$.

The above scales are used in combination with existing parameters to define the following dimensionless quantities:

$$\begin{gathered} \tilde{x} \equiv \frac{x}{\mathcal{L}}, \quad \tilde{t} \equiv \frac{t}{\mathcal{T}}, \quad \tilde{h} \equiv \frac{h}{H}, \quad \tilde{p} \equiv \frac{p}{\mathcal{P}}, \quad \tilde{q} \equiv \frac{q}{\mathcal{Q}_z}, \\ \tilde{b} \equiv \frac{b}{H}, \quad \tilde{\rho}_\alpha \equiv \frac{\rho_\alpha}{\rho_g^0}, \quad \text{and} \quad \tilde{\mathcal{I}}_\alpha^n \equiv \frac{2\mathcal{L}H\,\mathcal{I}_\alpha^n}{\dot{M}}. \end{gathered} \tag{3.33}$$

The following dimensionless groups are also used:

$$N_{cw} \equiv c_w \mathcal{P} \tag{3.34a}$$

$$R_{cw} \equiv c_r / c_w \tag{3.34b}$$

$$R_{cf} \equiv c_g / c_w \tag{3.34c}$$

$$R_A \equiv \mathcal{L} / H \tag{3.34d}$$

$$R_d \equiv \rho_g^0 / \rho_w^0 \tag{3.34e}$$

$$N_g \equiv \rho_w^0 g H / \mathcal{P} \tag{3.34f}$$

$$\mathcal{M} \equiv \lambda_g / (s_g \lambda_w) \tag{3.34g}$$

$$\Lambda_w^s \equiv \lambda_w^s H / (\lambda_w b) \tag{3.34h}$$

$$\mathcal{M}_z^s \equiv \lambda_g^s / \lambda_w^s \tag{3.34i}$$

$$\tilde{p}_c^E \equiv p_c^E / \mathcal{P} \tag{3.34j}$$

The last two of these dimensionless groups are new relative to Chapter 2. The seal mobility ratio $\mathcal{M}_z^s$ compares the mobility of gas leakage to that of water leakage, and is important for interpreting the effect of the relative permeability of gas in the seal (see §3.3.2.2). The dimensionless capillary entry pressure compares the capillary entry pressure to the characteristic pressure: Roughly, gas injection is likely to drive gas leakage if $\tilde{p}_c^E < 1$ and buoyancy is likely to drive gas leakage if $\tilde{p}_c^E < (1 - R_d) N_g$. Readers are referred to Chapter 2 for a discussion of the other 8 groups.

### 3.2.5 Model summary

Dropping the tildes, the above scalings and dimensionless groups allows for the model to be presented in dimensionless form as

$$N_{cw}(R_{cw}\rho_g^n + R_{cf})h^n\frac{\partial p^n}{\partial t} + \rho_g^n\frac{\partial h^n}{\partial t} - \frac{\partial}{\partial x}\left\{\rho_g^n h^n \mathcal{M}\left(\frac{\partial p^n}{\partial x} - \rho_g^n R_d N_g \frac{\partial h^n}{\partial x}\right) + \frac{\Lambda_w^s \rho_g^{s+1}}{2 s_g \rho_g^n}\frac{\partial}{\partial x}\left[(h^n)^2 q_{g,z}^{s+1}\right]\right\} = -\frac{R_A^2 \Lambda_w^s}{s_g}\left(\rho_g^{s+1} q_{g,z}^{s+1} - \rho_g^s q_{g,z}^s\right) + \mathcal{I}_g^n, \tag{3.35}$$

and

$$N_{cw}(R_{cw}+1)(1-s_g h^n)\frac{\partial p^n}{\partial t} - s_g\frac{\partial h^n}{\partial t} - \frac{\partial}{\partial x}\left\{(1-h^n)\left[\frac{\partial p^n}{\partial x} - N_g\frac{\partial h^n}{\partial x}\right] + \frac{\Lambda_w^s}{6}\frac{\partial}{\partial x}\left[(1-h^n)^2(q_{w,z}^s + 2q_{w,z}^{s+1})\right]\right\} = -{R_A}^2\Lambda_w^s(q_{w,z}^{s+1} - q_{w,z}^s) + s_g R_d \mathcal{I}_w^n, \tag{3.36}$$

which enforce global conservation of mass in aquifer $n$ for $n = s = 1 \cdots N_z$. The gas density in each aquifer is related to the pressure via

$$\rho_g^n(p^n) = 1 + N_{cw}R_{cf}(p^n - p^0). \tag{3.37}$$

The aquifers are coupled by water leakage according to

$$\frac{\Lambda_w^s}{2}(1-h^n)q_{w,z}^{s+1} + \left[\frac{\Lambda_w^s}{k_{rw}^\star}h^{n-1} + 1 + \frac{\Lambda_w^s}{2}(1-h^n)\right]q_{w,z}^s = -\left[p^n - p^{n-1} + N_g(h^{n-1} + b + 1 - h^n)\right], \tag{3.38}$$

for each seal $s$, $s = n = 2 \cdots N_z - 1$, and by gas leakage according to

$$q_{g,z}^s = -\mathcal{R}\mathcal{M}_z^s\left(p_w^{n,B} - p_g^{n-1,T} + \rho_g^s R_d N_g b\right) \tag{3.39}$$

for each seal $s$, $s = n = 2 \cdots N_z - 1$, where

$$p_w^{n,B} = p^n + (1 - h^n) \left[ N_g + \frac{\Lambda_w^s}{2} (q_{w,z}^{s+1} + q_{w,z}^s) \right] \tag{3.40}$$

and

$$p_g^{n-1,T} = \frac{1}{\xi_g^s} \left[ p^{n-1} - R_d N_g \rho_g^{n-1} h^{n-1} + (\xi_g^s - 1)(p_w^{n,B} + R_d N_g b \rho_g^s) \right]. \tag{3.41}$$

The capillary pressure along the underside of each seal is given by

$$\begin{aligned} p_c^{n-1,T} = &\left( \frac{1}{\xi_g^s} - \frac{1}{\xi_w^s} \right) p^{n-1} + \left( \frac{1}{\xi_w^s} - \frac{R_d \rho_g^{n-1}}{\xi_g^s} \right) N_g h^{n-1} \\ &+ \left( \frac{1}{\xi_w^s} - \frac{1}{\xi_g^s} \right) p_w^{n,B} - (1 - R_d \rho_g^s) N_g b + \left( \frac{1}{\xi_w^s} - \frac{R_d \rho_g^s}{\xi_g^s} \right) N_g b, \end{aligned} \tag{3.42}$$

where

$$\xi_w^s = 1 + h^{n-1} \frac{\Lambda_w^s}{k_{rw}^\star} \quad \text{and} \quad \xi_g^s = 1 + \left( \frac{\Lambda_w^s \mathcal{M}_z^s \rho_g^s h^{n-1}}{s_g \mathcal{M} \rho_g^{n-1}} \right) \mathcal{R}, \tag{3.43}$$

and the entry-pressure transition function $\mathcal{R}(p_c^{n-1,T})$ is as given in Eq. (3.22) above. Lastly, the system is closed with boundary and initial conditions, which are written in dimensionless form as $h^n(x, t = 0) = 0$ and $p^n(x, t = 0) = p^n(-L_x/2, t) = p^n(L_x/2, t) = p^0 - N_g[n + (n-1)b]$.

## 3.3 Results

As evidenced by the large number of dimensionless parameters, this model incorporates a large number of physical mechanisms that will interact in complex and sometimes counter-intuitive ways. Chapter 2 studied the coupling of fluid injection (both water and gas) with vertical and lateral pressure dissipation, the former being a direct result of water leakage. Here, having now extended the model presented in Chapter 2, to allow for gas leakage subject to a capillary entry threshold, the coupling of gas injection with the buildup of capillary pressure and subsequent

gas leakage is studied. In doing so, this chapter focus specifically on the likelihood of gas leakage and on the impact of gas leakage on the spatial distribution of gas at the end of injection. The time evolution of the gas plume and the pressure field, both during and after injection, is studied in Chapter 4.

This chapter focuses on a minimal system: Two aquifers ($N_z = 2$) separated by a permeable but fine-grained seal, with gas injection into the lower aquifer ($n = 1$). Rock properties are chosen that are consistent with the injection of $CO_2$ into a typical target reservoir for CCS—namely, thick sandstone aquifers and a thin mudstone seal. Fluid properties are chosen that are consistent with those of $CO_2$ and water at a depth of ∼1 km. An assumed injection rate of ∼2 Mt per year distributed along a 30 km injection array is used, in combination with an injection time of 10 years. This scenario motivates a set of dimensional reference parameter values, from which dimensionless reference parameter values are calculated. Both sets of parameters are summarised in Table 3.1. These parameter values are used below, except where explicitly indicated otherwise.

The model is solved numerically by discretising in space using a standard finite-volume method on a uniform grid and integrating in time using `MATLAB`'s stiff ODE solver `ODE15s` [see Appendices B and C, and Shampine and Reichelt, 1997]. At each time step, the vertical water fluxes are calculated by solving $N_x$ uncoupled linear algebraic systems of size $N_z - 1$, where $N_x$ is the number of horizontal gridblocks. Also imposed is no vertical flow through the bottom and top of the system (*i.e.*, $q^1_{w,z} = q^{N_z+1}_{w,z} = 0$).

### 3.3.1 Evolution of capillary pressure in the absence of gas leakage ($p_c^E \to \infty$)

Gas will begin to leak out of aquifer $n$ via seal $s + 1$ when the capillary pressure along the underside of the seal exceeds the entry pressure, $p_c^{n,T} > p_c^E$. The value

| **Parameter** | **Symbol** | **Value** |
|---|---|---|
| Number of aquifers | $N_z$ | 2 |
| Horizontal extent | $L_x$ | 100 km |
| Aquifer thickness | $H$ | 10 m |
| Aquifer porosity | $\phi$ | 0.3 |
| Aquifer permeability | $k$ | $10^{-13}$ m$^2$ |
| Seal thickness | $b$ | 0.5 m |
| Seal permeability | $k_s$ | $5 \times 10^{-19}$ m$^2$ |
| Seal entry pressure | $p_c^E$ | $\infty$ |
| Rock compressibility | $c_r$ | $3.0 \times 10^{-11}$ Pa$^{-1}$ |
| Reference pressure | $p^0$ | 10 MPa |
| Water viscosity | $\mu_w$ | $8 \times 10^{-4}$ Pa·s |
| Water density | $\rho_w$ | 1000 kg·m$^{-3}$ |
| Water compressibility | $c_w$ | $4.5 \times 10^{-10}$ Pa$^{-1}$ |
| Saturation of water in gas region | $s_{wr}$ | 0.2 |
| Relative permeability of water in gas region | $k_{rw}^\star$ | $10^{-3}$ |
| Gas viscosity | $\mu_g$ | $4 \times 10^{-5}$ Pa·s |
| Gas density | $\rho_g^0$ | 700 kg·m$^{-3}$ |
| Gas compressibility | $c_g$ | $1.5 \times 10^{-8}$ Pa$^{-1}$ |
| Saturation of gas in gas region | $s_g$ | 0.8 |
| Relative permeability of gas in gas region | $k_{rg}$ | 1 |
| Relative permeability of gas in seals | $k_{rg}^s$ | 1 |
| Mass injection rate | $\dot{M}$ | $2 \times 10^{-3}$ kg·s$^{-1}$·m$^{-1}$ |
| Injection time | $\mathcal{T}$ | 10 years |
| Compressibility number | $N_{cw}$ | $1.21 \times 10^{-4}$ |
| Rock-to-water compressibility ratio | $R_{cw}$ | $6.67 \times 10^{-2}$ |
| Gas-to-water compressibility ratio | $R_{cf}$ | 33.3 |
| Aspect ratio | $R_A$ | 18.77 |
| Density ratio | $R_d$ | 0.7 |
| Gravity number | $N_g$ | 0.37 |
| Aquifer mobility ratio | $\mathcal{M}$ | 25 |
| Seal mobility ratio | $\mathcal{M}_z^s$ | 20 |
| Water-leakage strength | $\Lambda_w^s$ | $10^{-4}$ |
| Seal-to-aquifer thickness ratio | $\tilde{b}$ | 0.05 |
| Horizontal extent | $\tilde{L}_x$ | 533 |

**Table 3.1:** Reference parameter values. Note that the dimensionless values (below the double-line) are calculated directly from the dimensional values (above the double-line). Note that the dimensional parameters listed here are identical to those used in Chapter 2 (listed in Table 1) with the exception of: $k_s$, $b$, $k_{rw}^\star$ and $\dot{M}$.

of $p_c^{n,T}$ is coupled to the thickness of the gas plume due to buoyancy; to the pressurisation of aquifer $n$ due to injection; to the pressurisation of aquifer $n+1$ due to vertical pressure dissipation via water leakage; and to gas leakage itself. It is therefore instructive to begin by considering the evolution of this capillary pressure in the absence of gas leakage, taking $p_c^E \to \infty$. In this limit, the model is identical to that presented in Chapter 2.

During gas injection into aquifer $n$, a plume of gas will form, thicken, and spread with time (Figures 3.2a, inset, and 3.2b, inset). As has been studied previously in some detail, the characteristic tongued shape of this plume will be controlled by several factors, including the mobility of gas relative to that of water ($\mathcal{M}$), the strength of buoyancy relative to injection ($(1-R_d)N_g$), the importance of compressibility relative to injection pressure ($N_{cw}$, $R_{cw}N_{cw}$, and $R_{cf}N_{cw}$), and the strength of vertical pressure dissipation relative to that of lateral pressure dissipation ($R_A^2\Lambda_w^s$) [*e.g.*, Nordbotten and Celia, 2006b, Mathias et al., 2009, Vilarrasa et al., 2010, and Chapter 2].

The limit $p_c^E \to \infty$ implies that $\mathcal{R}=0$ and therefore that $\xi_g^s = 1$ and $q_{g,z}^s = 0$ for all $x$, $t$, and $s$ (Eqs. 3.39 and 3.43). As a result, the vertical pressure distribution within the gas is gas-static (Eq. 3.8) and $p_c^{n,T}$ is therefore given by

$$p_c^{n,T} = \left(1 - \frac{1}{\xi_w^{s+1}}\right)\left(p^n - p_w^{n+1,B} - N_g b\right) - \left(R_d\rho_g^n - \frac{1}{\xi_w^{s+1}}\right)N_g h^n. \tag{3.44}$$

Note that this expression is a good approximation to $p_c^{n,T}$ even with gas leakage, because the model fundamentally assumes that the seals provide more resistance to vertical flow than the aquifers ($\Lambda_w^s \ll 1$) and it is expected that the gas will be much more mobile within the aquifers than the water ($\mathcal{M} \gg 1$).

This expression above for $p_c^{n,T}$ can be further simplified by considering the value of $\xi_w^{s+1} = 1 + \Lambda_w^s h^n / k_{rw}^\star$ (Eq. 3.43). Beneath and in the gas plume, vertical flow of water is resisted by two low permeabilities in series: The low relative permeability of water in the gas region ($k_{rw}^\star \ll 1$) and the low permeability of the

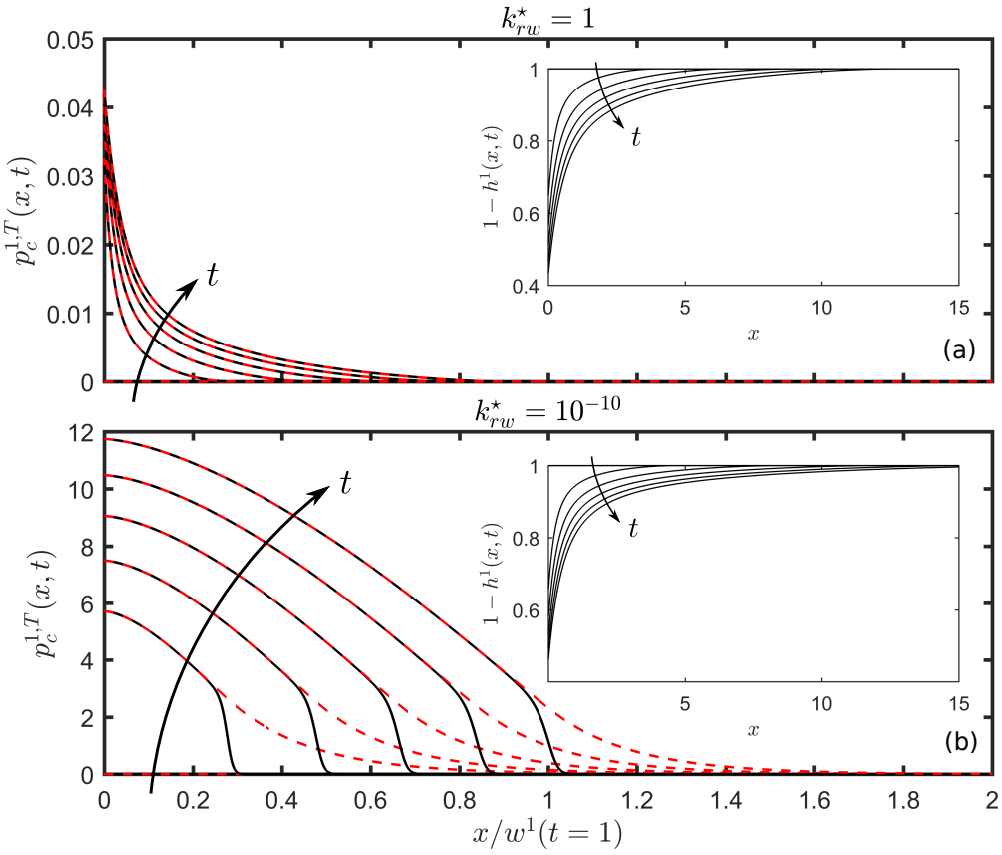


**Figure 3.2:** Gas injection into the bottom-most aquifer of a two layer system with $p_c^E = \infty$ and for (a) $k^\star_{rw} = 1$ and (b) $k^\star_{rw} = 10^{-10}$. The main plots show $p_c^{1,T}$ against $x/w(t=1)$, where $w(t)$ is the plume width, for $t = 0,\ 0.2,\ 0.4,\ 0.6,\ 0.8,$ and $1.0$. The insets show the plume shapes $1 - h^1$ against $x$ at the same times. In the main plots, shown are the actual value of $p_c^{n,T}$ as calculated from the full model (Eq. 3.44; solid black), as well as the approximate values appropriate to these limiting cases (Eqs. 3.45 and 3.46 in (a) and (b), respectively; dashed red).

seals ($k_s \ll k$). The quantity $\Lambda^s_w h^n / k^\star_{rw} = (h^n/\lambda^\star_w)/(b/\Lambda^s_w)$ measures the ratio of the former resistance to the latter.

In the limit where the seals dominate the total resistance to upward water flow under the gas plume, $b/\Lambda^s_w \gg h^n/\lambda^\star_w \implies \Lambda^s_w h^n/k^\star_{rw} \ll 1 \implies \xi_w \approx 1$ and the capillary pressure $p_c^{n,T}$ reduces to

$$p_c^{n,T} \approx (1 - R_d\rho_g^n)N_g h^n, \quad \text{for} \quad \Lambda^s_w h^n/k^\star_{rw} \ll 1, \tag{3.45}$$

or, in dimensional terms, $p_c^{n,T} \approx (\rho_w - \rho_g^n)g h^n$. Thus, the gas pressure is gas-static

from the interface upward ($p_g^{n,T} = p^n - R_d N_g \rho_g^n h^n$) and, if the gas offers negligible resistance to vertical flow of water, the water pressure is also nearly hydrostatic from the interface upward ($p_w^{n,T} \approx p^n - N_g h^n$). As a result, the capillary pressure at the top of the aquifer is simply given by the so-called buoyant overpressure in the gas, which mirrors the plume shape ($p_c^{n,T} \propto h^n$), as illustrated in Figure 3.2(a). In this limit, the entry pressure condition becomes identical to that of Woods and Farcas [2009].

In the opposite limit, where the gas region dominates the total resistance to upward water flow under the gas plume, $b/\Lambda_w^s \ll h^n/\lambda_w^\star \implies \Lambda_w^s h^n / k_{rw}^\star \gg 1 \implies \xi_w^{s+1} \gg 1$ and the capillary pressure instead reduces to

$$p_c^{n,T} \approx \underbrace{(p^n - R_d \rho_g^n N_g h^n)}_{\text{gas pressure}} - \underbrace{(p_w^{n+1,B} + N_g b)}_{\text{water pressure}}, \quad \text{for} \quad \Lambda_w^s h^n / k_{rw}^\star \gg 1. \tag{3.46}$$

Thus, the gas pressure is still gas-static from the interface upward ($p_g^{n,T} = p^n - R_d N_g \rho_g^n h^n$), but the water pressure at the top of the aquifer is now effectively hydraulically disconnected from the water pressure at the interface by the presence of the gas. As a result, the water pressure at the top of the aquifer is given by the pressure at the bottom of the aquifer above plus the hydrostatic difference across the seal. In other words, a very small value of $k_{rw}^\star$ in the gas region (strictly, $k_{rw}^\star \ll \Lambda_w^s h^n$) can enable a much larger pressure difference between the gas and the water at the top of the aquifer, and therefore a much larger capillary pressure. This is illustrated in Figure 3.2(b), having changed only the value of $k_{rw}^\star$ relative to Figure 3.2(a). The shape of the gas plume is very similar to that shown in Figure 3.2(a), but now somewhat broader due to the reduction in pressure dissipation. However, the capillary pressure is now more than two orders of magnitude larger, and it remains large over a much broader region; the latter is due to the development of a plateau in the water pressure above the gas plume (see §2.3.4.2). Note that the assumption that $\Lambda_w^s h^n / k_{rw}^\star \gg 1$ must always eventually break down near the advancing nose of the plume for any nonzero $k_{rw}^\star$, since there must always

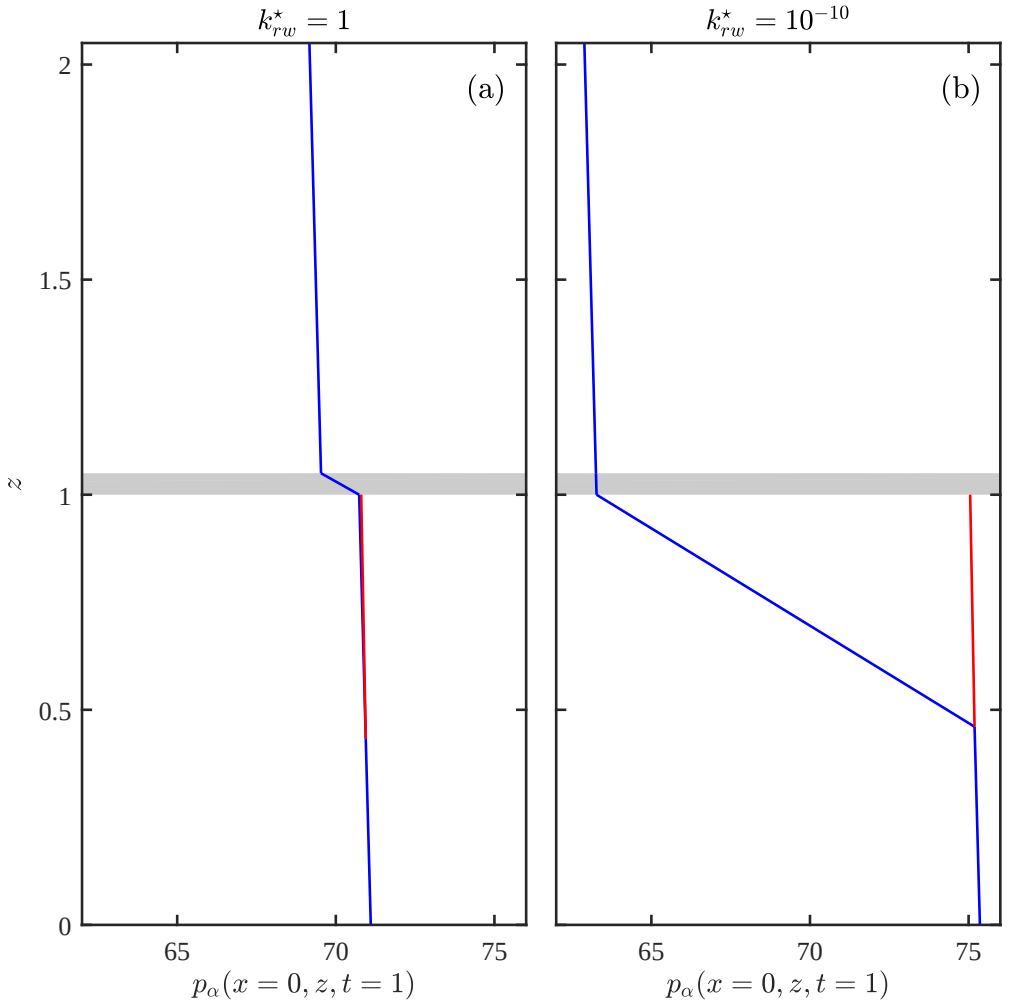


**Figure 3.3:** Phase pressure variation with depth, plotted at $x = 0$ and $t = 1$, and for $k^\star_{rw} = 1$ (a) and $k^\star_{rw} = 10^{-10}$ (b). The pressure in the water and the gas are plotted in blue and red respectively, and grey shading indicates the location of the intermediate seal.

exist some vanishing plume thickness at which the gas can no longer obstruct the water (*i.e.*, where $h^n \not\gg k^\star_{rw}/\Lambda^s_w$). In other words, the former buoyancy-dominated limit of $\Lambda^s_w h^n/k^\star_{rw} \ll 1$ must always apply sufficiently close to the edge of the gas plume.

The strong dependence of capillary pressure on $k^\star_{rw}$ can be further explained by considering the vertical distribution of pressure in each phase (Figure 3.3). In the limit where the gas offers no obstruction to vertical water flow ($\Lambda^s_w h^n/k^\star_{rw} \ll 1$), the pressure gradient in the injection aquifer, for each phase, is approximately phase-static (Figure 3.3a). In this scenario, the low permeability of the seals offers

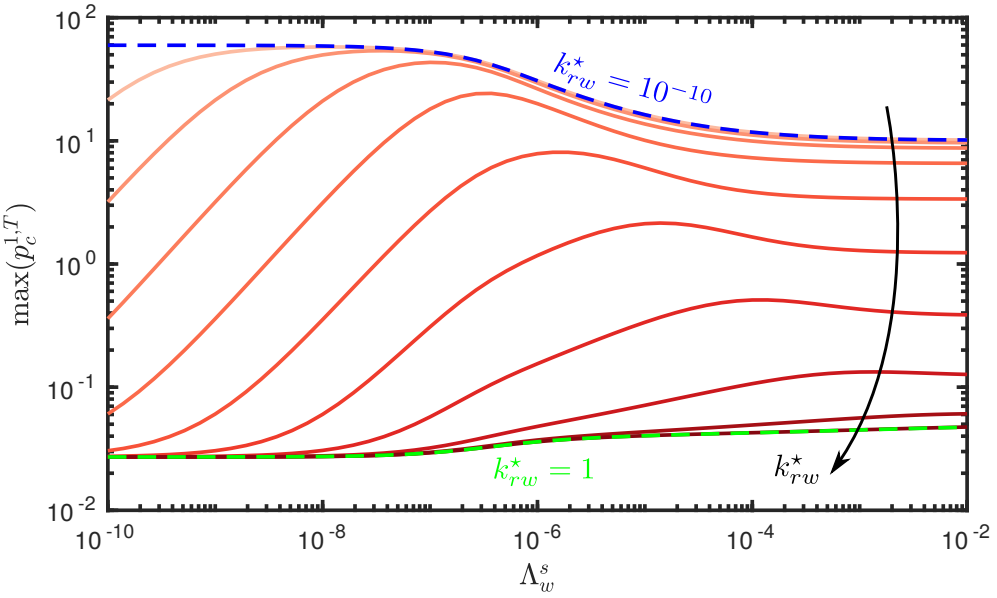


**Figure 3.4:** The maximum capillary pressure $\max(p_c^{1,T}) = p_c^{1,T}(x = 0, t = 1)$ is a strong function of both $\Lambda_w^s$ and $k^\star_{rw}$. Here, plotted $\max(p_c^{1,T})$ against $\Lambda_w^s$ for $\log_{10}(k^\star_{rw}) = -10, -9, -8, -7, -6, -5, -4, -3, -2$, and $0$ (light to dark). Also shown is the prediction of Eq. (3.46) for $k^\star_{rw} = 10^{-10}$ (dashed blue) and of Eq. (3.45) for $k^\star_{rw} = 1$ (dashed green). Note that $\max(p_c^{1,T})$ decreases by two to three orders of magnitude in varying $k^\star_{rw}$ from the former limit to the latter.

the principal resistance to vertical water flow. Accordingly, the pressure drop associated with vertical pressure dissipation is located exclusively within the seal (Figure 3.3a). In the opposite limit, where the low relative permeability of the gas provides the principal resistance to vertical water flow ($\Lambda_w^s h^n / k^\star_{rw} \gg 1$), the pressure gradient in the gas remains approximately gas-static. However, as the gas obstructs vertical water flow, the pressure drop associated with vertical pressure dissipation is now located within the gas region (Figure 3.3b). Furthermore, due to the limited amount of vertical pressure dissipation in this scenario, a larger pressure difference exists between the aquifers. These effects combine to create a substantial pressure difference between the fluid phases, that is maximum at the top of the injection aquifer (Figures 3.2, 3.3 and 3.4).

The maximum capillary pressure always occurs at the injection point ($x = 0$) and at the end of injection ($t = 1$), $\max(p_c^{n,T}) = p_c^{n,T}(x = 0, t = 1)$, and this maximum is sensitive to both $\Lambda_w^s$ and $k^\star_{rw}$ through their respective impacts on

pressure dissipation. Figure 3.4 plots $\max(p_c^{n,T})$ against $\Lambda_w^s$ for several different values of $k_{rw}^\star$ across its full range, highlighting the transition between the two limits discussed above ($k_{rw}^\star \approx 1$ and $k_{rw}^\star \ll 1$) and the orders-of-magnitude change in $\max(p_c^{n,T})$ as $k_{rw}^\star$ transitions between these two limits. Note also that $\max(p_c^{n,T})$ is weakly non-monotonic in $\Lambda_w^s$ for fixed $k_{rw}^\star$.

These results suggest that the buoyant overpressure may provide a substantial underestimate of the capillary pressure in the presence of vertical pressure dissipation, which has implications for the likelihood of gas leakage for typical geological parameters (see §3.4).

### 3.3.2 Gas leakage through a uniform seal

Finite values of $p_c^E$ are now considered, for which gas does eventually leak when buoyancy and/or injection is sufficiently strong. The strength and horizontal extent of gas leakage are controlled by several key parameters: $k_{rw}^\star$, as discussed above; $\Lambda_w^s$, which measures the resistance of the aquifers to water flow relative to that of seals; $\mathcal{M}_z^s$, which measures the resistance of the seals to water flow relative to their resistance to gas flow; and, of course, $p_c^E$. In the previous section, particular focus was devoted to the impact of $k_{rw}^\star$ on the potential for gas leakage. In this section, $k_{rw}^\star$ is now fixed to the reference value ($k_{rw}^\star = 10^{-3}$) and this section studies the roles of $\Lambda_w^s$, $\mathcal{M}_z^s$, and $p_c^E$ in determining the strength and extent of gas leakage, and the resulting distribution of gas in aquifers 1 and 2 at the end of injection.

#### 3.3.2.1 Varying $\Lambda_w^s$ and $p_c^E$ for fixed $\mathcal{M}_z^s$

First, $\mathcal{M}_z^s = 20$ is fixed to the reference value, allowing for the study of the roles of $\Lambda_w^s$ and $p_c^E$. To do so, the total mass of gas in aquifer 2 at the end of injection

is considered. Note that the total mass of gas in aquifer $n$ at time $t$ is given by

$$M_g^n(t) = \int_{-\infty}^{+\infty} \rho_g^n h^n \, \mathrm{d}x, \tag{3.47}$$

and the total mass of gas in the system is given by

$$M_g^{\mathrm{tot}}(t) = \sum_{n=1}^{N_z} M_g^n(t). \tag{3.48}$$

Here, a constant mass rate of gas injection $\mathcal{I}_g^1 = 2$ is prescribed until time $t = 1$ and it must therefore be the case that $M_g^{\mathrm{tot}}(t) = M_g^1(t) + M_g^2(t) = 2t$. Without gas leakage, it is expected that at the end of injection $M_g^1(t = 1) = 2$ and $M_g^2(t = 1) = 0$ (*i.e.*, that all of the gas is located in the injection aquifer). With gas leakage, it is expected that $M_g^2(t = 1) > 0$ and that $M_g^1(t = 1) = 2 - M_g^1(t = 1) < 2$.

The rate of gas leakage is expected to increase with $\Lambda_w^s$ since $q_{g,z}^1 \propto \Lambda_w^s$. The likelihood of exceeding the entry pressure also increases strongly with $\Lambda_w^s$ for $\Lambda_w^s \ll k_{rw}^\star / h^1$, and is insensitive to $\Lambda_w^s$ for $\Lambda_w^s \gg k_{rw}^\star / h^1$ (Figure 3.4). As a result, the total amount of gas leakage is expected to increase monotonically (or nearly so) as $\Lambda_w^s$ increases. Similarly, gas leakage starts earlier and occurs over a larger horizontal extent as $p_c^E$ decreases; the total amount of gas leakage is therefore expected to increase monotonically as $p_c^E$ decreases. Figure 3.5 illustrates this behaviour, showing that $M_g^2(t = 1)$ increases monotonically as $\Lambda_w^s$ increases and as $p_c^E$ decreases.

Now the shapes of the gas plumes in aquifers 1 and 2 are considered. The horizontal length over which gas leakage occurs is the horizontal length over which $p_c^{1,T}$ exceeds $p_c^E$, which depends on the horizontal distribution of $p_c^{1,T}$ and on the magnitude of $p_c^{1,T}$ relative to $p_c^E$. For larger values of $p_c^E$, leakage is localised near the injection well where $p_c^{1,T}$ is largest, as evidenced by the localised gas plume in aquifer 2 (Figure 3.6, upper left). As $p_c^E$ decreases at fixed $\Lambda_w^s$ (Figure 3.6, left to right), the gas plume in aquifer 2 grows broader as gas leakage starts earlier and

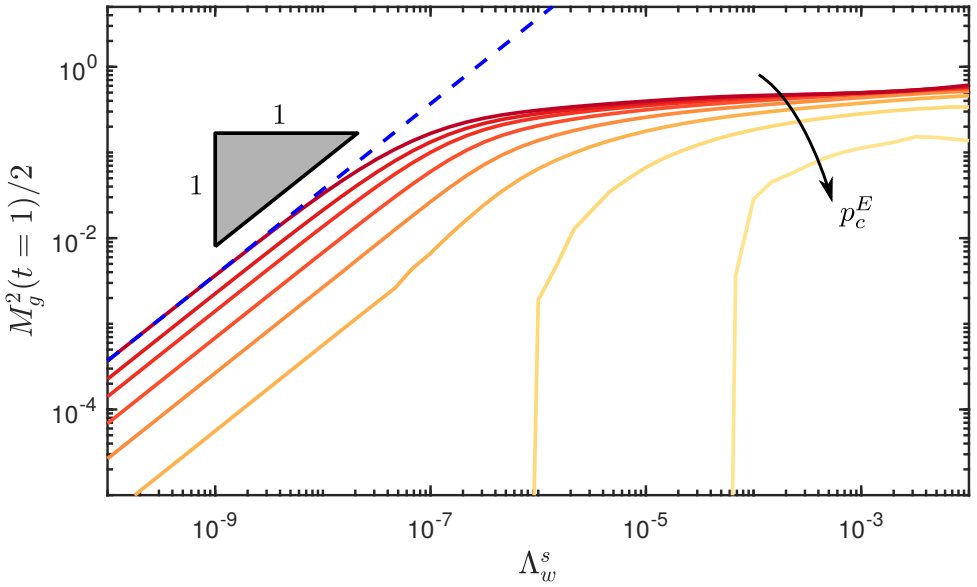


**Figure 3.5:** Mass fraction of gas in aquifer 2 at the end of injection, $M_g^2(t=1)/2$, plotted against $\Lambda_w^s$ for $\log_{10}(p_c^E) = -4, -3, -8/3, -7/3, -2, -5/3, -4/3$, and $-1$ (dark to light). The dashed blue line illustrates a slope of 1 for reference, indicating that $M_g^2(t=1) \propto \Lambda_w^s$ for small values of $\Lambda_w^s$. For the two largest values of $p_c^E$ shown here, the curves diverge downward at some critical value of $\Lambda_w^s$, below which the entry pressure is never exceeded and there is therefore no gas leakage ($M_g^2 \to 0$).

occurs over a larger horizontal extent, but also thinner as the increasing amount of gas leakage begins to have a stronger impact on the gas plume in aquifer 1. For low $p_c^E$, the horizontal extent of gas leakage approaches the full width of the plume in aquifer 1, leading to a plume of the same width in aquifer 2. As $\Lambda_w^s$ increases at fixed $p_c^E$ (Figure 3.6, dark to light colors), the leakage flux increases and the width of the leaking region broadens due to the broadening of $p_c^{1,T}$ (Figure 3.2). At high $p_c^E$, the gas plume in aquifer 2 grows thicker and broader as $\Lambda_w^s$ increases, whereas the gas plume in aquifer 1 shrinks gently over its entire extent while retaining its shape. At lower $p_c^E$, in contrast, the gas plume in aquifer 2 grows thicker and narrower as the rate of gas leakage becomes large enough to substantially decrease the extent of the gas plume in aquifer 1.

Moderate values of $p_c^E$ and moderate to high values of $\Lambda_w^s$ lead to a large leakage rate that partially but not entirely spans the gas plume in aquifer 1, the plumes

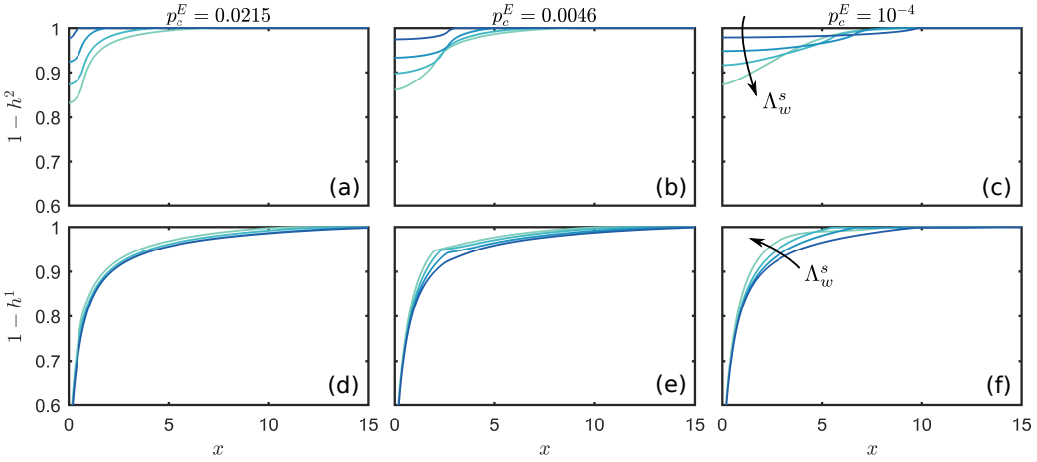


**Figure 3.6:** The shape of the gas plume in aquifer 1 (bottom row) and in aquifer 2 (top row) at the end of injection, $1-h^1(x, t=1)$ and $1-h^2(x, t=1)$, respectively, for three different values of $p_c^E$ (decreasing left to right). In each panel, results are shown for $\Lambda_w^s = 10^{-7}$, $10^{-6}$, $10^{-5}$, and $10^{-4}$ (dark to light colors). Recall that $k_{rw}^\star = 10^{-3}$.

in both aquifers develop a noticeable kink at the transition between the region that is losing/gaining gas and the region that is not. When gas leakage is either focused near the injection well (high $p_c^E$ and/or $\Lambda_w^s \ll k_{rw}^\star/h^1$) or distributed over the entire length of the gas plume in aquifer 1 (combination of low $p_c^E$ and/or $\Lambda_w^s \gg k_{rw}^\star/h^1$), the plumes in both aquifers are smooth.

These plume shapes are now quantified. For the gas plume in aquifer 1, the plume width $w^1(t)$ is considered, where $w^n(t)$ is the distance between the injection point and the place where the thickness of the plume in aquifer $n$ falls below an arbitrary threshold value (here, $10^{-6}$). The width of the plume in aquifer 1 at the end of injection, $w^1(t=1)$, decreases monotonically as $p_c^E$ decreases and nearly monotonically as $\Lambda_w^s$ increases (Figure 3.7a). Recall, however, that the width of the plume in aquifer 1 decreases strongly with $\Lambda_w^s$ even in the absence of gas leakage due to increasing vertical pressure dissipation, as discussed in detail in Chapter 2. To separate the reduction in $w^1(t=1)$ due to gas leakage from that due to vertical pressure dissipation, it is sensible to calculate the relative difference between the width for a particular value of $p_c^E$, $w^1(p_c^E)$, and the width for $p_c^E \to \infty$, $w^1(p_c^E \to \infty)$ (no gas leakage): $\delta w^1 = [w^1(p_c^E \to \infty) - w^1(p_c^E)]/w^1(p_c^E \to \infty)$

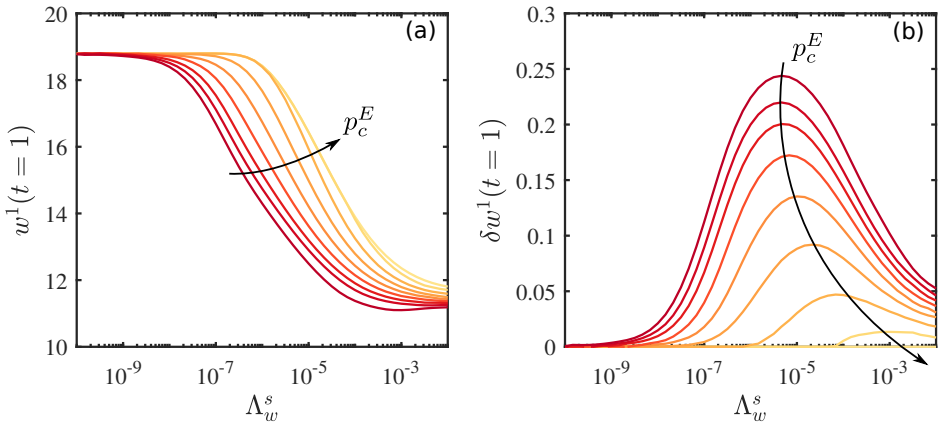


**Figure 3.7:** (a) Plume width in aquifer 1 at the end of injection, $w^1(t=1)$, plotted against $\Lambda_w^s$ for $\log_{10}(p_c^E) = -11/3, -3, -8/3, -7/3, -2, -5/3, -4/3, -1$, and $0$ (dark to light). In (b) the relative difference between $w^1(t=1)$ and its value for $p_c^E \to \infty$ (no gas leakage) is shown to separate the decrease in plume width due to gas leakage from the decrease in plume width due to vertical pressure dissipation.

(Figure 3.7b). Vertical pressure dissipation dominates the reduction in $w^1(t=1)$ for very low and very high values of $\Lambda_w^s$; very little gas leakage occurs in the former case, and vertical pressure dissipation is very strong in the latter case. For intermediate values of $\Lambda_w^s$, gas leakage leads to a plume that is up to about 25 % narrower than what would result from pressure dissipation alone.

For the gas plume in aquifer 2, the width at the end of injection $w^2(t=1)$ increases strongly and monotonically as $p_c^E$ decreases, but has a relatively weak and non-monotonic dependence on $\Lambda_w^s$ (Figure 3.8b). The maximum thickness of the gas plume in aquifer 2, $\max(h^2) = h^2(x=0, t=1)$, is easier to interpret, increasing monotonically as $\Lambda_w^s$ increases and as $p_c^E$ increases, although the latter dependence is much weaker (Figure 3.8c). It is found that $\max(h^2) \sim \Lambda_w^s$ for small $\Lambda_w^s$, which is expected since leakage is weak and $h^1$ and the pressure field are only mildly impacted by gas leakage. As $\Lambda_w^s$ increases, transition to $\max(h^2) \sim (\Lambda_w^s)^{1/5}$ is observed.

Lastly, the aspect ratio of the gas plume in aquifer 2, $\mathcal{A}^2 = w^2(t=1)/\max(h^2)$ is considered (Figure 3.8a). The aspect ratio increases strongly as $p_c^E$ decreases, suggesting that the increase in $w^2(t=1)$ dominates the increase in $\max(h^2)$—it

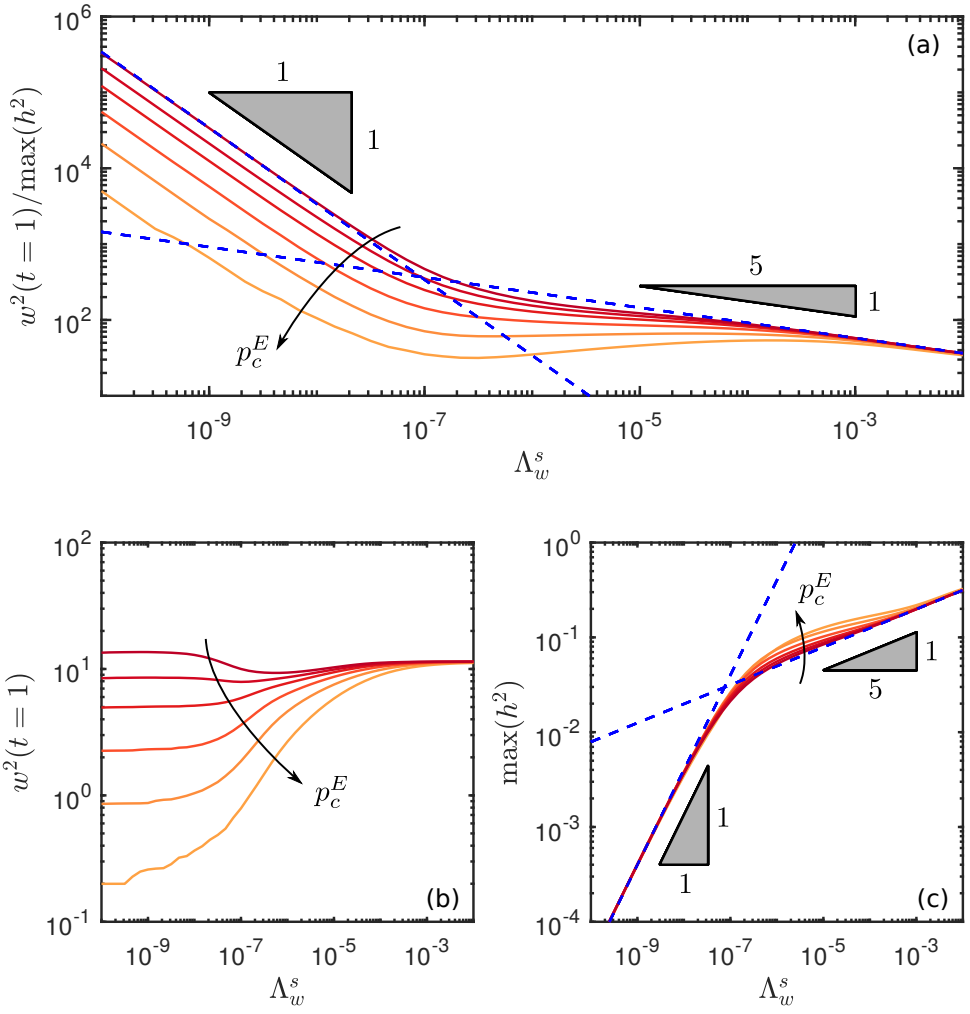


**Figure 3.8:** (a) The aspect ratio of the gas plume in aquifer 2, $\mathcal{A}^2 = w^2(t = 1)/\max(h^2)$, plotted against $\Lambda_w^s$ for $\log_{10}(p_c^E) = [-5/3,\ -2,\ -7/3,\ -8/3,\ -9/3$ and $-11/3]$ (dark to light), where $w^2(t = 1)$ is the width of this plume at the end of injection and $\max(h^2) = h^2(x = 0, t = 1)$ is the maximum thickness of this gas plume. Also plotted: (b) $w^2(t = 1)$ and (c) $\max(h^2)$ individually against $\Lambda_w^s$ for the same values of $p_c^E$.

is therefore always expected that a more elongated gas plume occurs in aquifer 2 for lower $p_c^E$. With regard to $\Lambda_w^s$, however, the scaling of $\max(h^2)$ dominates the scaling of $\mathcal{A}^2$ because $w^2$ does not exhibit a systematic trend, so $\mathcal{A}^2 \sim (\Lambda_w^s)^{-1}$ for small $\Lambda_w^s$, transitioning to $\mathcal{A}^2 \sim (\Lambda_w^s)^{-1/5}$ as $\Lambda_w^s$ increases. In other words, the gas plume in aquifer 2 will always grow taller relative to its width as $\Lambda_w^s$ increases (Figure 3.6).

#### 3.3.2.2 Effect of $\mathcal{M}_z^s$

Briefly considered below is the impact of varying $\mathcal{M}_z^s$ at fixed $\Lambda_w^s = 10^{-4}$ (the reference value). Recall that $\mathcal{M}_z^s \equiv (k_{rg}^s/\mu_g)/(k_{rw}^s/\mu_w)$ is the ratio of the mobility of gas in the seal to the mobility of water in the seal. Recall that $q_{g,z}^s \propto \mathcal{M}_z^s$, so it follows that the rate of gas leakage and therefore also the mass of gas in aquifer 2 to increase roughly linearly with $\mathcal{M}_z^s$ for small values of $\mathcal{M}_z^s$, where gas leakage plays a weak role in the overall pressure field (Figure 3.9a). As gas leakage becomes comparable to water leakage around $\mathcal{M}_z^s \sim 1$, gas leakage has an increasingly strong impact on pressure dissipation, and on the evolution of plume in aquifer 1, and $M_g^2(t=1)$ increases sublinearly as $\mathcal{M}_z^s$ increases further.

For fixed fluid viscosities, varying $\mathcal{M}_z^s$ is equivalent to varying the relative permeabilities in the seal. Physically, this can be interpreted as changing the fraction of pore volume in the seal that is available to conduct vertical gas leakage relative to vertical water leakage. In the absence of relative permeability effects, the maximum value of $\mathcal{M}_z^s$ is $\mu_w/\mu_g = 20$. In this limit, the seal is more conductive to gas than to water, and the local flux of gas across the seal exceeds that of water once $p_c^{1,T}$ exceeds $p_c^E$ (Figure 3.9b). In reality, it is likely that $k_{rg}^s < k_{rw}^s < 1$, such that relative permeability effects should generally decrease $\mathcal{M}_z^s$ relative to $k_{rg}^s = k_{rw}^s = 1$. As $\mathcal{M}_z^s$ decreases, the vertical gas flux decreases and the vertical water flux increases (Figure 3.9b). For small $\mathcal{M}_z^s$, the vertical gas flux scales as $q_{g,z} \sim \mathcal{M}_z^s$.

## 3.4 Implications for CCS

Considered below are the implications of the above results for CCS, with a particular focus on $CO_2$ injection at Sleipner—where $CO_2$ has been injected at an average rate of about $1\,\mathrm{Mt\,y^{-1}}$ since 1996. Note that, for purposes of this discussion, dimensional quantities are used below.

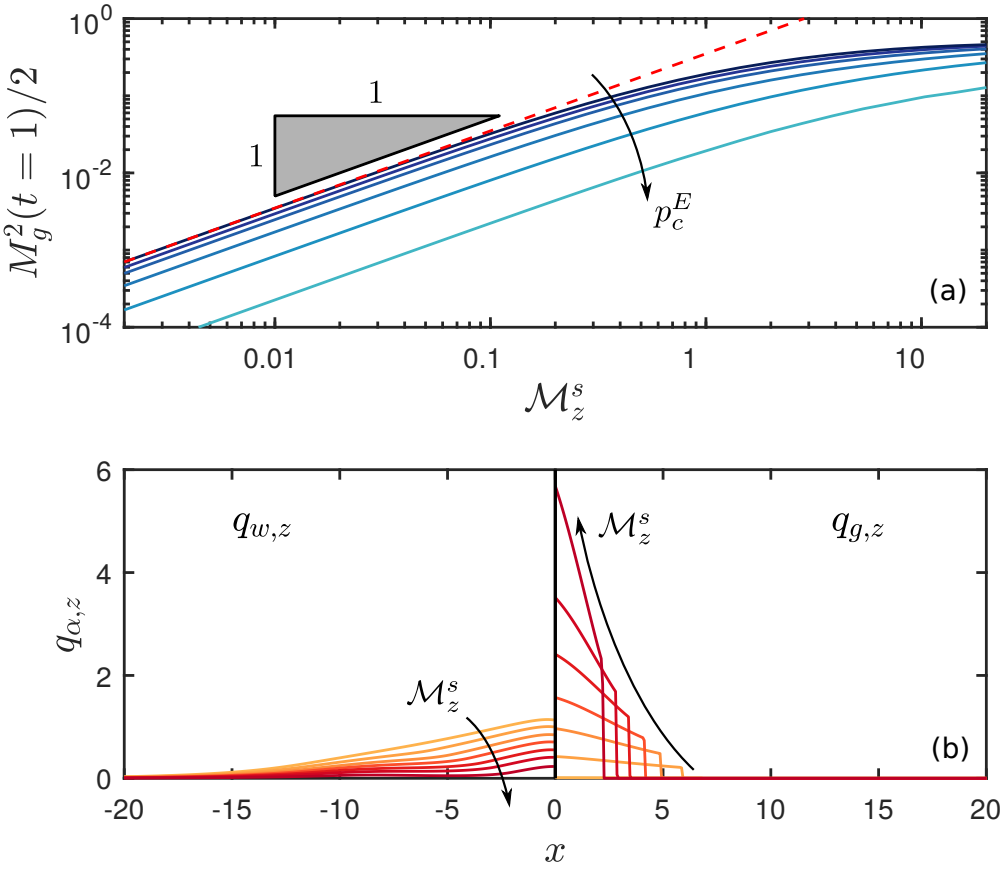


**Figure 3.9:** (a) Mass fraction of gas in the upper aquifer at the end of injection, $M_g^2(t=1)/2$, plotted against $\mathcal{M}_z^s$ for $\log_{10}(p_c^E) = -4$, $-2.8$, $-2.4$, $-2$, $-1.6$, and $-1.2$ (dark to light). (b) Vertical leakage flux of water $q_{w,z}^s$ (left half, $x < 0$) and of gas $q_{g,z}^s$ (right half, $x > 0$) for a fixed entry pressure and $\mathcal{M}_z^s = 0.01$, 0.39, 1.04, 2.00, 3.86, 7.46, and 20.00 (light to dark).

The entry pressure for a perfectly non-wetting phase invading a pore is approximately $p_c^E \approx 2\sigma/r$, where $\sigma$ is the interfacial tension and $r$ is the typical pore-throat radius. Chiquet et al. [2007] measured the $CO_2$-water interfacial tension to be $\sigma \approx 25\,\mathrm{mNm}^{-1}$ at reservoir conditions, and Kuila and Prasad [2013] measured the typical pore-throat radii of North Sea shales to be 10–100 nm. These values imply $p_c^E \approx 0.5$–$5$ MPa for a typical sealing layer at Sleipner, which is similar to the range of 2–5 MPa estimated by Chadwick et al. [2004].

In §3.3.1 above, it was shown that the magnitude and distribution of the capillary pressure at the base of a seal is very sensitive to the relative permeability $k_{rw}^\star$

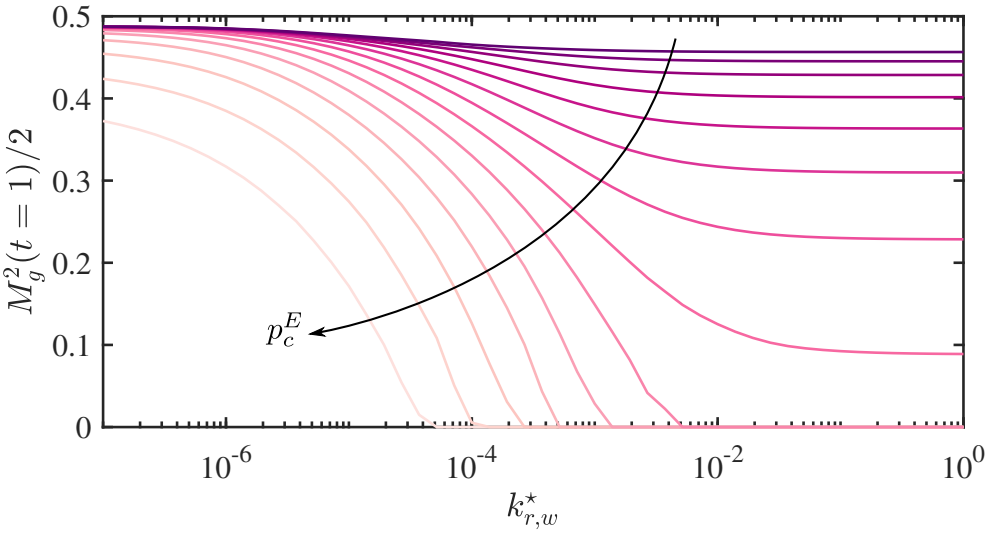


**Figure 3.10:** Mass of gas in the upper layer divided by total injected mass at the end of injection, as a function of the relative permeability of water in the gas region and plotted for $\log_{10}(p_c^E) = -3.5, -3.0, \cdots, -0.75, -0.5, -0.25$, and 0 (dark to light).

of water in the gas-saturated region, which originates in the conductivity and connectivity of residual water films there. Neglecting the resistance to water flow through this region by assuming $k^\star_{rw} = 1$ implies that the water column is very well connected across the gas region, such that the water pressure is nearly hydrostatic across the gas region and the capillary pressure along the base of the seal can be very well approximated by the buoyant overpressure in the gas, $p_c \approx (\rho_w - \rho_g)gh^n$, as has been assumed previously [*e.g.*, Woods and Farcas, 2009]. To exceed an entry pressure of $p_c^E \approx 2\,\text{MPa}$ would then require a $CO_2$ column of thickness $\sim 680\,\text{m}$, which is difficult to achieve. For the reference scenario, Figure 3.2(a) implies that the maximum capillary pressure for $k^\star_{rw} \approx 1$ is $p_c \approx 0.04\mathcal{P} \approx 11\,\text{kPa}$, where $\mathcal{P} \approx 0.27\,\text{MPa}$ is the characteristic pressure (see §3.32). This result would suggest that the capillary pressure cannot exceed the threshold for gas leakage. At Sleipner, where seismic data has been widely interpreted to show gas leakage across sealing layers, this conclusion, in addition to a vertical seismic anomaly, has led many to infer the presence of a conduit that provides a low-entry-pressure and high-permeability vertical channel for the gas leakage [*e.g.*, Chadwick et al., 2004, 2005, Bickle et al., 2007].

However, it was demonstrated above that decreasing $k^\star_{rw}$ leads to a substantial increase in the breadth and magnitude of $p_c$. Assuming that the gas region completely obstructs vertical water flow, $k^\star_{rw} \approx 0$, implies that the water pressure is effectively disconnected across the gas region, such that the water pressure is nearly hydrostatic across the seal and the capillary pressure along the base of the seal can be very well approximated by $p_c \approx [p^1 - \rho^n_g g h^n] - [p^{n+1,B}_w + \rho_w g b]$. For the reference scenario, Figure 3.2(b) implies that the maximum capillary pressure for $k^\star_{rw} \approx 0$ is $p_c \approx 12\mathcal{P} \approx 3.2\,\text{MPa}$. This capillary pressure, which is about 300 times larger than the previous estimate, is sufficiently high to suggest that gas leakage through the sealing layers at Sleipner is entirely plausible, and may occur instead of, or in addition to, gas leakage through a hypothetical conduit.

Reducing $k^\star_{rw}$ makes $CO_2$ leakage much more likely by substantially increasing the capillary pressure at the base of the seal, and would also greatly increase the amount of leakage by broadening the spatial distribution of this capillary pressure. Figure 3.10 shows the mass fraction of gas in the upper aquifer at the end of injection $M^2_g(t = 1)/2$ (*i.e.*, the fraction of injected gas that has leaked) as a function $k^\star_{rw}$ and $p^E_c$. The amount of gas leaked is very sensitive to $k^\star_{rw}$. Decreasing $k^\star_{rw}$ by 1–2 orders of magnitude can initiate leakage, or substantially amplify it. Unfortunately, the connectivity and conductivity of the water films in the gas-saturated region is poorly understood, making the appropriate value of $k^\star_{rw}$ very poorly constrained. Blunt [2017] provides a scaling analysis for flow transmitted through thin films in a sandstone and demonstrates that the relative permeability can be as low as $k^\star_{rw} \sim 5 \times 10^{-9}$. The most likely scenario is that $k^\star_{rw} \ll 1$, which suggests that gas leakage is much more likely than estimates based on buoyant overpressure might imply.

## 3.5 Conclusions

In this study, an upscaled theoretical model was derived for gas injection into a system of layered aquifers and seals, in which vertical leakage of both water and gas across the intervening seals was permitted. The model extends the framework developed in Chapter 2 to include gas leakage subject to a capillary threshold. The model is computationally efficient by virtue of being vertically integrated, which is essential for exploring the large parameter space that governs fluid migration and pressure dissipation in these systems.

After developing the model, gas injection into a two-aquifer system was considered for simplicity. §3.3.1 began by studying the buildup of capillary pressure on the underside of the seal during gas injection, taking $p_c^E \to \infty$ such that no gas leakage occurs. In this limit, the model is identical to that presented in Chapter 2. Two end-member scenarios in the evolution of this capillary pressure were identified, depending on the connectivity and conductivity of residual water films in the gas region, as parameterised by the relative permeability $k_{rw}^\star$ to water in that region. If the gas region provides very little resistance to vertical water flow relative to the seal ($k_{rw}^\star \gg \Lambda_w^s h_n$), then the capillary pressure along the underside of the seal is simply the phase-static pressure difference taken upward from the gas–water interface (*i.e.*, the buoyant overpressure at the top of the gas region) [Woods and Farcas, 2009]. As a result, the spatial distribution of the capillary pressure mirrors the shape of the gas plume: It has a sharp maximum at the injection well that declines rapidly towards the thin tongue. If the gas region instead provides the principal resistance to vertical water flow relative to the seal ($k_{rw}^\star \ll \Lambda_w^s h_n$), then the water pressure at the base of the seal is effectively disconnected from the water pressure at the gas–water interface and the capillary pressure is instead related to the hydrostatic pressure measured downward through the seal from the aquifer above. This limit leads to capillary pressures that are much larger (by more than two orders of magnitude for the scenarios studied here) over a much wider region

in space. It was demonstrated that this latter limit, in particular, may enable $CO_2$ leakage across interbedded shales at Sleipner.

Having established the key role of $k^\star_{rw}$ in the buildup of capillary pressure, the importance of several key parameters on vertical gas leakage was subsequently studied. It was shown that, as described previously by Woods and Farcas [2009] in the context of a single-layer model, that the capillary entry pressure sets the horizontal length scale over which gas leakage occurs: Gas leakage starts earlier and occurs over a broader region as $p_c^E$ decreases. It was demonstrated that increasing the conductivity of the seals relative to the aquifers (increasing $\Lambda_w^s$) increases the rate and therefore the total amount of gas leakage, as does increasing the mobility of gas in the seals relative to water (increasing $\mathcal{M}_z^s$). For small $\Lambda_w^s$ and/or small $\mathcal{M}_z^s$, the global pressure field is dominated by the water and the total amount of gas leakage increases linearly with $\Lambda_w^s$ and $\mathcal{M}_z^s$. As these parameters grow larger, gas leakage plays an increasingly important role in the pressure field and begins to suppress further growth in the leakage rate. It was also shown that reducing $p_c^E$ increases the aspect ratio of the leaked gas plume (in aquifer 2), whereas increasing $\Lambda_w^s$ decreases this aspect ratio.

Results presented in this chapter highlight the fact that vertical pressure dissipation via water leakage establishes a global pressure field that then plays a central role in the complex interactions that control gas injection, migration, and leakage in layered aquifers, even when the seals have a very low permeability relative to the aquifers (note the range of $\Lambda_w^s$ values considered here). One consequence of these interactions is the unexpectedly important role of $k^\star_{rw}$ for pressure dissipation, plume shape, and capillary pressure, as discussed here and in Chapter 2; the value of this quantity is very poorly constrained, but likely to be small.

These results suggest that aquifers and other subsurface reservoirs should not be considered in isolation when any pressurisation is expected, even for reduced-order models and even when the fluids of interest are expected to remain contained (*e.g.*,

$CO_2$, oil, or gas). This idea is not a new one among hydrologists and hydrogeologists [*e.g.*, Hunt, 1985], but it would appear that its implications for CCS and hydrocarbon production have not been fully appreciated.

In the next chapter, the model developed above is used to study post-injection migration of $CO_2$.

# Chapter 4

# Post-injection depressurisation and fluid migration

## 4.1 Introduction

In Chapters 2 and 3, theoretical models were developed in order to explore the physics and parameters that govern pressure dissipation, fluid migration and leakage in layered aquifers during injection. During injection, the primary mechanism for trapping a migrating injected gas plume (e.g., $CO_2$) is hydrodynamic trapping—that is, the high capillary entry pressure and low permeability of the overlying cap-rock constrains the $CO_2$ to remain within the injection aquifer (see §1.1.2.1). After injection, the overpressure associated with injection decays over a timescale that is considerably longer than the associated injection timescale ($\tau_{\text{buoyancy}} \gg \tau_{\text{injection}}$), and fluid migration becomes exclusively buoyancy-driven.

During buoyancy-driven $CO_2$ migration, secondary trapping mechanisms act to immobilise the $CO_2$. Capillary forces acting at the pore scale trap ganglia of non-wetting $CO_2$ when displaced by the wetting phase (water) (see §1.1.2.2). $CO_2$ is also weakly soluble in water, and dissolves on timescales comparable to that of post-injection migration. The dissolved $CO_2$-water mixture is denser than the ambient water, leading to a gravitational instability that causes the $CO_2$-saturated

water to sink via 'convective dissolution' (see §1.1.2.3)—effectively removing buoyant $CO_2$ that could otherwise potentially leak upward into shallower aquifers. Chemical reactions also remove $CO_2$ by transferring carbon into the solid phase ('mineral trapping') (see §1.1.2.4). However the kinetics of these reactions are very slow and are typically thought to be negligible for post-injection $CO_2$ migration. Capillary trapping, convective dissolution and mineral trapping all act to increase the storage efficiency. This Chapter studies the effects of the end-of-injection state (i.e., the plume shape and global pressure field at $t = \tau_{\text{injection}}$) on post-injection migration. The results presented below show that post-injection gas migration is strongly coupled to the end-of-injection state before migration converges to late-time self-similar spreading.

Due to the long timescales associated with post-injection fluid migration, reduced-order models that permit self-similar/analytical solutions are very popular. Previous studies of post-injection migration have focused primarily on reduced-order modelling of gravity currents. Huppert and Woods [1995] studied the problem of an incompressible gravity-current spreading in an unconfined aquifer and demonstrated that at late-times the nose of the gravity-current spreads as $x_N \sim t^{1/3}$. This late-time behaviour is valid for purely buoyancy driven flow—i.e., when the pressure imprint from injection has dissipated—and when viscous resistance from the ambient phase can be neglected—i.e. when the gravity current is thin compared to the aquifer-thickness ($h \ll H$). [Hesse et al., 2007] studied a similar problem in a confined aquifer and explored early- and late-time self-similar behaviour. They demonstrated that at early-times, buoyancy leads to an initial phase of tilting that is strongly dependent on the mobility ratio ($\mathcal{M}$), and in which the nose position scales as $x_N \sim t^{1/2}$. For $CO_2$ ($\mathcal{M} \approx 20$) this tilting period is likely to last $\sim 1000$ years. Hesse et al. [2007] also recover the late-time scaling of Huppert and Woods [1995] and explore the transition between these two regimes.

The shape of the gas plume and global pressure field at the end of subsurface gas injection ultimately govern the fluid dynamics immediately after injection

is switched off. However, previous studies using reduced-order gravity current models typically neglect retaining the imprint from injection, and often initialise the gas distribution as a step-function. One notable exception is that of MacMinn and Juanes [2009], who demonstrated that the shape of the plume at the end of injection has a strong impact on spreading behaviour and capillary trapping. Although MacMinn and Juanes [2009] impose a tongued initial plume shape, they do not retain the pressure imprint from injection and instead assume that this overpressure dissipates sufficiently fast such that the pressure distribution can be approximated using vertical equilibrium.

In this chapter, it is shown that both aspects of the end-of-injection state [i.e., $p(x, t = 1)$ and $h(x, t = 1)$] are key controls on post-injection fluid migration. This is achieved in §4.2 through a trivial modification to the source term in the governing equations developed in Chapters 2 and 3. Coupling between post-injection migration with both aspects of the end-of-injection state are studied independently before being combined later. In §4.3 the controls on single-phase post-injection depressurisation are briefly studied—highlighting, in particular, the effect of vertical pressure dissipation. Section 4.4 focuses on incompressible gravity currents that are initialised from an instantaneous release of gas—with particular focus given to the effect of the initial plume shape. In §4.5, distinct regimes of post-injection migration are identified when the full end-of-injection state is retained. In §4.6 and §4.7, the controls on the termination of gas leakage are briefly studied, with a particular focus on the decay of capillary pressure. Finally, in §4.8 the implications of the results are discussed within the framework of $CO_2$ injection.

## 4.2 Governing equations

In Chapters 2 and 3, coupled PDEs are derived that describe pressurisation and migration of a binary system of compressible fluids of differing densities—namely water and gas (i.e., $CO_2$)—in a laterally extensive system of layered aquifers. The

relatively thick, high-permeability aquifers are separated by thin, low-permeability seals through which the connected wetting phase can leak—resulting in vertical pressure dissipation (see Chapter 2). Provided sufficient capillary pressure is built-up during injection, the non-wetting gas can also leak (see Chapter 3). In these PDEs, fluid injection is prescribed by the source term $\mathcal{I}_\alpha^n = \dot{M}_\alpha^n(t)\delta(x)/H$, where $\dot{M}_\alpha^n$ is the mass flow rate per unit length into the page of a phase $\alpha$ and $\delta(x)$ is the Dirac delta function; the latter ensures injection into the centre of the $n^{\text{th}}$ aquifer (i.e. at $x = 0$). In the post-injection phase, for times greater than the injection time ($t > \mathcal{T}$) injection is 'turned off' and no source term appears on the right hand side of the governing PDEs. For all times, the source term can be extended to include the post-injection phase as:

$$\mathcal{I}_\alpha^n(x,t) = \frac{\dot{M}_\alpha^n(t)}{H}\,\delta(x)\left[\mathcal{H}(t) - \mathcal{H}(t-\mathcal{T})\right], \tag{4.1}$$

where $\mathcal{H}$ is the unit Heaviside function. Using this modified source term to incorporate the post-injection phase does not in any way alter the model derived in Chapters 2 and 3. Therefore the governing PDEs are unchanged, and are written as:

$$\phi\left[(H - s_g h^n)(c_r + c_w)\frac{\partial p^n}{\partial t} - s_g\frac{\partial h^n}{\partial t}\right] - \frac{\partial}{\partial x}\left\{\lambda_w(H-h^n)\left[\frac{\partial p^n}{\partial x} - \rho_w g\frac{\partial h^n}{\partial x}\right] + \frac{1}{6}\frac{\partial}{\partial x}\left[(H-h^n)^2(q_{w,z}^{n,B} + 2q_{w,z}^{n,T})\right]\right\} = -(q_{w,z}^{n,T} - q_{w,z}^{n,B}) + \frac{\mathcal{I}_w^n(x,t)H}{\rho_w}, \tag{4.2}$$

and

$$\begin{aligned}
&\rho_g^n \phi s_g \left[ (c_r + \frac{\rho_g^0}{\rho_g^n} c_g) h^n \frac{\partial p^{n,I}}{\partial t} + \frac{\partial h^n}{\partial t} \right] \\
&\quad - \frac{\partial}{\partial x} \left[ \rho_g^n \lambda_g h^n \left( \frac{\partial p^{n,I}}{\partial x} - \left( \rho_g^n g + \frac{\rho_g^{s+1}}{\rho_g^n} \frac{q_{g,z}^{s+1}}{\lambda_g} \right) \frac{\partial h^n}{\partial x} - \frac{h^n}{2\lambda_g} \frac{\rho_g^{s+1}}{\rho_g^n} \frac{\partial q_{g,z}^{s+1}}{\partial x} \right) \right] \\
&\quad = - \left( \rho_g^{s+1} q_{g,z}^{s+1} - \rho_g^s q_{g,z}^s \right) + \mathcal{I}_g^n(x,t) H,
\end{aligned} \tag{4.3}$$

where $\mathcal{I}_w^n(x,t)$ and $\mathcal{I}_g^n(x,t)$ are the new, time-dependent source terms for water and gas, respectively. The vertical fluxes that couple the aquifers are independent of the source term, and are therefore unchanged from those presented in Chapters 2 and 3. The appropriate equations are reiterated below for completeness:

$$\begin{aligned}
&\left( \frac{H - h^n}{2\lambda_w} \right) q_{w,z}^{s+1} + \left( \frac{h^{n-1}}{\lambda_w^\star} + \frac{b}{\lambda_w^s} + \frac{H - h^n}{2\lambda_w} \right) q_{w,z}^s \\
&\qquad = - \left[ p^n - p^{n-1} + \rho_w^0 g (h^{n-1} + b + H - h^n) \right],
\end{aligned} \tag{4.4}$$

and

$$q_{g,z}^{s+1} = -\mathcal{R}(p_c^{n,T}) \lambda_g^{s+1} \left( \frac{p_w^{n+1,B} - p_g^{n,T}}{b} + \rho_g^{s+1} g \right). \tag{4.5}$$

Equations (4.2) and (4.3) are the governing PDEs for water and gas respectively. Equation (4.4) is a linear system of coupled vertical fluxes that can be inverted to yield vertical water fluxes across each intermediate seal, and Equation (4.5) is the vertical Darcy flux of gas across seal $s+1$,i.e., between aquifers $n$ and $n+1$.

Note that these PDEs have not been modified to incorporate secondary trapping mechanisms. These secondary trapping mechanisms are considered beyond the scope of this work; instead, this chapter focuses on the coupling between the

end-of-injection state with intermediate-time, post-injection migration. The incorporation of secondary trapping mechanisms within the framework of this model is briefly discussed in §5.3.1. Also note that in modifying the source term, no new parameters have been introduced. Therefore, previous non-dimensionalisation and the resulting dimensionless groups are still appropriate. Recall that the system is scaled with the characteristic quantities:

$$\mathcal{L} \equiv \frac{\dot{M}\mathcal{T}}{2\phi s_g \rho_g^0 H}\,, \quad \mathcal{P} \equiv \frac{\phi \mathcal{L}^2}{\lambda_w \mathcal{T}} = \frac{\dot{M}\mathcal{L}}{2\lambda_w s_g \rho_g^0 H}\,, \quad \text{and} \quad \mathcal{Q}_z \equiv \frac{\lambda_w^s \mathcal{P}}{b}, \tag{4.6}$$

which arise from considering a rectangular plug of gas injected into a single aquifer. For fluid-displacement with a vertical front (i.e., $s_g\mathcal{M} = 1$ and $R_d = 1$), the plug will be of unit width ($w = 1$). The characteristic time ($\mathcal{T}$) used in Equation (4.6) is the injection time, which is typically tens of years. In Chapters 2 and 3 an injection time of $\mathcal{T} = 10$ years was used. It may seem inappropriate to retain characteristic scales based on injection in the post-injection period. Whilst it is possible to choose characteristic scales motivated by purely buoyancy-driven post-injection migration, it would not change the results presented below beyond rescaling them. This is because no further simplifications based on these scalings are made. The above scales are used in combination with the existing dimensionless quantities:

$$\begin{gathered} \tilde{x} \equiv \frac{x}{\mathcal{L}}, \quad \tilde{t} \equiv \frac{t}{\mathcal{T}}, \quad \tilde{h} \equiv \frac{h}{H}, \quad \tilde{p} \equiv \frac{p}{\mathcal{P}}, \quad \tilde{q} \equiv \frac{q}{\mathcal{Q}_z}, \\ \tilde{b} \equiv \frac{b}{H}, \quad \tilde{\rho}_\alpha \equiv \frac{\rho_\alpha}{\rho_g^0}, \end{gathered} \tag{4.7}$$

and the new dimensionless source term that incorporates a period of post-injection for times greater than the scaled injection time ($\tilde{t} = 1$):

$$\tilde{\mathcal{I}}_\alpha^n \equiv \frac{2\mathcal{L}H\,\mathcal{I}_\alpha^n}{\dot{M}}\left[\mathcal{H}(t) - \mathcal{H}(t-\mathcal{T})\right]. \tag{4.8}$$

As no new parameters have been introduced, additional/different dimensionless groups are not needed. The existing dimensionless groups are listed below for completeness[1]:

$$N_{cw} \equiv c_w \mathcal{P} \tag{4.9a}$$

$$R_{cw} \equiv c_r / c_w \tag{4.9b}$$

$$R_{cf} \equiv c_g / c_w \tag{4.9c}$$

$$R_A \equiv \mathcal{L} / H \tag{4.9d}$$

$$R_d \equiv \rho_g^0 / \rho_w^0 \tag{4.9e}$$

$$N_g \equiv \rho_w^0 g H / \mathcal{P} \tag{4.9f}$$

$$\mathcal{M} \equiv \lambda_g / (s_g \lambda_w) \tag{4.9g}$$

$$\Lambda_w^s \equiv \lambda_w^s H / (\lambda_w b) \tag{4.9h}$$

$$\mathcal{M}_z^s \equiv \lambda_g^s / \lambda_w^s. \tag{4.9i}$$

Dropping the tildes, the dimensionless system of governing equations can be written as:

$$N_{cw}(R_{cw}+1)(1-s_g h^n)\frac{\partial p^n}{\partial t} - s_g \frac{\partial h^n}{\partial t} - \frac{\partial}{\partial x}\left\{(1-h^n)\left[\frac{\partial p^n}{\partial x} - N_g \frac{\partial h^n}{\partial x}\right] + \frac{\Lambda_w^s}{6}\frac{\partial}{\partial x}\left[(1-h^n)^2(q_{w,z}^s + 2q_{w,z}^{s+1})\right]\right\} = -{R_A}^2 \Lambda_w^s (q_{w,z}^{s+1} - q_{w,z}^s) + s_g R_d \mathcal{I}_w^n \tag{4.10}$$

and

[1]To avoid undue repetition, readers are pointed to §2.2.4 and §3.2.4 for a detailed physical description of these dimensionless groups.

$$
\begin{aligned}
&N_{cw}(R_{cw}\rho_g^n + R_{cf})h^n \frac{\partial p^n}{\partial t} + \rho_g^n \frac{\partial h^n}{\partial t} \\
&- \mathcal{M}\frac{\partial}{\partial x}\left[\rho_g^n h^n \left(\frac{\partial p^n}{\partial x} - \left(\rho_g^n R_d N_g + \frac{\rho_g^{s+1}}{\rho_g^n}\frac{\Lambda_w^s}{s_g\mathcal{M}}q_{g,z}^{s+1}\right)\frac{\partial h^n}{\partial x} - \frac{\rho_g^{s+1}}{\rho_g^n}\frac{\Lambda_w^s}{2s_g\mathcal{M}}h^n\frac{\partial q_{g,z}^{s+1}}{\partial x}\right)\right] \\
&= -\frac{R_A^2\Lambda_w^s}{s_g}\left(\rho_g^{s+1}q_{g,z}^{s+1} - \rho_g^s q_{g,z}^s\right) + \mathcal{I}_g^n,
\end{aligned}
\tag{4.11}
$$

with

$$
\begin{aligned}
\frac{\Lambda_w^s}{2}(1-h^n)q_{w,z}^{s+1} + \left[\frac{\Lambda_w^s}{k_{rw}^\star}h^{n-1} + 1 + \frac{\Lambda_w^s}{2}(1-h^n)\right]q_{w,z}^s \\
= -\left[p^n - p^{n-1} + N_g(h^{n-1} + b + 1 - h^n)\right],
\end{aligned}
\tag{4.12}
$$

and

$$
q_{g,z}^{s+1} = -\mathcal{R}\mathcal{M}_z^s\left(p_w^{n+1,B} - p_g^{n,T} + \rho_g^n R_d N_g b\right). \tag{4.13}
$$

As in Chapters 2 and 3, for a system with $N_z$ aquifers, Equations (4.10) and (4.11) provide $2N_z$ coupled PDEs enforcing conservation of mass for gas and for water, respectively, in each aquifer $n = 1 \dots N_z$. Equation (4.12) is a linear system of $N_z - 1$ algebraic equations in the dimensionless vertical fluxes of water across each interior seal, $q_{w,z}^s$ for $s = 2 \dots N_z$, where $q_{w,z}^1 = q_{w,z}^{N_z+1} = 0$ is also imposed. Lastly, Equation (4.12) is used to calculate the dimensionless vertical gas flux across seal $s + 1$.

With the exception of §4.4—which studies the spreading of an unpressurised instantaneous release of gas—simulations presented here evolve using initial and boundary conditions that are identical to those used in Chapters 2 and 3: That is,

the layered aquifer system is initially water saturated, $h^n(x, t = 0) = 0$, and gas is not permitted to reach the lateral boundaries. This motivates the initial condition and boundary conditions that pressure is initially hydrostatic, and lateral boundaries remain hydrostatic:

$$p^n(x, t = 0) = p^n(-L_x/2, t) = p^n(L_x/2, t) = p^0 - N_g[n + (n - 1)b], \qquad (4.14)$$

recalling that the pressures $p^n$ are the pressures at the gas–water interface in each aquifer, which is the top of the aquifer in the absence of gas, and that $p^0$ is the initial pressure at the bottom of aquifer 1.

For times $t \leq 1$, the system evolves as described in Chapters 2 and 3; after which ($t > 1$) the injection source term is removed and the system is free to evolve until an arbitrary end time (typically $t = 10^4$).

Results presented below use the same reference case as used in Chapter 3: That is, this chapter considers a minimal system in which fluid injection into the bottom-most aquifer ($n = 1$), of a two aquifer ($N_z = 2$) system. Rock properties consistent with sandstone aquifers and mudstone seals are chosen in combination with fluid properties that are consistent with water and $CO_2$ at a reference depth of $\sim$1 km, located at the bottom of aquifer 1 ($z = 0$). The reference case considered involves injection of $\sim$2 MT per year, distributed along a 30 km array for a period of 10 years. From this scenario reference parameters are chosen, from which corresponding dimensionless quantities are calculated. Both dimensional and dimensionless quantities are listed in Table 3.1. Within the framework of this reference problem, several post-injection scenarios are considered: (i) water injection with and without permeable seals; (ii) migration of an instantaneous, fixed-volume release of gas; (iii) post-injection migration from the end-of-injection state; (iv) capillary pressure decay; (v) termination of post-injection gas leakage. In all scenarios—as in previous chapters—the governing system of equations are solved numerically by discretising in space using a standard finite volume scheme and integrated in time

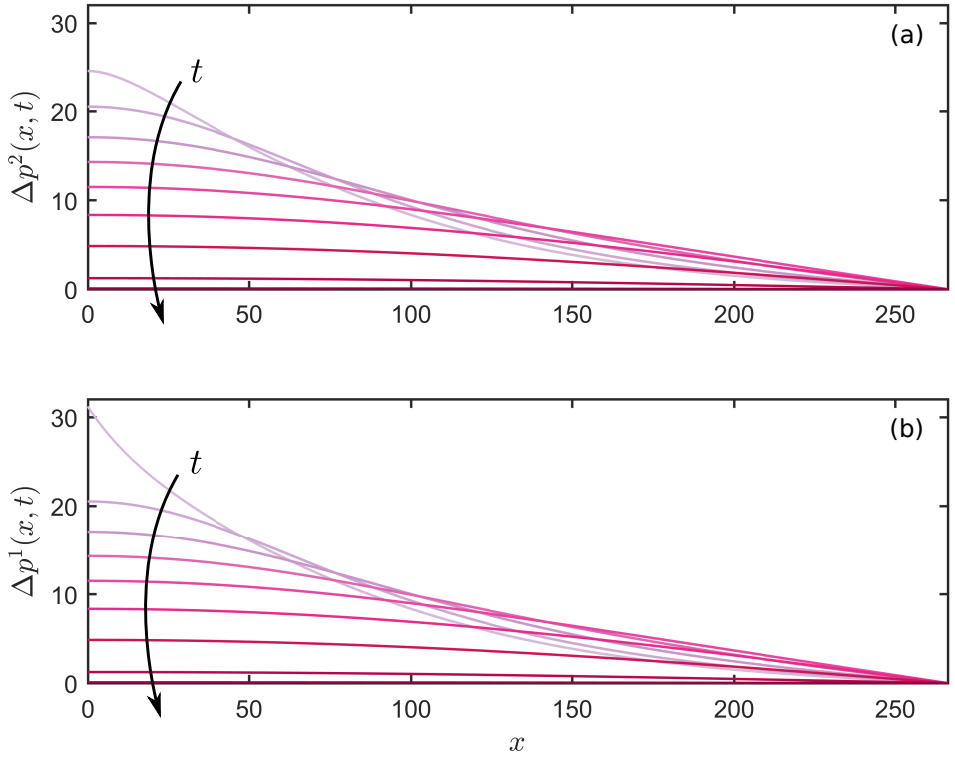


**Figure 4.1:** Pressure perturbation in space, at times $t = [1.0,\ 1.1,\ 1.3,\ 1.5,\ 2.0,\ 3.0,\ 5.0,$ and $19.7]$ in (a) the top aquifer $(n = 2)$ and (b) the injection aquifer $(n = 1)$.

using `MATLAB's` implicit solver for stiff ODEs, `ODE15s` [see Appendices B and C, and Shampine and Reichelt, 1997].

## 4.3 Water injection and depressurisation

Fluid injection into layered aquifers is discussed extensively in Chapters 2 and 3. This chapter considers the 'end of injection' as an initial condition for the post-injection phase. During both water injection and gas injection into layered aquifers, the degree of pressurisation at the end of injection is dependent on the leakage number $(\Lambda_w^s)$. For water injection with $\Lambda_w^s = 0$, the governing equations collapse into a single PDE describing the evolution of pressure in the injection

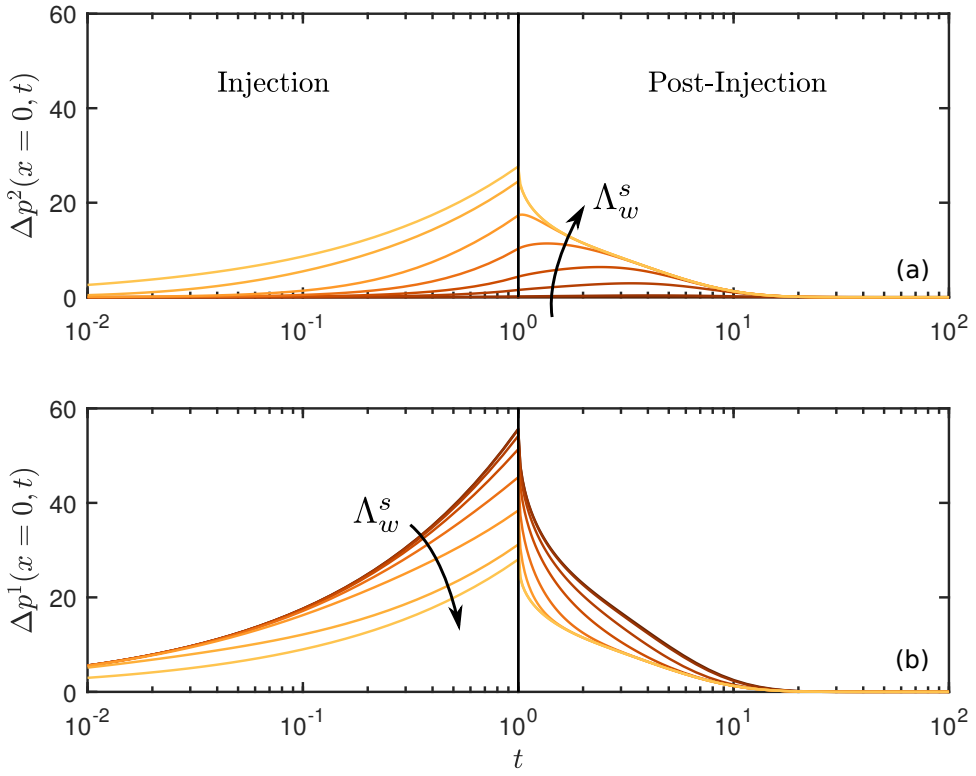


**Figure 4.2:** Pressure perturbation at $x = 0$ as a function of time in: (a) the injection aquifer, and (b) the above aquifer, both plotted for leakage numbers $\log_{10}(\Lambda_w^s) = [-10, \ -8.5, \ -7.5, \ -7, \ -6.5, \ -6, \ -5$ and $-2.5]$.

aquifer (see §2.3.1)—for which analytical solutions are determined. For scenarios with increasingly large leakage numbers, the degree of pressurisation in the injection aquifer decreases. Correspondingly, increasing the strength of vertical pressure dissipation increases pressuriation in the 'non-injection' aquifers.

When injection ends ($t = 1$), the source term associated with fluid injection switches off and the injection aquifer begins to depressurise. The overpressure in the injection aquifer drives flow away from the injection well, both horizontally and vertically. The ratio between vertical and lateral flow is controlled by $Q_s/Q_l = \lambda_w^s \mathcal{L}^2/(\lambda_w H b) = R_A^2 \Lambda_w^s$ (see Chapter 2), demonstrating that for a domain with a fixed aspect ratio, $\Lambda_w^s$ is the dominant control on the interplay between horizontal and vertical pressure dissipation. After injection has stopped, this pressure dissipation acts to decrease the pressure in the injection aquifer with time (Figures 4.1 and 4.2).

For $\Lambda_w^s = 0$, no vertical pressure dissipation occurs and therefore pressure perturbations related to injection and post-injection are exclusively confined to the injection aquifer. The lack of cross-stratal fluid migration results in maximum pressure build-up during injection, relative to scenarios with permeable seals ($\Lambda_w^s > 0$). During post-injection, the residual overpressure from injection drives a decaying fluid flux away from the injection site until the pressure returns to hydrostatic. For $\Lambda_w^s = 0$, this dissipative flux is purely horizontal and the pressure in the injection aquifer decays monotonically over a timescale of ∼10 injection times (Figure 4.2).

For high leakage numbers ($\Lambda_w^s \sim 1/R_A^2$ and larger), strong vertical pressure dissipation equilibrates the vertical pressure distribution between the aquifers. As such, the entire system acts like a single aquifer of dimensional thickness $\sim N_z H$ ($\sim 2H$ for reference parameters used in this section). Strong vertical pressure dissipation results in a minimum pressure in the injection aquifer ($n = 1$) and a maximum pressure in the non-injection aquifer ($n = 2$). During post-injection, the aquifers remain equilibrated in the vertical pressure distribution and the pressure in both aquifers decays monotonically with time at $x = 0$ (Figure 4.2).

For intermediate leakage numbers ($0 < \Lambda_w^s < 1/R_A^2$), the interplay between vertical and horizontal pressure dissipation is less straightforward. The strength of vertical pressure dissipation sets the pressure at the end of injection, with increasingly large $\Lambda_w^s$ monotonically reducing the pressure in the injection aquifer ($n = 1$) and increasing the pressure in all other aquifers ($n = 2$). As in other cases during post-injection, pressure is dissipated out of the injection aquifer, and the pressure at the injection well decreases monotonically with time. However, for intermediate leakage numbers, the pressure in aquifer 1 continues to drive an upwards water flux. This leads to a period of pressure increase, before the pressure collapses onto the late-time pressure curve defined by the strong-leakage limit (see Figure 4.2). Due to a greater perturbation from this late-time strong-leakage limit, the maximum pressure in aquifer 2 occurs at progressively later times for smaller leakage numbers.

## 4.4 Gravity currents from an instantaneous release of gas

Before studying the effects of depressurisation on the post-injection migration of gas, this section first considers purely buoyancy-driven fluid migration without depressurisation. This allows for the impact of the initial plume shape on post-injection gas migration to be studied independently of depressurisation. To avoid pressurising the aquifer during injection, the somewhat artificial but well-studied scenario of an instantaneous release of gas is considered [e.g., Huppert and Woods, 1995, Barenblatt, 1996, Hesse et al., 2007]. In this section the injection stage is neglected. At $t = 0$ the pressure throughout the system is initially hydrostatic (4.14), and a rectangular volume of gas is *instantaneously released* in aquifer 1:

$$h(x, t = 0) = \begin{cases} 1, & -\mathcal{W}_0 < x < \mathcal{W}_0 \\ 0, & \text{otherwise,} \end{cases} \tag{4.15}$$

where $\mathcal{W}_0$ is the initial plume half-width as measured from the initial well at $x = 0$. To explore the interactions between vertical water leakage and gravity-driven post-injection flow in a simplified system without depressurisation, several simulations are performed for differing values of $\Lambda_w^s$ and $k_{r,w}^\star$. As throughout Chapter 3, the simulations in this section use parameters listed in Table 3.1 except where explicitly indicated.

### 4.4.1 Single-aquifer gravity current evolution ($\Lambda_w^s = 0$)

For $\Lambda_w^s = 0$, Equations (4.10) and (4.11) reduce to two coupled PDEs that describe a compressible gravity current in a single porous aquifer. Assuming that pressure variations are nearly hydrostatic—and therefore of the order $\Delta p \sim (1 - Rd)N_g$—gas density variations in this system are of the order $\Delta\rho_g \sim N_{cw}R_{cf}(1 - Rd)N_g$.

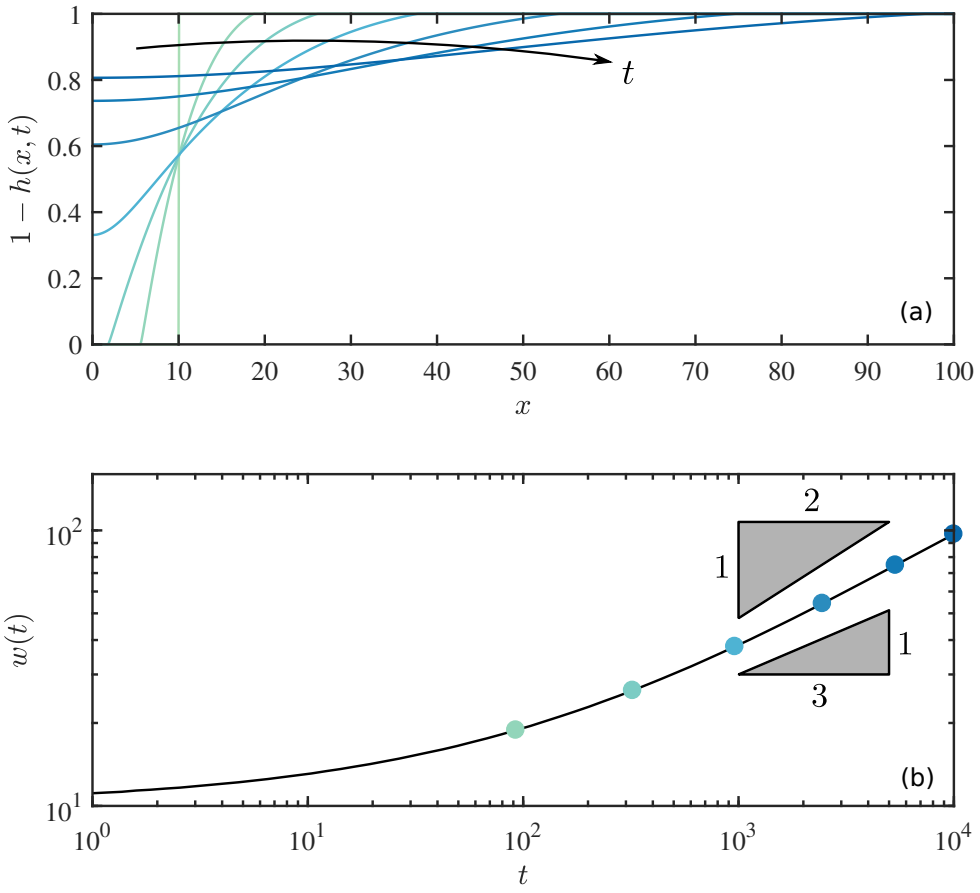


**Figure 4.3:** Evolution of a gravity current in a porous aquifer that spreads from an initial step with $\mathcal{W}_0 \approx 10$. The $CO_2$-water interface is plotted for dimensionless times $t = [0,\ 92,\ 322,\ 962,\ 2454,\ 5356$ and $10000]$ in (a). The width evolution with time is also plotted in (b), with coloured dots corresponding to times plotted in (a).

Taking typical values from Table 3.1 yields $\Delta\rho_g \sim 10^{-4} \ll \rho_g^0 \equiv 1$; meaning that compressibility effects are unimportant. Therefore, previous studies considering similar systems typically neglect terms related to compressibility, and instead solve a single PDE for an incompressible gravity current [e.g., Huppert and Woods, 1995, Hesse et al., 2007].

Here and throughout this thesis, the full compressible model is solved, even when terms related to compressibility are unimportant. Taking $N_{cw} = 0$ and $\Lambda_w^s = 0$, Equations (4.10) and (4.11) can be combined by eliminating the horizontal pressure gradient, leading to a single PDE that describes the evolution of the gas–water

interface:

$$\frac{\partial h}{\partial t} = (1 - R_d) N_g \mathcal{M} \frac{\partial}{\partial x} \left[ (1 - f)\, h \frac{\partial h}{\partial x} \right], \tag{4.16}$$

where

$$f = \frac{s_g \mathcal{M} h}{(s_g \mathcal{M} - 1)h + 1}. \tag{4.17}$$

Equation (4.16) is a non-linear diffusion equation that describes incompressible flow in a porous aquifer [e.g., MacMinn and Juanes, 2009].

For an incompressible gravity current in a single porous aquifer, the pressure distribution is approximately phase-static; meaning that water flow is short-range and mostly confined within the lateral extent of the migrating gas plume. For $t > 0$, the gas collapses and spreads in a long and thin plume against the base of seal 1, which is impermeable for $\Lambda_w^s = 0$. In the region where the gas plume is collapsing (i.e., $\partial h/\partial t < 0$), water displaces the collapsing plume. Conversely, the spreading gas plume must displace water in the region where $\partial h/\partial t > 0$. The strength of this viscous coupling, relative to buoyancy, ultimately governs spreading dynamics. At early times, before the interface detaches (i.e., when $h < H$ everywhere), the plume undergoes a phase of tilting. During initial tilting, the width of an unconfined incompressible gravity current in a single aquifer grows as $w \sim t^{1/2}$ and is strongly dependent on the viscosity ratio of the two fluids [Hesse et al., 2007]. At late times, the plume eventually becomes sufficiently thin that spreading becomes independent of the viscosity of ambient phase; the width subsequently grows as $w \sim t^{1/3}$. Figure 4.3(b) shows that the intermediate-time width evolution for this single-aquifer system (i.e., after the plume has detached) lies between the early- and late-time self-similar scalings described by Hesse et al. [2007], Huppert and Woods [1995] ($t^{1/3} < w < t^{1/2}$); highlighting the long timescales associated with

the post-injection phase—i.e. after $\sim 10^5$ years of post injection, the single-aquifer reference system has not reached late-time self-similarity.

### 4.4.2 Two-aquifer gravity current evolution $(0 < \Lambda_w^s < 1/R_A^2)$

In the previous section, an instantaneous release of gas was studied in the single-aquifer limit ($\Lambda_w^s = 0$) of a two aquifer system. In Chapter 2, the coupling between horizontal gas migration and vertical pressure dissipation during injection was studied extensively, demonstrating that weak vertical water flow across intermediate seals is strongly coupled to the migration of an injected plume—with vertical pressure dissipation resulting in lateral compaction of the plume. This Section briefly addresses the impact of pressure dissipation on the migration of an instantaneous release of gas.

As in §4.4.1, a reference system composed of two aquifers separated by a thin low permeable seal ($\Lambda_w^s \neq 0$) is used. For now, it is assumed that the entry pressure of the seal is sufficiently high ($p_c^E \sim \infty$) that gas leakage never occurs, allowing for an exclusive study of the coupling between vertical water leakage and post-injection gas migration. To enable direct comparison with the no-leakage limit ($\Lambda_w^s = 0$), this section uses the same initial condition as in §4.4.1. A step-function of gas [Equation (4.15)] is instantaneously released in aquifer 1 at $t = 0$, with an initial pressure distribution that is phase static: $p(x, t = 0) = p^0 - N_g + R_d N_g h(x, t = 0)$. Once again, the full system of compressible, dimensionless governing equations are solved over the interval $0 < t \leq 10^4$ for differing values of $k_{rw}^\star$ and $\Lambda_w^s$—the key variables that modulate vertical water through the gas saturated region and seals respectively. This chapter focuses on the early to intermediate post-injection period. This is achieved using a dimensionless end time of $t = 10^4$, which covers this period and the early-transition towards late-time self-similarity.

The strength of vertical water leakage is set by the magnitude of $R_A^2 \Lambda_w^s$ in the presence of a non-hydrostatic vertical pressure gradient and, for now, neglecting

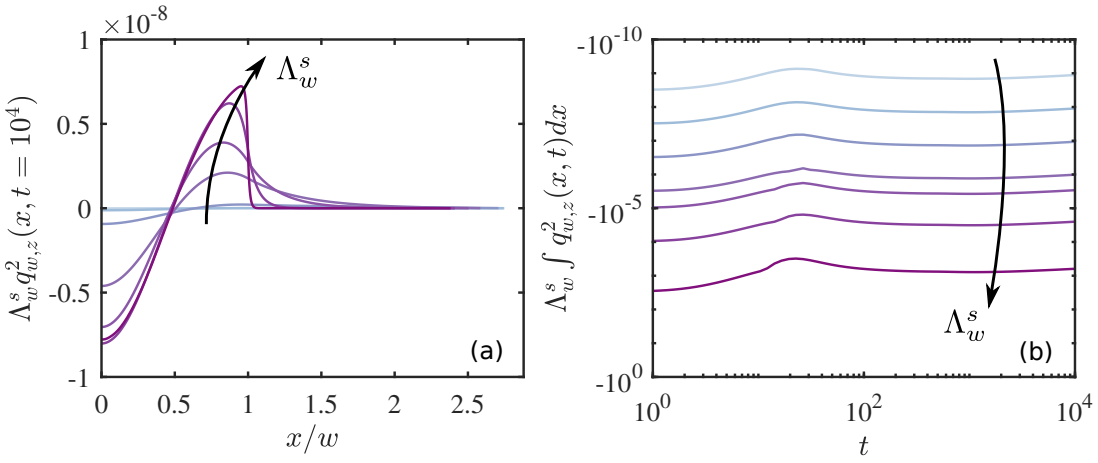


**Figure 4.4:** (a) Vertical water flux across the intermediary seal ($s = 2$) at $t = 10^4$ plotted against horizontal distance normalised by plume width, for leakage numbers $\log_{10}(\Lambda_w^s) = [-9, -8, -7, -6, -5.5, -4.5 \text{ and } -3]$. (b) Net vertical water flow across seal $s = 2$ plotted against time for the same values of $\Lambda_w^s$.

resistance to vertical water flow through thin films in the gas (i.e. $k_{rw}^\star = 1$). In these simulations, the aspect ratio ($R_A$) is fixed and the strength of pressure dissipation is varied through the leakage number $\Lambda_w^s$. In the 'no-leakage' limit ($\Lambda_w^s = 0$), no pressure dissipation occurs and the behavior is as described in §4.4.1. In the limit where the gas provides no resistance to vertical water flow ($k_{rw}^\star = 1$), increasing $\Lambda_w^s$ results in progressively stronger net downwards leakage (Figure 4.4b). The downwards direction of net flow is a direct consequence of the underpressure in the bottom-most aquifer associated with the presence of a less dense fluid that is approximately in phase-static equilibrium. By conservation of mass, water must flow in and replace the collapsing gas, and conversely water must be displaced by the growing gas front. When $\Lambda_w^s = 0$ (§4.4.1), this occurs in a classical lateral lock-exchange flow as described [e.g., Huppert and Woods, 1995, Hesse et al., 2007]. The addition of permeable intermediary seals allows for the development of a vertical component to this lock-exchange-type flow, whose strength increases with $\Lambda_w^s$. Although the migrating gas plume drives a net downwards flow of water, the direction and magnitude of water flow varies laterally. Figure 4.4(a) shows that at $t = 10^4$ (for $k_{rw}^\star = 1$) the majority of vertical water flow is confined within the lateral limits of the gas plume. In particular, most of the water that is displaced vertically must flow through the gas, suggesting that $k_{rw}^\star$ is of leading-order

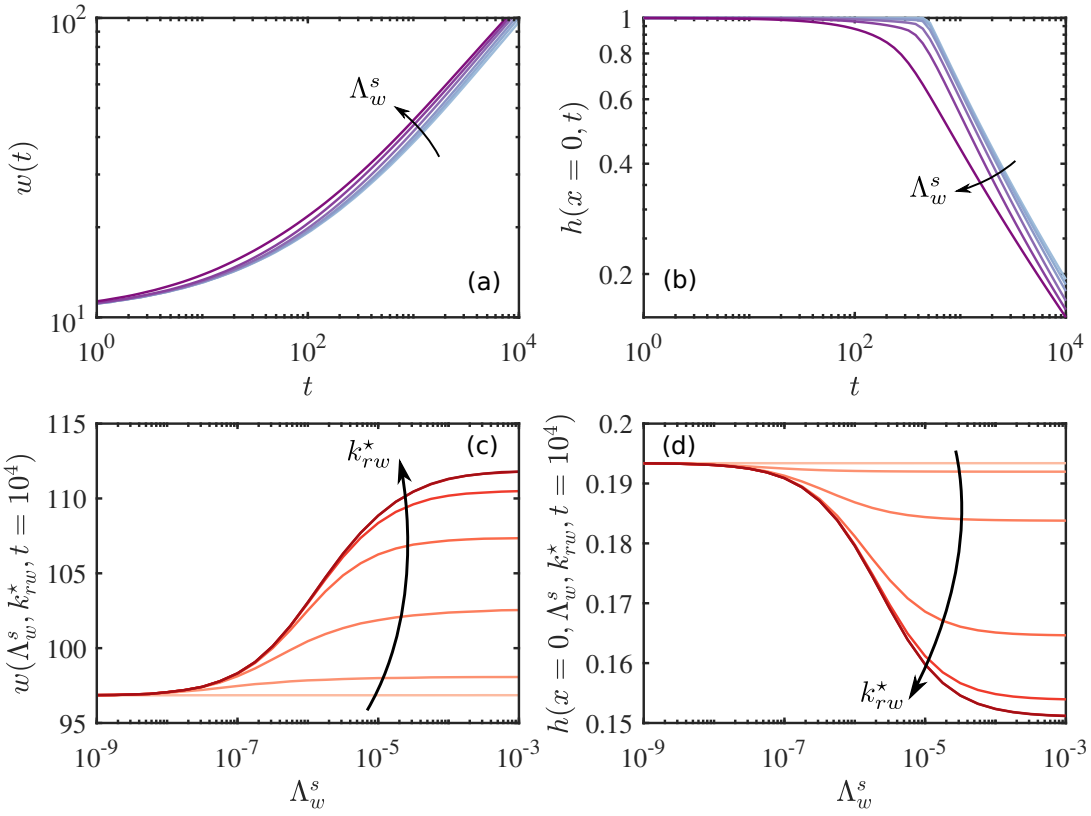


**Figure 4.5:** Evolution of a gravity current coupled to vertical pressure dissipation. (a) Plume width and (b) maximum plume height (at $x = 0$), both as a function of time and leakage number, with $\log_{10}(\Lambda_w^s) = [-9,\ -6.5,\ -6,\ -5.5,\ -5$ and $-4]$. (c) Plume width and (d) maximum plume height, both as functions of leakage number and relative permeability, with $\log_{10}(k_{rw}^\star) = [-10,\ -8,\ -7,\ -6,\ -5,\ -3$ and $0]$ and plotted at $t = 10^4$.

importance (see below). The flow is downward around the centre of the plume, decreasing in magnitude before becoming positive toward the nose. More specifically, a downwards water flow through seal $s = 2$ occurs directly above the region in which the gas plume is collapsing ($\partial h/\partial t < 0$). Similarly, upward water flow through the intermediate seal occurs above the region of the gas plume that is growing in thickness ($\partial h/\partial t > 0$).

The impact of pressure dissipation on the width of an instantaneous volume-release gravity current is opposite to its impact during injection, in that it widens rather than compacts the plume (Figure 4.5). Correspondingly, increased vertical water flow results in a plume that collapses faster relative to the no-leakage limit (Figure 4.5b). These results can readily be explained by the viscous coupling between the

two fluid phases. As the gas propagates horizontally, an exchange flow develops as a consequence of mass-conservation. Increasing $\Lambda_w^s$ results in stronger vertical water flow, reducing the strength of the lateral exchange flow. This effectively reduces the lateral viscous resistance provided by the water, making horizontal gas migration 'easier'. Vertical water leakage therefore only has a strong impact on gravity-current propagation when the motion of the water plays a role. At progressively later times, the plume becomes sufficiently thin that viscous resistance from the water becomes negligible, resulting in a transition towards late-time self-similarity [Huppert and Woods, 1995] where the width grows as $w \sim t^{1/3}$. Consequently, vertical water flow has a progressively weaker impact on gas migration at later times.

So far, results concerning the impact of vertical water flow on fluid migration following an instantaneous release of gas have neglected the resistance to vertical water flow through the gas plume, within which water remains connected through thin wetting films (i.e., assuming $k_{rw}^\star = 1$). Figure 4.4(a) shows that vertical water flow during gas migration is largely confined within the lateral extent of the plume (i.e., for $x/w < 1$). This is due to the approximately phase-static pressure distribution that drives the propagation of the gravity current. As the gas plume becomes vanishingly thin ($h \to 0$) the pressure distribution becomes hydrostatic. The resistance to vertical water flow through the gas region means that the relative permeability of water flowing through the gas region ($k_{rw}^\star$) has a dominant control on the magnitude of vertical water leakage. Decreasing $k_{rw}^\star$ decreases the strength of water leakage and subsequently suppresses the impact of the leakage number on plume width and height. For $k_{rw}^\star \sim 0$, effectively no vertical water flow occurs and the evolution of the plume becomes invariant to vertical water leakage, i.e., insensitive to $\Lambda_w^s$ (Figure 4.5c-d). In reality, $k_{rw}^\star$ is very poorly constrained. However, it is likely to be very small for industrial applications such as CCS. As such, these results suggest vertical water leakage is likely to have a very small (or negligible) impact on purely buoyancy-driven post-injection fluid

migration in layered aquifers.

### 4.4.3 Effect of initial plume shape

Realistic subsurface engineering operations do not lead to the instantaneous release of a fixed volume of gas. In this section the impact of initial plume shape on gas migration is considered. During fluid injection, the tongued plume shape arises from the nonlinear relationship between the plume thickness and the pressure-driven fluid velocity [Pegler et al., 2014a]; causing the fluid velocity of the less viscous phase to increase as its thickness decreases. This forms a highly-mobile thin tongue which acts to minimise viscous dissipation by minimising the velocity of the displaced, viscous brine. The formation of this tongued plume shape is closely related to the Saffman-Taylor instability [Saffman and Taylor, 1958, Pegler et al., 2014a]; with an injected gas plume acting as a single viscous finger under the influence of buoyancy. Dimensional expressions for the plume evolution during injection demonstrate that the shape is invariant to permeability, and is instead exclusively governed by the mobility ratio ($\mathcal{M}$) and geometric factors [Nordbotten and Celia, 2006b, MacMinn and Juanes, 2009]. A higher mobility ratio, increases the relative velocity of the mobile phase: Producing a plume shape with a longer and more pronounced tongue with a shallower gradient at the nose.

Although the controls on plume shape during gas injection into a single porous aquifer are well known, most fluid dynamical studies of post-injection have used a simplified initial condition, making the assumption that the late-time self-similar behaviour is—by definition—insensitive to the initial condition [Barenblatt, 1996]. One notable exception is the work of MacMinn and Juanes [2009] who studied the effects plume shape on capillary trapping by comparing numerical simulations of incompressible post-injection migration from both step-function and tongued initial conditions. In this study, [MacMinn and Juanes, 2009] showed that the late-time shape and evolution of the plume is invariant to the initial shape when

residual/capillary trapping is neglecting. However when residual trapping is included, the shape of the plume should not be neglected.

This section explores the effects of the initial plume shape on the migration of an instantaneous release of gas into a single, confined aquifer. Three different initial shapes are considered:

$$\text{Linear: } 1 - |x|/2, \qquad \text{for } 0 \leq |x| \leq 2, \tag{4.18a}$$

$$\text{Parabolic: } h(x, t = 0) = (x^2 - w_0^2)/w_0^2, \qquad \text{for } |x| \leq w_0 \tag{4.18b}$$

$$\text{Exponential: } h(x, t = 0) = e^{-|x|}, \tag{4.18c}$$

where $w_0 = 3/2$ is the initial width for the parabolic initial condition. The initial plume shapes defined by Equations 4.18a-c are plotted in Figure 4.6. Note that these these initial conditions have the same volume, such that Equations 4.18a-c satisfy:

$$\int_{-\infty}^{\infty} h(x, t = 0)\, dx \approx \int_{-\infty}^{\infty} \rho_g(x, t = 0) h(x, t = 0)\, dx \equiv 2. \tag{4.19}$$

As in §4.4.1-4.4.2 the pressure distribution is initially phase-static: $p(x, t = 0) = p^0 - N_g + R_d N_g h(x, t = 0)$, where $h(x, t = 0)$ are the initial plumes shapes defined by Equations 4.18a-c. The full system of dimensionless governing equations are subsequently solved in the single-aquifer limit ($\Lambda_w^s = 0$) until $t = 10^4$. All other parameters are held at their reference values.

Simulations initialised with a linear or parabolic initial condition evolve in a way that is qualitatively similar to the collapsing step-function (see §4.4.1). The thickest region—centered about $x = 0$—slumps, driving horizontal gas flow in a characteristic lock-exchange flow. The initial geometry of these plumes precludes them from developing a lock-exchange flow during the back-propagation phase, for which

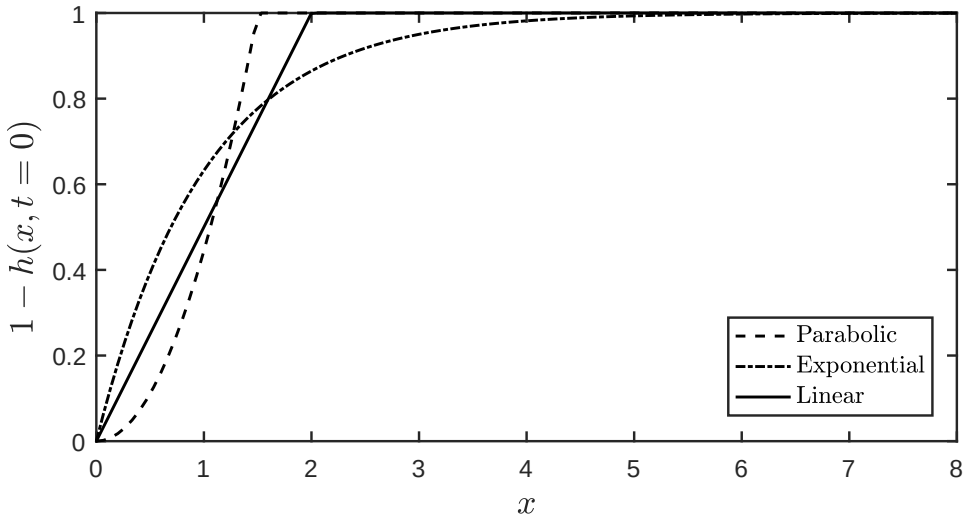


**Figure 4.6:** Initial plume shapes [as defined by Equations (4.18a)-c] used for testing the impact of plume shape on migration of an instantaneous release of gas.

$w \sim t^{1/2}$ is observed [Hesse et al., 2007]. Instead, these plumes collapse into long and thin gravity currents, with the width and maximum height monotonically increasing and decreasing with time, respectively (Figures 4.7a-b and 4.8). At $10^4$ years, the width has not become sufficiently thin for the ambient viscosity to be neglegible and the late-time $w \sim t^{1/3}$ scaling has yet to be reached. However, the width-vs-time curves for the linear and parabolic initial shapes converge for $t \gg 10^2$, suggesting that the dynamics are approaching self-similarity.

The simulation evolved from the exponential initial condition deviates significantly from previously described behaviour for $t \lesssim 10^2$. As with all instantaneously released plumes, the thickest region of the plume collapses (Figure 4.7). However this does not drive horizontal flow at the nose of the plume. Instead, the intermediate portion of the plume thickens while the nose remains fixed—giving the appearance that horizontal motion of the plume has stalled. Figure 4.8 shows that for $t < 200$ the width of the plume remains approximately constant. Once horizontal gas flow, driven by the collapsing plume, reaches the nose, the interfacial gradient increases and the nose begins to propagate horizontally. The width suddenly begins to grow, rapidly converging onto the intermediate-time evolution curves for the linear and parabolic initial conditions as all three curves transition

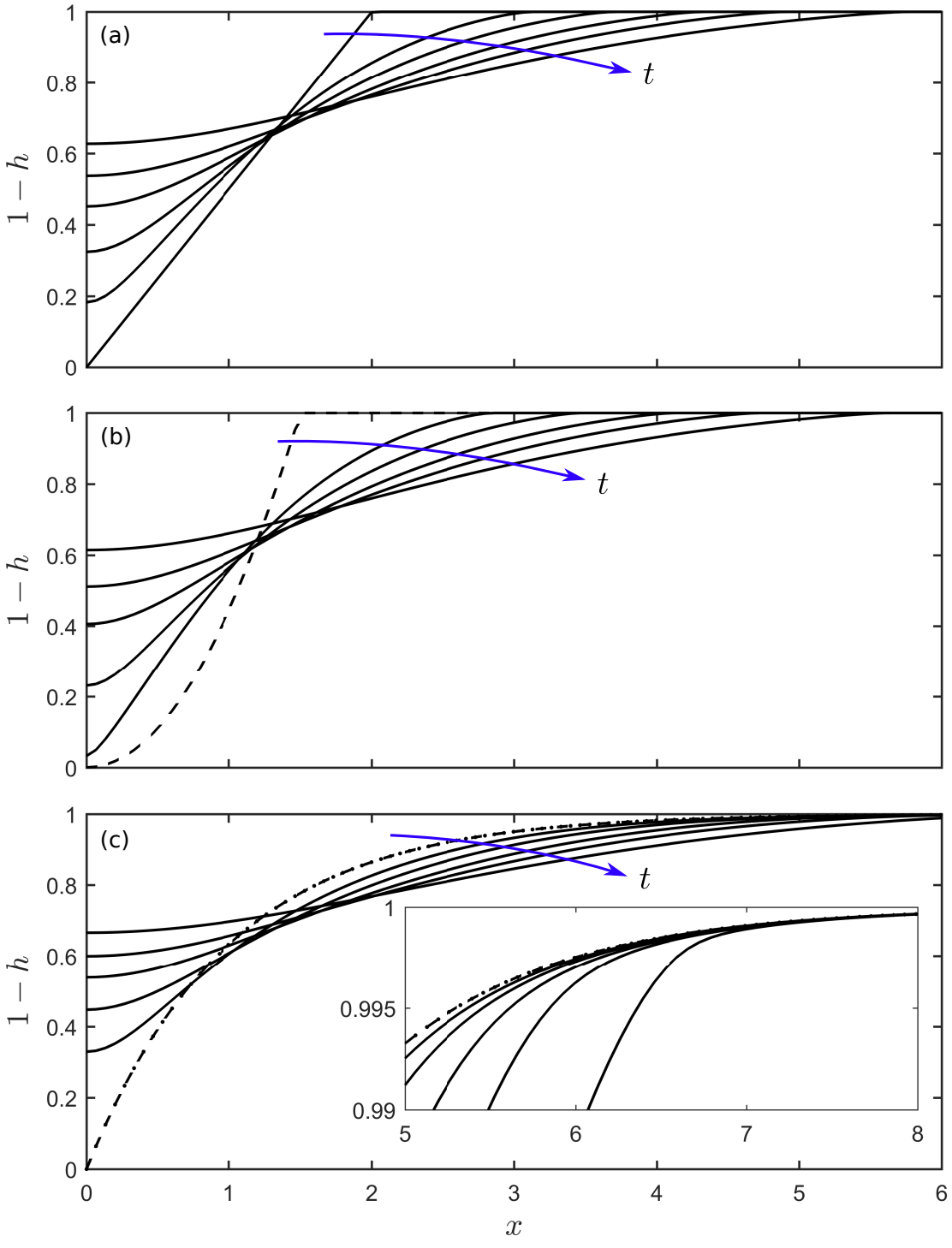


**Figure 4.7:** Plume shapes plotted at $t = [0, 3, 6, 10, 15, 25]$ for different initial plume shapes that are defined by defined by Equations $(4.18\text{a})$-c. The initial condition curves are the same as in Figure 4.6

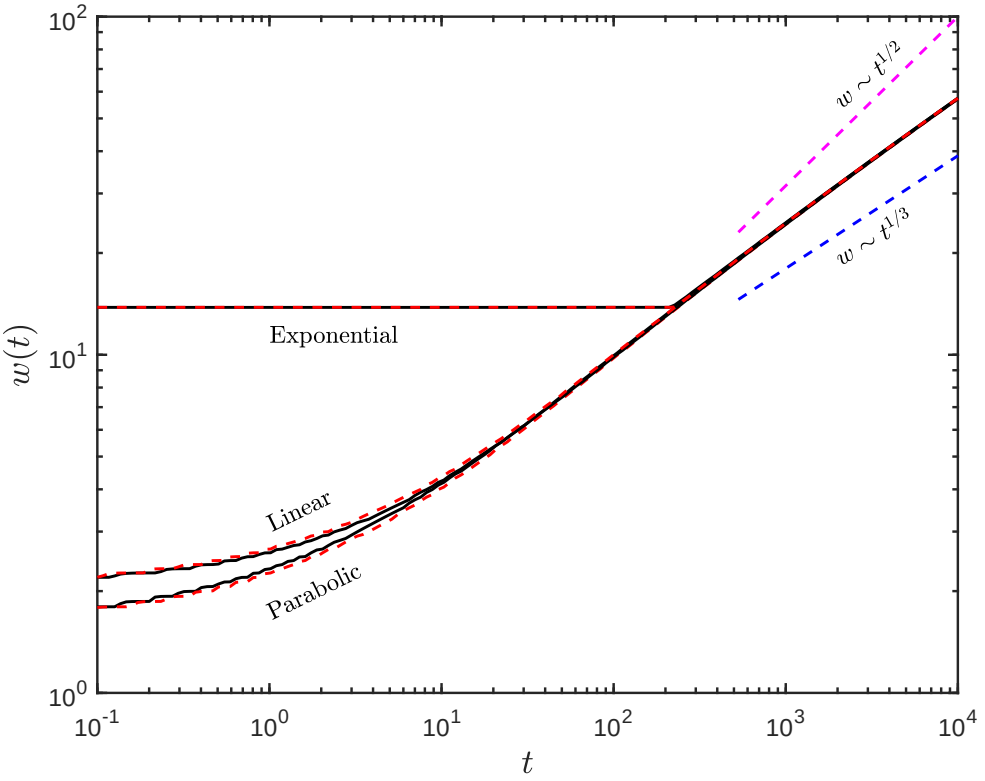


**Figure 4.8:** Evolution of the width of a gas plume after an instantaneous gas release of differing initial shapes. The full system of governing equations are plotted in solid black, and the solution to the corresponding incompressible single-aquifer PDE is plotted in dashed red.

towards late-time self-similarity (for $t \gg 10^2$). Recall from Chapter 2 that the width $w$ is defined as the distance between the injection point and the place where the plume thickness falls below an threshold value $\zeta$. Figure 4.9 demonstrates that $\zeta$ controls the sharpness of the transition between the stalled and un-stalled states. For increasingly large values of $\zeta$, the transition is smoother and begins at progressively earlier times. This result is an artefact of calculating the plume-width using an threshold and is caused by a reduced sensitivity to changes in $h(x,t)$ for larger values of $\zeta$.

These results suggest that the plume shape at the end of injection can have a significant impact on post-injection dynamics before the development of late-time self-similarity. The equivalent width–time evolution curves calculated for a fully

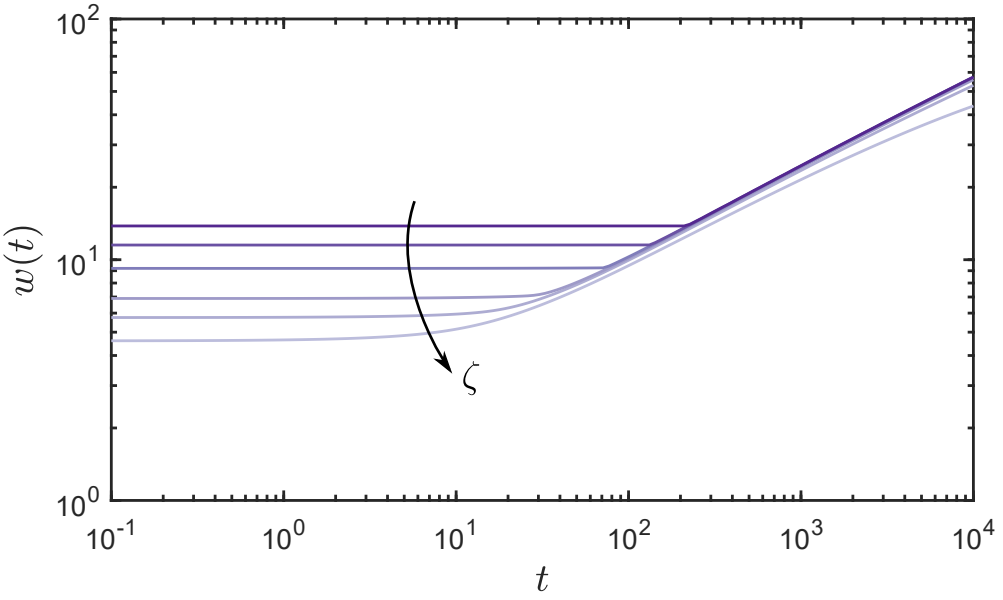


**Figure 4.9:** Evolution of the width of a gas plume that is instantaneously released from an initial exponential shape, plotted for width-threshold values $\log_{10}(\zeta) = [-2, -2.5, -3, -4, -5 \text{ and } -6]$.

incompressible model [Equation (4.16)] are also plotted on Figure 4.8. The excellent agreement between the standard incompressible PDE and the system of coupled compressible governing equations demonstrates that this observation is not an artefact of model complexity, and furthermore that the fluid dynamics causing this newly-observed nose-stalling phenomenon are independent of compressibility and pressure propagation. To investigate the physical mechanism that results in partial-stalling of horizontal gas migration when specific shapes of gas are released into a single aquifer, a brief analysis is now performed. Consider the evolution of the plume at its nose (i.e., where $h \to 0$). Using the product rule, Equation (4.16) can be expressed as

$$\frac{\partial h}{\partial t} = (1 - R_d) N_g \mathcal{M} \left[ \left( 1 - \frac{\partial f}{\partial x} \right) h \frac{\partial h}{\partial x} + (1 - f) \left( \frac{\partial h}{\partial x} \right)^2 + (1 - f) h \frac{\partial^2 h}{\partial x^2} \right]. \quad (4.20)$$

Towards the nose of the plume, Equation (4.20) converges to:

$$\begin{aligned}\lim_{h\to 0}\left[\frac{\partial h}{\partial t}\right] &= (1-R_d)N_g\mathcal{M}\lim_{h\to 0}\left[\left(1-\frac{\partial f}{\partial x}\right)h\frac{\partial h}{\partial x}+(1-f)\left(\frac{\partial h}{\partial x}\right)^2+(1-f)h\frac{\partial^2 h}{\partial x^2}\right]\\ &= (1-R_d)N_g\mathcal{M}\lim_{h\to 0}\left[(1-f)\left(\frac{\partial h}{\partial x}\right)^2\right]\\ &= (1-R_d)N_g\mathcal{M}\lim_{h\to 0}\left(\frac{\partial h}{\partial x}\right)^2.\end{aligned} \tag{4.21}$$

Furthermore, for $x > 0$, also consider the dimensional horizontal velocity of the nose $u_{\mathcal{N}}$ which can be expressed as:

$$u_{\mathcal{N}} = \frac{\mathrm{d}w}{\mathrm{d}t} = -\frac{\lambda_g}{\phi}\nabla p \approx -\frac{\lambda_g}{\phi}\left.\frac{\partial p}{\partial x}\right|_{\mathcal{N}}. \tag{4.22}$$

where $\left.\dfrac{\partial p}{\partial x}\right|_{\mathcal{N}}$ is the horizontal pressure gradient, evaluated at the nose of the plume. For incompressible flow in the absence of injection, the horizontal pressure gradient in the gas is given by:

$$\frac{\partial p}{\partial x} = (\rho_w - \rho_g)g\frac{\partial h}{\partial x}. \tag{4.23}$$

Substituting Equation (4.23) into (4.22), dividing by $\phi$ and making substitutions for various dimensionless groupings (Equation (4.9))—noting particular use of $\mathcal{P} \equiv \phi\mathcal{L}^2/(\lambda_w\mathcal{T})$—the dimensionless horizontal velocity of the nose can be expressed as:

$$u_{\mathcal{N}} = -s_g\mathcal{M}(1-R_d)N_g\left.\frac{\partial h}{\partial x}\right|_{\mathcal{N}}. \tag{4.24}$$

At the nose of the plume, the horizontal velocity $[u_{\mathcal{N}} \sim \partial h/\partial x|_{\mathcal{N}}]$ and thickness evolution $[\partial h/\partial t|_{\mathcal{N}} \sim (\partial h/\partial x|_{\mathcal{N}})^2]$ are both dependent on the gradient of the plume thickness at the nose. Now consider the plume whose shape is initially linear. From Equation (4.18a), the initial gradient (for $x > 0$) is $\partial h/\partial x|_{\mathcal{N}} = -1/2$.

As such, $u_{\mathcal{N}} = s_g\mathcal{M}(1 - R_d)N_g/2$ and $\partial h/\partial t|_{\mathcal{N}} = \mathcal{M}(1 - R_d)N_g/4$. Similarly, for the parabolic initial plume shape [Equation (4.18b)] the initial gradient at the plumes' nose ($x = x_{\mathcal{N}} = w_0$) is $\partial h/\partial x|_{\mathcal{N}} = -2x/w_0^2 = -2/w_0$. The initial velocity and rate of change of thickness at the nose of the plume are therefore $u_{\mathcal{N}} = 2s_g\mathcal{M}(1-R_d)N_g/w_0$ and $\partial h/\partial t|_{\mathcal{N}} = 4\mathcal{M}(1-R_d)N_g/w_0^2$ respectively. Now consider the initial evolution of the plume with an exponential initial shape (Equation (4.18c)). Note that an exponential function asymptotically approaches zero and therefore only reaches zero thickness at infinite distance from the injection well. Instead, consider the limit of the horizontal gradient of this plume as it becomes vanishingly thin:

$$\lim_{h\to 0}\frac{\partial h}{\partial x} = \lim_{h\to 0} -e^{-x} = \lim_{h\to 0} -e^{\ln(h)} = 0. \tag{4.25}$$

For both the parabolic and triangular plumes $\partial h/\partial x|_{\mathcal{N}}$ and $\partial h/\partial t|_{\mathcal{N}}$ are initially positive; meaning that at $t = 0$ the plume can thicken and propagate laterally. However an initial exponential shape has zero gradient as the nose. In the numerical simulation, the interfacial gradient associated with the thin tongue region is sufficiently small to suppress plume thickening and nose-propagation. Accordingly, a period in which the plume's nose does not propagate is observed (Figure 4.8). Physically, this nose-stalling can be explained by the relationship between the nose velocity and the plume thickness gradient. As $u_{\mathcal{N}} \sim \partial h/\partial x|_{\mathcal{N}}$ and $\partial h/\partial t|_{\mathcal{N}} \sim (\partial h/\partial x|_{\mathcal{N}})^2$, a shallow thickness gradient at the nose results in very slow motion of the nose, resulting in the appearance of a stalled plume. The slumping plume drives lateral gas flow towards the stalled nose, eventually increasing $\partial h/\partial x|_{\mathcal{N}}$—releasing the plume from its stalled constraint by driving lateral flow and allowing for a subsequent transition into a classical confined gravity current.

Gas injection leads to a plume that has a characteristic tongued shape that is qualitatively similar to the exponential shape, in that it is convex and with a small (but nonzero) gradient at the nose. However, whereas an exponential function

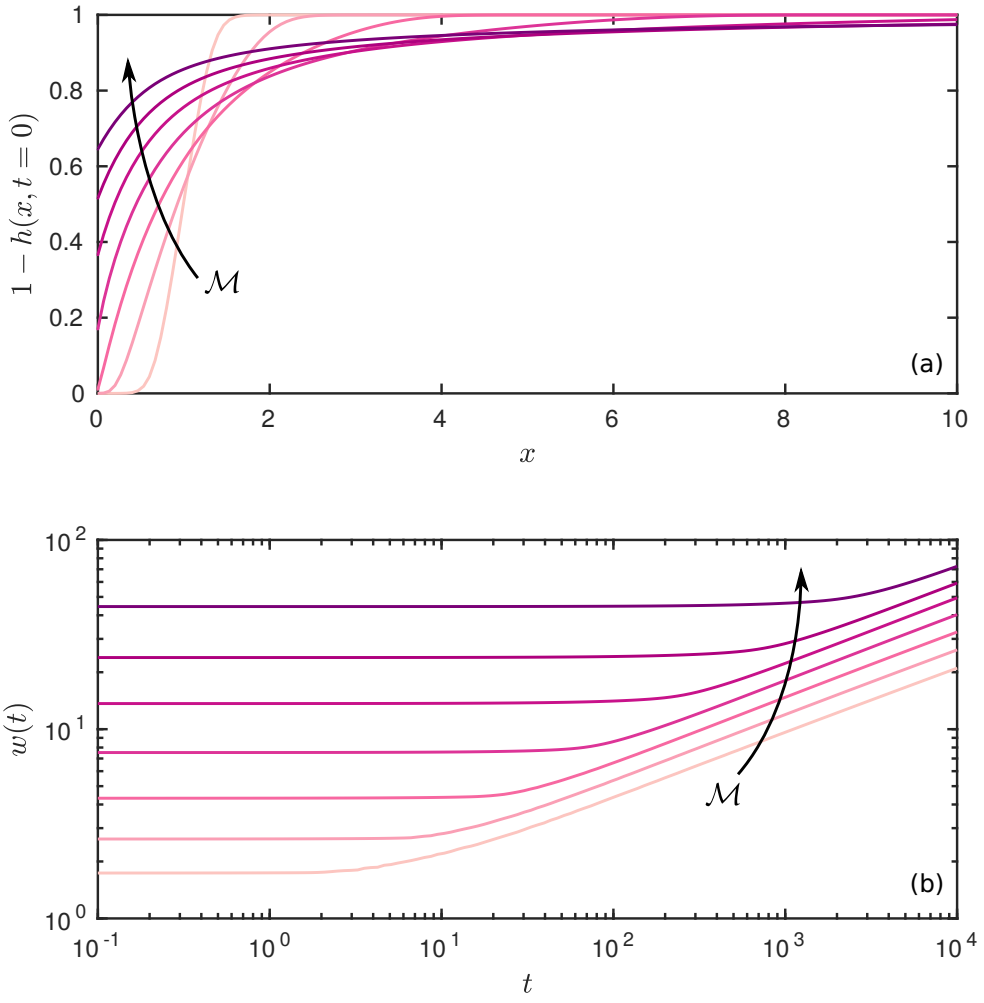


**Figure 4.10:** (a) Incompressible plume shape at the end of injection for $\mathcal{M} = [1, 2, 4, 8, 16, 30 \text{ and } 60]$. (b) Incompressible width-evolution, initialised from an instantaneous release of gas defined by the plumes in the top panel.

asymptotically approaches $h = 0$, a $CO_2$ plume, for example, has a finite width at which $h = 0$. Nevertheless, an injected gas plume may still have a sufficiently small thickness gradient at the nose to result in horizontal stalling. To demonstrate this, several initial plume shapes commensurate with incompressible fluid injection for various values of $\mathcal{M}$, at standard reference parameters, are instantaneously released into a single aquifer ($\Lambda_w^s = 0$). Plumes with a higher mobility ratio start the post-injection phase from a more tongued initial shape, and therefore evolve with a smaller thickness gradient at the nose of the plume (Figure 4.10a). As in

all simulations in this section, the pressure distribution is initially phase-static, and the system is allowed to evolve until $t = 10^4$.

Figure 4.10(b) shows that all plumes in the interval $1 \leq \mathcal{M} \leq 60$ experience a period of horizontal stalling—as defined by a period of constant width—before initiating classical gravity-current spreading. Plumes with lower mobility ratios experience a shorter period of horizontal stalling. For example, simulations with $\mathcal{M} = 1$ and $\mathcal{M} = 60$ do not grow in width for $\sim 1$ and $\sim 10^3$ dimensionless times respectively. This can readily be explained by considering the initial gradient as a function of mobility. An increase in mobility ratio increases the tonguing of the plume which markedly decreases $\partial h/\partial x|_{\mathcal{N}}$—the gradient that drives horizontal flow at the nose. These results demonstrate that, although 'real' gas plumes arising from industrial injection are not truly exponential in shape, they are sufficiently tongued to experience horizontal stalling in the absence of depressurisation.

## 4.5 Post-injection fluid migration

The previous section §4.4 established the importance of using the 'end-of-injection' plume shape as an initial condition to model post-injection gas migration. This section considers the combined effects of the end-of-injection plume shape and post-injection depressurisation on fluid migration in the same two-aquifer reference case used throughout this chapter. The abrupt transition from injection to post-injection is achieved through Equation (4.8), which switches off injection for $t > 1$. Accordingly, all numerical simulations in the section evolve from the pre-injection initial conditions used in previous chapters. All parameters used are as listed in Table 3.1 except where explicitly indicated otherwise. For now, the entry pressure ($p_c^E$) is once again assumed to be infinite, or sufficiently large that gas leakage does not occur. This allows for simpler interpretation of an already crowded parameter-space during post-injection migration.

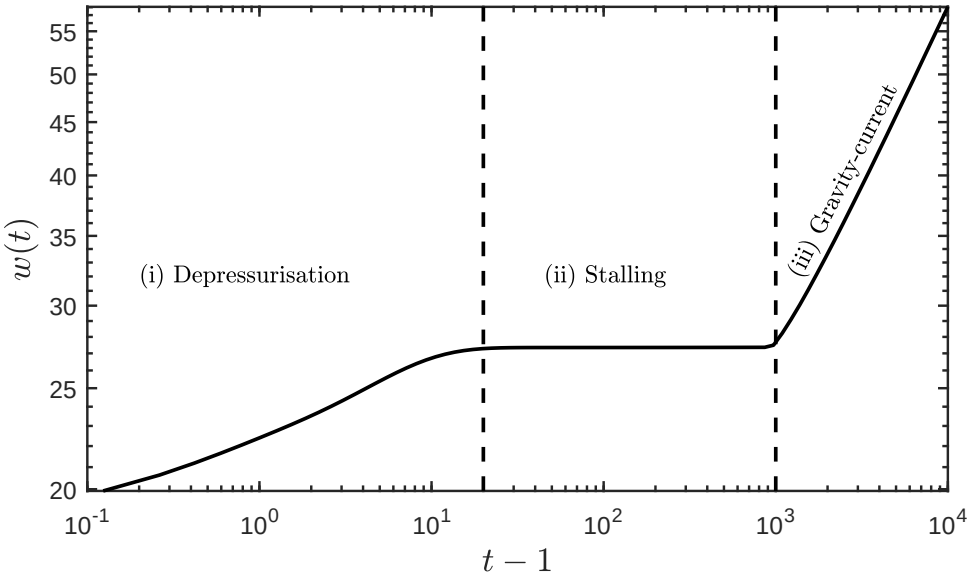


**Figure 4.11:** Width evolution regimes plotted for post-injection times ($t > 1$), for a simulation with reference parameters and $\Lambda_w^s = 10^{-9}$.

The post-injection phase represents a long transient between the end-of-injection state and late-time self-similarity. These results show that, during the transition towards classical confined gravity-current spreading, two distinct and previously unreported regimes of post-injection migration occur. All three regimes—(i) depressurisation, (ii) stalling and (iii) gravity-current—are distinguishable by considering the shape (specifically the width) of the plume (Figure 4.11). To build a complete picture of post-injection dynamics in a layered aquifer with pressure dissipation, each regime is now considered separately.

### 4.5.1 Depressurisation regime

At the end of fluid injection ($t = 1$) the aquifer is fully pressurised. The degree and distribution of overpressure throughout the layered aquifer system is covered extensively in Chapter 2. In summary: Vertical pressure dissipation is largely controlled by the ease with which water can flow vertically through intermediary seals ($\Lambda_w^s$) and, to a lesser degree, through thin films that connect the ambient phase through the gas region ($k_{rw}^\star$). Increased pressure dissipation (high $\Lambda_w^s$)

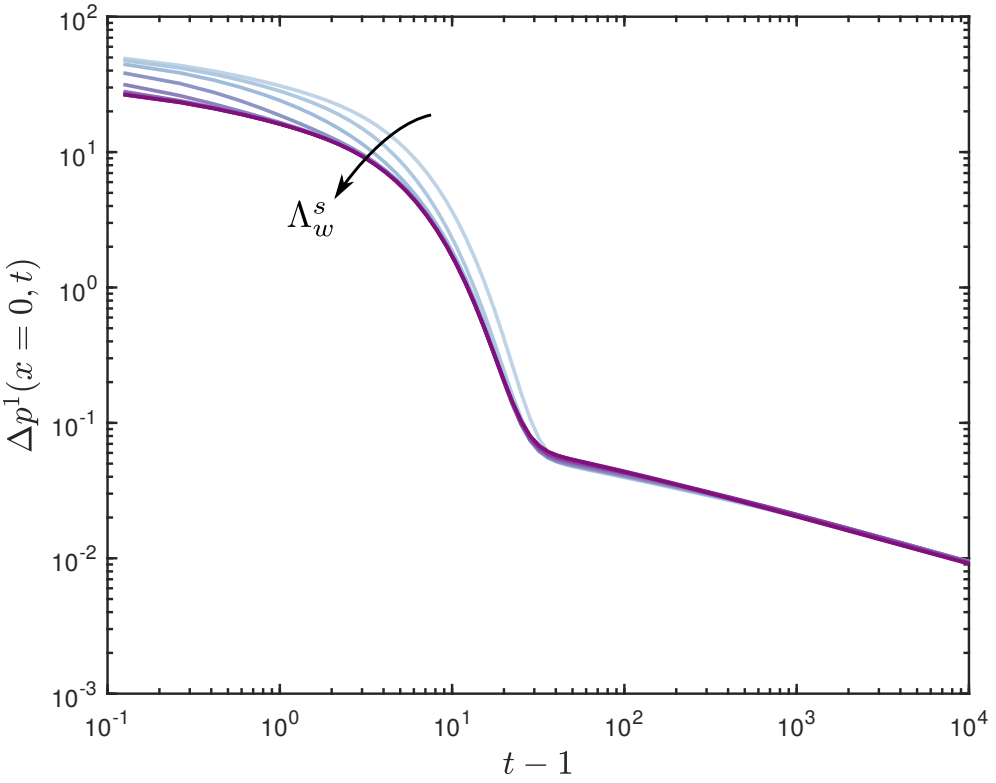


**Figure 4.12:** Pressure perturbation in the injection aquifer plotted against post-injection time for reference parameters and $\log_{10}(\Lambda_w^s) = [-9, \ -7.5, \ -7, \ -6.5, \ -6, \ -5.5, \ -5, \ -4$ and $-3]$.

results in a reduced end-of-injection overpressure in the injection aquifer ($n = 1$), and an increased end-of-injection overpressure in all other layers (here, $n = 2$). Depressurisation after gas injection is qualitatively similar to depressurisation after water injection (see §4.3): For $t > 1$, the pressure in the injection aquifer ($n = 1$) experiences a transient decay from the end-of-injection state, with the 'no-leakage' limit ($\Lambda_w^s = 0$) providing an upper bound for pressure (Figure 4.12). During the initial phase of depressurisation ($1 < t < 30$), depressurisation is sensitive to vertical water leakage. Strong pressure dissipation ($R_A^2 \Lambda_w^s \sim 1$) provides a lower bound for temporal pressure decay in the injection aquifer. This is for two principle reasons: Firstly, stronger pressure dissipation results in a lower pressure at the end of injection; secondly, stronger vertical pressure dissipation allows for more efficient pressure dissipation at all times (including during post-injection migration). As time progresses, the pressure front from the depressurising injection aquifer reaches

the top boundary of the system at progressively earlier times for higher values of $\Lambda_w^s$. As such, pressure decay curves for intermediate leakage numbers collapse onto the 'strong-leakage' limit at earlier times with an increase in $\Lambda_w^s$ (Figure 4.12). Depressurisation is complete when the pressure field has returned to a phase-static distribution (Figure 4.12).

At the end of $CO_2$ injection, the gas–water interface has a characteristic tongued plume shape that is indicative of a high mobility ratio [e.g., Nordbotten and Celia, 2006b, and Chapter 2]. In §4.4.3 it was demonstrated that the initial plume shape is important to the migration-dynamics of an instantaneously released volume of gas. Specifically, it was shown that convex plume shapes with small thickness gradients at the nose can stall—i.e., experience an extended period of negligible width growth—and that this does indeed occur for end-of-injection $CO_2$ plumes. However, when the post-injection phase is initiated with the residual overpressure imprint from injection, the plume does not immediately stall and instead slumps with a propagating tip (Figure 4.13a). The nose of the plume advances with time, maintaining the tongued shape (Figure 4.13a-inset). Without the overpressure from injection, this tongued plume shape resulted in immediate stalling at the onset of post-injection migration. During depressurisation, the decaying overpressure in the injection aquifer drives the plume forward for a transient period until this overpressure is dissipated. Once the pressure approaches phase-static equilibrium ($t > 10$) the plume begin stalling, which is signified by a marked decrease in the rate of width propagation (Figure 4.11).

Pressure dissipation does not significantly alter post-injection migration during the depressurisation regime. At the end of injection, stronger pressure dissipation compacts the plume, meaning that a system with a high leakage number will begin post-injection with a reduced width and thicker plume around the injection well. For $t > 1$, all gas plumes—irrespective of $\Lambda_w^s$—monotonically increase in width until $t \sim 10$ before transitioning to the 'stalling' regime (Figure 4.14).

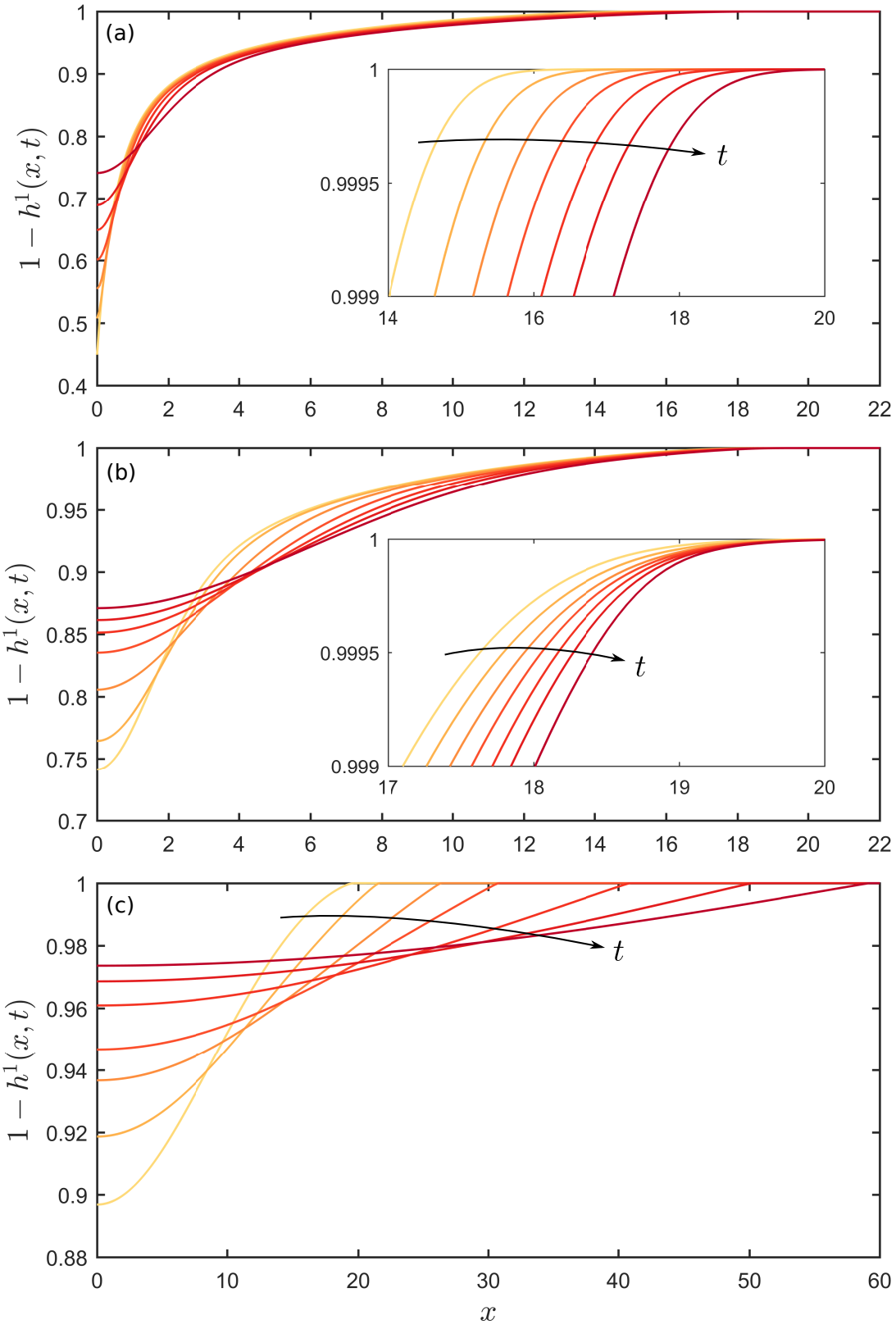


**Figure 4.13:** Plume shapes plotted for each post-injection regimes: (a) depressurisation regime, plotted for $t = [1.0,\ 1.1,\ 1.4,\ 2.0,\ 3.2,\ 5.1$ and $10.3]$; (b) stalling regime, plotted for $t = [10.2,\ 14.6,\ 29.4,\ 52.7,\ 74.7,\ 94.3$ and $119]$ and (c) gravity current regime, plotted for $t = [240,\ 483,\ 971,\ 1548,\ 3502,\ 6273$ and $10000]$. Note the change in axis scales with each panel. Inset panels provide zoomed in views of (a) and (b).

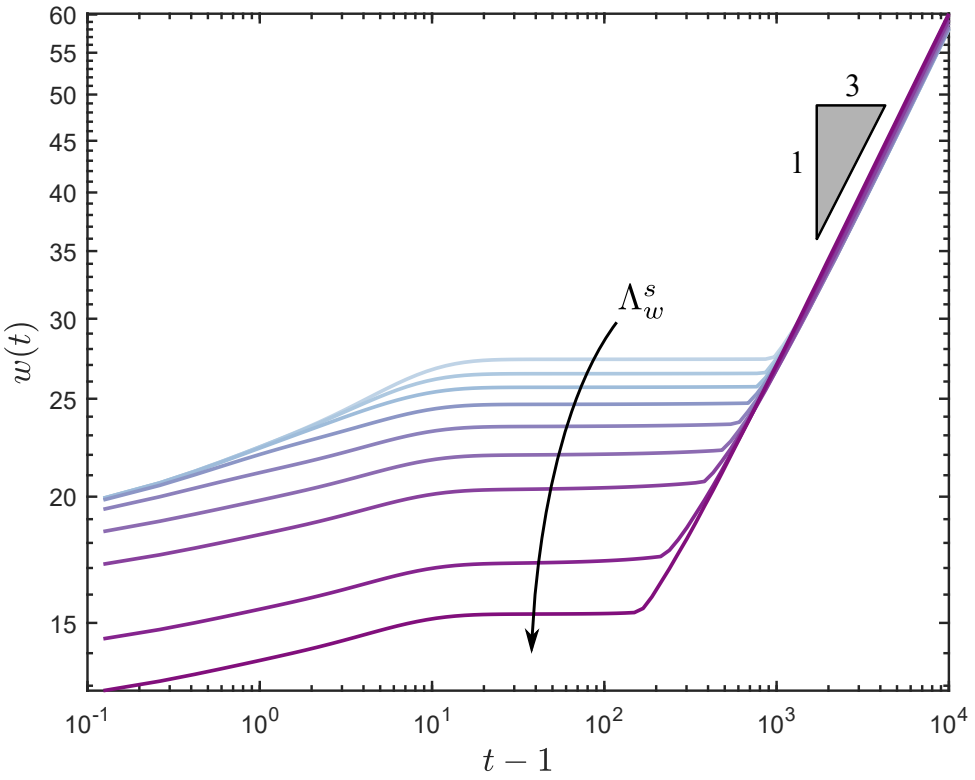


**Figure 4.14:** Plume width in the injection aquifer plotted against time after injection for $\log_{10}(\Lambda_w^s) = [-9,\ -7.5,\ -7,\ -6.5,\ -5.5,\ -5,\ -4$ and $-3]$.

### 4.5.2 Stalling regime

The stalling regime is defined as a period of negligible increase in plume width. During the 'depressurisation' regime, the slumping gas plume maintains it shape at the nose of the plume (Figure 4.13a). This means that, once the pressure becomes phase-static, the gradient at the plume's nose is very small—driving a negligible amount of lateral flow.

During stalling, the plume is nearly stationary near the nose while slumping near $x = 0$, which drives a thickening front towards the nose (Figure 4.13b). This thickening front eventually reaches the nose, increasing the local thickness gradient ($\partial h/\partial x|_{\mathcal{N}}$). Once slumping has increased $\partial h/\partial x|_{\mathcal{N}}$ to a non-negligible value, the nose of the plume moves at a non-negligible velocity and the width accordingly

grows. This marks the onset of the final post-injection regime, when the slumping plume begins transitioning towards late-time self-similarity. The termination of the stalling regime occurs earlier for simulations with higher leakage number (Figure 4.14). This is a consequence of the more compact plume shape that arises from stronger pressure dissipation during injection. Strong pressure dissipation creates a thicker plume around the injection well, providing more buoyancy to drive the slumping-induced thickening front towards the nose. Furthermore, for a more compact plume shape (higher $\Lambda_w^s$), the nose is closer to the injection well, and therefore the propagating thickening front interacts with the nose at earlier times, resulting in an earlier transition to the gravity-current regime.

### 4.5.3 Gravity-current regime

At the onset of the gravity-gravity current regime, the plume's nose becomes unstalled and the width begins to grow with time. The termination of the stalling regime is controlled by slumping gradually increasing the thickness gradient at the nose of the plume (see §4.4.3). Recall that the pressure imprint from injection fades before the stalling regime, so the pressure during the gravity-current regime is approximately phase-static. As such, the compressibility terms from the governing PDEs become negligible and the evolution of the interface can be determined by Equation (4.16) for scenarios without vertical water leakage. Accordingly, the behaviour of the depressurised post-injection gravity-current regime is similar to that described for the spreading of an instantaneous release of gas[2] (§4.4). The gas continues slumping into a long plume that eventually becomes sufficiently thin that spreading becomes insensitive to both the viscosity of the ambient water [e.g., Huppert and Woods, 1995] and the initial shape of the plume [Ball and Huppert, 2019]. At this late-time limit, the spreading process becomes self-similar and the width grows like $w \sim t^{1/3}$ [Huppert and Woods, 1995, Hesse et al., 2007]. By the

[2]Readers interested in a fuller description of gravity-currents in porous media are pointed to §4.4 or indeed works by Huppert and Simpson [1980], Huppert and Woods [1995], Barenblatt [1996], Shin et al. [2004], Hesse et al. [2007], Golding et al. [2017], Ball and Huppert [2019]

end-time of simulations presented here ($t = 10^4$), the width has almost reached the late-time spreading power law (Figure 4.14). The early-time spreading limit is typically observed for an instantaneous release of rectangular-shaped volumes of buoyant fluid. This shape permits an initial phase of tilting and 'back-propagation' described by Hesse et al. [2007], for which similarity solutions for width scale as $w \sim t^{1/2}$. In reality, injected gas does not have a rectangular shape at the end of injection, and instead the gas evolves, during post-injection migration, from a characteristic tongued shape that is controlled by the mobility ratio. As such, an initial back-propagation phase does not occur and the gravity-current regime evolves towards the late-time limit, which starts from the intermediate-time ($t^{1/2} < w < t^{1/3}$) limit described by Hesse et al. [2007].

The onset of the gravity-current regime occurs at progressively earlier times in numerical simulations with stronger vertical water leakage (Figure 4.14, and see §4.5.2). However, the width evolution is largely invariant to the leakage number during the gravity-current regime. As such, curves for different values of $\Lambda_w^s$ approximately collapse onto a single curve that governs the temporal width-evolution in the gravity current regime. This suggests a degree of self-similarity at intermediate-times, before the plume has become sufficiently thin for late-time self-similarity to develop.

## 4.6 Capillary pressure decay

In Chapter 3, the model developed in Chapter 2 was extended to include distributed vertical gas leakage within a theoretical model that couples lateral gas migration with horizontal and vertical pressure dissipation in a layered aquifer system. This extension relies on the introduction of a capillary entry pressure threshold [e.g Woods and Farcas, 2009] that explicitly states that gas leakage occurs when the capillary pressure exceeds the entry pressure ($p_c^E$) of the associated

seals. Accordingly, during injection the onset and rate of gas leakage are inherently coupled to the magnitude of the entry pressure, and the buildup of capillary pressure in the injection aquifer—which is itself governed by the shape of the gas–water interface and the pressure distributions in the two phases (see §3.3.1). During post-injection gas migration, the overpressure associated with injection decays with time and the pressure becomes phase static. This means that non-hydrostatic (i.e., injection) contributions to the capillary pressure dissipate after injection. As such, the parameters that govern the rate of capillary pressure decay sets the final distribution of gas across the layered aquifer by virtue of controlling the termination of gas leakage.

Two limiting cases for the state of capillary pressure were derived in §3.3.1, highlighting that the magnitude and shape of the capillary-pressure distribution at the top of the injection aquifer are controlled by the resistance to water flow through the gas-saturated region, as measured by (the inverse of) the relative permeability of water in this region ($k^{\star}_{rw}$). The post-injection evolution of capillary pressure is now explored for these two limits. Results presented herein are calculated from §4.5 and, correspondingly, only involve the vertical flow of water (i.e. $p_c^E \sim \infty$). Omitting gas flow here allows for the development of a theoretical understanding of the post-injection evolution of capillary pressure, without the additional complexity of a post-injection pressure field that is evolving with cross-stratal gas migration.

### 4.6.1 Post-injection $p_c$ evolution for $k^{\star}_{rw} \gg \Lambda^s_w h^n$

In the $k^{\star}_{rw} \gg \Lambda^s_w h^n$ limit, vertical water flow is unobstructed by the gas, allowing for the capillary pressure to be approximated by a phase-static distribution: $p_c \approx (1-R_d\rho_g)N_g h$. As such, the capillary pressure distribution mirrors the shape of the plume (see Chapter 3). During the post-injection phase, the evolution of capillary pressure is governed by two competing mechanisms: Gas expansion (variations

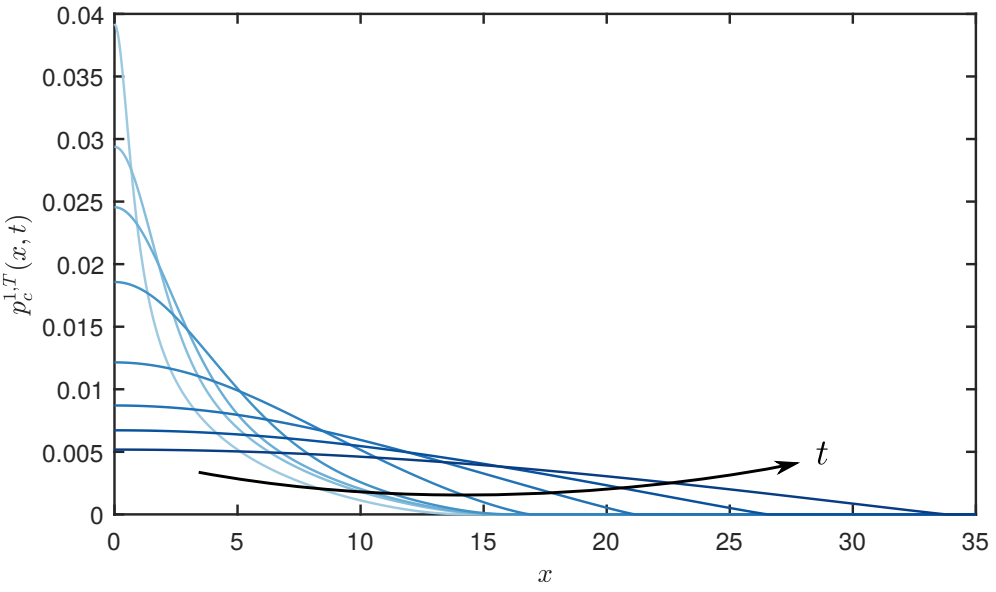


**Figure 4.15:** Spatial distribution of capillary pressure at the top of the injection aquifer plotted for $t = [2,\ 10,\ 21,\ 52,\ 190,\ 483,\ 971$ and $1995]$ and $k^{\star}_{rw} = 1$.

in $\rho_g$) and slumping (variations in $h$). As the gas density is assumed to depend linearly on the pressure $[\rho_g^n(p^n) = 1 + N_{cw}R_{cf}(p^n - p^0)]$ depressurisation leads to gas expansion (i.e., $\rho_g$ decreases as $p$ decreases). As for the plume shape, the post-injection evolution of the gas shape is described in detail above. Broadly, the slumping gas plume decreases in thickness around the injection well, driving a laterally propagating gravity-current.

For most parameters, the capillary pressure evolution follows variations in $h$: $p_c$ decreases around the injection well, and grows laterally with the propagation of the slumping gravity current (Figure 4.15). However when depressurisation and gas expansion are especially strong relative to buoyancy, the post-injection evolution of capillary pressure is more complicated. These effects are strongest around the injection well, where $\partial h/\partial t$ and $\partial \rho_g/\partial t$ are maximally negative. Stronger vertical leakage amplifies these effects (Figure 4.16). Correspondingly, for high values of $\Lambda_w^s$, gas expansion is less important during depressurisation and slumping dominates, resulting in a monotonic decrease in capillary pressure around the injection well with time (Figures 4.15 and 4.17). For vanishingly small values of the leakage number, pressure buildup becomes confined only to the injection aquifer, resulting

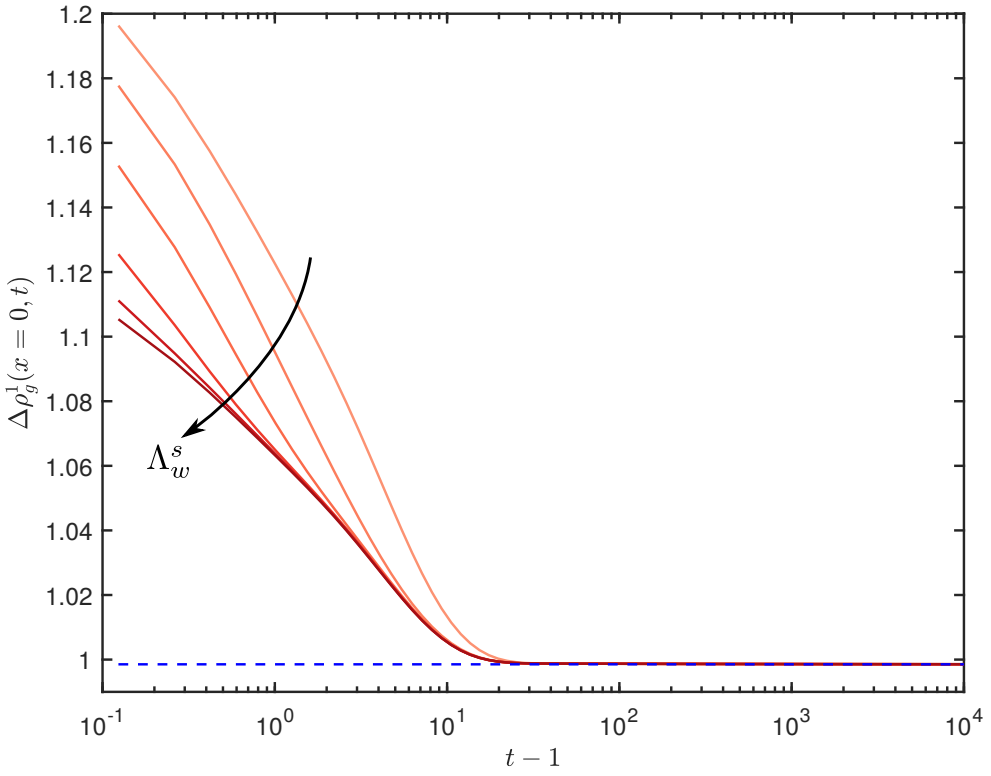


**Figure 4.16:** Maximum dimensionless gas density plotted against time after injection for $\log_{10}\Lambda_w^s = [-9, \ -7, \ -6.5, \ -6, \ -5.5 \text{ and } -3]$ and for $k_{r,w}^\star = 1$. The dashed blue line is the post-depressurisation limit: $\rho_g^1(x = 0, t \to \infty) \approx 1 - N_{cw}R_{cf}N_g$.

in maximum compression of the gas. Approaching $\Lambda_w^s \sim 0$, gas expansion terms in the simplified expression for capillary pressure dominate during the depressurisation phase, producing an increase in capillary pressure after $t = 1$. The duration of post-injection capillary pressure growth is on the order of an injection time for $\Lambda_w^s = 10^{-7}$ and increases as the leakage number tends to zero (Figure 4.17).

After depressurisation the overpressure is approximately phase-static: $p^n \approx (1 - h)N_g$. As $N_{cw}R_{cf}(1-h)N_g \ll 1$, it is trivial to see that after depressurisation the gas density returns to its dimensionless reference value ($\rho_g \approx 1 - N_{cw}R_{cf}N_g$) as $h \to 0$ (Figure 4.16). Therefore, after depressurisation, the evolution of capillary pressure is governed entirely by variations in the plume shape. A key quantity when ascertaining the likelihood of gas leakage is the maximum capillary pressure,

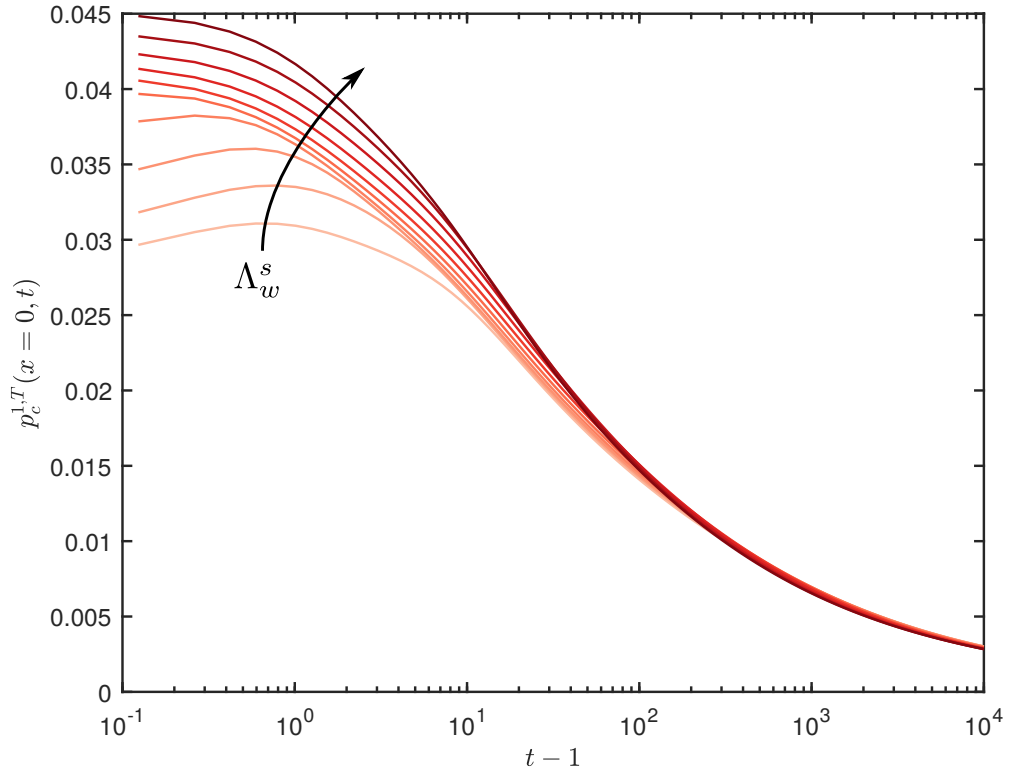


**Figure 4.17:** Maximum capillary pressure at the top of the injection aquifer plotted against time after injection for $\log_{10}(\Lambda_w^s) = [-9, \ -7, \ -6.5, \ -6, \ -5.5, \ -5, \ -4.5, \ -4, \ -3.5$ and $-3]$ and for $k_{r,w}^\star = 1$.

relative to the entry pressure. Once slumping dominates gas expansion contributions in $p_c \approx (1 - R_d\rho_g)N_g h$, the maximum capillary pressure decreases monotonically with time (Figure 4.17), reducing the probability of gas leakage in a system with homogeneous seals.

### 4.6.2 Post-injection $p_c$ evolution for $k_{rw}^\star \ll \Lambda_w^s h^n$

In the $k_{rw}^\star \ll \Lambda_w^s h^n$ limit, vertical water flow in the gas region is fully obstructed by the vanishingly small relative permeability of water in the gas region. In this limit, the capillary pressure is approximated by $p_c \approx [p^n - R_d\rho_g^n N_g h^n] - [p_w^{n+1,B} + N_g b]$, which implies that the water pressure at the top of the aquifer has become hydraulically disconnected from the interface pressure. This means that the capillary

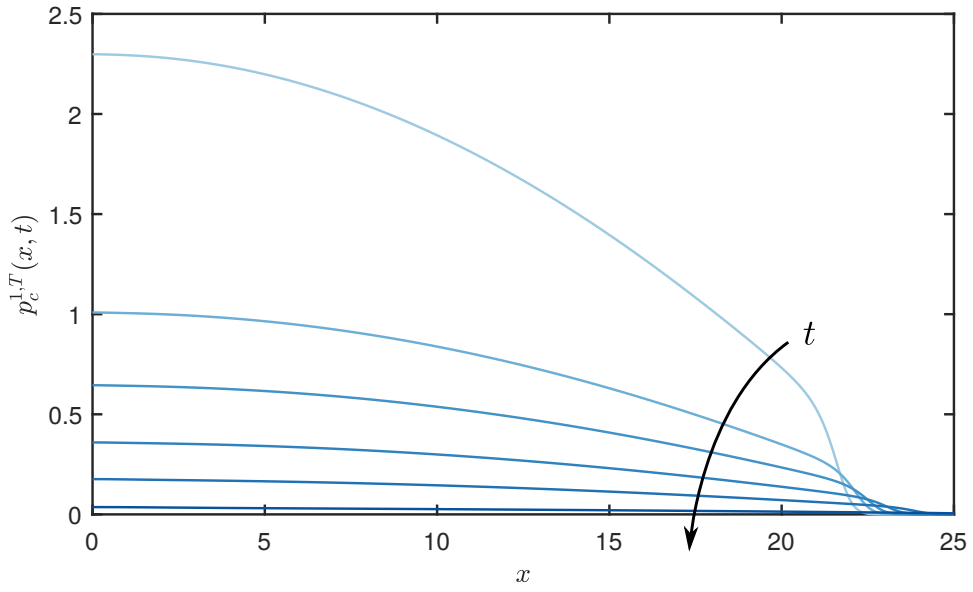


**Figure 4.18:** Plot of capillary pressure at the top of aquifer 1 as a function of $x$, for times $t = [1.1,\ 1.3,\ 1.4,\ 1.8,\ 2.9$ and $10.3]$ and for $k^{\star}_{rw} = 10^{-10}$.

pressure is more sensitive to vertical pressure dissipation, and a large pressure disconnect across the gas plume results in a larger capillary pressure that has a broader distribution that does not mirror the shape of the gas plume (see §3.3.1 and Figure 4.18).

The stronger coupling to pressure dissipation, combined with the dissimilarity between the capillary pressure and the gas distribution, suggests that depressurisation will have a leading order impact on the post-injection evolution of capillary pressure when $k^{\star}_{rw} \ll \Lambda^s_w h^n$. At $t = 1$, the capillary pressure, which depends on the water pressure in the overlying aquifer, is largest when vertical pressure dissipation is weak (small $\Lambda^s_w$). Early post-injection behaviour is dominated by slow slumping of the gas plume, and rapid depressurisation of the overpressure imprint from gas injection. As such, the early evolution of the capillary pressure in the $k^{\star}_{rw} \ll \Lambda^s_w h^n$ limit is characterised by rapid decay (Figures 4.18 and 4.19). After injection, pressure dissipation reduces the water pressure in the overlying aquifer, which reduces the water contribution to the capillary pressure ($p_w^{n+1,B}$). As the contribution to $p_c$ from the gas is predominantly governed by the shape of the gas plume—which evolves on timescales greater than depressurisation—the relatively

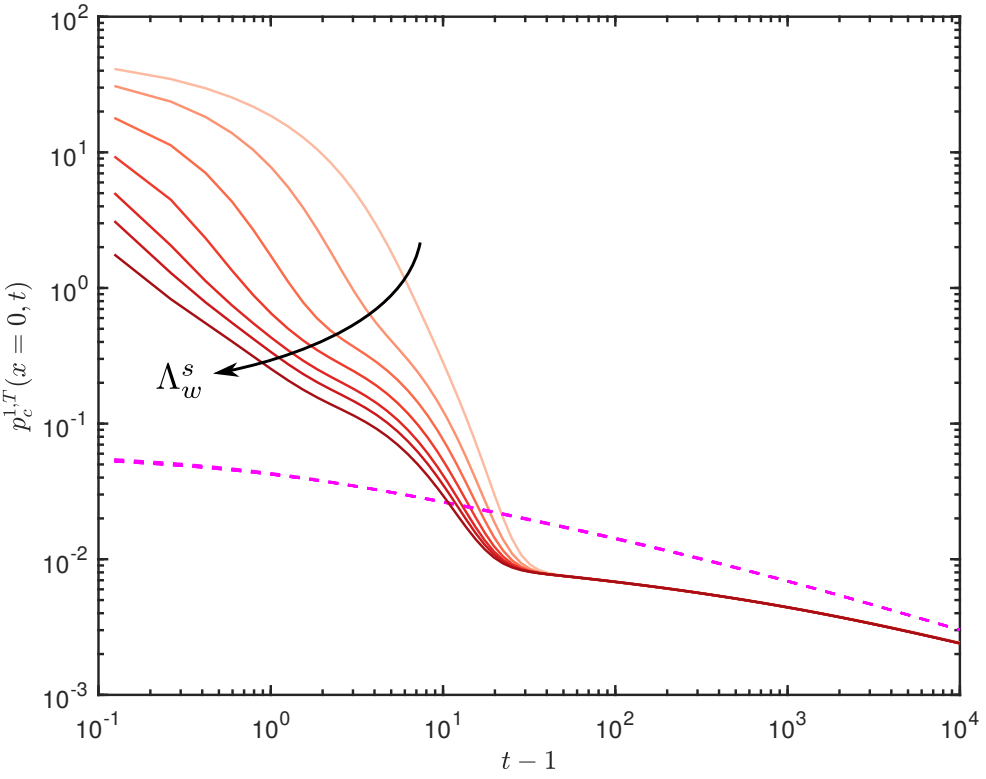


**Figure 4.19:** Maximum capillary pressure at the top of the injection aquifer plotted against time after injection for $\log_{10}(\Lambda_w^s) = [-7,\ -6.5,\ -6,\ -5.5,\ -5,\ -4.5$ and $-3]$ and for $k_{rw}^\star = 10^{-10}$. The dashed magenta lines are plotted for the post-depressurisation limit $[p_c \approx (1 - Rd)N_g h]$, and for the same values of $\Lambda_w^s$.

rapid decay of water pressure causes a correspondingly rapid decay of the capillary pressure. As such, capillary pressure decay is governed by the timescale and magnitude of overpressure in the overlying aquifer. Therefore capillary pressure decay at the $k_{rw}^\star \ll \Lambda_w^s h^n$ limit is highly sensitive to $\Lambda_w^s$. As $\Lambda_w^s$ increases towards $\Lambda_w^s \sim 1/R_A^2$, the vertical pressure distribution becomes uniform (see Chapter 2). This has the effect of reducing the capillary pressure by reducing the water pressure difference between the aquifers (Figure 4.19). The complex shape observed in Figure 4.19—which plots the maximum capillary pressure as a function of time after injection and $\Lambda_w^s$—is a result of the non-trivial interaction, over differing timescales, between three competing mechanisms that contribute to the capillary pressure: Gas slumping, gas expansion and depressurisation.

After depressurisation the pressure distribution is approximately phase-static:

$p_w^{n+1,B} \approx p^n - (h^n + b)N_g$ and $\rho_g \approx 1$. Substituting these expressions into $p_c \approx [p^n - R_d\rho_g^n N_g h^n] - [p_w^{n+1,B} + N_g b]$, further reduces the capillary pressure to $p_c \approx (1 - R_d)N_g h$: Meaning that, after depressurisation, the capillary pressure depends exclusively on the shape of the gas plume. Note that this limit is identical to the late-time capillary pressure expression for $k_{rw}^\star \gg \Lambda_w^s h^n$. At $t = 10^4$, there is still a small difference between this theoretical capillary pressure limit (which assumes no vertical flow), from the full model (Figure 4.19). This difference is maximum at $x = 0$, for which the Figure is plotted, and is related to non-hydrostatic components arising from weak vertical flow across the intermediate seal.

## 4.7 Post-injection termination of gas leakage

Chapter 3 explored and discussed the controls on gas leakage during gas injection into a layered aquifer system. Gas can leak locally from aquifer $n$ into aquifer $n + 1$ wherever the capillary pressure at the top of aquifer $n$, $p_c^{n,T}(x, t)$, exceeds the entry pressure, $p_c^E$. The local rate of gas leakage is proportional to $\mathcal{M}_z^S \Lambda_w^s \Delta p_g$, where $\mathcal{M}_z^S$ is the fluid mobility ratio in the seal and $\Delta p_g$ is the vertical pressure difference across the seal. The gas leakage rate is controlled by a complex interaction between various competing mechanisms. Pressure dissipation governs the degree of overpressure which drives vertical flow and sets the capillary pressure distribution through pressure buildup, compressibility and the shape of the gas plume. Hence, a vast array of dimensionless groups control the rate of gas leakage during injection (see Chapter 3). A similar degree of complexity is expected in the post-injection period, in which these parameters control the termination of gas leakage, which occurs when the capillary pressure falls below the entry pressure. Given the complex coupling that exists between the dynamics of the plume, horizontal and vertical pressure dissipation, capillary pressure buildup and decay, and gas leakage, the full characterisation of this extensive parameter space is beyond the scope of this work. Instead, this section shall explore one set of parameters

that yields a simple, yet informative, example that illustrates the post-injection termination of gas leakage. The end of gas leakage is particularly important to characterise in a layered system, as it sets the final mass distribution amongst the various aquifers and therefore provides a crucial constraint on the long-term fate of injected gas (e.g., $CO_2$ during CCS).

The scenario studied is a 'moderately leaky' adaptation of the reference case. All parameters are the same as in Table 3.1 with the exception of $\Lambda_w^s = 10^{-6}$ and $p_c^E = 0.015$. Gas is injected for $0 < t \leq 1$, and the gas plume is then allowed to evolve until $t = 10^3$. Recall that the reference value of $k_{rw}^\star$ is $k_{rw}^\star = 1$, so that capillary pressure evolves at the $k_{rw}^\star \gg \Lambda_w^s h^n$ limit. As such, the capillary-pressure threshold condition is equivalent to a thickness threshold condition [Woods and Farcas, 2009]:

$$h_{crit}(x,t) = p_c^E/(1 - R_d\rho_g(x,t))N_g, \qquad k_{r,w}^\star \approx 1 \tag{4.26}$$

where $h_{\text{crit}}$ is the critical thickness that must be exceeded for gas leakage to occur [i.e. $h(x,t) > h_{\text{crit}}(x,t)$]. Note that the critical thickness depends on the evolution of the gas density. Pressure buildup during injection results in an increase in $\rho_g$, which is maximum around the injection well where the largest pressures occur. This results in a weak monotonic increase in $h_{\text{crit}}$ during injection (Figure 4.20a). Around the injection well, the gas thickness grows much faster than $h_{\text{crit}}$; therefore, the capillary entry threshold is exceeded and gas leakage begins shortly after $t \approx 10^{-2}$. In this scenario, the injected gas in aquifer 1 thickens and spreads, such that the portion of the plume over which leakage occurs [$h(x,t) > h_{\text{crit}}(x,t)$] increases in breadth during injection. As a result, the total fraction of leaked gas ($M_g^2(t)/M_g^{\text{tot}}(t)$) increases monotonically with time for $0 < t < 1$ (Figure 4.20b).

After injection ($t > 1$), the gas plume begins slumping over a timescale much longer than that of the initial depressurisation phase (see §4.5.1, and Figure 4.21). During

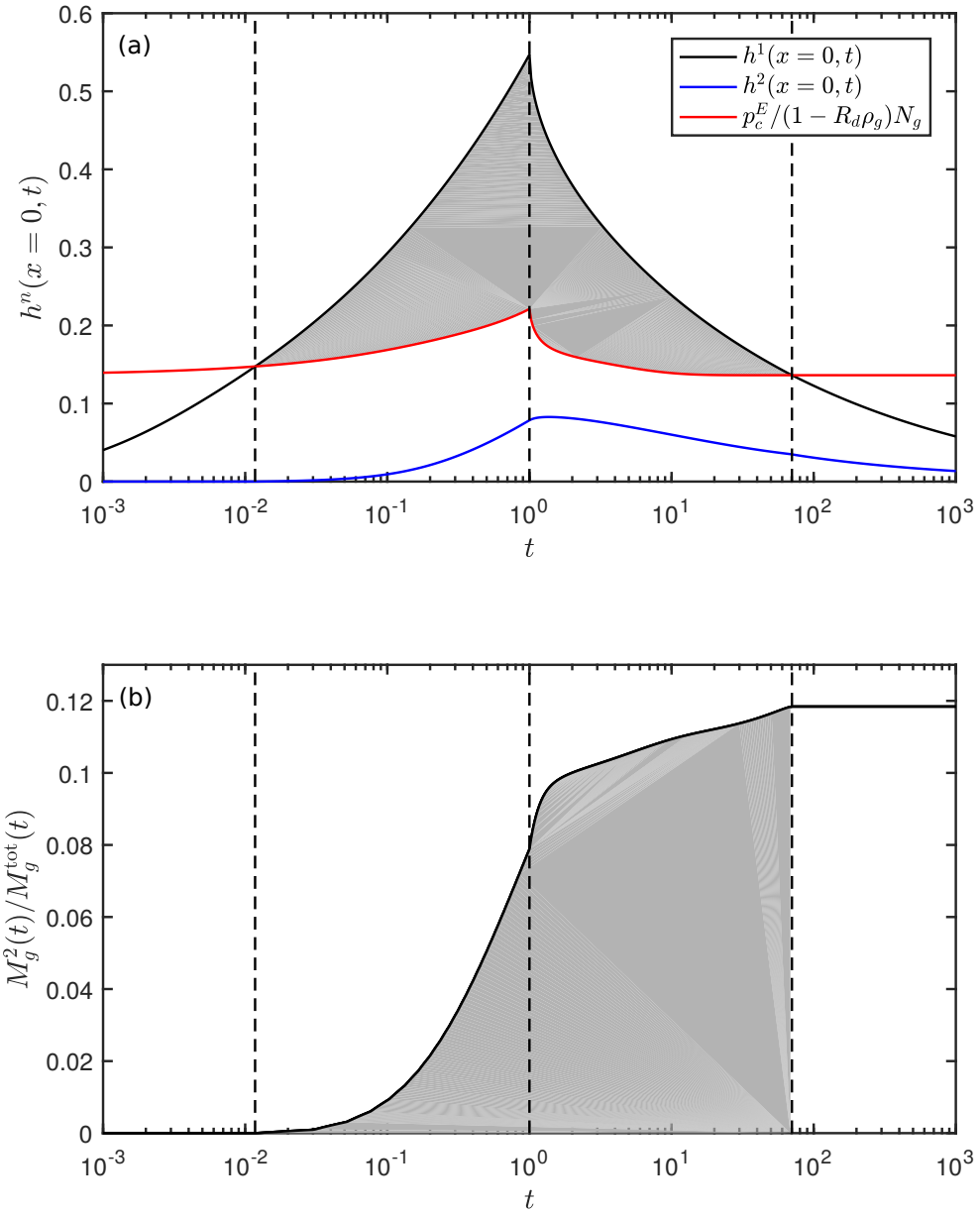


**Figure 4.20:** (a) Plot of maximum gas thickness (at $x = 0$) against time in the injection aquifer (black) and in the upper aquifer (blue). The critical thickness that must be exceeded for gas leakage to occur is plotted in red. (b) The mass fraction of gas in aquifer 2—i.e. the fraction of gas that has leaked. In both plots, times for which gas leakage occurs are indicated by grey shading. Dashed black lines indicate the initiation (left) and termination (right) of gas leakage, and the beginning of the post-injection period (middle).

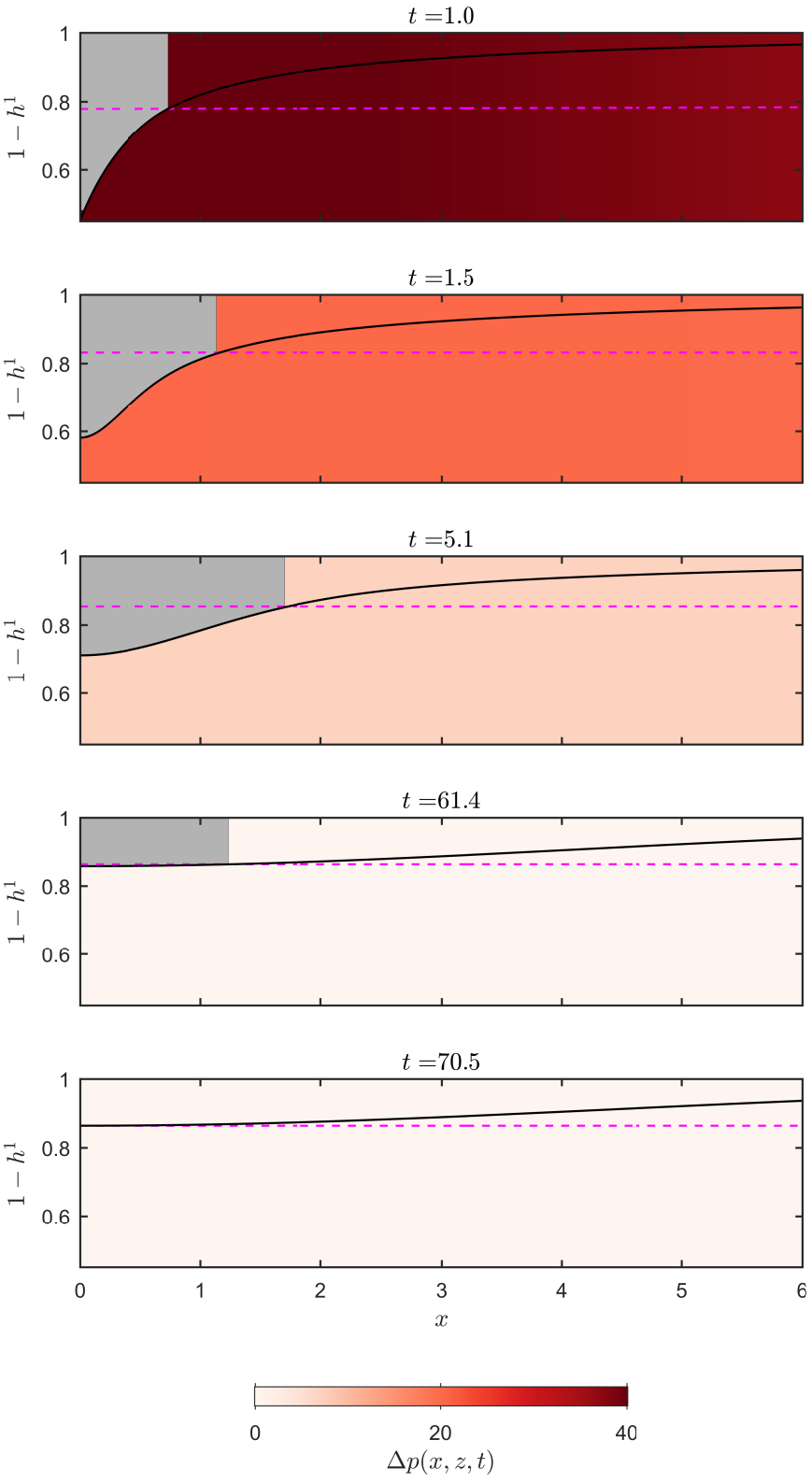


**Figure 4.21:** Shape of the gas plume in the lower aquifer for various times. The reconstructed water pressure perturbation from the initial hydrostatic condition is shaded in each panel, and the leakage threshold thickness is plotted as a dashed magenta line. The portion of the gas that can leak (i.e. $h(x,t) > h_{\text{crit}}(x,t)$) is shaded in grey.

depressurisation, the reduction in pressure results in expansion of the gas plume, which is maximal in the vicinity of the injection well ($x = 0$). Equation (4.26) suggests that post-injection gas expansion results in a weak and monotonic decay in $h_{\text{crit}}$ until depressurisation is finished—at $t \approx 20$—after which $h_{\text{crit}}$ becomes approximately constant (Figure 4.20a). As the rate of gas leakage is proportional to $\mathcal{M}_z^S \Lambda_w^s \Delta p_g(x,t)$, and both $\mathcal{M}_z^S$ and $\Lambda_w^s$ are fixed, the evolution of the vertical pressure gradient—which is inherently coupled to the dynamics of the gas (see Chapter 2)—controls the local rate of gas leakage during and after injection. The total mass flux of gas leaking across the seal is given by

$$\langle M_g \rangle = -\int_0^{w^1(t)} \frac{R_A^2 \Lambda_w^s}{s_g} \rho_g(x,t) \mathcal{R}(x,t) \mathcal{M}_z^s \Delta p_g(x,t)\, dx, \tag{4.27}$$

where $w^1(t)$ is the plume width in aquifer 1 and $\mathcal{R}(x,t)$ is the thresholding condition that sets the horizontal lengthscale over which gas leakage occurs. Depressurisation results in a decay in the overpressure that drives leakage. The spatial distribution of $\mathcal{R}(x,t)$ is set by the difference between $p_c(x,t)$ and $p_c^E$, which, for $k_{rw}^\star \gg \Lambda_w^s h^n$, is governed only by the plume shape and compressibility. Immediately after injection, the decay in the critical thickness required for gas leakage, results in gas leakage occurring over a greater lateral lengthscale (Figures 4.20 and 4.21)—causing a brief increase in the leakage rate after injection (Figure 4.20b). This results in a slight, and short-lived, thickening of the plume in aquifer 2 over the approximate interval $1 < t < 1.5$ (Figures 4.20a) and 4.22): Meaning that the uppermost gas plume is locally and briefly dominated by gas leakage in the immediate post-injection, relative to slumping.

As depressurisation and slumping continue, there is a competition between the decaying overpressure and changes in $\mathcal{R}(x,t)$. Figure 4.21 shows that the length over which gas is leaking initially increases due to both slumping of the plume and a decrease in $h_{\text{crit}}(x,t)$ (see above). At $t \approx 70$, the plume has slumped sufficiently that the capillary pressure threshold is no longer exceeded $[h(x,t) < h_{\text{crit}}(x,t)]$

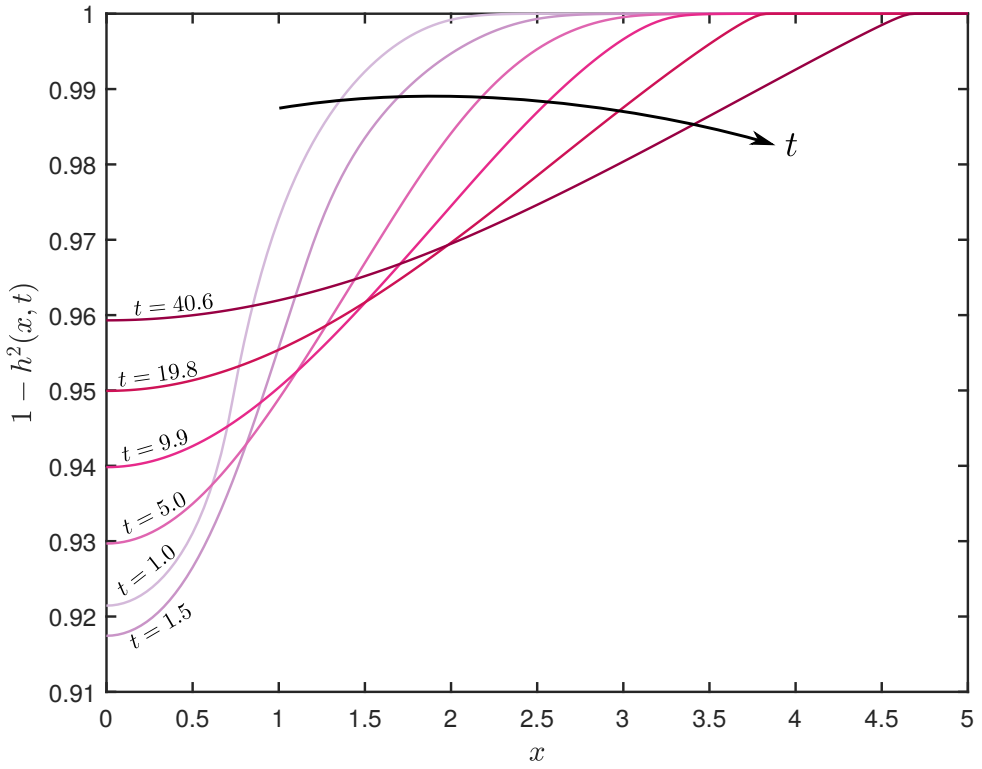


**Figure 4.22:** Gas plume shape in the upper aquifer ($n = 2$) at $t = 1$, 1.5, 5.0, 9.9, 19.8 and 40.6. Note that at early-times, gas leakage forces the plume to initially thicken around ($x = 0$) before slumping occurs.

and gas leakage terminates (Figures 4.20 and 4.22). After gas leakage has ended ($t > 60$), the slumping gas plumes in the two aquifers evolve in a mostly decoupled state. The termination of gas leakage occurs post-depressurisation, so that the plumes evolve largely as described in §4.5. In the injection aquifer ($n = 1$) gas leakage terminates during plume stalling (Figure 4.23). After ∼300 dimensionless times have elapsed, the gradient constraint at the nose has relaxed and the plume begins evolving as a classical gravity current (see §4.5). In the upper aquifer ($n = 2$), although a brief period of reduced width growth is observed, stalling does not occur (Figure 4.23). This is caused by distributed leakage and depressurisation producing a plume that is not sharply tongued (Figure 4.22). Instead of stalling, the upper gas plume begins transitioning towards late-time self-similarity at an earlier time than the injected gas plume (Figure 4.23).

This section has served to illustrate that a vast number of coupled mechanisms

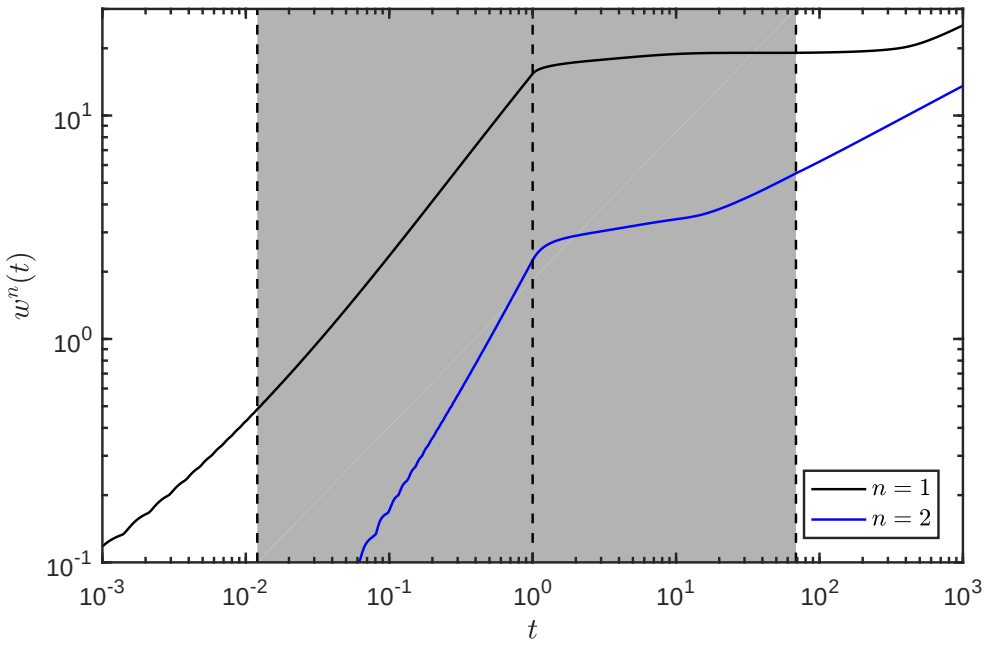


**Figure 4.23:** Width evolution in both aquifers of a two-aquifer system during ($t < 1$) and after ($t \geq 1$) injection. Grey shading is used to illustrate times for which vertical gas leakage occurs. Dashed black lines indicate the initiation (left) and termination (right) of gas leakage, and the beginning of the post-injection period (middle).

control the onset and termination of gas leakage during and after injection. This has been achieved through the study of an example suite of parameters, for which the entry-pressure threshold can be expressed as plume-thickness threshold [Equation (4.26)]. Accordingly, results from this simulation are easier to interpret than for scenarios in which $k^\star_{rw} \ll \Lambda^s_w h^n$. For geological $CO_2$ storage, however, $k^\star_{rw}$ and $p^E_c$ are likely to be considerably smaller and larger, respectively, than values used above. A very small value of $k^\star_{r,w}$ drastically increases the magnitude of the capillary pressure, and strongly couples the capillary pressure to vertical pressure dissipation—introducing further complexity to post-injection termination of gas leakage. Future work should be performed to more rigorously explore the parameter space associated with post-injection gas leakage. This important work, combined with other recommendations (see §5.3), would allow for quantitative predictions of post-injection behaviour at field sites where industrial gas injection into layered aquifers occurs—such as $CO_2$ injection and migration at Sleipner.

## 4.8 Geophysical discussion

Previous studies of the period after gas injection have largely focused on characterising self-similar regimes that allow for simple, yet elegant predictions of the long-term behaviour of the slumping gas plume [e.g., Huppert and Woods, 1995, Hesse et al., 2007]. Typically, these studies simplify the post-injection initial condition by neglecting pressure buildup and depressurisation and assuming that the pressure at the end of injection is phase-static. Furthermore, it is also common to neglect the tongued shape of the gas plume, which depends strongly on the mobility ratio, and evolve the plume from an initial step function. The above results have demonstrated that retaining the pressure and plume-shape imprint from injection can have drastic consequence on the evolution of $CO_2$ plume during post-injection migration. This has revealed the existence of two previously undescribed post-injection regimes ('depressurisation' and 'stalling'). Below, the implications of these results are discussed, and it is argued that considering the 'full' evolution of an injected $CO_2$ plume, over its entire life, is of critical importance for $CO_2$ storage.

### 4.8.1 Depressurisation

A key limitation on storing $CO_2$ in saline aquifers is that of pressure buildup [Szulczewski et al., 2012]. The pressure in the injection aquifer must not be allowed to reach an upper limit corresponding to a geomechanical failure criterion which is estimated from a geological survey, before being multiplied by a 'safety factor'. During the first post-injection regime—'depressurisation'—the fluid pressure built up during injection decays toward a phase-static distribution. The timescale of this decay is crucial in ascertaining when fluids can safely be injected back into the surrounding area without risk of activating geomechanical failure (e.g., faulting). Figure 4.2 shows that 10's of dimensionless times (100's of years for an injection period of 10's of years) are required for the pressure to become phase-static. This

means that potential future use of aquifers for injection must be carefully considered when selecting storage sites for $CO_2$ injection or waste water injection. Otherwise scenarios may occur in which ideally located aquifers are rendered unusable for future industrial applications by virtue of pressure limitations imposed by previous phases of injection.

### 4.8.2 Stalling

In §4.4.3 and §4.5.2 it was shown that post-injection migration is sensitive to the plume shape at the end of injection. The tongued plume shape has a very small thickness gradient at the nose ($\partial h/\partial x|_{\mathcal{N}}$) where $h \to 0$. The horizontal plume velocity $\partial w/\partial t|_{\mathcal{N}}$ and rate of thickness increase $\partial h/\partial t|_{\mathcal{N}}$ are both proportional to the thickness gradient $\partial h/\partial x|_{\mathcal{N}}$. This combination leads to a long period of stalling after depressurisation, during which the increase in width is negligible. This 'stalling' phenomenon is previously unreported, largely due to previous studies not considering the plume shape at the end of injection.

Negligible width growth is observed for parameters motivated by $CO_2$ storage over a timescale of $10^2 - 10^3$ dimensionless times ($10^3 - 10^4$ years). A considerable challenge for storing $CO_2$ in saline aquifers is using geophysical monitoring during and after injection to ensure that the injected $CO_2$ is secure, i.e., that $CO_2$ remains within the target aquifer. Due to the non-uniqueness of interpreting geophysical data, monitoring $CO_2$ with geophysical techniques is challenging. Furthermore, geophysical monitoring is expensive and provides economic constraints on the feasibility and lifetime of industrial $CO_2$ storage. Figure 4.11 shows that, after about 200 years of depressurisation, the width remains nearly constant for a further $\sim 10^4$ years. 4D seismic images are mostly used to interpret the motion of injected $CO_2$ in the subsurface. Stalling is likely to hinder the interpretation of repeat seismic images. For example, it is possible that if surveys must be conducted hundreds of

years after injection, observed width-stagnation may be interpreted as immobilisation due to secondary trapping mechanisms. It is not immediately clear what effect trapping will have on stalling. However, as the plume becomes very thin, the Bond number becomes large, meaning that capillary forces begin to dominate over buoyancy. This has the effect of blunting the nose of the plume [Zhao et al., 2014]. As blunting is likely to increase $\partial h/\partial x|_{\mathcal{N}}$, it may fully or partially suppress stalling. Stalling may therefore may be a theoretical artefact of neglecting capillarity. Due the approximation of a 2D flowfield with 1D equations, stalling may also be a theoretical artefact of vertical flow equilibrium. Clearly, further work is required to study the impact of capillarity, vertical flow equilibrium and plume shape on post-injection migration.

### 4.8.3 Post-stalling gravity-currents

The main goal of $CO_2$ storage is to safely sequester large quantities of $CO_2$ rather than emitting this $CO_2$ to the atmosphere. To achieve a meaningful reduction in emissions, the $CO_2$ must be trapped on timescales of $>10^3$ years [Benson and Cole, 2008]. This has motivated considerable interest in the long-term fate of $CO_2$ injected in saline aquifers [e.g., Hesse et al., 2008, MacMinn et al., 2010, 2011]. The late-time behaviour of $CO_2$ after injection is characterised by the spreading of incompressible gravity currents. This section has demonstrated that two earlier regimes occur before the development of a 'classical' representation of a gravity-current where the width asymptotically approaches a late-time width scaling ($w \sim t^{1/3}$). Nevertheless, results presented here suggest that the gravity-current regime does not fully initiate for thousands to tens of thousands of years—comparable to the timescale suggested by Benson and Cole [2008] for viable storage. Therefore, in neglecting depressurisation and stalling, previous studies on post-injection migration and trapping during the spreading of an incompressible

$CO_2$ gravity-current may not provide wholly representative predictions. Accordingly, it is recommended that future work is undertaken to incorporate trapping mechanisms into the model derived in this thesis (see §5.3.1). Although this would be straightforward in the sense of combining the above model with that of MacMinn et al. [2010, 2011], it would nevertheless involve a considerable amount of mathematical labour beyond the scope of this work.

## 4.9 Conclusions

In this chapter, a systematic study of the post-injection migration of gas and water has been performed. Initially, it was demonstrated that the single-aquifer model ($\Lambda_w^s = 0$) developed in this thesis reduces to the well known models of Huppert and Woods [1995], Hesse et al. [2007], MacMinn and Juanes [2009] in the incompressible limit ($N_{cw} \to 0$) and in the absence of residual trapping. Unlike previous incompressible studies, the model developed above retains the imprint from injection—i.e. the pressure and fluid distributions at $t = 1$—allowing for a more rigorous study of post-injection dynamics.

Much like during injection, 'strong-leakage' and 'no-leakage' limits were identified as endmembers for post-injection depressurisation. For intermediate leakage numbers ($10^{-7} \ll \Lambda_w^s \ll 1/R_A^2$) the pressure in aquifer 2 can locally rise until it transitions to the late-time strong-leakage limit. After many injection times have elapsed, pressure dissipation results in a decay in pressure that tends towards being phase-static.

The plume shape at the end of injection is crucial for determining the dynamics of horizontal spreading in the absence of a strong overpressure from injection. Plumes that have a pronounced tongued shape—as expected for $\mathcal{M} > 1$—experience a period of 'stalling', where the nose of the plume does not noticeably propagate. This stalling phenomenon is caused by a gradient in the interfacial thickness at the

nose of the gas plume that is sufficiently small that it drives negligible horizontal flow. During stalling, slumping drives a thickening front towards the nose. When this front reaches the nose, the gradient increases and the plume's width can grow—marking the end of stalling. For late times, the gas plume behaves as a confined gravity current in a porous aquifer [Huppert and Woods, 1995].

In the absence of vertical gas leakage, and in the presence of vertical pressure dissipation, it has been shown that post-injection gas migration is characterised by three distinct regimes that form a continuous evolution: Depressurisation, stalling and late-time gravity currents. This continuum approach to modelling post-injection migration is only possible if the full end-of-injection state is incorporated into a compressible model. Therefore the model developed in this thesis constitutes a unique tool for studying the entire life cycle of fluid injection into aquifers—layered or otherwise.

Subsequently, controls on the termination of gas leakage were studied. First, a study was performed on the interplay between horizontal and vertical pressure dissipation and the distribution of capillary pressure. It was shown that gas expansion, gas slumping and pressure dissipation are all coupled mechanisms that modify capillary pressure in the post-injection phase. Initially, during post-injection migration, the two capillary pressure limits ($k^{\star}_{rw} \gg \Lambda^{s}_{w} h^{n}$ and $k^{\star}_{rw} \ll \Lambda^{s}_{w} h^{n}$) are retained. These limits converge after depressurisation has approximately equilibrated the vertical pressure distribution. A brief example was also provided that demonstrated the vast number of coupled mechanisms that control the termination of gas leakage. The degree of complexity required to fully understand the controls on the termination of gas leaked was deemed beyond the scope of this current work, prompting recommendations for future work.

In summary, this chapter has shown that the model developed throughout this thesis can be applied to the well-studied problem of post-injection migration in the subsurface. Through retaining the end-of-injection state, results have identified

new flow regimes before the onset of late-time self-similarity, and demonstrated that there is clearly considerable work required on the topic of post-injection gas migration. The model developed above provides a powerful tool for researching these problems.

# Chapter 5

# Conclusions

## 5.1 Thesis summary

The large-scale injection of fluids into layered aquifers can lead to the development of complex flows that are poorly understood. Although geological stratification has been shown to have a crucial impact on flow, the majority of fluid dynamical studies for large-scale gas injection typically neglect layering. This thesis has aimed to characterise the dynamics of fluid injection into a system of layered aquifers. To achieve this, a novel and efficient, vertically-integrated theoretical model, based on a gravity current formulation, has been developed in Chapters 2 and 3. The model domain consists of an arbitrary number relatively thick, high permeability aquifers that are separated by thin, low permeability seals. All aquifers and seals were taken to be uniform and horizontal. The entire domain is assumed to be initially saturated with water, which is assumed to be the wetting phase. Both fluids (water and gas) and the rock matrix were taken to be compressible. A weak deviation from the classical gravity-current approach was introduced to account for a non-hydrostatic component to the vertical pressure distribution associated with weak vertical flow. This introduces new terms related to leakage into a set of coupled nonlinear PDEs that describe lateral flow within each aquifer. Imposing global conservation of mass leads to an invertible system of coupled equations for

vertical water flow and algebraic expressions for vertical gas flow. Without vertical flow, the model reduces to the planar equivalent of Mathias et al. [2011b].

### 5.1.1 Coupling pressure dissipation with lateral gas transport

In Chapter 2, the model development focused on fluid injection into a layered system in which only water can leak vertically. This requires that the capillary entry pressure of the seals is never exceeded during gas injection, meaning that gas remains within the injection aquifer. Conversely, the wetting phase—water—remains connected throughout the system. Fluid injection therefore dissipates pressure via both lateral and vertical water migration. Non-dimensionalisation of the governing PDEs shows that the ratio of vertical to horizontal pressure dissipation is predominantly governed by the leakage number [$\Lambda_w^s \equiv \lambda_w^s H/(\lambda_w b)$]. Through comparison with a full 2D groundwater flow model, it was shown that the reduced order model can accurately capture the full 2D pressure field in a layered domain, at a fraction of the computational cost. Two limiting cases for pressure buildup were then identified—'strong-leakage' and 'no-leakage'—in which, for water injection, the model can be further reduced to a single PDE that permits analytical solutions. In the 'no-leakage' limit, effectively infinite resistance to vertical flow confines the pressure perturbation to the injection layer. In the late-time 'strong-leakage' limit, the pressure perturbation is equally distributed vertically across all aquifers. As such, during water injection the pressure evolves as for injection into a single aquifer of thickness $N_z H$.

Although previous studies have also studied the reduction in pressure buildup due to vertical water flow [e.g., Birkholzer et al., 2009, Chang et al., 2013, Gasda and Aavatsmark, 2019], none have commented on the subsequent coupling with the dynamics of the gas plume. Results in Chapter 2 demonstrated that increased vertical pressure dissipation can significantly reduce the lateral extent of the gas

plume. This compaction is attributed to a reduction in the lateral pressure gradient that, alongside buoyancy, drives horizontal transport.

As water remains connected across the gas-saturated region through thin wetting films, it can conduct a weak vertical flux proportional to the relative permeability of water in the gas region ($k^{\star}_{rw}$). Increasing obstruction to vertical water flow from the gas (decreasing $k^{\star}_{rw}$), partially suppresses vertical pressure dissipation. However, as water can still flow vertically downwards through underlying seals, and upwards for distances $x > w$, vertical pressure dissipation still occurs and will always result in compaction of the gas plume for non-vanishing values of $\Lambda^{s}_{w}$.

### 5.1.2 Gas leakage

In Chapter 3, the theoretical model developed in the previous chapter was extended to allow for distributed vertical gas leakage, which occurs when the capillary pressure at the top of a gas-bearing aquifer exceeds a threshold capillary entry pressure. As such, a key constraint on the initiation of gas leakage, and subsequent dynamics, is the buildup of capillary pressure during injection (relative to entry pressure). Two limiting cases for capillary pressure buildup were identified. In the limit of $k^{\star}_{rw} \gg \Lambda^{s}_{w} h^{n}$, the gas provides no obstruction to vertical water flow, meaning that the capillary pressure simplifies to a phase-static distribution. In the limit of $k^{\star}_{rw} \ll \Lambda^{s}_{w} h^{n}$, the gas fully obstructs vertical water flow, thus decoupling the water pressure at the top of the aquifer from water pressure at the gas–water interface. Instead, the contribution from the water to the capillary pressure is approximated as hydrostatic across the overlying seal. The resulting capillary pressure distribution in this limit is broader and 2-3 orders of magnitude larger than the corresponding 'no obstruction' limit.

Several previous studies have relied on the approximation that emerges in the $k^{\star}_{rw} \gg \Lambda^{s}_{w} h^{n}$ limit. Correspondingly, due to the low associated capillary pressures, these studies assume that there is insufficient capillary pressure to initiate

gas leakage. Although $k^{\star}_{rw}$ is poorly constrained, it is likely to be very small. Accordingly, capillary pressure buildup is likely to be considerably stronger than previously assumed.

Subsequently in Chapter 3, the leading controls on gas leakage were studied. The magnitude of capillary pressure at the top of a gas-bearing aquifer, relative to the capillary entry pressure, sets the horizontal length scale over which gas leakage occurs. The rate of gas leakage is set by a complex interplay between capillary pressure buildup, pressure dissipation and fluid migration. It was demonstrated that the amount of leaked gas increases with the leakage number ($\Lambda^s_w$) and with the mobility of gas in the seals relative to that of water ($\mathcal{M}^s_z$). For small $\Lambda^s_w$ and $\mathcal{M}^s_z$, the pressure field is dominated by lateral and vertical water flow, resulting in a linear scaling between these quantities and the amount of gas leaked. For high values of $\Lambda^s_w$ and $\mathcal{M}^s_z$, gas leakage increasingly dominates the global pressure field and acts to suppress further gas leakage. Lastly, it was shown that, for typical parameters at Sleipner, the obstruction of vertical water flow through the gas region could plausibly result in a sufficient buildup of capillary pressure to trigger, or significantly enhance, $CO_2$ leakage.

### 5.1.3 Post-injection

In Chapter 4, post-injection dynamics were studied by 'switching-off' the injection term in the governing PDEs after the end of injection (i.e., $\mathcal{I}_\alpha = 0$ for $t \geq 1$). Previous studies of post-injection gas migration are typically concerned with the long term fate of $CO_2$. These studies have therefore neglected compressibility, allowing for the determination of similarity solutions to the corresponding single-aquifer PDE. Naturally, the late-time behaviour of self-similar systems is invariant to the shape of the plume at the end of injection. Accordingly, previous studies—with the exception of MacMinn and Juanes [2009], MacMinn et al. [2010, 2011]—typically do not retain the characteristic tongued end-of-injection plume shape,

and instead initialise the system with a step function to allow for comparison with experiments. The model developed in this thesis simulates both injection and post-injection phases in a continuum, and therefore fully retains both the pressure field and plume shape at the end of injection as initial conditions for post-injection migration. This approach has been used to develop unique insights into the dynamics of post-injection fluid migration, during which three principal regimes are identified: Depressurisation, stalling and gravity currents.

The depressurisation regime is marked by the decay of overpressure associated with fluid injection. As with during fluid injection, the evolution of pressure is controlled by the competition between horizontal and vertical pressure dissipation, manifested in 'no-leakage' and 'strong-leakage' limits that respectively provide upper and lower bounds on the pressure decay in the injection aquifer. After the end of injection, the pressure in overlying and underlying aquifers can continue to rise locally for some period of time. This increase occurs due to the delay associated with vertical pressure dissipation. This pressure increase ends when the pressure collapses to the late-time strong-leakage limit. During depressurisation, the role of buoyancy in post-injection gas migration becomes dominant relative to the decaying overpressure from injection. The depressurisation regime ends when the pressure distribution is approximately phase-static, which marks the onset of the subsequent 'stalling regime'.

The stalling regime is marked by a period of negligible growth in the width of the gas plume, which is a direct result of the end-of-injection plume shape. Typically, gas injection occurs for high mobility ratios ($\mathcal{M} \gg 1$), resulting in a plume that has a characteristic tongued shape during injection. In the absence of overpressure from injection, propagation of the nose of the plume is driven by the gradient in plume thickness ($\partial h/\partial x|_{\mathcal{N}}$). After depressurisation, when the flow is driven primarily by buoyancy, the thickness gradient for tongued plumes is insufficient for the gas plume to propagate laterally, or to build in thickness, producing a period in which the width of the plume does not appreciably grow (i.e., stalling).

Stalling occurs independent of compressibility effects, and it was demonstrated that a variety of convex/tongued plume shapes will stall. Plume shapes that do not produce small values of $\partial h/\partial x|_{\mathcal{N}}$ will not stall. For example, an instantaneously released step function will immediately develop an early-time spreading regime before transitioning towards late-time self-similarity [Hesse et al., 2007]. Stalling ends as slumping drives a thickening front towards the nose, resulting in growth in $\partial h/\partial x|_{\mathcal{N}}$ that eventually drives non-negligible flow at the nose. Although late-time self-similar behaviour is independent of the initial plume shape, this work has showed that end-of-injection plume shape is crucial for intermediate-time dynamics of a migrating gas plume.

After stalling, the plume begins behaving like a classic confined gravity current. As the overpressure from injection has mostly faded, the pressure distribution is approximately phase-static and is therefore controlled by the shape of the migrating plume. During the gravity-current regime, the plume continues slumping, driving lateral propagation that asymptotically approaches $w \sim t^{1/3}$ [Huppert and Woods, 1995, Hesse et al., 2007]. The plume evolves towards this late-time limit as it becomes sufficiently thin that the ambient water viscosity can be neglected.

The results summarised above assumed that the capillary entry pressure was sufficiently high that gas leakage never occurs. By calculating the capillary pressure evolution for these results, theoretical constraints on the termination of gas leakage were provided. It was shown that, as the pressure distribution becomes phase-static, the $k^{\star}_{rw} \gg \Lambda^{s}_{w} h^{n}$ and $k^{\star}_{rw} \ll \Lambda^{s}_{w} h^{n}$ limits for capillary pressure begin converging. Post-injection capillary pressure evolution was demonstrated to be nonlinear, and was shown to be largely controlled by three competing mechanisms: Gas expansion, gas slumping and pressure dissipation. Finally, a single example case of post-injection gas leakage was shown to demonstrate the complexity of the associated dynamics. This demonstration highlights the versatility of the model for studying the entire life of large-scale industrial gas injection and post-injection migration in a layered, and potentially leaky, stack of aquifers.

## 5.2 Limitations

In order to study the dynamics associated with fluid injection in layered aquifers, a new model was developed over the course of Chapters 2 and 3 before being trivially modified in Chapter 4 to study the post-injection behaviour. Vertically-integrated sharp-interface models—such as the model used in this work—are typically valid for large-scale, predominantly horizontal flows in which vertical gravity-segregation is fast [e.g., Simpson, 1982, Huppert and Woods, 1995, Golding et al., 2011]. Naturally, the formulation of this model has required the use of large number of assumptions that limit its validity and applicability. Accordingly, the model has numerous limitations that must be acknowledged, including:

- By design, the model domain consists of a regular layering of uniform aquifers and seals. As such, the model in its current form cannot be applied to study more realistic layered aquifers that often feature topography, local variations in thickness, terminating strata, and lateral heterogeneity.

- In neglecting compressibility in the seals, the model inherently assumes that aquifers are separated by thin seals. Figure 2.3 demonstrates that errors in the global pressure field increase with seal thickness. Therefore, the model cannot be used to study systems in which the seal thickness becomes comparable to aquifer thickness (i.e., when $b \sim H$).

- In using a gravity-current formulation, the model assumes that flow is predominantly horizontal. This approximation breaks down in regions of strong vertical flow, such as near wells during strong injection/extraction [e.g., Bandilla et al., 2019].

- In assuming the fluids are separated by a sharp interface, the model assumes that capillary effects in the transition zone can be neglected. Although Golding et al. [2013] demonstrated that the capillary transition zone does not play a leading-order role on the spreading dynamics of injected $CO_2$,

it is unknown if this approximation remains valid for other fluids—such as methane or hydrogen.

- The model derivation invokes the standard gravity current assumption that the saturation in each 'fluid region' is constant. In the gas region, a decrease in water saturation corresponds to an increase in capillary pressure. Most models for capillary pressure are very steep near the residual water saturation, such that very large variations in capillary pressure correspond to very small variations in water saturation. This feature motivates the assumption that, within the gas plume, $p_c$ can vary over a wide range while $s_w$ remains essentially constant. However, as relative permeability is a function of saturation, it is likely that capillary pressure buildup results in a small decrease in water saturation, which further reduces the vertical water flux. It is possible that this negative feedback, which supresses further vertical water leakage, may shift the capillary pressure buildup regime towards the $\Lambda_w^s h^n / k_{rw}^\star \gg 1$ limit; potentially resulting in more substantial capillary pressure buildup than described in Chapter 3. If true, this would suggest that $CO_2$ leakage during CCS is even more likely than shown during this thesis. Including this feedback effect is beyond the current scope of model, and would require incorporating a more rigorous formulation for multiphase vertical flow than is currently used.

- For scenarios involving gas leakage, the model assumes no gas storage in the seals and that the initial travel-time across the seal is negligible. As with neglecting compressibility in the seals, this approximation becomes increasingly poor for progressively thicker seals—further limiting the model to studying layered systems with thin sealing layers.

- Thermal effects have been neglected from the model. This approximation can be particularly problematic near injection wells or in thick aquifers with high geothermal gradients. Thermal effects become important in the context

of subsurface gas injection, where strong gradients in temperature lead to strong variations in viscosity, resulting in additional nonlinearities in the governing equations [e.g., Nordbotten et al., 2005].

- The model neglects chemical effects such as: phase changes, salt precipitation, multi-component phases and wettability alteration. The model is therefore at a significant disadvantage, relative to conventional reservoir simulators and standard multiphase flow models [e.g., TOUGH2-ECO2N Pruess et al., 1999, Pruess, 2005] for site-specific case studies.

Many of the impacts of the above limitations can be reduced, or removed altogether, through simple model extensions. Examples of these extensions, that form the basis of recommended future work, are discussed in detail in the next section.

## 5.3 Future work

The model developed in this thesis constitutes a unique tool for accurately and efficiently studying pressure buildup and fluid migration during and after fluid injection into a system of layered aquifers. While the reduced order model does not have all of the machinery of a full reservoir simulator, its efficiency allows for a systematic exploration of a vast parameter space that governs fluid dynamics in a stratified aquifer. Accordingly, through relatively simple extensions, the model can be tailored to investigate a diverse array of applications. Described below are numerous examples of model extensions that are recommended avenues of future work.

### 5.3.1 Model extension to include trapping mechanisms

As outlined in the introductory chapter, the ultimate fate of injected $CO_2$ depends on various trapping mechanisms, including: (1) Structural/hydrodynamic

trapping, where the high entry pressure and extremely low permeability of an overlying thick sealing formation traps the $CO_2$ in the target formation; (2) Residual/capillary trapping, where capillary forces disconnect and immobilise $CO_2$ at the pore scale; (3) Solubility trapping, where $CO_2$ dissolves in the ambient water and which is enhanced by a gravitational instability. As the uppermost boundary is assumed to be perfectly impermeable, hydrodynamic trapping is inherently included in the model. Several incompressible single-aquifer gravity-current models have incorporated both residual and solubility trapping [e.g., Hesse et al., 2008, Juanes et al., 2010, MacMinn et al., 2010, Gasda et al., 2011, MacMinn et al., 2011, 2012]. In Chapter 4 it was shown that both compressibility and retaining the complete end-of-injection state [$p(x, t = 1)$ and $h(x, t = 1)$] are crucial in capturing the complete post-injection transition towards late-time self-similarity. Therefore, incorporating these trapping mechanisms into the model using the methods outlined in the above-referenced studies would likely provide new insights into the storage capacity of aquifers, and layered aquifers in particular, for geological $CO_2$ storage. The interactions between pressure dissipation and compressibility within the framework of previously outlined post-injection flow regimes are likely to alter the efficiency of trapping. For example, during post-injection stalling, the plume grows negligibly in width, reducing the length of the gas–water interface relative to an un-stalled scenario. As the rate of $CO_2$ dissolution depends on the interfacial length, plume stalling is likely to temporarily reduce the rate of $CO_2$ dissolution and partially suppress dissolution trapping.

### 5.3.2 Relaxing the constraint of thin seals

Interpretation of seismic images of Sleipner and other natural analogues [e.g., Foschi et al., 2014, 2018], suggest that a vertical segregation of gas in reservoirs that are separated by thin seals is commonplace in the subsurface. These observations prompted the derivation of a model that utilizes a layered domain in which

high permeability aquifers are separated by thin low permeability seals, such that $b \ll H$. Figure 2.3 in Chapter 2 shows that the RMS error, relative to a full 2D groundwater flow model, decreases as $b$ becomes progressively smaller. Note, however, that diffusive pressure dissipation does not inherently require that the intermediate seals are thin. Indeed, recent work by Gasda and Aavatsmark [2019] presents a model in which pressure is dissipated vertically out of a solitary layer into semi-infinite seals above and below. As in this thesis, they provide an efficient system of coupled 1D PDEs that demonstrates that diffusive pressure dissipation reduces pressure buildup in the injection layer. They do not consider the coupling between vertical pressure dissipation and the dynamics of the gas plume.

Extending the model to allow for thicker seals by solving an additional vertical diffusion equation for pressure in the seals is entirely possible without a great loss in computational efficiency. This would be an important step in generalising the model to allow for simulations of flow in arbitrary reservoir geometries that are more realistic than the uniform horizontally layered aquifers used in this study.

### 5.3.3 Extending to pseudo-3D

The extension of the model presented in earlier chapters to pseudo-3D is relatively straightforward. Consider conservation of mass for an arbitrary phase $\alpha$:

$$\frac{\partial}{\partial t}\left(\rho_\alpha \phi s_\alpha\right) + \boldsymbol{\nabla} \cdot \left(\rho_\alpha \boldsymbol{q}_\alpha\right) = \mathcal{I}_\alpha, \tag{5.1}$$

where the divergence of the mass flux in three dimensions is given by

$$\boldsymbol{\nabla} \cdot \left(\rho_\alpha \boldsymbol{q}_\alpha\right) = \frac{\partial}{\partial x}\left(\rho_\alpha q_{\alpha,x}\right) + \frac{\partial}{\partial y}\left(\rho_\alpha q_{\alpha,y}\right) + \frac{\partial}{\partial z}\left(\rho_\alpha q_{\alpha,z}\right). \tag{5.2}$$

From this point the derivation continues as outlined in Chapters 2 and 3. A new mass flux derivative in the $y$ direction will appear, making a set of already

visually imposing PDEs even more cumbersome. Although this mathematical extension is relatively trivial, implementing it numerically is more complicated. The computation memory required for a uniform domain with $\mathcal{L}_x = \mathcal{L}_y$ will square relative to the pseudo-2D model. To alleviate run time and memory concerns, it is recommended that any extension of the code used in this project uses an unstructured adaptive grid. This grid should be designed to resolve the fine details of the plume; in particular, the resolution should be maximum around the injection well, where steepest gradients in $h$ are located.

### 5.3.4 Extension to include variable topography

One key assumption used in the derivation of the model used throughout this thesis is that all the aquifers and seals are uniformly distributed and perfectly horizontally bedded. As gas migration is predominantly gravity driven, it is well known that variable topography can influence the migration of gas. Indeed, many studies have shown that topography has a leading-order control on the distribution of fluids during injection at Sleipner [e.g., Chadwick and Noy, 2010, Andrew et al., 2015, Cowton et al., 2018].

A simple extension to the model to include topographic variations has been developed, but a full exploration of gas migration in topographically variable aquifers is beyond the scope of this work. Consider the top of an aquifer with arbitrary topography that is represented by some function $f(X, Z)$ in a Cartesian frame $[X, Z]$. Any point on this function has a complimentary coordinate system $[x, z]$ where $x$ and $z$ are unit vectors pointing parallel and orthogonal to $f(X, Z)$, which has slope $\varphi(x)$ (see Figure 5.1). The aquifer is of constant thickness $H$, such that the bottom of the aquifer is parallel everywhere to the upper surface. The thin seals ($b \ll H$) that separate the aquifers are defined such that they are parallel to the aquifers. As such, one only needs to define a single surface $f(X, Z)$ and then

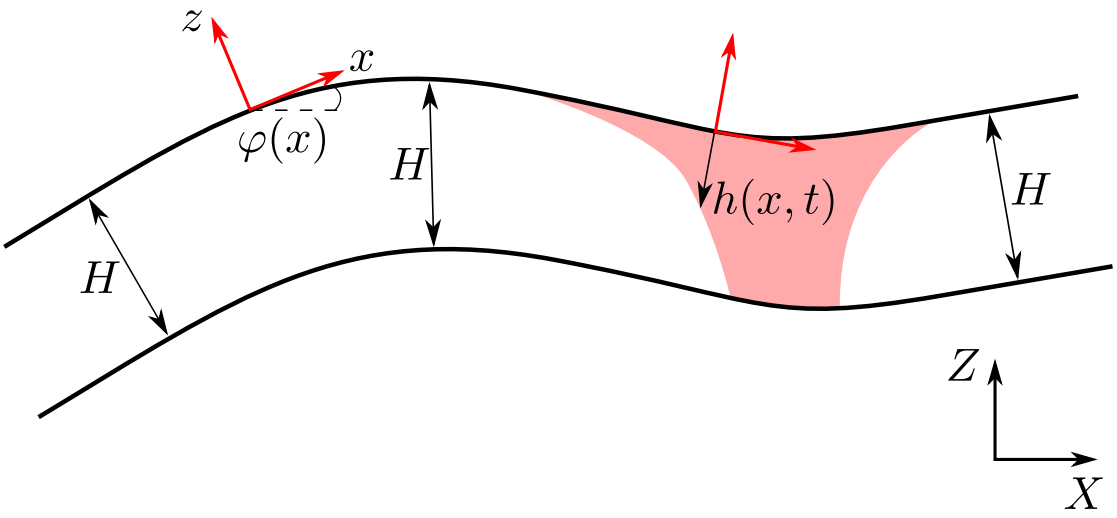


**Figure 5.1:** A section of the extended topographic model in a single-aquifer of constant thickness $H$. Note that the coordinate system $(x, z)$ is aligned tangential and orthogonal to the upper boundary of the aquifer and is not aligned with the reference Cartesian system, except when $\varphi = 0$.

calculate curves parallel to $f(X, Z)$ that are separated by distances defined by the thickness of the aquifers and the seals[1].

A brief summary of the associated derivation is provided here, along with the end-result—governing PDEs for gas and water flow, with leakage in topographic domain. The derivation begins, as in all chapters, by defining conservation of mass for an arbitrary phase $\alpha$:

$$\frac{\partial}{\partial t}\left(\rho_\alpha \phi s_\alpha\right) + \boldsymbol{\nabla} \cdot \left(\rho_\alpha \boldsymbol{q}_\alpha\right) = \mathcal{I}_\alpha. \tag{5.3}$$

In the topographic coordinate frame $[x, z]$, flow can be resolved into two principal orthogonal components: (1) Along-slope in the $x$ direction and (2) across-slope in the $z$ direction. Note that $z$ does not point vertically upward unless $\varphi = 0$. The two components of the Darcy flux for phase $\alpha$ in the $n^{th}$ aquifer are:

[1]The calculation of parallel surfaces is achieved numerically using parallel_curve.m—A function available on the MATLAB File Exchange (see www.mathworks.com/matlabcentral/fileexchange/27873-parallel-curves).

$$q^n_{\alpha,x} = -\lambda^n_\alpha \left( \frac{\partial p_\alpha}{\partial x} + \rho_\alpha g \sin\left[\varphi(x)\right] \right) \tag{5.4a}$$

$$q^n_{\alpha,z} = -\lambda^n_\alpha \left( \frac{\partial p_\alpha}{\partial z} + \rho_\alpha g \cos\left[\varphi(x)\right] \right). \tag{5.4b}$$

From here, the derivation proceeds as outlined in Chapters 2 and 3. The pressure field is obtained by rearranging and integrating Equations (5.4)b. The same assumed vertical flow structures outlined in Chapters 2 and 3 are applied, but now in the new topographic coordinate system. Proceeding with the now well-established derivation procedure yields governing PDEs for gas and water in the $n^{th}$ topographically-varying aquifer,

$$\begin{aligned} &\phi\left[(H - s_g h^n)(c_r + c_w)\frac{\partial p^n}{\partial t} - s_g \frac{\partial h^n}{\partial t}\right] \\ &- \frac{\partial}{\partial x}\left\{\lambda_w (H - h^n)\left[\frac{\partial p^n}{\partial x} - \rho_w g \cos(\varphi)\frac{\partial h^n}{\partial x} + \rho_w g \sin(\varphi)\right]\right. \\ &\left. + \frac{1}{6}\frac{\partial}{\partial x}\left[(H - h^n)^2 (q^{n,B}_{w,z} + 2q^{n,T}_{w,z})\right]\right\} = -(q^{n,T}_{w,z} - q^{n,B}_{w,z}) + \frac{\mathcal{I}^n_w H}{\rho_w} \end{aligned} \tag{5.5}$$

and

$$\begin{aligned} &\rho^n_g \phi s_g \left[(c_r + \frac{\rho^0_g}{\rho^n_g} c_g) h^n \frac{\partial p^{n,I}}{\partial t} + \frac{\partial h^n}{\partial t}\right] - \frac{\partial}{\partial x}\left[\rho^n_g \lambda_g h^n \left(\frac{\partial p^{n,I}}{\partial x}\right.\right. \\ &\left.\left. - \left\{\rho^n_g g \cos(\varphi) + \frac{\rho^{s+1}_g}{\rho^n_g}\frac{q^{s+1}_{g,z}}{\lambda_g}\right\}\frac{\partial h^n}{\partial x} - \frac{h^n}{2\lambda_g}\frac{\rho^{s+1}_g}{\rho^n_g}\frac{\partial q^{s+1}_{g,z}}{\partial x} + \rho_g g \sin(\varphi)\right)\right] \\ &= -\left(\rho^{s+1}_g q^{s+1}_g - \rho^s_g q^s_g\right) + \mathcal{I}^n_g H. \end{aligned} \tag{5.6}$$

Noting that, as the topography is gently sloping, terms involving $\partial\varphi/\partial x$ have been neglected. These governing PDEs are essentially identical to those presented in

Chapter 3 with a few key difference: (1) The new governing equations apply vertical equilibrium and weak deviations from vertical equilibrium in the topographic coordinate system; (2) A gravitational component $\rho_\alpha g \sin(\varphi)$ now appears in the along-slope direction ($x$) in the flux divergence term; (3) The gravitational contribution multiplying $\partial h/\partial x$ is now multiplied by a factor of $\cos(\varphi)$ to account for the new local topographic coordinate system. The equations that couple the aquifers through vertical flow are similarly altered. The pseudo-vertical fluxes are oriented normal to the seals (i.e. in the $z$ direction). For small values of $\varphi$, this approximation is sensible and does not lead to large errors. A derivation—that is not shown here for brevity—demonstrates that the extension to a topographic framework means that vertical flux terms that include $\rho_\alpha g$ become multiplied by $\cos(\varphi)$. For example the linear system of equations that couple vertical water flow becomes:

$$\left(\frac{H-h^n}{2\lambda_w}\right) q_{w,z}^{s+1} + \left(\frac{h^{n-1}}{\lambda_w^\star} + \frac{b}{\lambda_w^s} + \frac{H-h^n}{2\lambda_w}\right) q_{w,z}^{s} = -\Big[p^n - p^{n-1} + \rho_w g \cos(\varphi)(h^{n-1} + b + H - h^n)\Big]. \tag{5.7}$$

Some basic benchmarking and exploration of gas injection and migration in topographically varying aquifers has been performed. Although this section is not the place for a detailed discussion of preliminary results, it is worth viewing two sets of results. Figure 5.2 shows the drastic effect that even small angles can have on post-injection gas migration. Figure 5.3 shows how upslope post-injection migration can lead to the formation of a gas cap. These two simple examples highlight an array of potentially interesting scenarios that the model can easily be adapted to explore. Furthermore, once a model that incorporates variable topography—preferably in pseudo-3D—has been fully developed, it is possible to simulate injection and migration for 'real world' case studies (e.g., Sleipner).

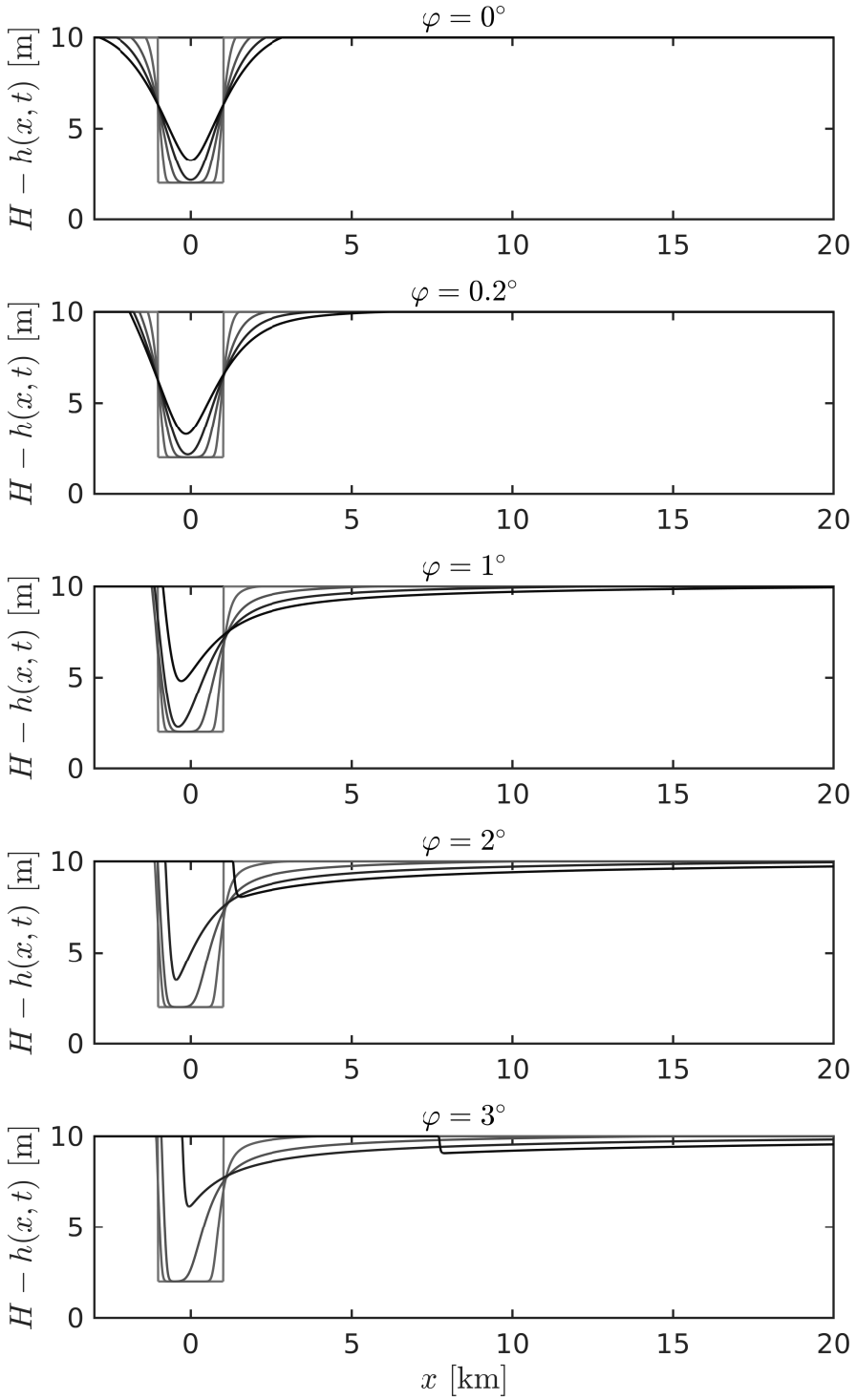


**Figure 5.2:** Plume shapes at $t = [0,\ 20,\ 100,\ 250 \text{ and } 500]$ after the instantaneous release of $CO_2$ in aquifers with uniform slope $\varphi$.

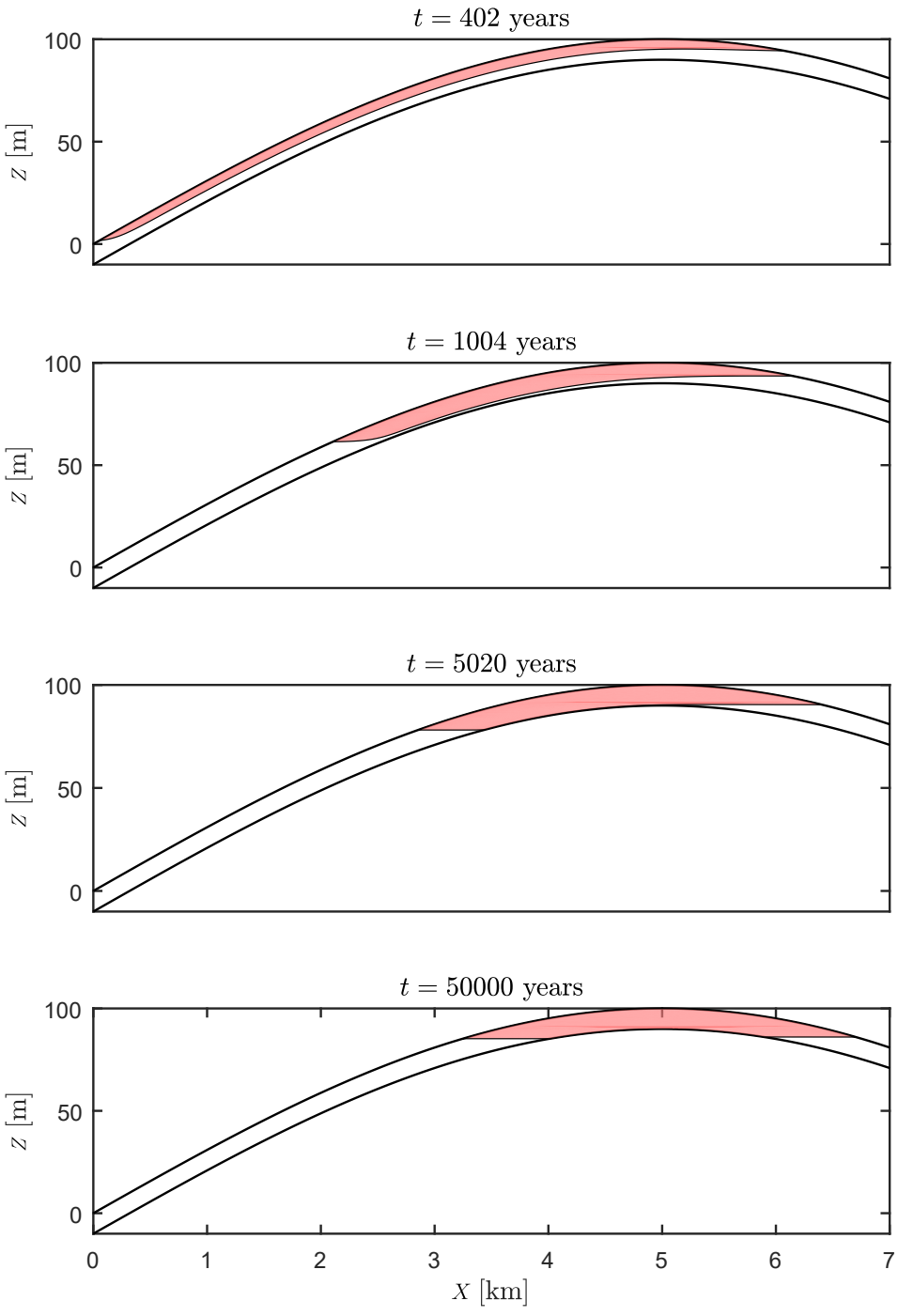


**Figure 5.3:** Upslope migration of gas (plotted in pink for various times), leading to the formation of a gas-cap in an antiformal structure, after an instantaneous release of an arbitrary volume of gas into a single aquifer at some distance downslope.

### 5.3.5 Geological heterogeneity

Extending single aquifer gravity current models to include vertical flow in a stratified system of aquifers and seals (i.e., vertical heterogeneity) has been a considerable task. For simplicity, simulations presented in this thesis have neglected lateral heterogeneity. This assumption is inconsistent with real subsurface aquifers, in which considerable variations in key parameters are observed. Lateral heterogeneity occurs across all scales that are important to fluid flow. At the pore scale, flow is dominated by the heterogeneous distribution of pore/throat sizes and geometries [e.g., Krevor et al., 2011]. Is is impossible to include pore scale variations in basin scale models of fluid flow. At length scales of $10 - 10^4$ m, variations in depositional facies can produce variations in porosity, permeability, wettability and entry pressure. In the case of permeability and entry pressure, these variations can span multiple orders of magnitude. Seismic analysis at Sleipner reveals the presence of a high permeability ($\sim$ 10D) sloping channel that subsequent simulations have suggested is responsible for a large lobe of northward migrating $CO_2$ [Zweigel et al., 2004, Williams and Chadwick, 2017, Cowton et al., 2018].

The theoretical model developed in this thesis is capable of incorporating simple heterogeneity that has a length scale greater than the grid size. Heterogeneous distributions of aquifer and seal parameters can be readily assigned. For example, consider a simple proof of concept case where a smooth but random distribution of capillary entry pressure is assigned to each seal in a four aquifer system. Comparisons with an equivalent simulation with homogeneous entry pressures reveal that heterogeneity in $p_c^E$ can have a significant impact on gas leakage and fluid distributions (Figure 5.4). When gas leakage occurs during gas injection into the bottom-most aquifer of a layered aquifer system with uniform seals, a symmetric and upward tapering stack of gravity-currents is formed (Figure 5.4, left panel). Conversely, gas leakage in the same system with a heterogeneous distribution in $p_c^E(x)$ produces a complex array of smaller gravity-currents (Figure 5.4, right

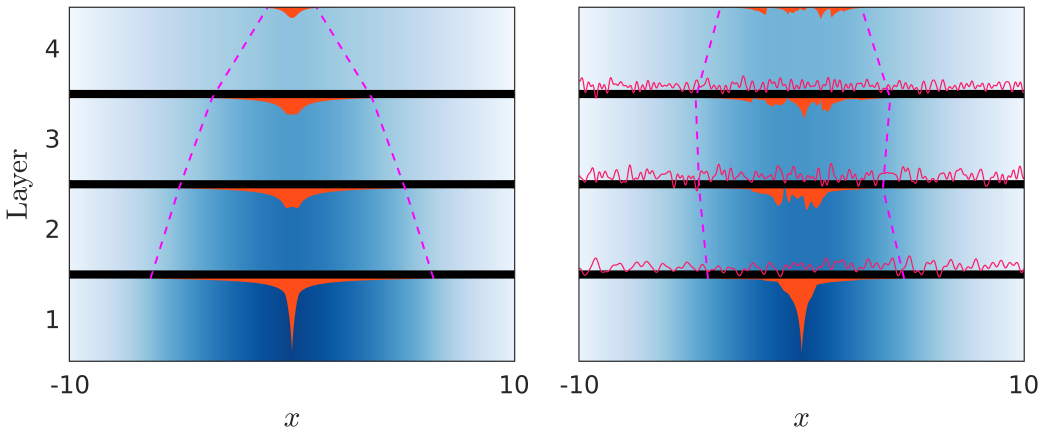


**Figure 5.4:** Plume shapes at the end of gas injection into aquifer 1 of a four-aquifer system containing a uniform and heterogeneous capillary-pressure distribution ($\tilde{p}_c^E = 0.3$) in the left and right panels, respectively. The heterogeneous distribution of $p_c^E$ is assigned with a smoothed-random function (plotted in red). The dashed magenta lines indicate the plume-width in each aquifer.

panel). The overall gas distribution displays no symmetry and has no pronounced tapering structure. This tapering effect, or lack thereof, may be visible in seismic images and may therefore provide some indication of gas leakage mechanisms in layered aquifers during CCS.

In Chapters 2 and 3 a new method was outlined for simulating distributed leakage within a layered aquifer system. Both the aquifers and seals in these systems are isotropic and homogeneous across their lateral extents. In numerous reservoirs/aquifers, interpretation of seismic images has inferred that geological heterogeneity has resulted in focused vertical leakage [e.g., Hurst et al., 2003, Crutchley et al., 2010, Sun et al., 2012, Foschi et al., 2014]. For example, at Sleipner a high permeability chimney/conduit/pipe is believed to focus $CO_2$ leakage across multiple aquifer, producing a system of stacked $CO_2$ gravity currents [e.g., Chadwick et al., 2004, 2005, Bickle et al., 2007]. Conduits are merely one of a diverse suite of geological structures that allow for the bypass of sealing layers [e.g., Cartwright et al., 2007]. Previously, it has been assumed that there is insufficient capillary pressure buildup for distributed leakage to occur. However, in Chapter 3 it was shown that low values of $k_{rw}^{\star}$ result in capillary pressures that are orders of magnitude larger than previously estimated from phase-static buoyant overpressure

($p_c^{n,T} \approx \Delta\rho g h$). This means that there likely exists a complex interplay between distributed and focused leakage that remains unexplored. To provide constraints on leakage mechanisms in aquifers that are targets for $CO_2$ storage, further investigations should be performed into the interactions between focused and distributed leakage.

### 5.3.6 Geomechanics & induced seismicity

It is well documented that subsurface industrial fluid injection or extraction can 'induce' or 'trigger' seismicity [e.g., Segall, 1989, Majer et al., 2007, Keranen et al., 2014, Pollyea et al., 2019]. Earthquakes are sudden releases in stored elastic strain energy along a fault plane that occur when a critical effective stress $\tau_{crit}$ is exceeded:

$$\tau_{crit} = \mu(\sigma_n - p) + \tau_0, \tag{5.8}$$

where $\mu$ is the coefficient of friction along the fault plane, $\sigma_n - p$ is the (tension-positive) effective normal stress (the difference between total normal stress $\sigma_n$ and pore pressure $p$) and $\tau_0$ is the cohesive strength of the fault plane [Ellsworth, 2013]. There are two principal mechanisms for triggering earthquakes by alteration of the effective stress [Simpson et al., 1988]: changes in pore pressure ($p$) and poroelastic deformation of the rock (changes in $\sigma_n$). The model presented in earlier chapters constitutes a novel and efficient method for solving for pore pressure during and after fluid injection into a system of layered aquifers. Therefore, given a known initial stress field, it is possible to calculate changes to the effective stress. Figure 5.5 compares the lithostatic effective stress to the overpressure at the end of gas injection into a seven-aquifer system that was considered in Chapter 2. The lithostatic stress can be approximated by $\sigma'_{\text{litho}} \approx (\rho_r - \rho_w)g(1-\phi)\Delta z$ where $\rho_r$ is the rock/sediment density (taken here to be constant for simplicity) and $\Delta z$ is the thickness of the overlying rock. Hydraulic fracturing occurs when the overpressure

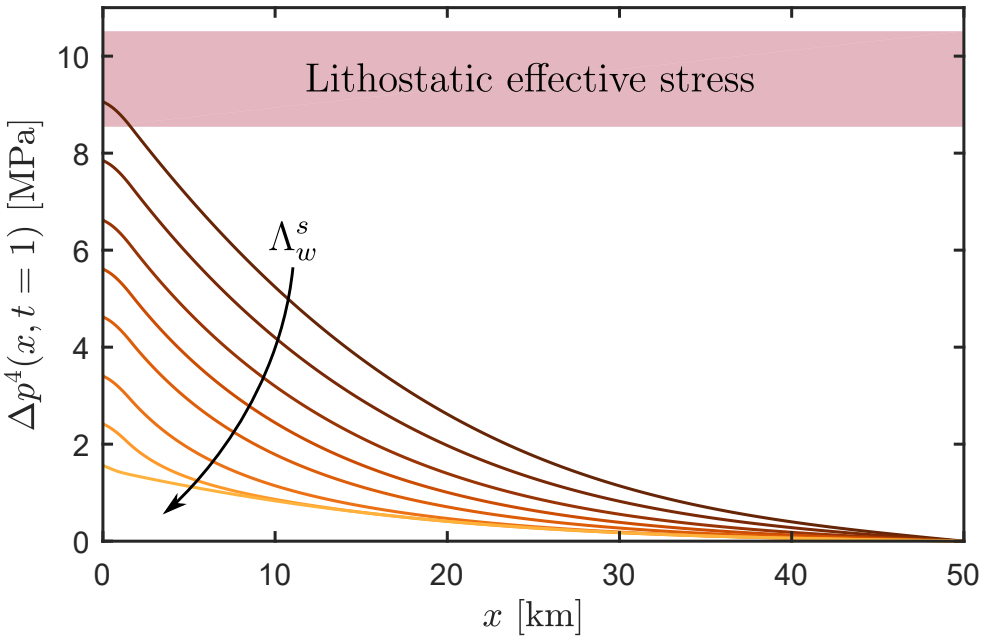


**Figure 5.5:** Overpressure at the end of gas injection into the central aquifer ($n = 4$) of a seven-aquifer system, plotted for reference parameters used in Chapter 2 (see table 2.1) and for $\log_{10}(\Lambda_w^s) = [-10,\ -7,\ -6.6,\ -6.3,\ -6,\ -5.6,\ -5$ and $-3]$. Shaded in pink is the lithostatic effective stress at 1 km, assuming a rock density of $\rho_r = 2450 \pm 150$ kg m$^{-3}$.

from injection exceeds the lithostatic effective stress ($\Delta p > \sigma'_{\text{litho}}$), which occurs in Figure 5.5 for vanishingly small leakage numbers. Vertical pressure dissipation reduces the maximum overpressure, and therefore reduces the risk of hydraulically fracturing the overburden. Stronger injection, lower compressibility and stronger confinement all act to increase pressure buildup, and therefore increase the likelihood of hydraulic fracture.

The efficiency of the model would allow for a Monte-Carlo analysis in which numerous runs are compared with a failure condition. This would allow for a stochastic prediction of the likelihood of failure in simple layered systems. To study the effect of rock deformation would require coupling with the full machinery of poroelasticity. This would be a considerable task, but remains of potential interest due to the numerous benefits of coupling geomechanics to an efficient subsurface flow model [Jha and Juanes, 2007].

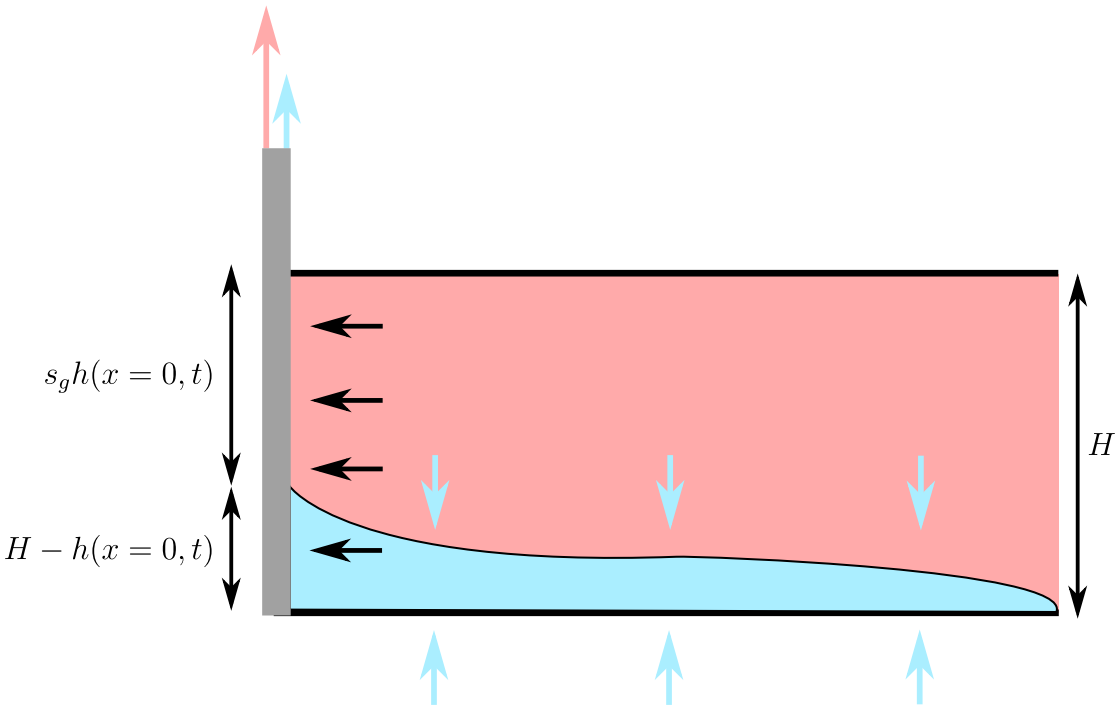


**Figure 5.6:** Illustration of interface-upconing during production from a well that spans the entire thickness of an aquifer. Light blue arrow indicate vertical water flow associated with vertical pressure dissipation.

### 5.3.7 Fluid extraction and EOR

This thesis has focused on characterising the dynamics associated with the injection of fluids, nominally gas or water, into layered aquifers. It is relatively trivial to modify the model developed in this thesis to study the extraction of fluids for industrial applications such as water or hydrocarbon production in layered reservoirs. During extraction from a well that spans the entire vertical extent of an aquifer of thickness $H$, both water and gas will be extracted in proportions that depend on the fluid saturations and the thickness of the gas column (Figure 5.6). Applying mass conservation and basic geometric considerations yields the total mass per unit length into the page ($M^{\text{out}}$) flowing into the well,

$$M^{\text{out}}(t) = s_g h(x=0,t)\rho_g(x=0,t)q_g^{\text{out}} + [1 - h(x=0,t)]\rho_w q_w^{\text{out}} \tag{5.9}$$

where the Darcy flux of an arbitrary phase $\alpha$ flowing into the well is given by

$$q_\alpha^{\text{out}} = -\lambda_\alpha \frac{\partial p_\alpha}{\partial x}\bigg|_{x=0}. \tag{5.10}$$

The fraction of each phase extracted from the well is therefore given by

$$\mathcal{F}_w(t) = \frac{[1-h(x=0,t)]\rho_w q_w^{\text{out}}}{s_g h(x=0,t)\rho_g(x=0,t)q_g^{\text{out}} + [1-h(x=0,t)]\rho_w q_w^{\text{out}}} \tag{5.11a}$$

$$\mathcal{F}_g(t) = 1 - \mathcal{F}_w(t). \tag{5.11b}$$

It must therefore hold that $\mathcal{F}_w(t)\mathcal{I}_w + \mathcal{F}_g(t)\mathcal{I}_g = \mathcal{I}$. Multiplying Equations (5.11)a and (5.11)b with the sink term in the governing equations yields a set of coupled PDEs with a simple constant extraction condition. For a system with $n$ aquifers and vertical pressure dissipation with no gas leakage the PDE for water is given by

$$\phi\left[(H-s_g h^n)(c_r+c_w)\frac{\partial p^n}{\partial t} - s_g\frac{\partial h^n}{\partial t}\right] - \frac{\partial}{\partial x}\left\{\lambda_w(H-h^n)\left[\frac{\partial p^n}{\partial x} - \rho_w g\frac{\partial h^n}{\partial x}\right] + \frac{1}{6}\frac{\partial}{\partial x}\left[(H-h^n)^2(q_{w,z}^{n,B}+2q_{w,z}^{n,T})\right]\right\} = -(q_{w,z}^{n,T}-q_{w,z}^{n,B}) - \mathcal{F}_w(t)\frac{\mathcal{I}_w^n H}{\rho_w}. \tag{5.12}$$

Similarly, the governing PDE for gas is given by

$$\rho_g^n \phi s_g\left[(c_r + \frac{\rho_g^0}{\rho_g^n}c_g)h^n\frac{\partial p^n}{\partial t} + \frac{\partial h^n}{\partial t}\right] - \frac{\partial}{\partial x}\left[\rho_g^n h^n \lambda_g\left(\frac{\partial p^n}{\partial x} - \rho_g^n g\frac{\partial h^n}{\partial x}\right)\right] = -\mathcal{F}_g(t)\mathcal{I}_g^n H. \tag{5.13}$$

Note that the sign on the last term on the right-hand side of both equations is now negative (i.e., a sink).

For most cases of long term industrial fluid extraction, a constant extraction rate is unattainable. Instead a constant pressure condition is applied, which leads to a natural decline in production due to the decay in overpressure provided by the buoyant phase [e.g., Ehlig-Economides and Ramey Jr, 1981]. This means that the mass extraction rate per unit time is instead a function of time $\mathcal{I}_\alpha(t)$ which can be calculated using Darcy's law. For both internal fluid extraction boundary conditions (constant rate or constant pressure), the extraction of a less-dense fluid overlying a denser fluid leads to the development of the classical hydrological upconing phenomenon [e.g., Dagan and Bear, 1968, Bear, 1972, Strack, 1972, Nordbotten and Celia, 2006a]. Although interface upconing was originally described in the context of saltwater intrusion in coastal aquifers, the production of buoyant hydrocarbons (oil or gas) also leads to the development of upconing [e.g., Muskat, 1949, Chappelear and Hirasaki, 1976]. During hydrocarbon production, the upconing interface results in an increasing fraction of extracted ambient water. This increasing 'water cut' eventually poses an economic constraint on extraction, due to the cost of re-injecting produced water, making further hydrocarbon extraction unprofitable.

Adapting the model to allow for fluid extraction would allow for numerous interesting cases to be studied. First would be to study the impact of vertical pressure dissipation on fluid extraction. During gas production, water will also be extracted at an ever increasing rate due to the decline in $h(x = 0, t)$. This means that during gas production, the coupling to water flow will become stronger with time. As vertical pressure dissipation modifies the coupling between water and gas in a system of layered aquifers, it is likely that vertical pressure dissipation will have a similarly large impact on fluid extraction.

Secondly, once an extraction condition has been implemented, the model would be well-suited to study Enhanced Oil Recovery (EOR) which utilizes simultaneous extraction and injection of fluids to increase the efficiency of hydrocarbon production [e.g., Lake, 1989, Blunt et al., 1993]. Most studies of EOR use reservoir simulators

that include a great deal of physical, chemical and thermodynamical machinery—often in a complex and heterogeneous 3D domain. As such, these models cannot fully explore the associated parameter space. With little effort, the model can be easily adapted to provide a comprehensive overview of the fluid dynamics of EOR. One notable weakness of the model in its current form, relative to reservoir simulators, is that it would be incapable of dealing with the flooding of 'exotic' fluids (e.g., Non-Newtonian polymers) that require complex equations of state.

A final area of unexplored curiosity is that of the interaction between non-Darcy (post-linear) flow, pressure dissipation and fluid production. During fluid extraction, the convergence of flow lines near the well can amplify the otherwise-negligible role of inertia [e.g., Şen, 1988, 1990, Kohl et al., 1997, Kolditz, 2001, Mathias et al., 2008]. These moderate Reynolds number flows—known as Darcy-Forchheimer flows—require the introduction of inertial terms to Darcy's law [Forchheimer, 1901]. Extending the derivation to account for Darcy-Forchheimer flow would allow for the study of interaction between horizontal and vertical pressure dissipation on turbulent fluid extraction.

# Appendix A

# Derivation for a compressible gravity current in a single uniform aquifer

In this thesis, theoretical models—based on a compressible gravity current formulation—are derived that describe fluid injection and migration in a layered aquifer system. Below a brief derivation is provided for a gas-water gravity current in a single confined horizontal porous layer.

Consider a uniform aquifer of thickness $H$ (Figure A.1). The aquifer has porosity $\phi$, and uniform and isotropic permeability $k$. The aquifer is initially fully saturated with water $[s_w(x, z, t = 0) = 1]$, with density $\rho_w$ and dynamic viscosity $\mu_w$. For

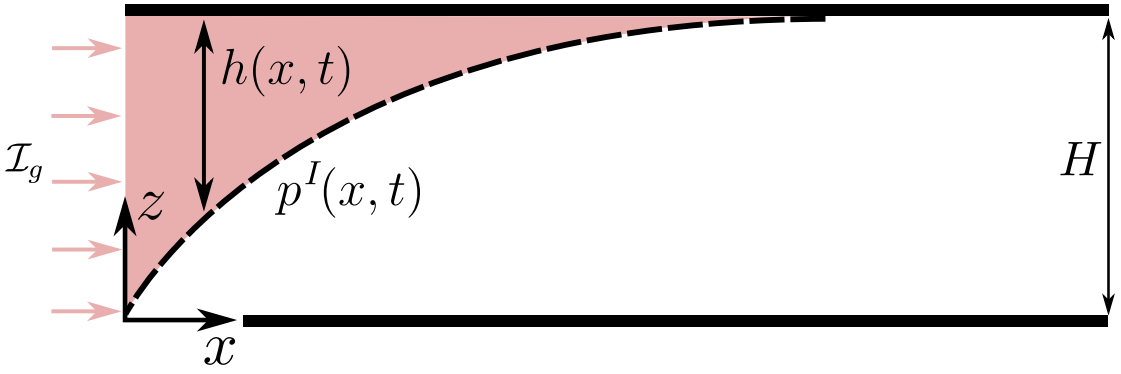


**Figure A.1:** A gravity current of gas (in pink) that is injected into a uniform porous layer that is initially saturated with water (white).

$t > 0$, gas is injected at $x = 0$ over the thickness of the layer. The gas has dynamic viscosity $\mu_g$ ($\mu_g < \mu_w$) and density $\rho_g$ ($\rho_g < \rho_w$).

The fluids are assumed to be immiscible and segregated by gravity, such that a region primarily saturated with gas overlies a region exclusively saturated with water. Saturation variations are predominantly confined to a thin transition zone. However, when buoyancy forces are much stronger than capillary forces (such as here) this transition zone can be neglected, and instead approximated by a sharp interface. The thickness of the gas plume $h$ is defined such that the interface is located at $z = H - h$ (Figure A.1) where $H$ is the thickness of the layer. As viscous and buoyancy forces dominate over capillary forces in the bulk of the plume, capillary pressure is neglected at the interface. The Bond number (Bo) is the ratio between buoyancy and capillary forces and is defined, for this system, as

$$\mathrm{Bo} \equiv \frac{\Delta\rho g H d}{\sigma} \tag{A.1}$$

where $d$ is the characteristic pore diameter. Assuming typical values for $CO_2$ injection into a porous sandstone aquifer with a thickness of $H \sim 50$ m, $\Delta\rho \sim 300$ kg m$^{-3}$, a typical pore diameter of $d \sim 10$ $\mu$m and $\sigma \sim 25$Nm$^{-1}$ yields a Bond number of Bo $\sim 60$—suggesting that buoyancy is dominant over capillarity. Using the above, a critical gas thickness ($h_{\mathrm{crit}} \sim \sqrt{\sigma/\Delta\rho g d}$) can be estimated, below which capillary forces become increasingly dominant. Using the above values, the critical thickness is estimated as $h_{\mathrm{crit}} \sim 0.9$ m; demonstrating that the bulk of the plume is likely unaffected by capillarity. Below this critical thickness, capillarity acts to blunt the leading edge of a buoyancy-driven gravity current [Zhao et al., 2014].

As with most studies that consider gravity currents in porous media [e.g., Huppert and Woods, 1995, Zheng et al., 2015], variations in saturation are neglected, meaning that each fluid region is assumed to have a constant saturation. For

$0 < z < H - h$, the pore space is fully saturated with water ($s_w = 1$). For $H - h < z < H$, the pore space is occupied by gas and some residual water ($s_g \equiv 1 - s_{wr}$, where $s_g > s_{wr}$). Golding et al. [2013] showed that for $CO_2$ injection during CCS, saturation is relatively constant in the bulk of each phase and the saturation transition zone is relatively narrow. Golding et al. [2013] further demonstrates that including additional equations that solve for saturation variations do not significantly alter the dynamics of a propagating two-phase gravity current. This is especially true during $CO_2$ injection, where both viscous and buoyancy forces exceed capillary forces in the bulk of the plume. Therefore this constant-saturation approximation is likely valid throughout this work. Furthermore, assigning a constant saturation to each fluid region leads to constant relative permeability in each fluid region, which reduces the nonlinearity of the governing equations.

Now that a simple framework for fluid injection into a uniform porous layer has been outlined, a set of governing equations can now be derived to describe the migration of gravity currents in this system. The derivations begins by defining a linear constitutive relation that accounts for the compressibility of an arbitrary phase $\alpha$

$$\rho_\alpha(p_\alpha) = \rho_\alpha^0 \left[1 + c_\alpha(p_\alpha - p^0)\right], \tag{A.2}$$

where $p_\alpha$ is the pressure of phase $\alpha$, $\rho_\alpha^0$ is the density of phase $\alpha$ at reference pressure $p^0$, and $c_\alpha$ is the compressibility of phase $\alpha$ about $p^0$ ($c_\alpha \equiv (1/\rho_\alpha^0)(\mathrm{d}\rho_\alpha/\mathrm{d}p)|_{p^0}$). In assuming that fluid density varies exclusively with pressure, thermal expansion in both phases has been neglected. Given that North Sea geothermal gradients are typically in the range 18–44 °C km$^{-1}$ [e.g., Evans and Coleman, 1974], a 50 m thick gas column will experience a maximum temperature change of 2.2 °C—which is often considered insufficient to warrant the inclusion of thermal expansion [e.g.,

Mathias et al., 2011b]. Below, a governing expression is derived for a compressible gravity current of the (buoyant) gas phase.

Conservation of mass for gas in the aquifer is given by

$$\frac{\partial}{\partial t}\left(\rho_g \phi s_g\right) + \boldsymbol{\nabla} \cdot \left(\rho_g \boldsymbol{q}_g\right) = \mathcal{I}_g, \tag{A.3}$$

where $s_g$ is the saturation of gas, $\boldsymbol{q}_g$ is the Darcy flux of gas, and $\mathcal{I}_g$ is a source term that prescribes the local mass rate of gas injection per unit volume. Using Darcy's law, the Darcy flux of gas is written as:

$$\boldsymbol{q}_g = -\frac{k k_{rg}}{\mu_g}\left(\boldsymbol{\nabla} p_g + \rho_g g \hat{\boldsymbol{e}}_z\right), \tag{A.4}$$

Gravity currents are predominantly horizontal flows, meaning that the vertical component of the Darcy flux is negligible compared to the horizontal component ($q_{g,z} \ll q_{g,x}$). Vertical equilibrium is now invoked by assuming that the vertical Darcy flux is negligible ($q_{g,z} \approx 0$). This assumption implies that the vertical pressure must be approximately gas-static,

$$\frac{\partial p_g}{\partial z} \approx -\rho_g g \qquad z^I \leq z \leq H, \tag{A.5}$$

where $z^I = H - h$ is the vertical location of the gas-water interface and recall that there is no gas below the gas plume ($s_g = 0 for 0 < z < z^I$). This expression is integrated to give the pressure distribution in the gas-saturated region,

$$p_g(x, z, t) \approx p(x, t) - \rho_g g[z - z^I(x, t)] \qquad z^I \leq z \leq H, \tag{A.6}$$

where $p(x, t)$ is the pressure along the gas-water interface. At the interface, the capillary pressure has been neglected, as it is typically much smaller than the gas-static pressure ($p_c \ll \rho_g^0 g H$). Therefore it is assumed that the water and gas

pressure are equal along the interface [$p(x,z) = p_g(x, z = H - h) = p_w(x, z = H - h)$]. This standard assumption has been widely used by previous studies of gravity currents in porous media [e.g., Bear, 1972, Huppert and Woods, 1995, Yortsos, 1995].

By differentiating Equation (A.6) with respect to the horizontal coordinate, the lateral pressure gradient can be given by

$$\frac{\partial p_g}{\partial x} \approx \frac{\partial p}{\partial x} - \rho_g g \frac{\partial h}{\partial x} \qquad z^I \leq z \leq H, \tag{A.7}$$

Here, terms related to gas-static density variations, which are of order $\rho_g^0 g H c_g \ll 1$, have been neglected. Recombining A.4 and A.7 allows for the horizontal gas flux to be written as

$$q_{g,x}(x,z,t) \approx -\frac{k k_{rg}}{\mu_g}\left(\frac{\partial p}{\partial x} - \rho_g g \frac{\partial h}{\partial x}\right) \qquad H - h \leq z \leq H, \tag{A.8}$$

where $k_{rg}$ is now the constant and uniform relative permeability to gas in the gas region. There is no gas below the interface, so $q_{g,x} = 0$ for $0 \leq z \leq H - h$. The assumption that the flow is predominantly horizontal now suggests vertical integration of A.3 over the thickness of the aquifer,

$$\int_0^H \frac{\partial}{\partial t}\left(\rho_g s_g \phi\right)\, \mathrm{d}z + \int_0^H \boldsymbol{\nabla} \cdot \left(\rho_g \boldsymbol{q}_g\right)\, \mathrm{d}z = \int_0^H \mathcal{I}_g \, \mathrm{d}z. \tag{A.9}$$

To avoid cumbersome presentation of this integration—which is a relatively standard procedure [e.g., Bear, 1972, Huppert and Woods, 1995, Gasda et al., 2009, Mathias et al., 2011b]—each term is now integrated separately. The first term on

the left-hand side of Eq. A.9 becomes

$$\begin{aligned}\int_0^H \frac{\partial}{\partial t}(\rho_g \phi s_g)\,\mathrm{d}z &\approx \frac{\partial}{\partial t}(\rho_g \phi s_g h) \\ &\approx \rho_g \phi s_g \left[(c_r + \frac{\rho_g^0}{\rho_g} c_g) h \frac{\partial p}{\partial t} + \frac{\partial h}{\partial t}\right],\end{aligned} \tag{A.10}$$

where $s_g$ is now the constant and uniform saturation of gas in the gas region, $c_r \equiv (1/\phi)(\partial\phi/\partial p)$ is the compressibility of the porous layer, and it has once again been assumed that $\rho_g^0 g H c_g \ll 1$. Many studies often assume that $\rho_g^0/\rho_g \approx 1$. However to maintain generality for applications in which the gas is highly compressible (e.g., methane migration) this assumption is not made here.

Using Equations (A.4) and (A.7) and again assuming that $\rho_g^0 g H c_g \ll 1$, the second term on the left-hand side of Eq. (A.9) becomes

$$\begin{aligned}\int_0^H \boldsymbol{\nabla} \cdot \left(\rho_g \boldsymbol{q}_g\right)\,\mathrm{d}z &= \frac{\partial}{\partial x}\left(\int_0^H \rho_g q_{g,x}\,\mathrm{d}z\right) + \left(\rho_g q_{g,z}\right)\Big|_0^H \\ &\approx \frac{\partial}{\partial x}\left[-\rho_g h \frac{k k_{rg}}{\mu_g}\left(\frac{\partial p}{\partial x} - \rho_g g \frac{\partial h}{\partial x}\right)\right].\end{aligned} \tag{A.11}$$

Combining Equations A.10 and A.11 with the right-hand side of Eq. A.9, which trivially integrates as $\mathcal{I}_g H$, yields a governing equation for a compressible buoyant gravity current that is comparable to the axisymmetric version first presented by Mathias et al. [2011b],

$$\rho_g^n \phi s_g \left[(c_r + \frac{\rho_g^0}{\rho_g} c_g) h \frac{\partial p}{\partial t} + \frac{\partial h}{\partial t}\right] - \frac{\partial}{\partial x}\left[\rho_g h \lambda_g \left(\frac{\partial p}{\partial x} - \rho_g g \frac{\partial h}{\partial x}\right)\right] = \mathcal{I}_g H, \tag{A.12}$$

where $\lambda_g \equiv k k_{rg}/\mu_g$ is the mobility of gas in the gas region and $\mathcal{I}_g$ is the vertically averaged mass injection rate of gas per unit volume into the aquifer.

Next a governing PDE for the dense (water) component for a gravity current in a single aquifer is derived. It is assumed that the denser phase, which is taken here to be water ($\alpha = w$), has no source term and therefore conservation of mass for the water in the porous layer is given by

$$\frac{\partial}{\partial t}\left(\rho_w \phi s_w\right) + \boldsymbol{\nabla} \cdot \left(\rho_w \boldsymbol{q}_w\right) = 0, \tag{A.13}$$

where $s_w$ is the water saturation and $\boldsymbol{q}_w$ is the Darcy flux of water—which is given by Darcy's law,

$$\boldsymbol{q}_w = -\frac{k k_{rw}}{\mu_w}\left(\boldsymbol{\nabla} p_w + \rho_w g \hat{\boldsymbol{e}}_z\right), \tag{A.14}$$

where $k_{rw}$ is the relative permeability to water flow, $\mu_w$ is the dynamic viscosity of water, which is taken to be constant and uniform, and $p_w$ is the water pressure. Again, vertical equilibrium is invoked—meaning that water flow is predominantly horizontal ($q_{w,z} \approx 0$) and that in the water saturated region the pressure distribution is approximately hydrostatic.

$$\frac{\partial p_w}{\partial z} \approx -\rho_w g \qquad 0 \leq z \leq H - h, \tag{A.15}$$

which can be integrated to give the pressure distribution in the water

$$p_w(x, z, t) \approx p(x, t) + \rho_w g (H - h - z), \tag{A.16}$$

where $p(x, t)$ is the pressure along the gas-water interface. Combining Equations A.14 and A.16 yields an expression for the horizontal Darcy flux of water in the porous layer

$$q_{w,x}(x,t) \approx -\frac{k}{\mu_w}\left(\frac{\partial p}{\partial x} - \rho_w g \frac{\partial h}{\partial x}\right), \tag{A.17}$$

where it has been assumed that $k_{rw}$ in the fully water saturated region. Continuing the same procedure followed for gas, Equation (A.13) is now vertically integrated

$$\int_0^{H-h} \frac{\partial}{\partial t}\left(\rho_w \phi\right)\, \mathrm{d}z + \int_0^{H-h} \boldsymbol{\nabla}\cdot\left(\rho_w \boldsymbol{q}_w\right)\, \mathrm{d}z = 0, \tag{A.18}$$

where $s_w = 1$ in the water saturated region ($0 \leq z \leq H-h$). Much like for gas, the first term on the left-hand side of Equation (A.18) becomes

$$\begin{aligned}\int_0^{H-h} \frac{\partial}{\partial t}(\rho_w\phi)\,\mathrm{d}z &\approx \frac{\partial}{\partial t}[\rho_w^n \phi(H-h) + \rho_w\phi(1-s_g)h] \\ &\approx \rho_w\phi\left[(c_r+c_w)(H-s_g)\frac{\partial p}{\partial t} - s_g\frac{\partial h}{\partial t}\right],\end{aligned} \tag{A.19}$$

where it is assumed that $c_w(p_w - p^0) \ll 1$ and therefore that $\rho_w \approx \rho_w^0$. Integrating the second term of Equation (A.18) yields

$$\begin{aligned}\int_0^{H-h} \boldsymbol{\nabla}\cdot\left(\rho_w\boldsymbol{q}_w\right)\,\mathrm{d}z &\approx \frac{\partial}{\partial x}\left(\int_0^{H-h} \rho_w q_{w,x}\,\mathrm{d}z\right) \\ &\approx \frac{\partial}{\partial x}\left(-\rho_w\frac{k}{\mu_w}(H-h)\left[\frac{\partial p}{\partial x} - \rho_w g\frac{\partial h}{\partial x}\right]\right)\end{aligned} \tag{A.20}$$

Recombining (A.19) and (A.20), and remembering that the conservation Equation (A.13) has no source/sink term, yields the governing equation for a dense compressible gravity-current

$$\phi\left[(H-s_g h)(c_r+c_w)\frac{\partial p}{\partial t} - s_g\frac{\partial h}{\partial t}\right] - \frac{\partial}{\partial x}\left[\lambda_w(H-h)\left(\frac{\partial p}{\partial x} - \rho_w g\frac{\partial h}{\partial x}\right)\right] = 0, \tag{A.21}$$

where $\lambda_w \equiv k/\mu_w$ is the mobility of water in the water region.

Equations (A.12) and (A.21) are two coupled nonlinear PDEs in terms of the interface pressure $p(x,t)$ and the thickness of the gas plume $h(x,t)$. Note again that, by assuming vertical equilibrium and by performing vertical integration, the order of these governing equations have been reduced—that is, a 2D problem in $x$ and $z$ is now described by 1D PDEs in $x$.

The next stage in the analysis of these equations is to present characteristic scales, which are used to write the governing PDEs in dimensionless form. This non-dimensionalisation has been performed in Chapter 2 and is therefore not repeated here. In the limit of $\Lambda_w^s = 0$, equations presented in Chapters 2-4 reduce to an equivalent dimensionless model for compressible gravity-currents in a single aquifer. A detailed analysis of fluid injection into a uniform horizontal aquifer has been presented by many previous studies [e.g., Huppert and Woods, 1995, Mathias et al., 2011a, Pegler et al., 2014a, Zheng et al., 2015, Golding et al., 2011]. Under certain limits, the model derived in earlier chapters reduces to these familiar models.

# Appendix B

# Finite volume methods

Throughout this thesis, spatial discretisation is performed using a basic Finite Volume Method (FVM). The FVM approach is to ensure that the governing PDE is satisfied over finite and discrete control volumes that may be non-uniformly spaced [e.g., Mazumder, 2015]. As such, the finite volume method can be considered an approach to solving the integral form of

$$\frac{\partial M}{\partial t} + \frac{\partial F}{\partial x} = 0. \tag{B.1}$$

where $F$ is a flux term (in $x$) and $M$ is the fluid mass—or quantity being conserved. In general, the governing 1D PDEs contained in this work can be expressed in this form, provided that source and sink terms (i.e. injection and leakage) have been neglected. Now, define a staggered grid such that an arbitrary *grid cell* $i$ is bounded by *grid interfaces* $i - \frac{1}{2}$ and $i + \frac{1}{2}$ that are separated by a distance $\Delta x_i$ (Figure B.1).

At an arbitrary time $t = t_\tau$ the averaged mass of fluid in the $i^{th}$ cell is given by

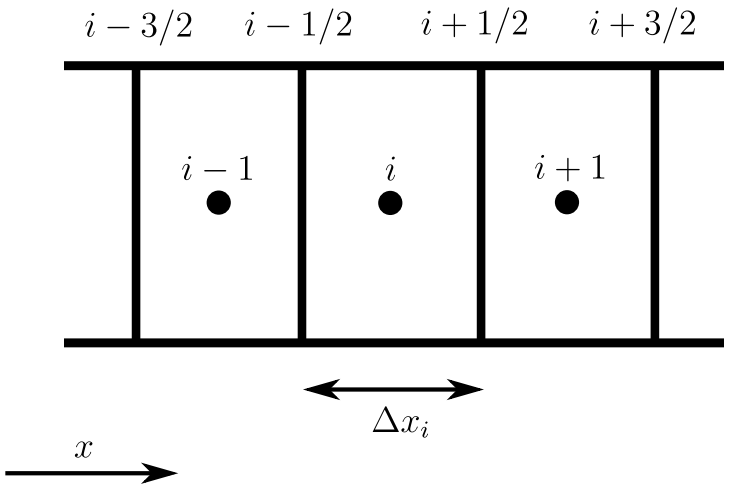


**Figure B.1:** A simple uniform finite volume grid. Note that cells $i$ and $i+1$ are separated by interface $i+1/2$.

$$\langle M(x,t_\tau)\rangle = \frac{1}{x_{i+1/2}-x_{i-1/2}}\int_{x_{i-1/2}}^{x_{i+1/2}} M(x,t_\tau)dx. \tag{B.2}$$

Similarly, at time $t = t_{\tau+1}$ the averaged mass of fluid in the $i^{\text{th}}$ cell is

$$\langle M(x,t_{\tau+1})\rangle = \frac{1}{x_{i+1/2}-x_{i-1/2}}\int_{x_{i-1/2}}^{x_{i+1/2}} M(x,t_{\tau+1})dx. \tag{B.3}$$

Integrating Equation (B.1) with respect to time and rearranging for $M(x,t_{\tau+1})$ yields

$$M(x,t_{\tau+1}) = M(x,t_\tau) - \int_\tau^{\tau+1}\frac{\partial F}{\partial x}\,dt \tag{B.4}$$

Substituting Equation (B.4) into Equation (B.3) yields an expression for the average mass at time $t_{\tau+1}$ in the $i^{\text{th}}$ cell

$$\langle M(x,t_{\tau+1})\rangle = \frac{1}{x_{i+1/2}-x_{i-1/2}}\int_{x_{i-1/2}}^{x_{i+1/2}}\left[M(x,t_\tau) - \int_\tau^{\tau+1}\frac{\partial F}{\partial x}\,dt\right]dx. \tag{B.5}$$

Expanding out this expression and reversing the order of integration yields

$$\langle M(x,t_{\tau+1})\rangle = \frac{1}{\Delta x_i}\int_{x_{i-1/2}}^{x_{i+1/2}} M(x,t_\tau)\,dx - \frac{1}{\Delta x_i}\int_{\tau}^{\tau+1}\left\{\int_{x_{i-1/2}}^{x_{i+1/2}}\frac{\partial F}{\partial x}\,dx\right\}dt \quad \text{(B.6)}$$

where $\Delta x_i \equiv x_{i+1/2} - x_{i-1/2}$. Substituting Equation (B.2) into Equation (B.6), evaluating the second term of Equation (B.6) at the cell interfaces and rearranging yields

$$\langle M(x,t_{\tau+1})\rangle - \langle M(x,t_\tau)\rangle = -\frac{1}{\Delta x_i}\int_{\tau}^{\tau+1}\left\{F_{i+\frac{1}{2}} - F_{i-\frac{1}{2}}\right\}dt \quad \text{(B.7)}$$

where $F_{i-\frac{1}{2}}$ and $F_{i+\frac{1}{2}}$ are the fluxes evaluated at interfaces $x = x_{i-1/2}$ and $x = x_{i+1/2}$ respectively. Finally, differentiating with respect to time yields the finite volume discretisation for the average rate of change of $M$ in the $i^{th}$ cell due to a localised divergence of flux

$$\frac{d\langle M_i\rangle}{dt} + \frac{1}{\Delta x_i}\left\{F_{i+\frac{1}{2}} - F_{i-\frac{1}{2}}\right\} = 0. \quad \text{(B.8)}$$

Extending Equation (B.1) to include terms for the loss/gain of fluid mass through vertical leakage $[\Delta M(\dot{x},t)_z]$ and fluid injection $[\mathcal{I}(x)]$ yields:

$$\frac{\partial M}{\partial t} + \frac{\partial F}{\partial x} = \Delta M_z(\dot{x},t) + \mathcal{I}(x), \quad \text{(B.9)}$$

which is implemented in a finite volume discretisation as

$$\frac{d\langle M_i\rangle}{dt} + \frac{1}{\Delta x_i}\left\{F_{i+\frac{1}{2}} - F_{i-\frac{1}{2}}\right\} = \Delta M_z(\dot{x}_i,t) + \mathcal{I}(x_i). \quad \text{(B.10)}$$

The corresponding finite volume discretisation for the $(i+1)^{th}$ cell is written as:

$$\frac{d\langle M_{i+1}\rangle}{dt} + \frac{1}{\Delta x_{i+1}}\left\{F_{i+\frac{3}{2}} - F_{i+\frac{1}{2}}\right\} = \Delta M_z(\dot{x_{i+1}}, t) + \mathcal{I}(x_{i+1}). \tag{B.11}$$

Comparing Equations (B.10) and (B.11) within the framework of the specified grid (Figure B.1), it is clear to see that the flux leaving the $i^{th}$ cell is exactly equal to the flux entering the $(i+1)^{th}$ cell. As such, finite volume methods are conservative by construction, and are therefore widely used in problems concerning fluid flow.

Finite Volume methods are a technique for spatially discretising PDEs. As such, Equations (B.8), (B.10) and (B.11) still have a temporal derivative that must be integrated in time to obtain numerical solutions for the governing PDEs. In this work, `MATLAB`'s proprietary ODE solvers are used for time integration—as detailed in Appendix C.

# Appendix C

# ODE solvers in MATLAB

This appendix briefly summarises MATLAB's Ordinary Differential Equation (ODE) solvers that are used to integrate the governing PDEs in time. First, the core concepts and features of these solvers are introduced within the framework of a simple system of coupled ODEs.

## C.1 Solving the Lorenz attractor problem with ODE45

The Lorentz attractor problem is a system of three coupled nonlinear ODEs, whose solution exhibit simple chaotic behaviour, and is defined as:

$$\frac{\mathrm{d}x}{\mathrm{d}t} = \sigma(y - x), \tag{C.1a}$$

$$\frac{\mathrm{d}y}{\mathrm{d}t} = x(\rho - z) - y, \tag{C.1b}$$

$$\frac{\mathrm{d}z}{\mathrm{d}t} = xy - \beta z, \tag{C.1c}$$

where $\sigma$, $\rho$ and $\beta$ are constant parameters.

`MATLAB`'s ODE solvers integrate, in time, initial value problems and require as input arguments:

1. A function (`odefunc`) that mathematically defines the function to be numerically integrated.
2. The timespan or times (`ts`) for which solutions are output.
3. The initial condition of the system (`xyz0`).
4. Aditional solver constraints and parameters (`options`).

The `odefunc` for the Lorenz attractor, with parameters $\sigma = 10$, $\rho = 28$ and $\beta = 8/3$, is trivially implemented in matlab with the following code.

```
function dXdt  = odefunc(t,X)

  r = 28;
  s = 10;
  b = 8/3;

  dXdt = zeros(3,1);

  dXdt(1) = s*(X(2) - X(1));
  dXdt(2) = X(1)*(r-X(3)) - X(2);
  dXdt(3) = X(1)*X(2) - b*X(3);

end
```

The `MATLAB` code below defines the initial condition $x(t = 0) = 1$, $y(t = 0) = 0$ and $z(t = 0) = 0$, defines a vector of solution times $t_0 = 0$, $t_1 = 0.01$, $t_2 =$

$0.02 \cdots t_N = 30$, calls the ODE solver `ODE45` with default `options`, and finally unpacks the solution into vectors for each orthogonal Cartesian coordinate.

```
clear all; close all; clc;

xyz0 = [1 0 0 ];
ts = 0:0.01:30;

[ts,xyz] = ode45('odefunc',ts,xyz0);
xs = xyz(:,1);
ys = xyz(:,2);
zs = xyz(:,3);
```

Unless specified, `MATLAB`'s ODE solvers integrate the `odefunc` in time using an adaptive timestepping algorithm. Figure C.1 shows the numerical solutions, for all times, provided by `ODE45` and shows the bifurcation behaviour associated with this problem.

## C.2 Integrating PDEs using the Method of Lines

Although the Lorenz attractor ODEs provides a simple, elegant and visually-striking introduction to using `MATLAB`'s ODE solvers, this thesis requires solutions to coupled PDEs that describe multiphase flow in the subsurface. This thesis makes repeated use of the 'method of lines' (MOL), in which the governing PDEs are spatially discretised (in this work using a standard finite volume method (see Appendix B)—forming a set of coupled ODEs [e.g., Wouwer et al., 2005, Goudarzi et al., 2016]. These coupled ODEs are subsequently implicitly integrated in time using `MATLAB`'s stiff solver ODE15s [Shampine and Reichelt, 1997, Shampine and

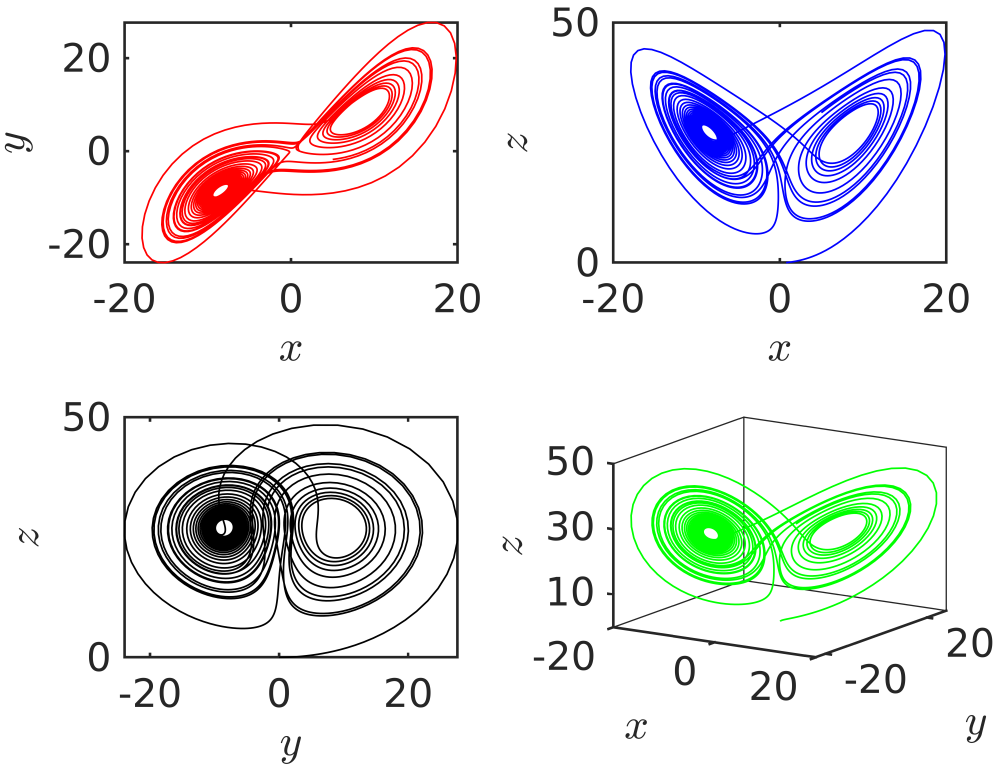


**Figure C.1:** Numerical solution to the Lorenz attractor problem.

Thompson, 2001].

One of the many `options` that can called as input argument in `MATLAB`'s ODE solvers is the Jacobian pattern matrix, which specifies the dependencies of each discretised point in space. At each time step, `MATLAB` uses the Jacobian pattern matrix to compute only the non-sparse elements of the system. For stiff problems, the Jacobian pattern matrix can evolve in time and the Jacobian pattern matrix must be calculated at each time step. Providing *a priori* Jacobian pattern matrix can dramatically improve computational efficiency [e.g., Goudarzi et al., 2016], as it avoids inverting for the sparse dependencies at each time step. In the model-system, there are two PDEs, for $h^n(x,t)$ and $p^n(x,t)$, per aquifer, and each discretised point depends $[j]$ on its horizontal $[j-1$ and $j+1]$ and vertical

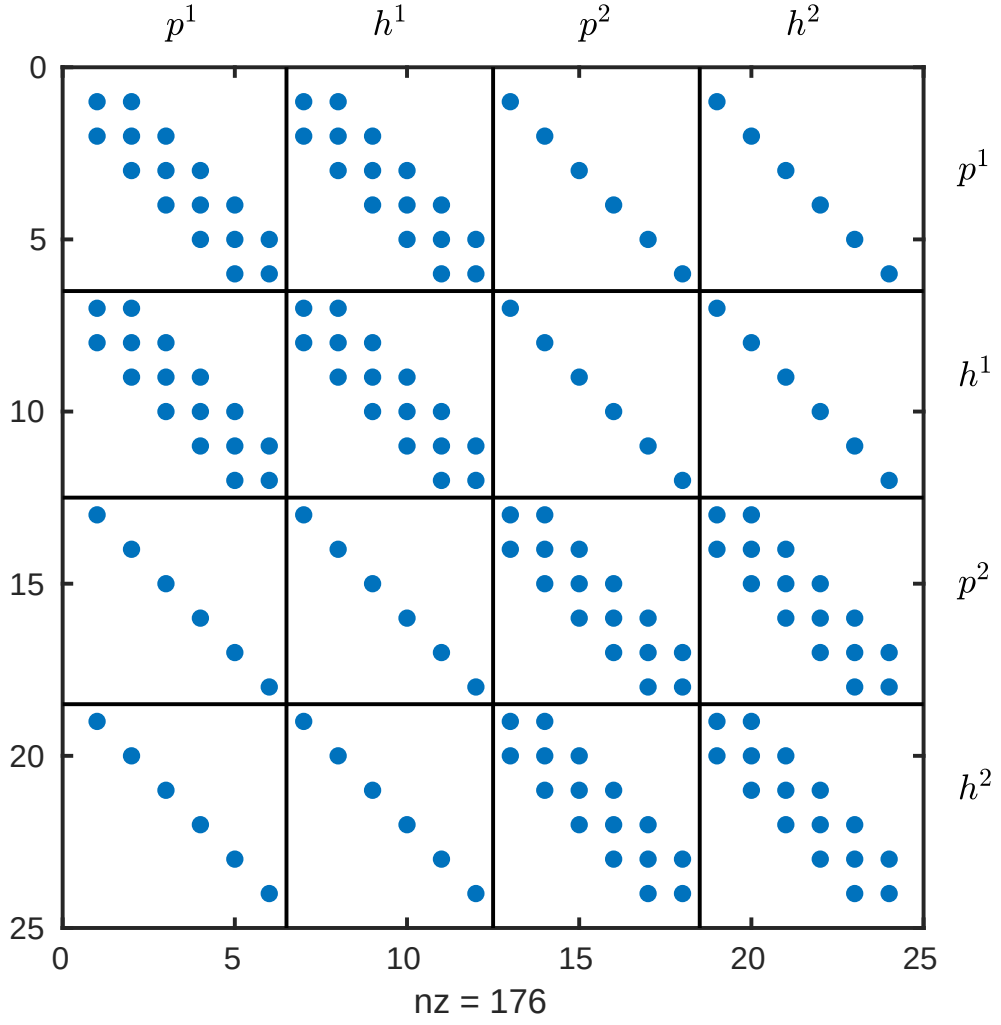


**Figure C.2:** Jacobian pattern for system of coupled ODEs with $N_z = 2$, $N_x = 6$ and 176 *nonzero* elements (nz).

$[j - (N_z - n)N_x$ and $j + (N_z - n)N_x]$ neighbours, where $N_x$ is the total number of horizontal grid cells, $N_z$ is the total number of aquifers and $n$ is the aquifer number. Figure C.2 shows the characteristic 'block diagram', which illustrates the Jacobian matrix pattern for a system with 6 horizontal cells and 2 aquifers. The code that generates the Jacobian pattern matrices is displayed below. An increase in horizontal resolution and/or the number of aquifers in the system increases the sparseness and number of nonzero elements in the Jacobian matrix pattern.

```
% >>> Code for creating Jacobian pattern Matrix --- Jpat <<<
% >>> LTJ & CWM

J1 = spdiags(ones(Nx,3),[-1,0,1],Nx,Nx);
J2 = spalloc(2*Nx,2*Nx,12*Nx);
J2(   1:  Nx,1:Nx) = J1; J2(   1:Nx  ,Nx+1:2*Nx) = J1;
J2(Nx+1:2*Nx,1:Nx) = J1; J2(Nx+1:2*Nx,Nx+1:2*Nx) = J1;
J3 = speye(Nx,Nx);
J4 = spalloc(2*Nx,2*Nx,4*Nx);
J4(   1:  Nx,1:Nx) = J3; J4(   1:Nx  ,Nx+1:2*Nx) = J3;
J4(Nx+1:2*Nx,1:Nx) = J3; J4(Nx+1:2*Nx,Nx+1:2*Nx) = J3;

Jpat = spalloc(2*Nx*Nz,2*Nx*Nz,12*Nx*Nz+((Nz^2)-Nz)*4*Nx);

for irow=1:Nz
    for icol=1:Nz
        irowstart = 2*Nx*(irow-1)+1;
        irowstop = 2*Nx*(irow-1)+2*Nx;
        icolstart = 2*Nx*(icol-1)+1;
        icolstop = 2*Nx*(icol-1)+2*Nx;
        if irow==icol
            Jpat(irowstart:irowstop,icolstart:icolstop) = J2;
        else
            Jpat(irowstart:irowstop,icolstart:icolstop) = J4;
        end
    end
end
```

# Bibliography

J. M. Acton, H. E. Huppert, and M. G. Worster. Two-dimensional viscous gravity currents flowing over a deep porous medium. *Journal of Fluid Mechanics*, 440: 359–380, 2001.

H. Alnes, O. Eiken, and T. Stenvold. Monitoring gas production and $CO_2$ injection at the Sleipner field using time-lapse gravimetry. *Geophysics*, 73(6):WA155–WA161, 2008.

H. Alnes, O. Eiken, S. Nooner, G. Sasagawa, T. Stenvold, and M. Zumberge. Results from Sleipner gravity monitoring: Updated density and temperature distribution of the $CO_2$ plume. *Energy Procedia*, 4:5504–5511, 2011.

J. C. Andrew, R. S. Haszeldine, and B. Nazarian. The Sleipner $CO_2$ storage site: using a basin model to understand reservoir simulations of plume dynamics. *First Break*, 33(6):61–68, 2015.

M. Andrew, B. Bijeljic, and M. J. Blunt. Pore-by-pore capillary pressure measurements using X-ray microtomography at reservoir conditions: Curvature, snap-off, and remobilization of residual $CO_2$. *Water Resources Research*, 50 (11):8760–8774, 2014.

R. Arts, O. Eiken, R. A. Chadwick, P. Zweigel, L. Van der Meer, and B. Zinszner. Monitoring of $CO_2$ injected at Sleipner using time-lapse seismic data. *Energy*, 29(9-10):1383–1392, 2004.

S. Bachu. Sequestration of $CO_2$ in geological media: criteria and approach for site selection in response to climate change. *Energy conversion and management*, 41(9):953–970, 2000.

S. Bachu, W. Gunter, and E. Perkins. Aquifer disposal of $CO_2$: hydrodynamic and mineral trapping. *Energy Conversion and management*, 35(4):269–279, 1994.

A. Baklid, R. Korbol, and G. Owren. Sleipner vest $CO_2$ disposal, $CO_2$ injection into a shallow underground aquifer. In *SPE Annual Technical Conference and Exhibition*. Society of Petroleum Engineers, 1996.

T. V. Ball and H. E. Huppert. Similarity solutions and viscous gravity current adjustment times. *Journal of Fluid Mechanics*, 874:285–298, 2019.

C. J. Ballentine, M. Schoell, D. Coleman, and B. A. Cain. 300-myr-old magmatic $CO_2$ in natural gas reservoirs of the west Texas permian basin. *Nature*, 409 (6818):327, 2001.

K. W. Bandilla, B. Guo, and M. A. Celia. A guideline for appropriate application of vertically-integrated modeling approaches for geologic carbon storage modeling. *International Journal of Greenhouse Gas Control*, 91:102808, 2019.

G. I. Barenblatt. *Scaling, self-similarity, and intermediate asymptotics: dimensional analysis and intermediate asymptotics*, volume 14. Cambridge University Press, 1996.

J. Bear. *Dynamics of fluids in porous media*. Courier Corporation, 1972.

J. Bear. *Hydraulics of groundwater*. Courier Corporation, 1979.

S. M. Benson and D. R. Cole. $CO_2$ sequestration in deep sedimentary formations. *Elements*, 4(5):325–331, 2008.

S. M. Benson and F. M. Orr. Carbon dioxide capture and storage. *MRS bulletin*, 33(4):303–305, 2008.

M. Bickle, R. A. Chadwick, H. E. Huppert, M. Hallworth, and S. Lyle. Modelling carbon dioxide accumulation at Sleipner: Implications for underground carbon storage. *Earth and Planetary Science Letters*, 255(1-2):164–176, 2007.

J. T. Birkholzer, Q. Zhou, and C.-F. Tsang. Large-scale impact of $CO_2$ storage in deep saline aquifers: A sensitivity study on pressure response in stratified systems. *International Journal of Greenhouse Gas Control*, 3(2):181–194, 2009.

M. Blunt, F. J. Fayers, and F. M. Orr Jr. Carbon dioxide in enhanced oil recovery. *Energy Conversion and Management*, 34(9-11):1197–1204, 1993.

M. J. Blunt. *Multiphase flow in permeable media: A pore-scale perspective*. Cambridge University Press, 2017.

F. C. Boait, N. J. White, M. J. Bickle, R. A. Chadwick, J. A. Neufeld, and H. E. Huppert. Spatial and temporal evolution of injected $CO_2$ at the Sleipner Field, North Sea. *Journal of Geophysical Research*, 117:B03309, 2012.

W. S. Broecker. Climatic change: are we on the brink of a pronounced global warming? *Science*, 189(4201):460–463, 1975.

R. H. Brooks and A. T. Corey. Properties of porous media affecting fluid flow. *Journal of the Irrigation and Drainage Division*, 92(2):61–90, 1966.

J. A. Cartwright, M. Huuse, and A. Aplin. Seal bypass systems. *AAPG bulletin*, 91(8):1141–1166, 2007.

H. Celius and K. Ingeberg. The impact of $CO_2$ taxation on oil and gas production in norway. In *SPE Health, Safety and Environment in Oil and Gas Exploration and Production Conference*. Society of Petroleum Engineers, 1996.

R. A. Chadwick and D. Noy. History-matching flow simulations and time-lapse seismic data from the Sleipner $CO_2$ plume. In *Geological Society, London, Petroleum Geology Conference series*, volume 7, pages 1171–1182. Geological Society of London, 2010.

R. A. Chadwick, P. Zweigel, U. Gregersen, G. Kirby, S. Holloway, and P. Johannessen. -geological characterization of $CO_2$ storage sites: Lessons from Sleipner, Northern North Sea. In *Greenhouse Gas Control Technologies-6th International Conference*, pages 321–326. Elsevier, 2004.

R. A. Chadwick, R. Arts, and O. Eiken. 4d seismic quantification of a growing $CO_2$ plume at Sleipner, North Sea. In *Geological Society, London, Petroleum Geology Conference series*, volume 6, pages 1385–1399. Geological Society of London, 2005.

R. A. Chadwick, G. Williams, N. Delepine, V. Clochard, K. Labat, S. Sturton, M.-L. Buddensiek, M. Dillen, M. Nickel, and A. L. Lima. Quantitative analysis of time-lapse seismic monitoring data at the Sleipner $CO_2$ storage operation. *The Leading Edge*, 29(2):170–177, 2010.

C. Chalbaud, M. Robin, J. Lombard, F. Martin, P. Egermann, and H. Bertin. Interfacial tension measurements and wettability evaluation for geological $CO_2$ storage. *Advances in Water Resources*, 32(1):98–109, 2009.

K. W. Chang, M. A. Hesse, and J. Nicot. Reduction of lateral pressure propagation due to dissipation into ambient mudrocks during geological carbon dioxide storage. *Water Resources Research*, 49(5):2573–2588, 2013.

J. Chappelear and G. Hirasaki. A model of oil-water coning for two-dimensional, areal reservoir simulation. *Society of Petroleum Engineers Journal*, 16(02):65–72, 1976.

P. Chiquet, J.-L. Daridon, D. Broseta, and S. Thibeau. $CO_2$/water interfacial tensions under pressure and temperature conditions of $CO_2$ geological storage. *Energy Conversion and Management*, 48(3):736–744, 2007.

L. Cowton, J. Neufeld, N. White, M. Bickle, G. Williams, J. White, and R. A. Chadwick. Benchmarking of vertically-integrated $CO_2$ flow simulations at the

Sleipner Field, North Sea. *Earth and Planetary Science Letters*, 491:121–133, 2018.

G. J. Crutchley, I. A. Pecher, A. R. Gorman, S. A. Henrys, and J. Greinert. Seismic imaging of gas conduits beneath seafloor seep sites in a shallow marine gas hydrate province, Hikurangi Margin, New Zealand. *Marine Geology*, 272 (1-4):114–126, 2010.

G. Dagan and J. Bear. Solving the problem of local interface upconing in a coastal aquifer by the method of small perturbations. *Journal of Hydraulic Research*, 6 (1):15–44, 1968.

L. P. Dake. *Fundamentals of Reservoir Engineering*, volume 8. Elsevier, 1983.

H. P. G. Darcy. *Les Fontaines publiques de la ville de Dijon. Exposition et application des principes à suivre et des formules à employer dans les questions de distribution d'eau, etc.* V. Dalamont, 1856.

P. de Anna, B. Quaife, G. Biros, and R. Juanes. Prediction of the low-velocity distribution from the pore structure in simple porous media. *Physical Review Fluids*, 2(12):124103, 2017.

P.-G. De Gennes, F. Brochard-Wyart, and D. Quéré. *Capillarity and wetting phenomena: drops, bubbles, pearls, waves.* Springer Science & Business Media, 2013.

R. de Loubens and T. S. Ramakrishnan. Analysis and computation of gravity-induced migration in porous media. *Journal of Fluid Mechanics*, 675:60–86, 2011.

C. A. Ehlig-Economides and H. J. Ramey Jr. Transient rate decline analysis for wells produced at constant pressure. *Society of Petroleum Engineers Journal*, 21(01):98–104, 1981.

T. Eidvin, F. Riis, and Y. Rundberg. Upper Cainozoic stratigraphy in the central North Sea (Ekofisk and Sleipner fields). *Norsk Geologisk Tidsskrift*, 79(2):97–128, 1999.

W. L. Ellsworth. Injection-induced earthquakes. *Science*, 341(6142):1225942, 2013.

T. R. Evans and N. Coleman. North Sea geothermal gradients. *Nature*, 247(5435): 28, 1974.

A. Farcas and A. W. Woods. The effect of drainage on the capillary retention of $CO_2$ in a layered permeable rock. *Journal of Fluid Mechanics*, 618:349–359, 2009.

R. Farokhpoor, B. J. Bjørkvik, E. Lindeberg, and O. Torsæter. Wettability behaviour of $CO_2$ at storage conditions. *International Journal of Greenhouse Gas Control*, 12:18–25, 2013.

R. A. Feely, C. L. Sabine, K. Lee, W. Berelson, J. Kleypas, V. J. Fabry, and F. J. Millero. Impact of anthropogenic $CO_2$ on the $CaCO_3$ system in the oceans. *Science*, 305(5682):362–366, 2004.

P. Forchheimer. Wasserbewegung durch boden. *Z. Ver. Deutsch, Ing.*, 45:1782–1788, 1901.

M. Foschi, J. A. Cartwright, and F. J. Peel. Vertical anomaly clusters: Evidence for vertical gas migration across multilayered sealing sequences. *AAPG Bulletin*, 98(9):1859–1884, 2014.

M. Foschi, J. A. Cartwright, and C. W. MacMinn. Sequential vertical gas charge into multilayered sequences controlled by central conduits. *AAPG Bulletin*, 102 (5):855–883, 2018.

R. A. Freeze. Henry Darcy and the fountains of Dijon. *Groundwater*, 32(1):23–30, 1994.

A.-K. Furre, O. Eiken, H. Alnes, J. N. Vevatne, and A. F. Kiær. 20 years of monitoring $CO_2$-injection at Sleipner. *Energy procedia*, 114:3916–3926, 2017.

S. Gasda, J. Nordbotten, and M. A. Celia. Vertically averaged approaches for $CO_2$ migration with solubility trapping. *Water Resources Research*, 47(5), 2011. ISSN 1573-1499. doi: 10.1007/s10596-019-09857-0.

S. E. Gasda and I. Aavatsmark. Estimation of reduced pressure buildup due to brine seepage using a convolution technique. *Computational Geosciences*, pages 1–16, 2019.

S. E. Gasda, J. M. Nordbotten, and M. A. Celia. Vertical equilibrium with sub-scale analytical methods for geological $CO_2$ sequestration. *Computational Geosciences*, 79(1):15–27, 2009.

M. J. Golding, J. A. Neufeld, M. A. Hesse, and H. E. Huppert. Two-phase gravity currents in porous media. *Journal of Fluid Mechanics*, 678:248–270, 2011.

M. J. Golding, H. E. Huppert, and J. A. Neufeld. The effects of capillary forces on the axisymmetric propagation of two-phase, constant-flux gravity currents in porous media. *Physics of Fluids*, 25(3):036602, 2013.

M. J. Golding, H. E. Huppert, and J. A. Neufeld. Two-phase gravity currents resulting from the release of a fixed volume of fluid in a porous medium. *Journal of Fluid Mechanics*, 832:550—577, 2017.

S. Goudarzi, S. A. Mathias, and J. G. Gluyas. Simulation of three-component two-phase flow in porous media using method of lines. *Transport in Porous Media*, 112(1):1–19, 2016.

F. Gozalpour, S. Ren, and B. Tohidi. $CO_2$ eor and storage in oil reservoir. *Oil & gas science and technology*, 60(3):537–546, 2005.

D. H. Green and H. F. Wang. Specific storage as a poroelastic coefficient. *Water Resources Research*, 26(7):1631–1637, 1990.

I. Gunn and A. W. Woods. On the flow of buoyant fluid injected into a confined, inclined aquifer. *Journal of Fluid Mechanics*, 672:109–129, 2011.

M. A. Hesse and A. W. Woods. Buoyant dispersal of $CO_2$ during geological storage. *Geophysical Research Letters*, 37:L01403, 2010.

M. A. Hesse, H. A. Tchelepi, B. J. Cantwell, and F. M. Orr Jr. Gravity currents in horizontal porous layers: transition from early to late self-similarity. *Journal of Fluid Mechanics*, 577:363–383, 2007.

M. A. Hesse, F. M. Orr Jr., and H. A. Tchelepi. Gravity currents with residual trapping. *Journal of Fluid Mechanics*, 611:35–60, 2008.

D. R. Hewitt, J. A. Neufeld, and J. R. Lister. Ultimate regime of high rayleigh number convection in a porous medium. *Physical Review Letters*, 108(22):224503, 2012.

D. R. Hewitt, J. A. Neufeld, and N. J. Balmforth. Shallow, gravity-driven flow in a poro-elastic layer. *Journal of Fluid Mechanics*, 778:335–360, 2015.

J. J. Hidalgo, J. Fe, L. Cueto-Felgueroso, and R. Juanes. Scaling of convective mixing in porous media. *Physical review letters*, 109(26):264503, 2012.

J. T. Houghton, L. Meiro Filho, B. A. Callander, N. Harris, A. Kattenburg, and K. Maskell. *Climate change 1995: The science of climate change: contribution of working group I to the second assessment report of the Intergovernmental Panel on Climate Change*, volume 2. Cambridge University Press, 1996.

B. Hunt. Flow to a well in a multiaquifer system. *Water Resources Research*, 21 (11):1637–1641, 1985.

H. E. Huppert and J. A. Neufeld. The fluid mechanics of carbon dioxide sequestration. *Annual Review of Fluid Mechanics*, 46(1):255–272, 2014.

H. E. Huppert and J. E. Simpson. The slumping of gravity currents. *Journal of Fluid Mechanics*, 99(4):785–799, 1980.

H. E. Huppert and A. W. Woods. Gravity-driven flows in porous layers. *Journal of Fluid Mechanics*, 292:55–69, 1995.

A. Hurst, J. A. Cartwright, M. Huuse, R. Jonk, A. Schwab, D. Duranti, and B. Cronin. Significance of large-scale sand injectites as long-term fluid conduits: evidence from seismic data. *Geofluids*, 3(4):263–274, 2003.

S. Iglauer, C. Pentland, and A. Busch. $CO_2$ wettability of seal and reservoir rocks and the implications for carbon geo-sequestration. *Water Resources Research*, 51(1):729–774, 2015.

IPCC. Carbon Dioxide Capture and Storage. Special Report prepared by Working Group III of the Intergovernmental Panel on Climate Change, Cambridge, UK, 2005.

M. Jaccard, N. Rivers, and D. Keith. Carbon taxes, the economy and the poor. *The Financial Post*, page 1, 2007.

L. T. Jenkins, M. Foschi, and C. W. MacMinn. Impact of pressure dissipation on fluid injection into layered aquifers. *Journal of Fluid Mechanics*, 877:214–238, 2019a.

L. T. Jenkins, M. Foschi, and C. W. MacMinn. Gas injection and leakage in layered aquifers. *arXiv:1908.08137*, 2019b.

B. Jha and R. Juanes. A locally conservative finite element framework for the simulation of coupled flow and reservoir geomechanics. *Acta Geotechnica*, 2(3): 139–153, 2007.

R. Juanes, C. W. MacMinn, and M. L. Szulczewski. The footprint of the $CO_2$ plume during carbon dioxide storage in saline aquifers: Storage efficiency for capillary trapping at the basin scale. *Transport in Porous Media*, 82(1):19–30, 2010.

M. Kang, J. M. Nordbotten, F. Doster, and M. A. Celia. Analytical solutions for two-phase subsurface flow to a leaky fault considering vertical flow effects and fault properties. *Water Resources Research*, 50(4):3536–3552, 2014.

K. M. Keranen, M. Weingarten, G. A. Abers, B. A. Bekins, and S. Ge. Sharp increase in central Oklahoma seismicity since 2008 induced by massive wastewater injection. *Science*, 345(6195):448–451, 2014.

T. J. Kneafsey and K. Pruess. Laboratory flow experiments for visualizing carbon dioxide-induced, density-driven brine convection. *Transport in porous media*, 82 (1):123–139, 2010.

I. N. Kochina, N. N. Mikhailov, and M. V. Filinov. Groundwater mound damping. *International Journal of Engineering Science*, 21(4):413–421, 1983.

T. Kohl, K. Evans, R. Hopkirk, R. Jung, and L. Rybach. Observation and simulation of non-Darcian flow transients in fractured rock. *Water Resources Research*, 33(3):407–418, 1997.

O. Kolditz. Non-linear flow in fractured rock. *International Journal of Numerical Methods for Heat & Fluid Flow*, 11(6):547–575, 2001.

S. C. Krevor, R. Pini, B. Li, and S. M. Benson. Capillary heterogeneity trapping of $CO_2$ in a sandstone rock at reservoir conditions. *Geophysical Research Letters*, 38(15), 2011.

U. Kuila and M. Prasad. Specific surface area and pore-size distribution in clays and shales. *Geophysical Prospecting*, 61(2):341–362, 2013.

L. W. Lake. Enhanced oil recovery. 1989.

E. Lemmon. Thermophysical properties of fluid systems. *NIST Chemistry WebBook*, 1998.

Y. Liang, B. Wen, M. A. Hesse, and D. DiCarlo. Effect of dispersion on solutal convection in porous media. *Geophysical Research Letters*, 45(18):9690–9698, 2018.

M. G. Little and R. B. Jackson. Potential impacts of leakage from deep $CO_2$ geosequestration on overlying freshwater aquifers. *Environmental science & technology*, 44(23):9225–9232, 2010.

C. W. MacMinn and R. Juanes. Post-injection spreading and trapping of $CO_2$ in saline aquifers: impact of the plume shape at the end of injection. *Computational Geosciences*, 13(4):483, 2009.

C. W. MacMinn and R. Juanes. Buoyant currents arrested by convective dissolution. *Geophysical Research Letters*, 40(10):2017–2022, 2013.

C. W. MacMinn, M. L. Szulczewski, and R. Juanes. $CO_2$ migration in saline aquifers. Part 1. Capillary trapping under slope and groundwater flow. *Journal of fluid mechanics*, 662:329–351, 2010.

C. W. MacMinn, M. L. Szulczewski, and R. Juanes. $CO_2$ migration in saline aquifers. Part 2. Capillary and solubility trapping. *Journal of Fluid Mechanics*, 688:321–351, 2011.

C. W. MacMinn, J. A. Neufeld, M. A. Hesse, and H. E. Huppert. Spreading and convective dissolution of carbon dioxide in vertically confined, horizontal aquifers. *Water Resources Research*, 48(11), 2012.

E. L. Majer, R. Baria, M. Stark, S. Oates, J. Bommer, B. Smith, and H. Asanuma. Induced seismicity associated with enhanced geothermal systems. *Geothermics*, 36(3):185–222, 2007.

S. A. Mathias, A. P. Butler, and H. Zhan. Approximate solutions for forchheimer flow to a well. *Journal of Hydraulic Engineering*, 134(9):1318–1325, 2008.

S. A. Mathias, P. E. Hardisty, M. R. Trudell, and R. W. Zimmerman. Approximate solutions for pressure buildup during $CO_2$ injection in brine aquifers. *Transport in Porous Media*, 79(2):265–284, 2009.

S. A. Mathias, G. J. G. M. de Miguel, K. E. Thatcher, and R. W. Zimmerman. Pressure buildup during $CO_2$ injection into a closed brine aquifer. *Transport in porous media*, 89(3):383–397, 2011a.

S. A. Mathias, G. J. González Martínez de Miguel, K. E. Thatcher, and R. W. Zimmerman. Pressure buildup during $CO_2$ injection into a closed brine aquifer. *Transport in Porous Media*, 89(3):383–397, 2011b.

S. Mazumder. *Numerical methods for partial differential equations: finite difference and finite volume methods*. Academic Press, 2015.

M. Muskat. Physical principles of oil production., 1949, 1949.

M. Muskat and M. W. Meres. The flow of heterogeneous fluids through porous media. *Physics*, 7(9):346–363, 1936.

P. Nejat, F. Jomehzadeh, M. M. Taheri, M. Gohari, and M. Z. A. Majid. A global review of energy consumption, $CO_2$ emissions and policy in the residential sector (with an overview of the top ten $CO_2$ emitting countries). *Renewable and sustainable energy reviews*, 43:843–862, 2015.

J. A. Neufeld, D. Vella, and H. E. Huppert. The effect of a fissure on storage in a porous medium. *Journal of Fluid Mechanics*, 639:239–259, 2009.

J. A. Neufeld, M. A. Hesse, A. Riaz, M. A. Hallworth, H. A. Tchelepi, and H. E. Huppert. Convective dissolution of carbon dioxide in saline aquifers. *Geophysical Research Letters*, 37(22), 2010.

J. A. Neufeld, D. Vella, H. E. Huppert, and J. R. Lister. Leakage from gravity currents in a porous medium. Part 1. A localized sink. *Journal of Fluid Mechanics*, 666:391–413, 2011.

S. P. Neuman. Theoretical derivation of Darcy's law. *Acta Mechanica*, 25(3-4): 153–170, 1977.

J.-P. Nicot. Evaluation of large-scale $CO_2$ storage on fresh-water sections of aquifers: An example from the Texas Gulf Coast Basin. *International Journal of Greenhouse Gas Control*, 2(4):582–593, 2008.

J.-P. Nicot, S. A. Hosseini, and S. V. Solano. Are single-phase flow numerical models sufficient to estimate pressure distribution in $CO_2$ sequestration projects? *Energy Procedia (Proceedings of the 10th International Conference on Greenhouse Gas Control Technologies)*, 4:3919–3926, 2011.

J. M. Nordbotten and M. A. Celia. An improved analytical solution for interface upconing around a well. *Water Resources Research*, 42(8), 2006a.

J. M. Nordbotten and M. A. Celia. Similarity solutions for fluid injection into confined aquifers. *Journal of Fluid Mechanics*, 561:307–327, 2006b.

J. M. Nordbotten, M. A. Celia, and S. Bachu. Injection and storage of $CO_2$ in deep saline aquifers: Analytical solution for $CO_2$ plume evolution during injection. *Transport in Porous media*, 58(3):339–360, 2005.

E. H. Oelkers, S. R. Gislason, and J. Matter. Mineral carbonation of $CO_2$. *Elements*, 4(5):333–337, 2008.

N. Oreskes. The scientific consensus on climate change. *Science*, 306(5702):1686–1686, 2004.

S. S. Pegler, H. E. Huppert, and J. A. Neufeld. Fluid injection into a confined porous layer. *Journal of Fluid Mechanics*, 745:592–620, 2014a.

S. S. Pegler, H. E. Huppert, and J. A. Neufeld. Fluid migration between confined aquifers. *Journal of Fluid Mechanics*, 757:330–353, 2014b.

S. S. Pegler, E. L. Bain, H. E. Huppert, and J. A. Neufeld. Fluid invasion of an unsaturated leaky porous layer. *Journal of Fluid Mechanics*, 777:97–121, 2015.

C. H. Pentland, R. El-Maghraby, S. Iglauer, and M. J. Blunt. Measurements of the capillary trapping of super-critical carbon dioxide in Berea sandstone. *Geophysical Research Letters*, 38(6), 2011.

R. M. Pollyea, M. C. Chapman, R. S. Jayne, and H. Wu. High density oilfield wastewater disposal causes deeper, stronger, and more persistent earthquakes. *Nature communications*, 10(1):3077, 2019.

D. Pritchard. Gravity currents over fractured substrates in a porous medium. *Journal of Fluid Mechanics*, 584:415–431, 2007.

D. Pritchard, A. W. Woods, and A. J. Hogg. On the slow draining of a gravity current moving through a layered permeable medium. *Journal of Fluid Mechanics*, 444:23–47, 2001.

K. Pruess. *ECO2N: A TOUGH2 fluid property module for mixtures of water, NaCl, and $CO_2$*. Lawrence Berkeley National Laboratory Berkeley, 2005.

K. Pruess, C. Oldenburg, and G. Moridis. TOUGH2 user's guide version 2. Technical report, Ernest Orlando Lawrence Berkeley National Laboratory, Berkeley, CA (US), 1999.

M. R. Raupach, G. Marland, P. Ciais, C. Le Quéré, J. G. Canadell, G. Klepper, and C. B. Field. Global and regional drivers of accelerating $CO_2$ emissions. *Proceedings of the National Academy of Sciences*, 104(24):10288–10293, 2007.

A. Riaz, M. A. Hesse, H. Tchelepi, and F. Orr. Onset of convection in a gravitationally unstable diffusive boundary layer in porous media. *Journal of Fluid Mechanics*, 548:87–111, 2006.

J. Rogelj, M. Den Elzen, N. Höhne, T. Fransen, H. Fekete, H. Winkler, R. Schaeffer, F. Sha, K. Riahi, and M. Meinshausen. Paris agreement climate proposals need a boost to keep warming well below 2°C. *Nature*, 534(7609):631, 2016.

J. Roof. Snap-off of oil droplets in water-wet pores. *Society of Petroleum Engineers Journal*, 10(01):85–90, 1970.

P. G. Saffman and G. I. Taylor. The penetration of a fluid into a porous medium or hele-shaw cell containing a more viscous liquid. *Proceedings of the Royal Society of London. Series A. Mathematical and Physical Sciences*, 245(1242):312–329, 1958.

P. Segall. Earthquakes triggered by fluid extraction. *Geology*, 17(10):942–946, 1989.

Z. Şen. Analytical solution incorporating nonlinear radial flow in confined aquifers. *Water Resources Research*, 24(4):601–606, 1988.

Z. Şen. Nonlinear radial flow in confined aquifers toward large-diameter wells. *Water Resources Research*, 26(5):1103–1109, 1990.

L. F. Shampine and M. W. Reichelt. The MATLAB ODE suite. *SIAM journal on scientific computing*, 18(1):1–22, 1997.

L. F. Shampine and S. Thompson. Solving DDEs in MATLAB. *Applied Numerical Mathematics*, 37(4):441–458, 2001.

J. Shin, S. Dalziel, and P. Linden. Gravity currents produced by lock exchange. *Journal of Fluid Mechanics*, 521:1–34, 2004.

D. Simpson, W. Leith, and C. Scholz. Two types of reservoir-induced seismicity. *Bulletin of the Seismological Society of America*, 78(6):2025–2040, 1988.

J. E. Simpson. Gravity currents in the laboratory, atmosphere, and ocean. *Annual Review of Fluid Mechanics*, 14(1):213–234, 1982.

S. Solomon, D. Qin, M. Manning, K. Averyt, and M. Marquis. *Climate change 2007-the physical science basis: Working group I contribution to the fourth assessment report of the IPCC*, volume 4. Cambridge university press, 2007.

O. Strack. Some cases of interface flow towards drains. *Journal of Engineering Mathematics*, 6(2):175–191, 1972.

Q. Sun, S. Wu, J. A. Cartwright, and D. Dong. Shallow gas and focused fluid flow systems in the Pearl River Mouth Basin, northern South China Sea. *Marine Geology*, 315:1–14, 2012.

M. L. Szulczewski, C. W. MacMinn, H. J. Herzog, and R. Juanes. Lifetime of carbon capture and storage as a climate-change mitigation technology. *Proceedings of the National Academy of Sciences of the United States of America*, 109(14): 5185–5189, 2012.

P. Talwani and S. Acree. Pore pressure diffusion and the mechanism of reservoir-induced seismicity. In *Earthquake Prediction*, pages 947–965. Springer, 1985.

G. M. G. Teige, W. L. H. Thomas, C. Hermanrud, P.-E. Øren, L. Rennan, O. B. Wilson, and H. G. Nordgård Bolås. Relative permeability to wetting-phase water in oil reservoirs. *Journal of Geophysical Research*, 111:B12204, 2006.

G. van der Kamp and J. E. Gale. Theory of Earth tide and barometric effects in porous formations with compressible grains. *Water Resources Research*, 19(2): 538–544, 1983.

D. Vella, J. A. Neufeld, H. E. Huppert, and J. R. Lister. Leakage from gravity currents in a porous medium. Part 2. A line sink. *Journal of Fluid Mechanics*, 666:414–427, 2011.

V. Vilarrasa, D. Bolster, M. Dentz, S. Olivella, and J. Carrera. Effects of $CO_2$ compressibility on $CO_2$ storage in deep saline aquifers. *Transport in porous media*, 85(2):619–639, 2010.

J. M. West, J. Pearce, M. Bentham, and P. Maul. Issue profile: environmental issues and the geological storage of $CO_2$. *European Environment*, 15(4):250–259, 2005.

G. A. Williams and R. A. Chadwick. An improved history-match for layer spreading within the Sleipner plume including thermal propagation effects. *Energy Procedia*, 114:2856–2870, 2017.

A. W. Woods and A. Farcas. Capillary entry pressure and the leakage of gravity currents through a sloping layered permeable rock. *Journal of Fluid Mechanics*, 618:361–379, 2009.

A. V. Wouwer, P. Saucez, W. Schiesser, and S. Thompson. A matlab implementation of upwind finite differences and adaptive grids in the method of lines. *Journal of computational and applied mathematics*, 183(2):245–258, 2005.

T. Xu, J. A. Apps, and K. Pruess. Numerical simulation of $CO_2$ disposal by mineral trapping in deep aquifers. *Applied geochemistry*, 19(6):917–936, 2004.

X. Xu, S. Chen, and D. Zhang. Convective stability analysis of the long-term storage of carbon dioxide in deep saline aquifers. *Advances in Water Resources*, 29(3):397–407, 2006.

Y. C. Yortsos. A theoretical analysis of vertical flow equilibrium. *Transport in Porous Media*, 18(2):107–129, 1995.

T. Young. III. An essay on the cohesion of fluids. *Philosophical transactions of the royal society of London*, (95):65–87, 1805.

B. Zhao, C. W. MacMinn, H. E. Huppert, and R. Juanes. Capillary pinning and blunting of immiscible gravity currents in porous media. *Water Resources Research*, 50(9):7067–7081, 2014.

Z. Zheng, B. Guo, I. C. Christov, M. A. Celia, and H. A. Stone. Flow regimes for fluid injection into a confined porous medium. *Journal of Fluid Mechanics*, 767: 881–909, 2015.

P. Zweigel, R. Arts, A. E. Lothe, and E. B. Lindeberg. Reservoir geology of the utsira formation at the first industrial-scale underground $CO_2$ storage site

(Sleipner area, North Sea). *Geological Society, London, Special Publications*, 233(1):165–180, 2004.